UNIVERSITÄT
BERN

Graduate School for Cellular and Biomedical Sciences

University of Bern

Functional Architecture of the Tripartite Attachment Complex of *Trypanosoma brucei*

PhD Thesis submitted by

Philip Stettler

for the degree of

PhD in Biochemistry and Molecular Biology

Supervisor

Prof. Dr. André Schneider

Department of Chemistry, Biochemistry and Pharmaceutical Sciences

Faculty of Science of the University of Bern

Co-advisor

Prof. Dr. Torsten Ochsenreiter

Institute of Cell Biology

Faculty of Science of the University of Bern

Accepted by the Faculty of Medicine, the Faculty of Science and the Vetsuisse Faculty of the University of Bern at the request of the Graduate School for Cellular and Biomedical Sciences.

Bern, Dean of the Faculty of Medicine

Bern, Dean of the Faculty of Science

Bern, Dean of the Vetsuisse Faculty Bern

Content

Abstract

Eukaryotic cells are highly complex and contain many organelles. One of the defining features of eukaryotes is the mitochondrion, which is a remnant of the endosymbiotic event that gave rise to this domain of life. This Thesis features mitochondrial genome inheritance systems and highlights the systems found in *Trypanosoma brucei*, a member of the understudied Discoba supergroup. Mitochondrial genome inheritance has been studied since many years. However, how the replicated mitochondrial genomes are segregated during cell division is not well understood. In human and yeast cells, which are comparatively closely related species classified as Opisthokonta in the supergroup Amorphea, mitochondrial genomes are packed in nucleoids which are trafficked along cytoskeletal structures. Similar principles may apply to the mitochondria of land plants, which belong to the supergroup Archaeplastida, although there are also clear differences. Outside of these two supergroups, the mitochondrial genome segregation system of *T. brucei* is the only one that has been thoroughly investigated. *T. brucei* has a single mitochondrion with a genome that is condensed into a single nucleoid, known as the kinetoplast. The kinetoplast is segregated during cell division by basal body movements. This is made possible by a protein complex that connects the two structures: the tripartite attachment complex (TAC). The TAC consists of at least nine subunits, each present in several hundred to a few thousand copies. The role, localization, and direct interaction partners of the nine TAC subunits are well known. This Thesis contains two studies focusing on the TAC. The first one highlights the contact site between the outer and inner mitochondrial membranes of the TAC and the second focuses on the assembly of the mitochondrial outer membrane TAC module. A third study, which is not related to the TAC, reports the discovery of a novel pathway regulating mitochondrial DNA replication.

The first study focuses on TAC60 and p166, two TAC subunits located in the outer and inner mitochondrial membranes, respectively. Previous studies have shown that these proteins interact directly to form a unique and permanent contact site between the outer and inner mitochondrial membranes that is essential for TAC function. Our goal was to characterize this interaction at a molecular level. We identified the interaction domains down to the amino acid level. Our results suggest that hydrophobic interfaces are at the core of this membrane contact site. This was an unexpected finding, as the interaction domains in both proteins contain well conserved charged amino acids.

In the second study we investigated the assembly of the mitochondrial outer membrane TAC module. This module is the most complex of the three TAC modules. It contains five subunits:

pATOM36, TAC40, TAC42, TAC60, and TAC65. Although the TAC assembles *de novo* and unidirectionally from the basal body towards the kinetoplast, the subunits of the mitochondrial outer membrane TAC module do not strictly follow this order. In this study, we identified four detergent-soluble assembly intermediates, which can be grouped into two classes. One class contains an oligomeric TAC40 subcomplex, as well as two more complicated TAC40-, TAC42-, TAC60-containing subcomplexes which likely originate from a shared assembly pathway. The second class contains a single subcomplex containing pATOM36 and TAC65. Our results suggest that the largest assembly intermediate from the first class merges with the assembly intermediate of the second class to form the mitochondrial outer membrane TAC module. In addition, we show that the N-terminal domain of TAC60 is essential for this last step.

The third study focuses on kinetoplast DNA maintenance and replication and is unrelated to the TAC. The kinetoplast is an intricate DNA network containing two classes of circular DNA molecules, maxicircles and minicircles. We identified a novel pathway relevant for maxicircle level regulation in *T. brucei*, comprising the three proteins MaRF11, TbPam16, and TbPam18. Notably, TbPam16 and TbPam18 are orthologs of proteins involved in mitochondrial protein import in other lineages. Our findings revealed that in trypanosomes, these proteins have acquired lineage-specific functions. Together with the newly discovered MaRF11 protein, they contribute to the regulation of maxicircle replication by yet unknown, life cycle stage-specific pathways. Interestingly, TbPam16 and TbPam18 are mitochondrial inner membrane proteins and this localization is essential for their function in maxicircle maintenance and/or replication.

1. Introduction

1.1 Eukaryogenesis and the endosymbiotic theory

Planet earth formed around 4.54 billion years ago [1]. Habitable environments, such as surface water pools and solid crusts, may have formed around 4.3 billion years ago [2]. Recent research suggests that early ecosystems emerged rapidly. Although these ecosystems were likely species-rich, it is widely accepted that all modern cellular life shares a single ancestor: the Last Universal Common Ancestor (LUCA) (Figure 1) [3]. LUCA is thought to have evolved around 4.2 billion years ago and was likely an anaerobic prokaryotic acetogen [4]. The precise timing of the divergence leading to the three domains of life—Bacteria, Archaea, and Eukarya—is less certain. However, Bacteria may have originated from an ancestral lineage around 3.4 billion years ago, while the archaeal lineage likely emerged around 2.8 billion years ago (Figure 1) [5]. The origin of eukaryotes remained unclear until the early 21st century, when genetic analyses revealed that Archaea are a paraphyletic group, which includes the eukaryotes [6]. Consequently, Eukarya are now recognized as the youngest of the three domains that likely emerged shortly after the Great Oxidation Event, around 2.0-1.8 billion years ago (Figure 1) [7].

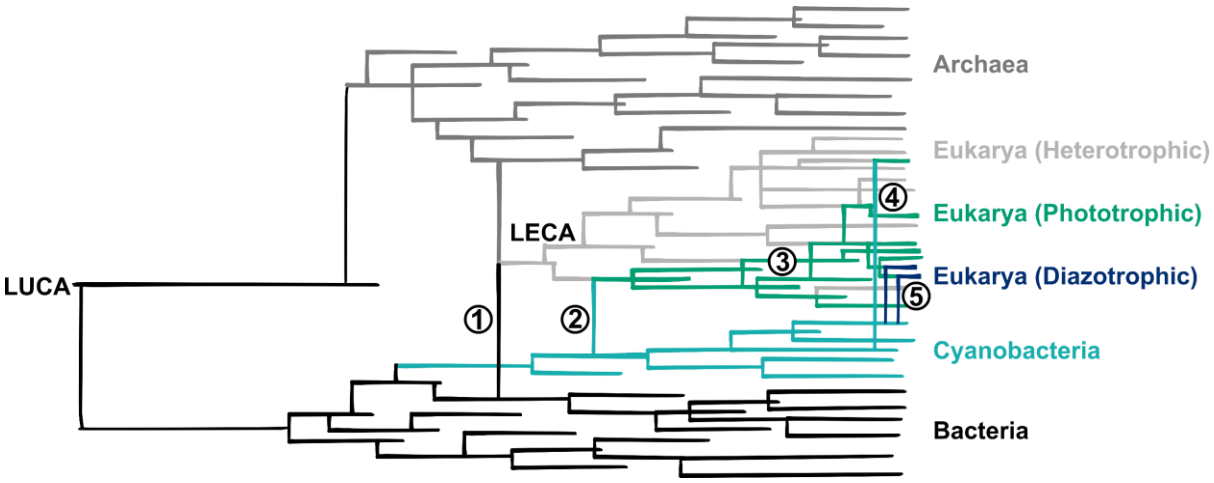

Figure 1. **Phylogenetic history of extant cellular life**. This phylogenetic tree illustrates the evolutionary history of Bacteria, Archaea, and Eukarya with a spotlight on the emergence and radiation of the Eukarya. Numbers and length of nodes and branches have been placed arbitrarily. The temporal emergence of the labelled lineages is shown to scale. The tree displays only endosymbiotic events that resulted in extant lineages and does not include transient events or the role of non-cellular life. Numbered events are: Emergence of the mitochondrion (1), the chloroplasts (2), secondary and more complex plastids (3), the chromatophore (4), and nitrogen-fixing organelles (5) which gave rise to diazotrophic eukaryotes that are independent of organic nitrogen. LUCA: last universal common ancestor, LECA: last eukaryotic common ancestor.

The Bacteria, Archaea, and Eukarya have been the widely accepted three domains of cellular life for several decades [8, 9]. However, genetic research has revealed that only Bacteria and Archaea qualify as fundamental domains, while Eukarya represent a distinct lineage with an evolutionary origin that is still being debated. This complex evolutionary path is known as "eukaryogenesis", the origin of complex cellular life and all modern eukaryotes [10, 11]. Although many hypotheses have been proposed, including scenarios in which viruses play a critical role [10-12], the process remains poorly understood. Nevertheless, it is evident that a key event was the metabolic enslavement of an endosymbiotic Bacterium, the early mitochondrion, by an archaeal host cell (Figures 1 & 2) [13]. Although the idea that mitochondria originated through endosymbiosis was first proposed in the early 20th century, it did not gain broader acceptance until 1967, when the "endosymbiotic theory" was repopularized [14]. As a result, mitochondria are now considered a defining feature of eukaryotic cells. Importantly, the few extant lineages that lack mitochondria have been shown to be descendants of organisms that have lost mitochondria secondarily. This supports the view that Eukarya are a monophyletic group that share a single common ancestor [15, 16].

The currently widely accepted stages of eukaryogenesis state that eukaryotes arose from an Archaea of the Asgard superphylum [17, 18], which entered into a symbiotic relationship with an Alphaproteobacterium (illustrated in figure 1) [19]. However, it remains unclear whether Eukarya are a sister group to modern Asgard Archaea, or if they are phylogenetically nested within this superphylum [20]. Similarly, the precise evolutionary origin of the Alphaproteobacterium involved in this event is still unresolved [21, 22]. A major point of debate is precisely when during eukaryogenesis the endosymbiont was incorporated, especially whether the host cell had already developed a nucleus, and what the initial mutual benefits were [23]. The supply of excess energy of the endosymbiont to the host may have been a central aspect [24]. However, the metabolic route by which this energy may have been provided is unknown. One attractive possibility is the hydrogen metabolism [25]. Additionally, the Great Oxidation Event, which predates eukaryotic radiation, likely impacted eukaryogenesis significantly [26].

Although many questions about the endosymbiotic theory and the origin of eukaryotes remain debated, it is well established that the mitochondrion is derived from a free-living Bacterium. Furthermore, the mitochondrion is not the only eukaryotic organelle with such an origin. Throughout evolutionary history, eukaryotes have repeatedly engulfed endosymbionts, some of which have been retained and transformed into organelles in several lineages that emerged since the Last Eukaryotic Common Ancestor (LECA) (Figure 1). Endosymbiotic events can be categorized as primary endosymbiotic events, where the endosymbiont is of bacterial origin, or

as secondary or higher-order endosymbiotic events, where endosymbionts are eukaryotes containing organelles from earlier endosymbiotic events. Additionally, serial endosymbiosis describes endosymbiotic events occurring in host cells that already contain organelles derived from endosymbiosis [27]. Notable examples of organelles that arose through serial (secondary) endosymbiosis include chloroplasts, chloroplast-derived secondary or higher-order plastids, chromatophores, as well as nitrogen fixing organelles and endosymbionts (Figure 2).

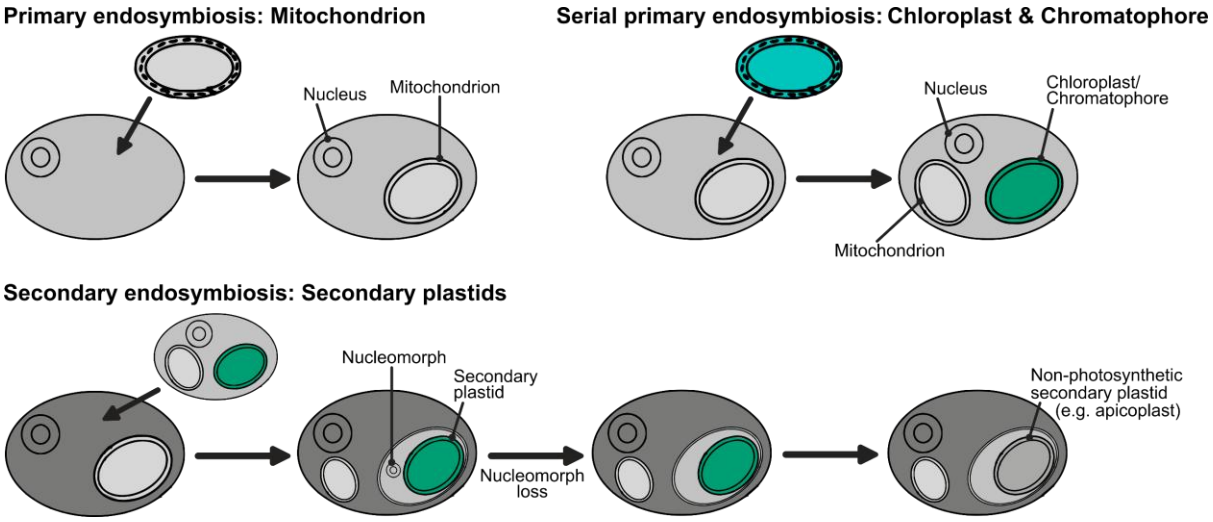

Figure 2. **Illustrations of primary and secondary endosymbiosis**. The top left panel illustrates the primary endosymbiosis resulting in the mitochondrion. Whether the host cell contained a nucleus is debated. The top right panel displays the serial primary endosymbiotic uptake of a Cyanobacterium-like cell by an eukaryote giving rise to primary plastids like chloroplasts and chromatophores. The bottom panel illustrates a secondary endosymbiosis where a eukaryotic host cell takes up a chloroplast-containing eukaryote giving rise to secondary plastids. The nuclear genome of the eukaryotic endosymbiont is termed the nucleomorph, which in some lineages has been lost. The loss of photosynthetic activity of the secondary plastid can give rise to organelles with diverse functions such as the apicoplast. Images adapted from [28].

1.2 Endosymbiosis-derived eukaryotic organelles

The following chapters will explore the origin, evolution, and function of eukaryotic organelles that emerged through endosymbiosis. Particular emphasis will be placed on one of these organelle's defining features: their genomes. The focus will be on how these organellar genomes are maintained and segregated during cell division.

1.2.1 Mitochondrion and mitochondria-derived organelles

Mitochondria have been retained in almost all eukaryotic lineages and have likely greatly contributed to the complexity and diversity of modern eukaryotes [10, 29]. Extant eukaryotes are highly adapted organisms that thrive in nearly every habitat. The use and demand for

mitochondrial activities in these organisms is consequently highly diverse, which has driven the evolution of specialized mitochondria. In some groups, such specializations have continued to a point where the resulting organelles hardly resemble classical mitochondria, two such examples are hydrogenosomes and mitosomes (Figure 3) [30].

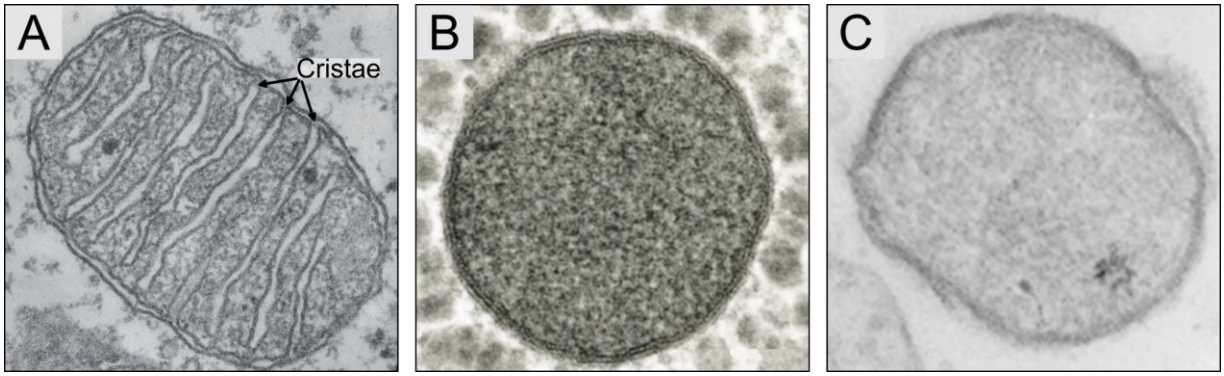

Figure 3. **Transmission electron microscopy images of mitochondria and mitochondria-derived organelles.** (A) Mitochondrion with well-developed cristae. Image adapted from [31]. (B) and (C) a hydrogenosome and a mitosome which lack cristae. Images adapted from [32].

Despite their long coevolution with the eukaryotic host cell, all mitochondria, as well as mitochondria-derived hydrogenosomes and mitosomes, still share some traits with their free-living relatives. Notably, these organelles are surrounded by two membranes, known in mitochondria as the mitochondrial outer membrane (OM) and inner membrane (IM). These membranes have been inherited from the Alphaproteobacterium [14]. Mitochondria also contain their own genome and possess the machinery necessary for transcription and translation. However, this genome has been drastically reduced over time, and has been completely lost in most hydrogenosomes and mitosomes [30]. Importantly, rather than disappearing, a large proportion of the endosymbiont's genes has been transferred to the nuclear genome of the host cell (Chapter 1.3.1) [33-35]. Consequently, the majority of mitochondrial proteins, and all proteins of hydrogenosomes and mitosomes, are synthesized in the cytosol of the eukaryotic cell and imported into the organelles (see chapter 1.5.1.1) [36, 37]. Notably, this gene transfer process has occurred independently in the different eukaryotic lineages since the divergence of LECA and continues even in modern eukaryotes [35, 38].

Hydrogenosomes and mitosomes are highly specialized organelles found in most eukaryotic supergroups [30]. This suggests that these organelles evolved independently from mitochondria multiple times, raising questions about how hydrogenosomes and mitosomes should be defined. Both organelle groups have been studied mostly in model organisms of two genera: *Trichomonas,* for hydrogenosomes, and *Giardia*, for mitosomes [30]. *Trichomonas* and other organisms, where hydrogenosome-like organelles have been found, are anaerobic eukaryotes

which have streamlined organelles allowing the generation of ATP by substrate-level phosphorylation in the absence of oxygen. This process generates hydrogen gas [39]. Interestingly, the ability to generate hydrogen gas rather than water during oxidative phosphorylation has since also been described in classical mitochondria, which may help to explain why hydrogenosomes have evolved in several unrelated lineages [40]. Mitosomes, in contrast, are unique among mitochondria-related organelles in that they do not produce ATP. Their essential function is the biosynthesis of iron-sulfur clusters, a vital metabolic role inherited from their mitochondrial ancestor [41]. Due to their highly streamlined functions, hydrogenosomes and mitosomes have greatly reduced proteomes [42, 43], and reflected by the absence of oxidative phosphorylation processes, both organelle groups typically lack crista-folds on their IM (Figure 3BC) [44, 45]. The lack of an organellar genome in most hydrogenosomes and mitosomes lowers some evolutionary constraints that act during cell proliferation and segregation. Nevertheless, these organelles cannot form *de novo* and must be properly segregated during cell division. This segregation is coordinated by dynamin-like proteins, which play a crucial role in their biogenesis and distribution [44, 46, 47].

Mitochondria share the essential pathways for iron-sulfur cluster biogenesis with hydrogenosomes and mitosomes [41]. But in addition, mitochondria have also been shown to play a role in controlling reactive oxygen species, calcium signalling, lipid biogenesis and trafficking, apoptosis, and energy production [48-50]. Unlike hydrogenosomes and mitosomes, mitochondria have cristae in their IM, which are critical for oxidative phosphorylation (Figure 3A) [51]. This process drives and consumes the electrochemical gradient of the mitochondrial IM [52]. For many years, mitochondrial research was largely limited to some species of the Animalia and Fungi, resulting in a narrow view of mitochondrial diversity. However, findings over the past few decades have revealed that mitochondria are far more diverse than once thought. They can exist as numerous rod-shaped organelles, as dynamic networks that undergo continuous fission and fusion, or in a few lineages even as single large organelles [47, 49, 53, 54]. Like hydrogenosomes and mitosomes, mitochondria cannot form *de novo* and have to be evenly segregated during cell division. In most organisms, dynamin-like proteins mediate mitochondrial fission [47, 55, 56]. However, to which extent and how mitochondrial segregation is controlled is in most cases not well understood and the same applies to the inheritance of the mitochondrial genomes (Chapter 1.3.3).

1.2.2 Chloroplasts and chloroplast-derived plastids

Chloroplasts and chloroplast-derived plastids can be traced back to a single primary endosymbiotic event (Figures 1&2). While some studies date this event to around 900 million years ago [57-59], other results suggest an origin of the chloroplast as early as 1.9 billion years ago [60-62]. It is thought that the chloroplast evolved from a Cyanobacterium similar to the extant species *Gloeomargarita lithophora*. This Cyanobacterium became an endosymbiont in the common ancestor of green algae and land plants (Chloroplastida), red algae (Rhodophyta) and glaucophyte algae (Glaucophyta) [57-59, 63-65]. This early photosynthetic organelle must have greatly increased the fitness of its host cell, giving rise to phototrophic eukaryotic life. The impact of the early plastid is reflected in the numerous secondary, tertiary, and even higher-order endosymbiotic events that followed the emergence of the first plastid and allowed the horizontal transfer of phototrophy to at least five extant monophyletic eukaryotic supergroups. Interestingly, not all plastids retained their photosynthetic function. In some lineages, plastids became non-photosynthetic, as seen in the apicoplast of the Apicomplexa [28, 57].

1.2.2.1 Chloroplasts and plastids of land plants and green, red, and glaucophyte algae

Chloroplasts and chloroplast-like organelles found in modern land plants, green algae, red algae, and glaucophyte algae are primary organelles that share a monophyletic origin [57]. Although textbooks often depict chloroplasts as oval-shaped structures to reflect their bacterial ancestry, their morphology is highly variable [66]. Chloroplasts are enclosed by two organellar membranes, both of which have been inherited from their cyanobacterial ancestor [67]. Photosynthesis occurs in special compartments of the chloroplast stroma called thylakoids (Figure 4A) [68]. Thylakoids are internal membranes that form diverse shapes where the photosystem and the chloroplast ATP synthase complexes are localized. Similar to the IM of mitochondria, the thylakoid membranes are polarized and this membrane potential is used to generate ATP in the stroma of the chloroplast. This energy is used by enzymes of the Calvin cycle to generate glucose and other metabolites [69].

In addition to photosynthetic chloroplasts, a variety of chloroplast-like organelles have evolved, particularly in land plants (Figure 4B) [70]. These organelles enable the land plants to form highly specialized, organ-like tissues. Proplastids are undifferentiated plastids that contain all components to develop into chloroplasts or other types of plastids. They are typically found in undifferentiated cells and gametes. During germination, proplastids first differentiate into etioplasts which are non-photosynthetic plastids and later into functional chloroplasts provided they are exposed to light. In non-photosynthetic tissues, however, proplastids give rise

to specialized storage plastids. Examples include: starch-storing amyloplasts, lipid- and terpenoid-synthesizing and -storing elaioplasts, and protein-storing proteinoplasts. Specialized plastids can also develop from active chloroplasts. These include chromoplasts, which accumulate colouring carotenoids, and gerontoplasts, which are non-photosynthetic and linked to senescence processes [70].

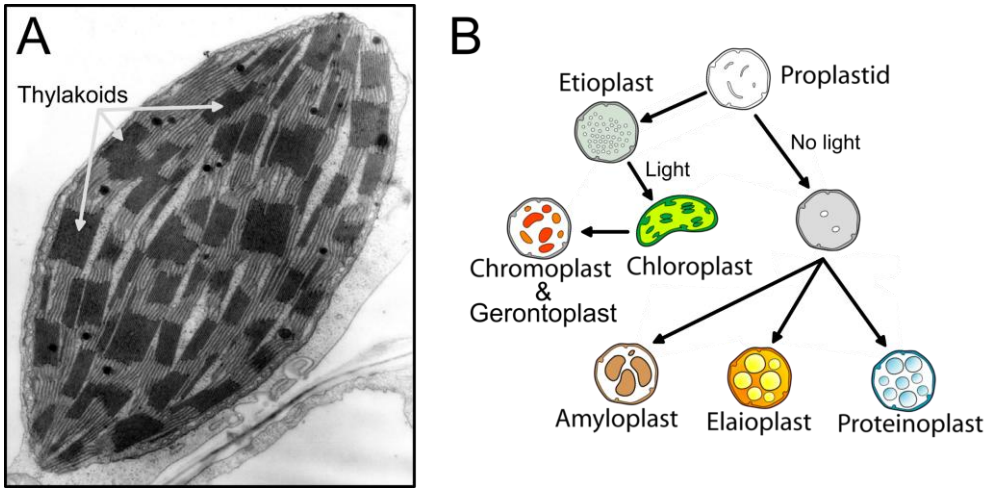

Figure 4. **Chloroplast morphology and development of chloroplasts and specialized plastids in land plants.** (A) Transmission electron microscopy image of a land plant chloroplast with prominent thylakoids. Image adapted from [71]. (B) Illustrations of plastid types and their development in land plants. Images adapted from wikiwand.com.

Chloroplasts and chloroplast-like organelles contain their own genomes and are capable of both transcription and translation. However, many plastid genes have been lost or transferred to the nuclear genome during evolution, resulting in highly reduced plastid genomes. Consequently, chloroplasts and chloroplast-like organelles, similar to mitochondria, depend heavily on the import of proteins encoded by nuclear genes [72]. In some non-photosynthetic lineages, plastid genomes have even been lost completely [73, 74]. Nevertheless, the majority of cells containing chloroplasts or chloroplast-like organelles face the challenge of inheriting functional copies of these organelles with intact genomes to daughter cells during cell division.

Similar to the genomes of Cyanobacteria, the chloroplast genome is organised into nucleoids, which are compact, protein-bound DNA structures that typically contain multiple copies of the chloroplast genome [75]. A single chloroplast often contains several nucleoids that are distributed throughout the stroma and have been shown to associate with thylakoids [76, 77]. Proteomic studies of nucleoids have identified numerous associated proteins, many of which are unlikely to have originated from the ancestral Cyanobacterium. These proteins include enzymes involved in DNA replication and transcription, as well as those potentially responsible for DNA packaging and the anchoring of nucleoids to thylakoids [78, 79]. Despite progress in

understanding nucleoid structures, the mechanisms by which replication and, most critically, segregation of nucleoids are accomplished during cytokinesis remain unknown [77, 80]. Only a few enzymes, such as DNA gyrases, recombinases, and holiday junction resolvases, have been linked to nucleoid separation [81-83]. It has been proposed that the connection to the thylakoid membrane may provide a segregation mechanism [84]. However, live cell imaging studies have revealed that chloroplast nucleoids likely dissolve, or at least evenly distribute within the stroma, during chloroplast division [85, 86]. However, the factors that mediate this process remain unknown [77, 85, 86]. Although most Archaeplastida species contain multiple chloroplasts per cell, each containing several nucleoids, it is expected that their inheritance is controlled rather than random. This is particularly evident in certain *Chlamydomonas* species, which are unicellular organisms that contain only a single chloroplast. Through insertional mutagenesis, a *C. reinhardtii* strain with a single chloroplast nucleoid per cell has been generated [87]. This strain displayed unequal chloroplast nucleoid segregation, possibly because the replicated nucleoid could not dissociate during cytokinesis [85]. Due to their single chloroplast, *Chlamydomonas* may become a valuable model organism to study chloroplast nucleoid inheritance.

1.2.2.2 Apicoplast and plastids from secondary and more complex endosymbiosis

Plastids have been transferred horizontally across eukaryotic supergroups through numerous secondary, tertiary, and even more complex endosymbiotic events (illustrated in figure 1). Today, secondary plastids are found in species belonging to the supergroups TSAR, Haptista, Cryptista, and Discoba [28]. These lineages are extremely species-rich, with an estimated one million extant species existing [88, 89].

Plastids that originated through secondary or higher-order endosymbiosis have a particularly complex biogenesis. While primary plastids have two organellar membranes, secondary plastids have four; two inner membranes derived from the primary plastid, and two outer membranes derived from the eukaryotic endosymbiont (primary host) and from the secondary host cell, after phagocytosis (see figure 2). As a result, the transport of metabolites and macromolecules into and out of secondary plastids is much more complex than for primary plastids [90]. Given the immense species diversity, many of these transport processes remain poorly understood.

Secondary or higher-order symbiosis results in a cell containing at least four genomes: the nuclear and mitochondrial genome of the secondary host, and the nuclear and plastid genomes of the eukaryotic endosymbiont (Figure 5) [91]. Similar to the transfer of plastid genes to the

host's nuclear genome observed in primary plastids, nuclear genes of the eukaryotic endosymbiont are often either transferred to the nuclear genome of the secondary host or are simply lost [92-96]. Consequently, the nuclear genome of the eukaryotic endosymbiont becomes highly reduced and is referred to as a nucleomorph. Maintaining and particularly segregating both the secondary plastid genome and the nucleomorph during cytokinesis is likely to be highly complex. Early studies have shown that nucleomorphs lack mitotic spindles and segregate prior to plastid division [97-99]. More recent studies have further revealed that nucleomorph-encoded genes are transcribed in a cell cycle-independent manner, yet nucleomorph replication and secondary plastid division are both controlled by the secondary host cell [100]. Despite these insights, the molecular mechanisms governing these intricate processes remain largely unknown.

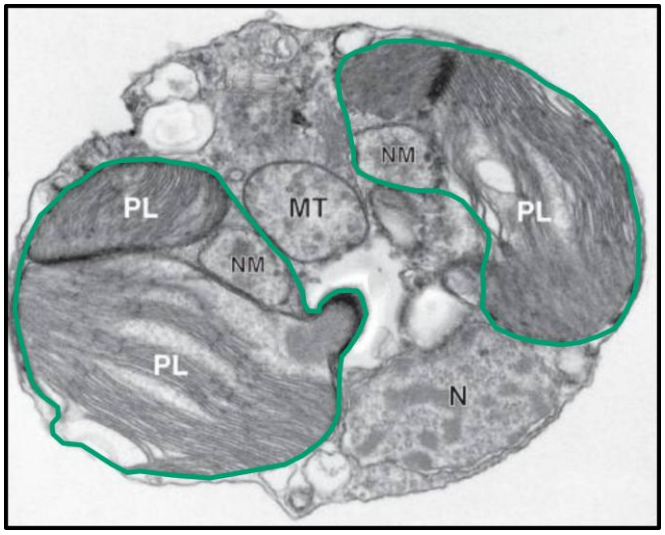

Figure 5. **Transmission electron microscopy image of *Bigelowiella natans*, a unicellular algae species with secondary plastids.** The cell contains three secondary plastids (PL) and two nucleomorphs (NM). Additionally annotated compartments are the host cell nucleus (N) and the mitochondrion (MT). The secondary host-derived organellar membranes are highlighted in green. Image adapted from [101].

In one example of a non-photosynthetic secondary plastid, the apicoplast from the Apicomplexa, the nucleomorph has been lost entirely [28]. Interestingly, recent research revealed that the Apicomplexa are polyphyletic, and apicoplast-like plastids evolved in at least three independent events [102, 103]. As expected from a secondary plastid, the apicoplast is surrounded by four membranes [104]. Despite lacking photosynthetic activity, apicoplast-like plastids have been retained likely due to their contribution to isoprenoid biogenesis and, in some lineages, the synthesis of tetrapyrroles and fatty acids [105]. Research on apicoplasts has primarily focused on a few model organisms, including the causative agents of malaria (*Plasmodium* spp.), toxoplasmosis (*Toxoplasma* spp.), and cryptosporidiosis (*Cryptosporidium* spp.). These organisms typically possess a single apicoplast that is closely associated with the cell's single mitochondrion [106, 107]. While the mechanisms of apicoplast division are not well

understood, it is known that apicoplast division is synchronized with the cell cycle and may involve the centrosome [104, 106]. Like most plastids, the apicoplast contains a highly reduced genome that encodes only a few protein-coding and RNA genes [108, 109]. However, the reason for the apicoplast genome retention is unclear. One hypothesis found that only two essential genes are encoded by the apicoplast genome. Interestingly, these two genes have already been transferred to the nucleus in other secondary plastid-containing lineages. This raises the possibility that the apicoplast genome could be lost eventually [105]. As in other plastids, the apicoplast genome is organized in nucleoids. In *Toxoplasma gondii*, the apicoplast has a single nucleoid which contains around 25 copies of the genome [110]. The replication and segregation of the genome are synchronized with the nuclear cell cycle and, similar to chloroplasts, a DNA gyrase is essential for nucleoid segregation [110, 111]. However, the molecular mechanisms of these processes remain unknown.

1.2.3 Chromatophore of *Paulinella*

Beyond the primary plastids of extant Archaeplastida (Chapter 1.2.2.1), a separate endosymbiotic event led to the establishment of primary plastids within a monophyletic group of unicellular free-living photoautotrophic amoebae of the genus *Paulinella [112, 113]*. These unique plastids, known as chromatophores, evolved from a cyanobacterial ancestor closely related to modern *Synechococcus* or *Prochlorococcus* species approximately 90 to 140 million years ago (illustrated in figure 1) [114]. Hence, chromatophores are relatively young organelles, making *Paulinella* spp. valuable model systems to study the early stages of organellogenesis [115].

Paulinella spp. contain two chromatophores, each of which is surrounded by two membranes and an intermediate peptidoglycan wall. The IM and the peptidoglycan wall are likely derived from the original cyanobacterial endosymbiont, while the OM is thought to be host-derived [116]. Chromatophore maintenance is tightly coordinated with the nuclear cell cycle (Figure 6). During cell division, each daughter cell inherits a single chromatophore, which only divides after cytokinesis. This coordination implies a complex level of nuclear control. Recent studies have identified around 200 nuclear-encoded proteins that may be involved in regulating chromatophore maintenance and division [117].

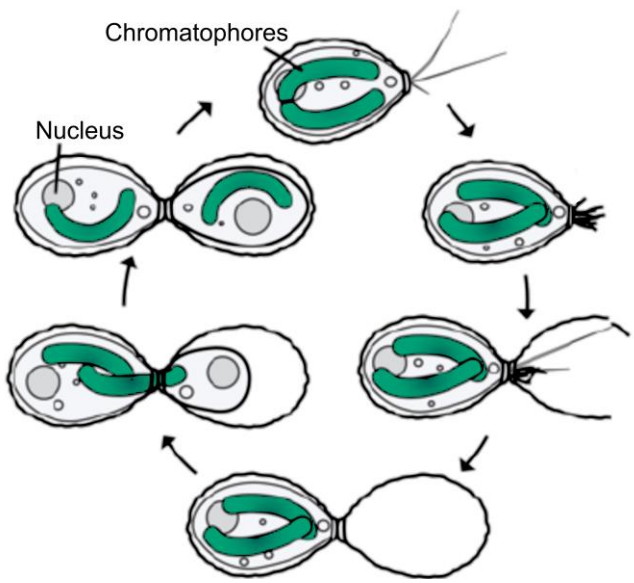

Figure 6. **Cell cycle stages of *Paulinella* spp.** Illustrations highlighting the morphology and segregation of chromatophores during the cell cycle of *Paulinella* spp. Illustrations adapted from [118].

Compared to other organelles, chromatophores have relatively large, gene-rich genomes. Genome sequencing efforts of three *Paulinella* species have revealed that chromatophores encode around 900 genes. When compared to free-living Cyanobacteria, this suggests that modern chromatophores retain around 25% of their ancestral genes [119, 120]. Interestingly, comparative analyses indicate that, when these species diverged around 60 million years ago, the chromatophore genome had already shrunk to about 35% of its original size [120]. This rapid gene loss may have been a crucial step in allowing the host cell to gain control over the endosymbiont [121]. As with other organelles, some originally chromatophore-encoded protein genes have been transferred to the host's nuclear genome, and the chromatophore now makes use of these proteins through protein import [122]. Interestingly, similar to what has been hypothesized for mitochondria and chloroplast-derived plastids, some of these nuclear-encoded, chromatophore-targeted proteins appear to have originated from Bacteria other than the cyanobacterial ancestor [123]. Since genome reduction is likely still ongoing, the chromatophore's current ~1 Mb circular and single-chromosome genome is expected to continue losing genetic information over time [120].

Chromatophores contain a single copy of their genome [118]. This implies the presence of a precisely controllable chromatophore genome segregation system. The chromatophore genome encodes orthologs of most genome segregation factors known from Cyanobacteria [119]. However, genome segregation in Cyanobacteria remains poorly understood, and the segregation of the chromatophore genome in *Paulinella* spp. has not yet been studied.

1.2.4 Nitrogen-fixing endosymbionts and organelles: Diazoplast and Nitroplast

Nitrogen fixation is a highly energy-demanding process that is widespread in Bacteria and Archaea, but rare among eukaryotes [124, 125]. However, in recent evolutionary history, a few algae species have acquired nitrogen-fixing endosymbionts, allowing diazotrophic lifestyles (illustrated in figure 1) [125, 126]. Some of these endosymbionts have undergone metabolic adaptations and depend on the import of proteins from their host cell. Therefore, they are now classified as early-stage organelles and have been named nitroplasts and diazoplasts [127, 128]. The ability of nitroplasts and diazoplasts to fix atmospheric nitrogen is likely to be a significant advantage for their hosts [128, 129].

Nitroplasts, also known as UCYN-A, have been described as *Candidatus Atelocyanobacterium thalassa* [130]. These are found in prymnesiophyte algae and have been extensively studied in cultured strains of *Braarudosphaera bigelowii*, a marine algae species with a global distribution (Figure 7AB) [131, 132]. The origin of this endosymbiosis has been dated to approximately 91 million years ago, and the persistence of nitroplasts in modern species suggests a stable long-term relationship [133], although some *B. bigelowii* cultivars have been observed to eventually lose their nitroplasts [134]. Nitroplasts retain much of the morphology typical to free-living Cyanobacteria and are enclosed within a host-derived membrane. Despite this, they have experienced extensive gene loss and have lost the ability to perform photosynthesis, rendering them dependent on the host cell for survival [135, 136]. Nitroplasts acquire essential proteins from the host cell by protein import. Interestingly, the imported proteins are of host cell origin and organellar gene transfer from the nitroplast to the host cell nucleus has not been detected [128].

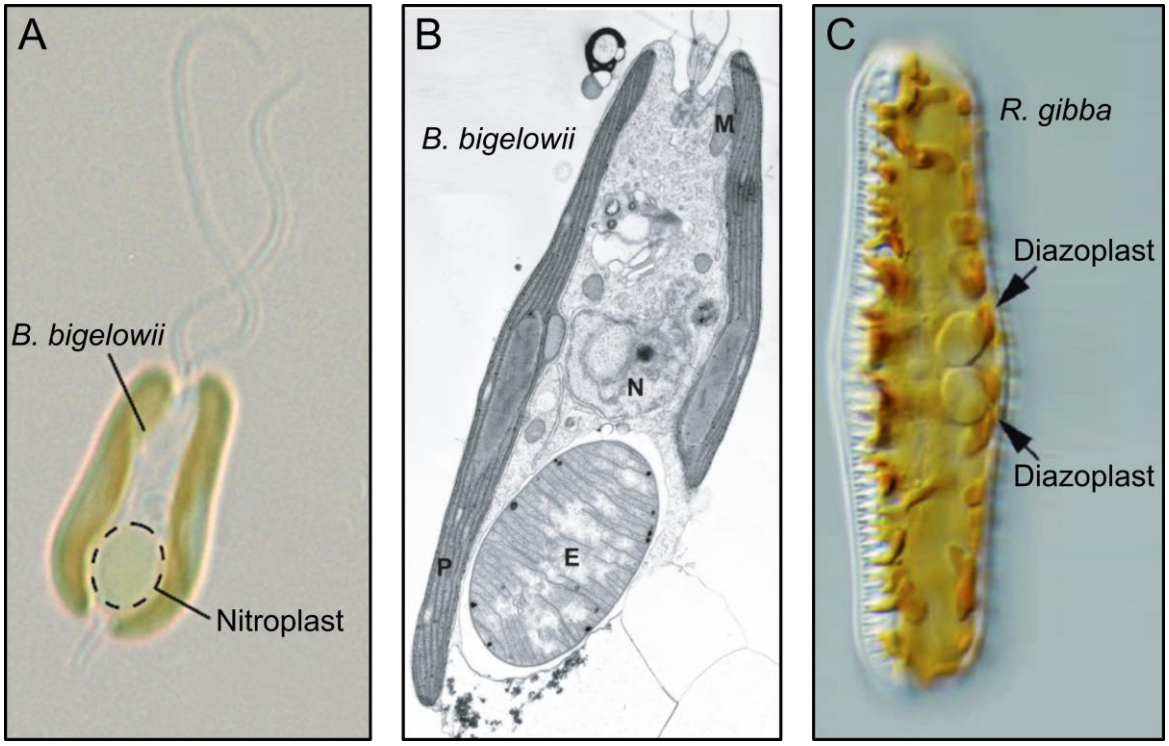

Figure 7. **Nitroplast and diazoplast.** (A) *Braarudosphaera bigelowii* cell captured by light microscopy. Image adapted from [137]. (B) *B. bigelowii* cell imaged by transmission electron microscopy. The cell contains a single nitroplast (E). Further organelles are labelled: Nucleus (N), mitochondria (M), secondary plastids (P). Image adapted from [134]. (C) *Rhopalodia gibba* cell imaged by light microscopy that contains two diazoplasts. Image adapted from [138].

B. bigelowii cells harbour a single nitroplast that proliferates in synchronization with the host cell (Figure 7AB) [134]. The division of the nitroplast occurs at a similar time in the cell cycle as the mitochondrial fission, but before secondary plastid and nuclear segregation. However, how the processes are temporally controlled and how the single nature of the nitroplast can be maintained are unknown [128].

In contrast to nitroplasts, diazoplasts have so far been generally classified as endosymbionts rather than organelles. They occur in diatoms of the genera *Rhopalodia* and *Epithemia*, both members of the Rhopalodiaceae [139]. The endosymbiotic event that gave rise to diazoplasts is estimated to have occurred around 35 million years ago. Their ancestral lineage is closely related to that of nitroplasts, as well as to modern Cyanobacteria of the genera *Crocosphaera* and *Zehria [139, 140]*. Like nitroplasts, diazoplasts have retained much of the morphology of their free-living ancestors and are enclosed within a host-derived membrane [127, 141]. However, reflecting their relatively recent origin, the metabolic integration between the host and endosymbiont is less advanced compared to that seen in nitroplasts or other established organelles. Like nitroplasts, diazoplasts have lost key genes required for photosynthesis. This loss, which results in low oxygen levels inside the endosymbiont, allows them to fix nitrogen

continuously throughout the day and night. This is in contrast to free-living *Crocosphaera* species which can fix nitrogen only at night [129]. Recent research has identified nonfunctional diazoplast-to-nucleus DNA transfers and six nucleus-encoded proteins have been localized in the proteome of the endosymbiont [127]. Should this be confirmed, the diazoplast could be considered an early-stage organelle rather than an endosymbiont.

Epithemia spp. contain one or two diazoplasts which are divided prior to cytokinesis (Figure 7C) [129, 139]. The presence of diazoplasts in several extant species of two genera suggests that diazoplast inheritance is stable and well controlled [127].

1.3 Mitochondrial genomes

Eukaryotes are highly diverse. Around two million species have been described, but it is estimated that around 8.7 million species exist [142, 143]. Eukaryotes are currently grouped into eight to nine supergroups and some additional lineages [144, 145]. Reflecting this vast diversity and approximately two billion years of partly independent evolution, mitochondrial genomes have undergone remarkable diversification. As a result, modern mitochondrial genomes vary significantly in size, gene content, gene expression strategies, and even in their genetic codes. In addition, different lineages exhibit striking differences in the organization of mitochondrial genomes and their modes of inheritance [146].

1.3.1 Mitochondrial genome content

A unifying feature of mitochondrial genomes is their highly reduced genetic content. While free-living Bacteria typically require a minimum of around 400 protein-coding genes [147], mitochondrial genomes may encode as few as one or two up to as many as 67 [148-150]. This drastic reduction is possible because mitochondria rely heavily on the import of proteins from the host cell, which enabled the transfer of many mitochondrial genes to the nuclear genome, or their complete loss. Notably, the mitochondrial genome of the LECA likely contained only slightly more genes than the most gene-rich mitochondrial genomes found today [151-153]. However, since LUCA, widespread and simultaneous losses and transfers of genes have occurred in multiple independently evolving lineages. Interestingly, these losses or transfers of mitochondrial genes were not random, suggesting that certain protein-coding genes are inherently more likely to be retained in the mitochondrial genome [154].

A central question is why the transfer or loss of mitochondrial genes is beneficial. Several hypotheses have been proposed to explain this phenomenon, focusing on factors such as endosymbiotic control, metabolic efficiency, energetic advantage, and genome protection. The

widespread loss of mitochondrial genes is likely due to their redundancy, as many have been functionally replaced by nuclear-encoded genes of eukaryotic origin or by genes acquired through horizontal gene transfer [154]. A notable example is the mitochondrial phage-derived RNA polymerase found in most eukaryotes [155, 156]. From a bioenergetic perspective, the loss of redundant genes is advantageous, as it reduces the energetic cost of gene maintenance and expression [157]. However, also the transfer of genes to the nuclear genome provides a bioenergetic advantage, which is partly explained by the high copy number of mitochondrial genomes (chapter 1.3.2) [157]. Beyond energy savings, gene transfer also enables more precise metabolic and functional regulation of the organelle by the host cell. Furthermore, it has been hypothesised that nuclear genes are more stable than organellar genes. Mitochondrial DNA is particularly vulnerable to two major genetic threats: Damage from reactive oxygen species produced during oxidative phosphorylation, and the accumulation of harmful mutations due to limited genetic recombination, following the Muller's ratchet [154]. This DNA protection hypothesis has been the most widely used explanation for mitochondrion-to-nucleus gene transfers in the past. However, the bioenergetic benefit hypothesis is currently the most prominent explanation. Unlike genome protection, which may only provide long-term advantages at the population level, bioenergetic efficiency directly increases the fitness of individual organisms likely making it a stronger selective force for gene transfer [158].

Despite the benefits of reducing or even eliminating the mitochondrial genome, almost all eukaryotes have mitochondria with their own small genomes. The reasons for the retention are a subject of much debate. Some hypotheses propose that keeping certain genes within the mitochondrion allows for faster metabolic adaptation [159]. In organisms with many mitochondria per cell, local gene expression would enable precise control of individual mitochondria. Another often-discussed hypothesis is that some mitochondrial genes encode proteins that may be harmful outside the mitochondrion or could be difficult to import into the organelle. This hypothesis is supported by large-scale comparative studies of mitochondrial genomes, which have identified high protein hydrophobicity as a key factor influencing gene retention [154, 158, 160-162]. Highly hydrophobic proteins could aggregate in the cytosol or at any point during protein import and thus not allow the gene transfer.

1.3.2 Mitochondrial genome organization

Mitochondrial genomes can be circular, linear, or even branched linear molecules [163]. The entire genome can be encoded on a single DNA molecule or it can be split into multiple or even thousands of DNA molecules [163]. In some lineages, such as Animalia and Fungi,

mitochondrial genomes tend to be streamlined and compact, rarely exceeding 50 kb in length [146]. In contrast to that, mitochondrial genomes of land plants (Embryophyta) are typically much larger due to the presence of long non-coding regions, with some genomes exceeding 10 Mb [146, 164]. Consequently, the size of the mitochondrial genome in these species exceeds even that of most free-living Bacteria, despite encoding only a small number of genes. At the opposite extreme, certain members of the Alveolata possess some of the smallest known mitochondrial genomes, with sizes around 6 kb and only a few encoded genes [53]. Notably, this vast diversity in genome size and structure does not correlate with the phylogenetic relationships or the biology of species [146].

Mitochondrial genomes are typically organized in nucleoids, a trait inherited from the bacterial ancestor [165]. Mitochondrial nucleoids have primarily been studied in model organisms such as yeast, humans, and, to a lesser extent, higher plants [166-170]. In these species, a single mitochondrion can contain anywhere from one to several dozen nucleoids (Figure 8). Apart from some core proteins, nucleoids are highly heterogeneous in their protein composition and mitochondrial DNA copy number, even within a single mitochondrion [171]. Nucleoids typically contain one or a few copies of the mitochondrial genome [167, 168, 172]. Many proteins have been found to localize within nucleoids, although the roles of many of them remain unclear [167, 169]. Key proteins are high-mobility group (HMG)-containing proteins that bind DNA and facilitate a histone-like DNA compaction [173]. Other nucleoid-associated proteins are involved in DNA replication, repair, and transcription [167, 169]. However, significant variability in nucleoid structure, both between species and even within individual mitochondria, makes it challenging to define a universal nucleoid model. While many species exhibit what can be considered “typical” nucleoids, some lineages have evolved far more complex mitochondrial genome architectures. One of the most extreme examples is the kinetoplast of the Kinetoplastida, which contains thousands of interlinked DNA molecules (chapter 1.5.2).

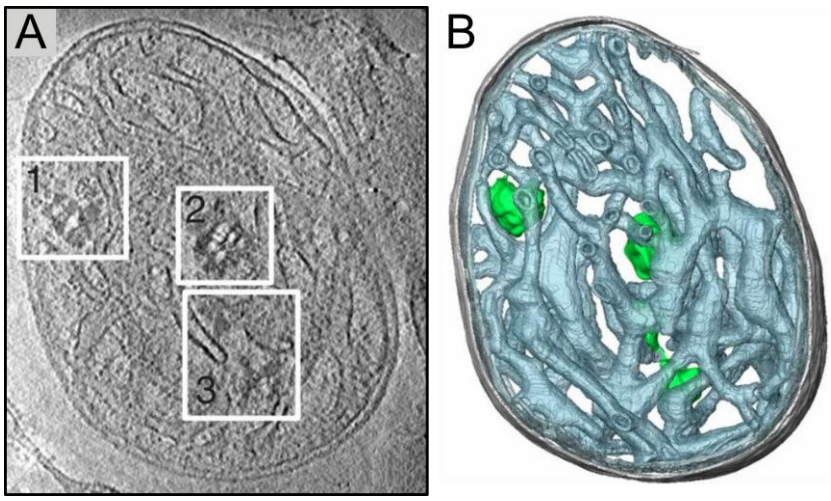

Figure 8. **Mitochondrial DNA compaction in nucleoids.** (A) Image of a bovine heart mitochondrion captured by transmission electron microscopy. Three visual nucleoids are framed by white boxes. (B) A picture illustrating a reconstruction of the image shown in (A) where cristae are coloured blue and nucleoids green. Images adapted from [174].

1.3.3 Mitochondrial genome inheritance

Faithful inheritance of the mitochondrial genome is essential for proper cellular function. This process relies on precise DNA replication and the division and equal segregation of mitochondrial nucleoids during both mitochondrial fission and cell division.

Mitochondrial DNA replication relies on nuclear-encoded DNA polymerases, which appear to have been independently acquired multiple times throughout eukaryotic evolution. In several model organisms within the Opisthokonta, the primary mitochondrial DNA polymerase is of bacteriophage origin [175, 176]. In contrast, other lineages such as the Chloroplastida and Kinetoplastida utilize Bacteria-derived polymerases [177, 178]. Notably, recent studies suggest that many species likely use multiple mitochondrial DNA polymerases, though their specific roles are not fully understood [178, 179]. Nevertheless, while mitochondrial DNA replication certainly requires precise host cell control, the replication itself may be not fundamentally different from the replication of nuclear or bacterial DNA.

The division and segregation of mitochondrial nucleoids are crucial processes that occur prior to or during mitochondrial fission and cell division. Different eukaryotes have evolved a variety of distinct and highly specialized systems to manage these steps. Interestingly, these mechanisms cannot be traced back to the alphaproteobacterial ancestor. Extant Alphaproteobacteria utilize a dedicated chromosome segregation system known as the parABS system [180]. However, no mitochondrial orthologs of parABS components have been found. Instead, eukaryotes have developed entirely new systems to ensure the proper division and inheritance of mitochondrial nucleoids. The following chapters discuss some of the characterized nucleoid division and segregation factors in mammals, budding yeast, and land

plants. Chapter 1.5.3 and subsequent sections will discuss the unique mechanisms used by *Trypanosoma brucei*.

1.3.3.1 Mammals (Mammalia)

Mammalian mitochondria typically contain a small number of nucleoids [181], with each nucleoid likely housing a single copy of the mitochondrial genome [172, 181]. The mitochondrial DNA is compacted by several factors, most notably by the highly abundant HMG-box protein TFAM, which also functions as a transcription factor [182, 183]. Mammalian cells possess dynamic mitochondrial networks, where the organelles constantly undergo fission and fusion events [184]. This high degree of structural plasticity makes it difficult to precisely track the movement and segregation of nucleoids. However, early evidence that nucleoids are not located in the matrix but are bound to the IM, suggested a key role of the IM and cristae in nucleoid trafficking [185].

Recently, the interplay of the mitochondrial nucleoid with the IM-bound mitochondrial contact site and cristae organizing system (MICOS), the OM protein Miro1, and KIF5B, a microtubule-associated motor protein, has been demonstrated in an elegant study using super-resolution microscopy in living cells (Figure 9) [186]. This study proposed that mitochondrial nucleoids interact with the MICOS at the IM. Notably, the mechanism behind the IM association is not well known and many other proteins have also been proposed to facilitate this connection [185, 187]. The MICOS complex interacts with Miro1 which resides in the OM. Finally, it is the interaction of Miro1 with KIF5B that connects the mitochondrial nucleoids to microtubule filaments and that facilitates their active transport and segregation during dynamic mitochondrial tubulation [186]. Additionally, Miro1 is associated with ER–mitochondria encounter structures (ERMES), which are known to define mitochondrial fission sites. Hence, the ER also contributes to the spatial distribution and segregation of nucleoids [188]. Together, these findings emphasize that mammalian mitochondria form dynamic networks, in which IM-bound nucleoids are actively positioned and segregated through their connections to microtubules and to the endoplasmic reticulum [186].

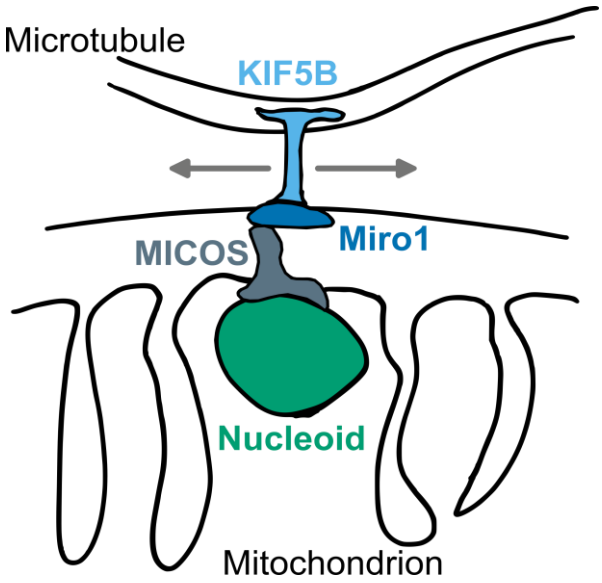

Figure 9. **Nucleoid trafficking system in mammalian cells.** Illustration depicting the factors involved in nucleoid-IM association and microtubule-mediated trafficking in mammalian cells.

1.3.3.2 Yeast (*Saccharomyces cerevisiae*)

Saccharomyces cerevisiae is arguably the most extensively studied model organism for mitochondrial biogenesis. During active growth and proliferation, *S. cerevisiae* typically contains one or a few large, tubular mitochondria. In contrast, during the stationary phase, the cells have many but much smaller mitochondria [167]. Stationary cells grown under aerobic conditions may contain around 141 nucleoids each likely holding one or two copies of the mitochondrial genome (Figure 10A). Under anaerobic conditions, however, stationary-phase cells contain only an average of seven aggregated nucleoids, each of which contains around 20 copies of the genome (Figure 10B) [189]. Mitochondrial DNA is compacted by the ARS-binding factor 2 (Abf2), a yeast ortholog of the mammalian TFAM, which organizes the DNA into a chromatin-like structure [190, 191]. Nevertheless, yeast nucleoids comprise over 35 distinct proteins, and DNA compaction has been observed even in Abf2-depleted strains [167, 192].

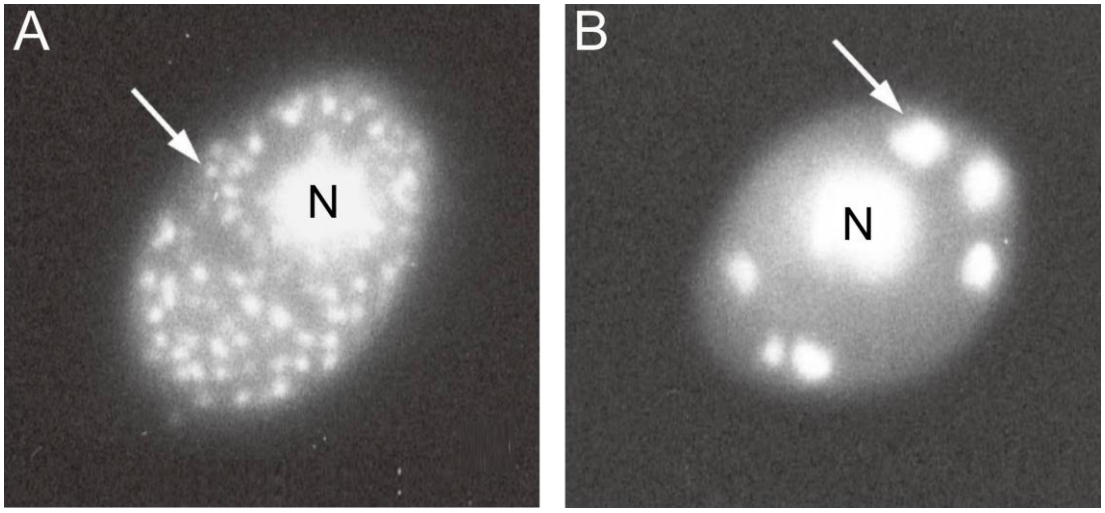

Figure 10. **Nucleoids in *S. cerevisiae*.** Fluorescence microscopy images visualizing the DNA (nuclear and mitochondrial) of each an *S. cerevisiae* cell grown in aerobic (A) or anaerobic (B) conditions. Arrows point at individual nucleoids, the nuclear DNA is indicated (N). Images adapted from [167].

Several lines of evidence suggest that nucleoid trafficking and segregation mechanisms are conserved between yeast and mammals [167]. Mitochondrial nucleoids in *S. cerevisiae* are also IM-associated, but the molecular details of this connection are not known. Studies have shown that nucleoids are transported along microtubules and actin filaments, guiding them toward daughter buds in dividing cells. This process likely supports the controlled inheritance of the mitochondrial genome, but the precise mechanisms remain unclear [167, 193-196].

In yeast, the Ca^{2+}-binding Miro GTPase Gem1, the ortholog of mammalian Miro1, plays a role in the ERMES complex [197]. As in mammalian cells, ERMES helps to define sites of mitochondrial fission and contributes to the division and segregation of mitochondrial nucleoids [198]. The underlying processes are, however, not known.

1.3.3.3 Land plants (Embryophyta)

Mitochondrial biogenesis and particularly the inheritance of mitochondrial genomes is still poorly understood in eukaryotic lineages outside of the Opisthokonta. However, studies in land plants, especially in model organisms such as *Arabidopsis thaliana, Nicotiana tabacum,* and *Vigna radiata*, have provided valuable insights into alternative mechanisms. Cells of land plants typically contain several hundred mitochondria that undergo frequent fission and fusion events (Figure 11A) [199]. Each mitochondrion contains typically a single nucleoid, although mitochondria lacking nucleoids can be readily observed (Figure 11B) [200, 201]. This observation suggests that mitochondrial genome segregation in land plants may not be tightly

regulated and could occur in a largely stochastic manner [202]. Interestingly, this heterogeneity in mitochondrial genome copy numbers appears to be reversible. Massive mitochondrial fusion events, which were reported during germination in *A. thaliana*, may serve to homogenize the mitochondrial population [203].

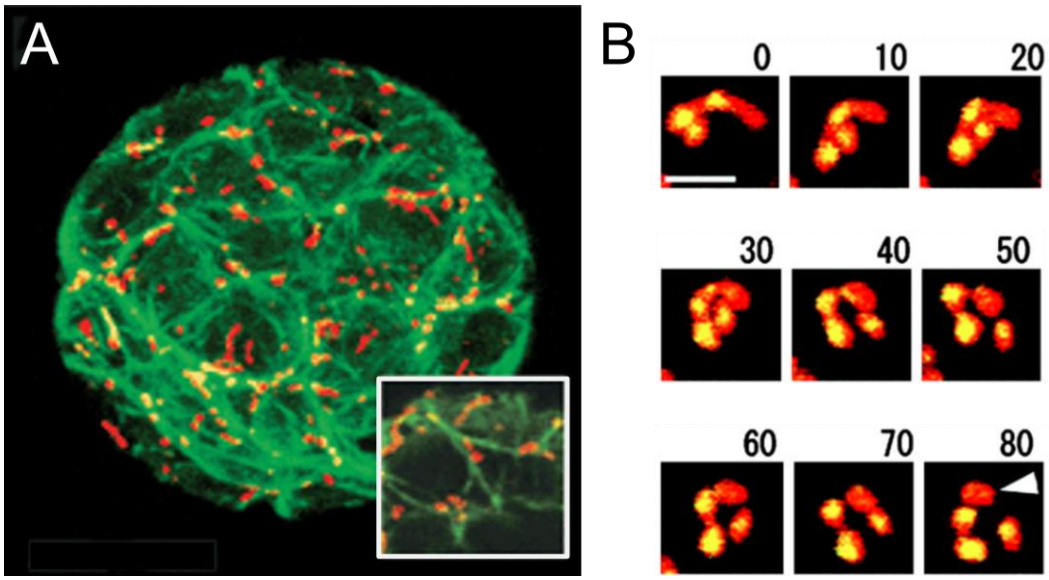

Figure 11. **Mitochondrial trafficking and fission in land plants.** (A) Fluorescence microscopy image of a *Nicotiana tabacum* cell showing actin filaments (green) and mitochondria (red). The inset on the bottom right shows a magnification. Image adapted from [204]. (B) Time course observations in seconds of mitochondrial fission in *N. tabacum*. Mitochondria are shown in red, mitochondrial DNA in yellow. Mitochondrial fission frequently produces mitochondria without detectable DNA (indicated by arrow head). Images adapted from [201].

The structure and composition of land plant mitochondrial nucleoids are not well understood. In *A. thaliana*, several proteins have been associated with nucleoid formation [205, 206]. One key factor appears to be the ATPase Family AAA Domain-Containing Protein 3 (ATAD3), as its absence leads to the disruption of mitochondrial nucleoids [206]. Notably, ATAD3 is likely a mitochondrial IM protein, suggesting a link between mitochondrial nucleoids and the IM in land plants as well [206]. Supporting this idea, a study in *Vigna radiata* also reported IM association of mitochondrial nucleoids and proposed possible connections to the OM and cytoskeletal elements [166]. Additionally, mitochondrial distribution in *N. tabacum* has been shown to depend on actin filaments (Figure 11A) [204]. Despite these findings, the mechanisms of mitochondrial and nucleoid trafficking and segregation in land plants remain largely uncharacterized and require further investigation.

1.4 *Trypanosoma brucei*

Trypanosoma brucei is a hemoflagellate protozoan that is naturally found in the tropical regions of sub-Saharan Africa. *T. brucei* occurs within the distribution range of tsetse flies (*Glossina* spp.), which serve as the transmission vectors for this mammalian pathogen. Tsetse flies feed on the blood of a wide range of mammals, most of which are suitable hosts for *T. brucei*, contributing to the high prevalence of the species. Unfortunately, two host groups are particularly vulnerable to tsetse fly bites and subsequent *T. brucei* infections: Humans and their domesticated livestock [207]. If left untreated, infections in either group can be fatal. The ongoing interaction between the pathogen and human populations has significantly impacted the recent history of African civilisations [208]. A lack of understanding of disease origins, transmissions, and treatments caused epidemic-like outbreaks in several countries in the late 19th and the early and late 20th century alongside the massive agricultural impact [209]. Consequently, the biology of *T. brucei* reached into the focus of researchers and physicians, aiming to prevent disease outbreaks and cure patients. These efforts have been successful in recent years, with several countries reporting the elimination of *T. brucei*-borne diseases [209-211]. Additionally, research has revealed that *T. brucei* and its relatives are only distantly related to many eukaryotic model organisms [144]. As a unicellular organism with unique cellular features, such as a single mitochondrion, *T. brucei* has become a valuable model for studying fundamental processes in eukaryotic cells and for exploring the evolutionary origins of eukaryotes [212].

Interestingly, some relatives of *T. brucei* are pathogens affecting humans, livestock, or crops. *T. cruzi*, for example, is the causative agent of Chagas disease in Latin America [213]; several *Leishmania* species are responsible for various forms of leishmaniasis [214]; and *Phytomonas* species can infect agricultural crops, reducing plant health and crop yields [215]. Beyond these well-known pathogens, the Trypanosomatidae are remarkably diverse. Several hundred species have been described, all of which are obligate parasites [216]. Hence, trypanosomatids likely play crucial ecological roles which we have yet to understand.

1.4.1 *Trypanosoma brucei* as a pathogen

The evolutionary origin of *T. brucei* remains unclear. One proposed model suggests that *T. brucei* descended from a free-living bodonid species [207]. These bodonid ancestors likely invaded ancient insect species during the Mezozoic era, as suggested by a fossil dated to ~110 million years ago [217]. The emergence of blood feeding insects later allowed the monoxenous parasites to alternate between different hosts in a dixenous life cycle [218]. While the

hypothesized Mesozoic origin indicates a Gondwanan emergence of the lineage, it is unclear whether the transition to blood feeding insect hosts and the adaption of a dixenous lifestyle occurred before or after the breakup of the supercontinent [207]. What is clear, however, is that both *T. brucei* and its vector, the tsetse fly, were initially retained only in today tropical sub-Saharan Africa. This suggests a long co-evolutionary history between *T. brucei* and hominids, including humans, whose radiation started in this region [219]. Consequently, humans, as well as most African mammals, have evolved defence mechanisms against *T. brucei* [219, 220]. However, since the Holocene epoch, several events possibly linked to the emergence of highly populated human civilisations have resulted in the emergence of certain *T. brucei* ecotypes that can evade human immune defences. Under traditional Linnaean binomial nomenclature, these ecotypes were historically classified as separate species or subspecies [207]. However, modern genetic analyses have shown that these classifications lack monophyly and exhibit insufficient genetic divergence to justify their classification as distinct species [207, 221-227]. In the following paragraphs, the recently proposed ecotype nomenclature by Lukeš *et al*. is used [207]. In subsequent chapters, unless otherwise specified, the term *T. brucei* will refer to the ecotype *T. brucei forma brucei* (*T. brucei f. brucei*).

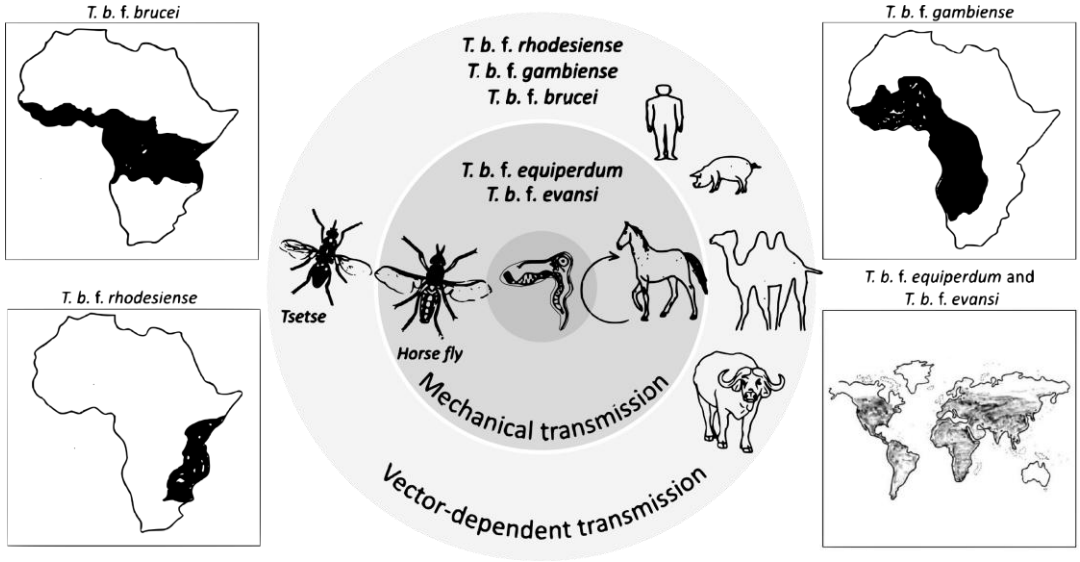

Figure 12. ***T. brucei* ecotypes**. Summary of natural occurrences and transmission mechanisms of the five currently accepted ecotypes of *T. brucei*. Illustration adapted from [207].

T. brucei f. brucei refers to the ecotype that is widely distributed across tropical sub-Saharan Africa. It is likely that this form is the original ecotype, which co-evolved with hominids and native African wildlife (Figure 12) [207, 219]. Over the course of this long co-evolutionary relationship, many host species have developed effective defence mechanisms against infections. Notably, the human defence mechanism stems from a plasma protein, the apolipoprotein-L1 (APOL1), which is a trypanolytic molecule [228]. In contrast, most domesticated mammal breeds have not evolved such defences, making them highly susceptible to *T. brucei f. brucei*. Infections in livestock can result in a disease known as Nagana that often leads to severe outbreaks and devastating livestock losses for farmers and pastoral communities [229].

Recent events, likely taking place in the last 10'000 years, have given rise to four divergent *T. brucei* ecotypes: *T. brucei f. gambiense*, *T. brucei f. rhodesiense*, *T. brucei f. evansi*, and *T. brucei f. equiperdum* (Figure 12) [207].

T. brucei f. gambiense and *T. brucei f. rhodesiense* are human-infective ecotypes transmitted by tsetse flies. While most African wildlife species show a degree of tolerance to these parasites, their ability to infect humans stems from their resistance to the human trypanolytic protein APOL1 [209, 219]. In humans, infections with these ecotypes cause human African trypanosomiasis (HAT), commonly known as 'sleeping sickness'. There are two forms of the disease: West African HAT, caused by *T. brucei f. gambiense*, and East African HAT, caused by *T. brucei f. rhodesiense* [209]. West African HAT is the more prevalent form, accounting for 98% of reported cases in recent years [230]. The east African HAT has a much lower prevalence, but infections are more severe and end fatal if untreated in most cases [231].

T. brucei f. evansi and *T. brucei f. equiperdum* are ecotypes which have lost the dixenous lifestyle [207]. Mutations in the ATP synthase have allowed these ecotypes to partially or fully lose their mitochondrial genomes, rendering them unable to proliferate outside a mammalian bloodstream [232, 233]. Consequently, these parasites are not dependent on a specific transmission vector and instead switch between hosts through mechanical transmission. In tropical sub-Saharan Africa, tsetse flies, which feed multiple times per day, may still serve as incidental vectors. However, other blood-feeding animals can also transmit the parasites in a similar manner [234, 235]. Notably, *T. brucei f. equiperdum* is primarily transmitted through direct contact during the mating of host animals, setting it apart from other *T. brucei* ecotypes [236]. These adaptations have enabled both ecotypes to spread far beyond the natural range of tsetse flies. Today, they have been reported in numerous regions across both the Old and New

Worlds (Figure 12) [207, 235]. While *T. brucei f. equiperdum* is restricted to equids, *T. brucei f. evansi* is a pathogen of many domesticated and wild mammals, and although human infections have been reported, they are exceptional [234-237]. Infections in these species cause diseases known as surra (*T. brucei f. evansi*) and dourine (*T. brucei f. equiperdum*) which are often fatal [234, 236].

T. brucei makes use of remarkable strategies to evade the host's immune system responses. As eukaryotic organisms, their metabolism is similar to that of the host, making it difficult to find chemotherapeutics with high specificity. Lack of specific treatments, combined with difficulties in controlling the tsetse fly vector, likely contributed to the resurgence of *T. brucei*-related epidemics in the late 1990s [209]. However, recent advances have led to the development of new and promising drugs, some of which are already in use. These treatments have played a significant role in reducing disease prevalence and have supported the successful elimination of HAT in several countries in recent years [207, 210, 230].

1.4.2 Life cycle

The dixenous lifestyle of *T. brucei* demands a considerable metabolic and morphological adaptability and flexibility. Unsurprisingly, the parasite undergoes dramatic changes in its transcriptome and proteome during the transitions between hosts, including a complete replacement of its surface coat [238-240].

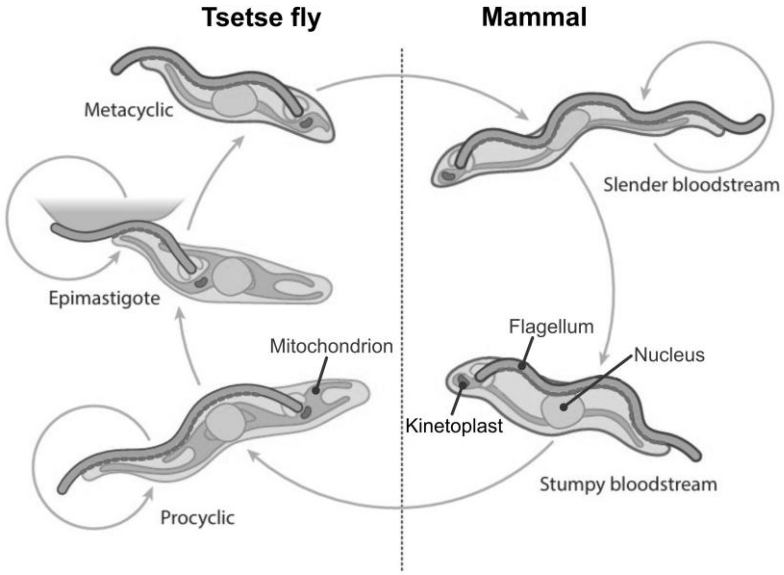

Figure 13. ***T. brucei* life cycle**. Illustrations of the main life cycle stages of *T. brucei*. Arrows indicate the progression between forms and closing loop circles indicate the proliferative life cycle stages. Illustration adapted from [241].

The proliferative type of the parasite in the mammalian bloodstream is known as the long slender bloodstream form (Figure 13) [242]. These cells express a cell coat consisting of variable surface glycoproteins [243]. These proteins are highly immunogenic and trigger strong host immune responses, leading to characteristic fever spikes that correlate with parasitaemia levels [244]. However, this surface coat is very dynamic and *T. brucei* is able to generate a seemingly unlimited diversity of the variable surface glycoprotein by genetic recombination and transcriptional control [245-247]. As a result, the host immune system can only target a subset of parasites at any given time, as each parasite has only a single VSG type, making a complete clearance nearly impossible. Long slender bloodstream form cells express and secret oligopeptides, the stumpy inducing factors, which are sensed through a quorum sensing pathway [248-250]. As a result, high parasitaemia triggers the formation of short stumpy bloodstream form parasites, a non-dividing stage arrested in the G_0 phase of the cell cycle (Figure 13) [251]. These parasites display metabolic adaption required to invade the gastrointestinal system of the tsetse fly, where they are taken up to during a blood meal of the insect. Once inside the fly, short stumpy forms shift their metabolism to adapt to the glucose-poor environment of the midgut and differentiate into the proliferative procyclic form (Figure 13) [252]. These cells display a completely remodelled surface coat consisting of two types of procyclins: EP and GPEET [253, 254]. Procyclic form cells migrate from the midgut toward the salivary glands, undergoing morphological transitions, including a switch to a surface coat dominated by EP procyclins [254]. The invasion of the proventriculus is associated with proliferative epimastigotes which carry yet another surface coat characterized by *brucei* alanine-rich proteins (BARP) (Figure 13) [255]. Epimastigotes then undergo an asymmetrical cell division to produce a non-dividing form that eventually migrates to the salivary glands [256]. There, they undergo metacyclogenesis, which includes another asymmetrical division that generates mammalian-infective metacyclic trypomastigotes (Figure 13) [257]. Notably, the metacyclic cells are already coated with the variable surface glycoprotein, a preadaptation for the invasion of the mammalian bloodstream [252]. Finally, embedded in the tsetse fly's salivary gland secretion fluids, the metacyclic trypomastigotes are transmitted to a new mammalian host during a blood meal. Once inside the host, they transform into the proliferative long slender bloodstream form, thus completing the life cycle.

1.5 Mitochondrion of *Trypanosoma brucei*

The mitochondria of *T. brucei* and its kinetoplastid relatives are remarkable organelles that have repeatedly surprised researchers throughout the history of mitochondrial research. One particularly striking discovery was that, unlike most known eukaryotes, kinetoplastids harbour a single mitochondrion, an unusual feature that raised significant interest in the biogenesis of this organelle [49].

The following chapters will explore some of the most remarkable aspects of mitochondrial biogenesis in *T. brucei*, with a special focus on the structure and inheritance of its unique mitochondrial genome, the kinetoplast.

1.5.1 Mitochondrial biogenesis of *Trypanosoma brucei*

T. brucei harbours a single mitochondrion throughout its entire life and cell cycle. Given the parasite's highly specialized life stages, it's not surprising that the role of the mitochondrion in cellular metabolism changes significantly, especially between life cycle stages [258].

During the procyclic stage, *T. brucei* primarily uses proline, and when available glucose, as energy sources. ATP is generated through both oxidative phosphorylation and substrate-level phosphorylation within the mitochondrion [259-262]. By contrast, in the bloodstream stages, *T. brucei* exploits the constant abundance of glucose in the host's blood, relying mainly on substrate-level phosphorylation linked to glycolysis that occurs partly in specialized peroxisomes called glycosomes [258, 263, 264]. As a result, the procyclic form derives a significant proportion of its energy from mitochondrial activity, whereas the bloodstream forms produce little to no energy in the mitochondrion [258]. Despite this reduced role in energy production, the mitochondrion remains essential in bloodstream forms since it is the sole site of iron-sulfur cluster biosynthesis and also contributes to calcium signalling, fatty acid metabolism, and amino acid metabolism [49, 265, 266]. However, the morphology of the mitochondrion in procyclic and bloodstream form parasites is vastly different [267]. In the procyclic form, the mitochondrion is large and highly branched, with well-developed cristae on the IM to support active oxidative phosphorylation. In contrast, the bloodstream forms have a smaller tubular mitochondrion with fewer cristae [264, 267].

Despite these metabolic and morphological differences between these life cycle stages, fundamental processes required for mitochondrial biogenesis must be continuously active. In *T. brucei*, such processes are the import of mitochondrial proteins and tRNAs, mitochondrial gene

expression, including extensive mRNA editing, and the maintenance of the mitochondrial genome.

1.5.1.1 Protein import

In recent years, the mitochondrial proteomes of various eukaryotes have been characterized. Interestingly, despite vast differences in lifestyles the general sizes of mitochondrial proteomes are remarkably similar across distantly related species, even between single-celled and multicellular organisms [268-271]. However, the mitochondrial genomes of all known eukaryotes encode only a few protein genes (chapter 1.3.1). Hence, mitochondria rely on excessive protein import of nuclear encoded and cytosolically translated protein precursors. Interestingly, despite the monophyletic origin of mitochondria [272, 273], the protein import machineries of mitochondria differ substantially across eukaryotic supergroups [274-276].

In yeast and humans, mitochondrial protein import has been studied in detail. Both organisms possess five distinct pathways to import precursor proteins [36]. In depth characterization of the mitochondrial protein import in *T. brucei* has shown that trypanosomes and their relatives use five nearly identical import routes, although the involved systems sometimes show only very limited orthology (Figure 14) [274].

One of the five protein import routes describes the import of a relatively small group of mitochondrial proteins, the α-helical-anchored OM proteins (Figure 14). Interestingly, this import route is the most diverse mitochondrial protein import pathway and substantial differences have been reported even between yeast and human, which belong to the same eukaryotic supergroup [36]. Taken together, three evolutionary unrelated insertase systems, the MIM complex of yeast [277], the MTCH1/MITCH2 duo of human [278], and pATOM36 of trypanosomes [279] have been shown to insert α-helical proteins into the OM. Despite no sequence homology, the MIM complex and pATOM36 could even be functionally interchanged highlighting the convergent evolution of this import route [280].

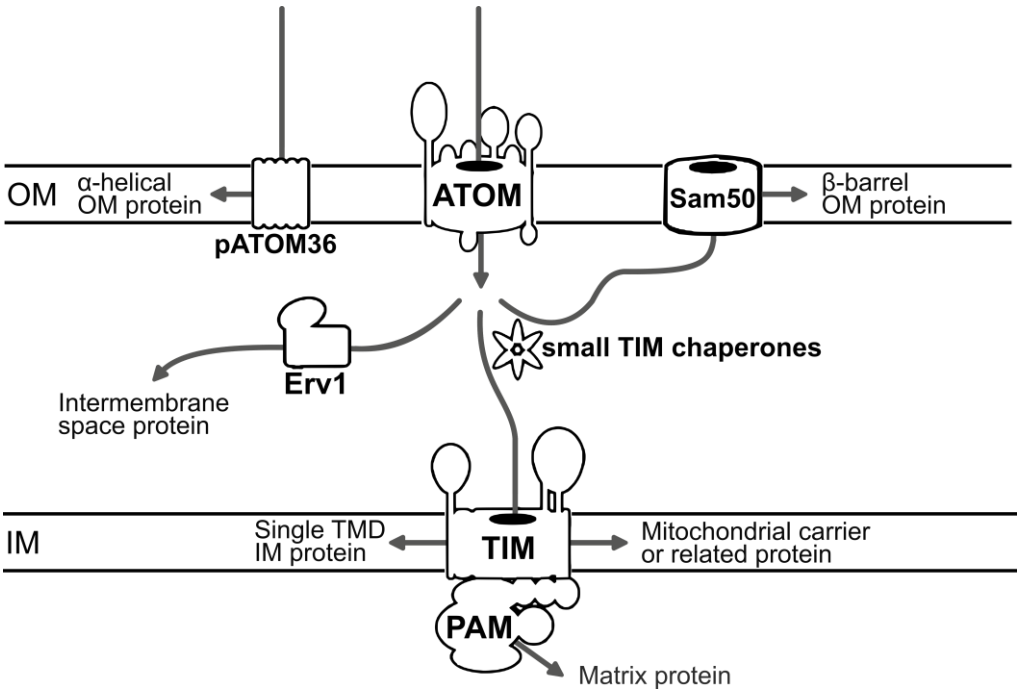

Figure 14. **Mitochondrial protein import pathways of *T. brucei***. Schematic illustration of the main translocases and import machineries of the five discussed import pathways. OM: mitochondrial outer membrane, IM: mitochondrial inner membrane, TMD: α-helical transmembrane domain. Illustrations adapted from [281].

Essentially all yeast and human mitochondrial proteins are initially imported by the translocase of the outer membrane (TOM) complex into the intermembrane space [36]. An orthologous translocase has been identified in *T. brucei*, which has been termed the atypical TOM (short ATOM) complex (Figure 14) [282]. However, the two machineries contain several subunits which have been acquired independently and thus cannot be traced back to a single origin [282]. It is widely accepted that the main translocation pore subunits Tom40 and ATOM40, as well as the complex organizing subunits Tom22 and ATOM14 are orthologous [274]. In contrast, neither of the two ATOM complex receptor subunits nor any of three subunits involved in the regulation of the complex have orthologs in the human or yeast TOM complexes [274]. Nevertheless, some if not all of the unrelated subunits may be functional analogs, which is also supported by the identical count of unique subunits of the TOM and ATOM complexes [283, 284]. The human and yeast TOM complexes have almost identical molecular structures [285-287]. Consequently, the molecular structure of the ATOM complex will have to get solved to evaluate how similar the architectures of the TOM and ATOM complexes are.

All mitochondria contain a small number of β-barrel OM proteins [288]. The import route of this protein class is well conserved [275]. β-barrel OM protein precursors are imported by the ATOM complex into the intermembrane space. After the translocation, β-barrel OM precursor proteins are stabilized by small TIM chaperones (Figure 14). *T. brucei* has six such chaperones [289],

although one of them may have a noncanonical function [290], and all are likely orthologs of yeast small TIM chaperones [282]. However, the trypanosomal process of β-barrel protein precursor stabilization by small TIM chaperones has not been studied yet [282]. OM insertion of β-barrel protein precursors is performed by the well conserved sorting and assembly machinery (SAM) complex (Figure 14). In yeast and human, the SAM complex consists of a central insertase, Sam50, and two peripheral capping factors, Sam35 and Sam37 [291]. In *T. brucei*, the ortholog, Sam50 (formerly annotated as Tob55), has been shown to function likewise [292]. An ortholog of Sam35 is encoded in the genome of *T. brucei,* while a Sam37 gene is absent. However, the function of the Sam35 ortholog has not yet been investigated [282]. The SAM complex may therefore differ from the yeast or human complex but more research is needed.

Despite consisting of unrelated subunits, the TOM and ATOM complex facilitate essentially identical import pathways [282]. Apart from the import of β-barrel OM precursor proteins, the translocation across the OM of all precursors of intermembrane space, IM, and matrix proteins is facilitated by these complexes (Figure 14). Many intermembrane space proteins are characterized by intramolecular disulfide bonds formed between cysteine side chains [293]. These disulfide bonds are introduced post import and are essential for the protein stability and function. In *T. brucei*, the sulfhydryl oxidase TbErv1 is essential for the catalysis of this oxidation [271, 294]. Erv1 enzymes are well conserved among eukaryotes, however, in yeast Erv1 depends on the interplay with the mitochondrial intermembrane space import and assembly protein 40 (Mia40) for reoxidation [274]. The redox cycle of *T. brucei* may be Mia40-independent as an ortholog of this gene could not be detected, however, the substitution of the function by a yet unknown enzyme cannot be ruled out [274].

The fourth and fifth mitochondrial protein import routes use, in addition to the ATOM complex, a second translocase, the translocase of the inner membrane (TIM) complex (Figure 14) [282]. Trypanosomes have a single TIM complex that is essential for the biogenesis of all nuclear-encoded IM and matrix proteins [295]. This is in great contrast to yeast or human systems, and likely also to the ancient system of LECA, which possess two distinct TIM complexes dedicated to the fourth and fifth import pathways [36, 282]. The fourth pathway is the route taken mainly by the large class of mitochondrial metabolite carrier proteins (MCP) [282]. These are α-helically anchored integral membrane proteins, the majority of which have six such domains. These overall hydrophobic MCPs are challenging import substrates and therefore require chaperones in the intermembrane space to prevent protein aggregation [282]. Hence, in *T. brucei*, MCP import depends on the ATOM complex, the small TIM chaperones in the intermembrane space, and the single TIM complex [295].

The fifth mitochondrial protein import pathway is the route taken by matrix proteins or IM proteins with generally only a single α-helical transmembrane domain (Figure 14). This pathway is well conserved and most of the substrates are characterized by an N-terminal presequence, an amphipathic α-helix of variable length with a positive charge [296]. This presequence is recognized by receptors of both the ATOM and TIM complexes and is likely the reason for the N-to-C-terminal import of the precursor proteins [282, 297]. The TIM complex subunit of *T. brucei* that is responsible for protein precursor translocation is a yeast Tim22 ortholog [295, 298]. In yeast, which have two different TIM complexes, Tim22 is part of the TIM22 complex that is responsible for the IM insertion of MCPs [299]. Hence, the ability of the single *T. brucei* TIM complex to facilitate the import of both substrate classes, MCPs and presequence containing proteins, is unusual and suggests a gain of function of this Tim22 ortholog [295]. Indeed, it was shown that the TIM complex in *T. brucei* does require additional factors for the translocation of presequence containing proteins [295, 300]. After import, the presequence is cleaved by the conserved matrix processing peptidase [301].

Protein import into the mitochondrion, especially across the IM, requires energy. The import of presequence containing proteins is facilitated by the ATP-dependent presequence translocase-associated motor (PAM). The PAM of *T. brucei* is unusual and lacks some of the orthologs found in other systems [302]. Interestingly, two of these orthologs, TbPam16 and TbPam18, are essential J-domain proteins in procyclic *T. brucei*, but they are neither structurally nor functionally associated with mitochondrial protein import [302]. Instead, TbPam27, a non-orthologous euglenozoan-specific J-domain protein has taken over their function [302]. This homologue replacement in the PAM may have been an important step allowing the TIM22-like TIM complex of *T. brucei* to gain the ability for presequence containing precursor protein import [274].

1.5.1.2 tRNA biogenesis

Mitochondrial translation, like all translation systems, requires a full set of tRNAs and their respective aminoacyl-tRNA synthetases. However, the mitochondrial genome of *T. brucei* does not encode any tRNAs [303]. Instead, all mitochondrial tRNAs are nuclear-encoded and must get imported from the cytosol [304-306]. This is a situation comparable with mitochondria of other eukaryotic groups. However, in some lineages, most prominently in some Animalia, Fungi, and Embryophyta, mitochondrial genomes encode complete sets of mitochondrial tRNAs. [307, 308].

Multiple lines of evidence from *T. brucei* and other trypanosomatids have led to the conclusion that these organisms source mitochondrial tRNAs from the cytosolic pool of mature and aminoacylated tRNAs [309, 310]. These tRNAs are targeted to the mitochondrion by the eukaryotic translation elongation factor 1 alpha (eEF1α) [311]. In *T. brucei*, mitochondrial tRNA import is mediated by the same main translocase complexes responsible for protein import, the ATOM and TIM complexes [312]. However, several subunits essential for protein import are not required for tRNA import. For instance, within the ATOM complex, neither of the two receptor subunits involved in protein precursor recognition are necessary for tRNA translocation [313]. Similarly, for translocation across the IM, only the core TIM complex is required and all accessory components associated with the import of presequence containing proteins, including the PAM, are dispensable [314]. The fact that tRNA import is independent of the PAM raises questions about the driving force behind this process, particularly given that tRNA and protein import occur independently [313]. Importantly, the required energy may not be exclusively intramitochondrial, as tRNA translocation across the OM and IM appears to be coupled [314].

T. brucei imports aminoacylated tRNAs into its mitochondrion [310]. However, to maintain efficient translation, the mitochondrion requires aminoacyl-tRNA synthetases to recharge tRNAs. All mitochondrial aminoacyl-tRNA synthetases are encoded in the nucleus, and interestingly, with only three exceptions, a single gene gives rise to both the mitochondrial and the cytosolic synthetase [271, 315]. This dual targeting requires stable pools of the same enzyme to be maintained in both compartments. In the case of the isoleucine aminoacyl-tRNA synthetase, this is achieved by alternative trans-splicing of the primary transcript introducing a presequence into the open reading frame of some mRNAs only [316]. In *Leishmania tarentolae*, another trypanosomatid, some aminoacyl-tRNA synthetase genes are known to contain internal mitochondrial targeting signals and alternative splicing results in mitochondrially targeted or cytosolically retained enzymes [315]. Despite the shared genes for most mitochondrial and cytosolic aminoacyl-tRNA synthetases in *T. brucei*, the mitochondrial synthetases required to charge the tRNAs decoding the tryptophan, aspartate, and lysine codons are distinct from their cytosolic counterparts and are encoded in independent nuclear genes [317-319]. The reasons for mitochondria-specific aminoacyl-tRNA synthetases vary. In the case of the tryptophanyl-tRNA synthetase, the demand arises from the ‘UGA’-STOP codon reassignment to a tryptophan codon in the mitochondrion, but not in the cytosol where the canonical genetic code is used [320]. However, since the nuclear genome encodes a single tryptophan decoding tRNA gene, the mitochondrial population of this tRNA has to be modified by a C→U modification which

affects the recognition by the cytosolic tryptophanyl-tRNA synthetase. Hence, mitochondria require a specific tryptophanyl-tRNA synthetase which recognizes the modified anticodon loop of the tRNA [319]. The needs for mitochondria-specific aspartyl-tRNA and lysyl-tRNA synthetases are less well known. In the case of aspartyl-tRNA synthetase, the mitochondrial tRNA may contain a specific nucleotide modification that requires a dedicated enzyme for charging [318]. The mitochondrial lysyl-tRNA synthetase is activated only upon mitochondrial import by a C-terminal cleavage, suggesting a possible cytosolic misfunction of the enzyme [317].

Another unique feature of mitochondrial tRNA biogenesis in *T. brucei* involves the tRNA required for translation initiation and methionine codon decoding. Bacterial and eukaryotic translation initiation is fundamentally different in the way that Bacteria use tRNAs carrying formylated methionine, a strategy also employed by mitochondria [321]. Interestingly, *T. brucei* has only a single gene encoding the methionyl-tRNA synthetase responsible for charging both the cytosolic and mitochondrial elongator methionine tRNAs. Hence, to generate the translation initiator tRNA, the mitochondrion requires a formyltransferase. This enzyme formylates a subpopulation of the charged methionine tRNAs effectively converting them into functional initiator tRNAs [322]. Hence, this methionyl-tRNA of *T. brucei* is used in three pathways, for the translation elongation in the cytosol and in the mitochondrion, and for translation initiation in the mitochondrion. Despite this unusual versatility of this tRNA, the recognition of the initiator tRNA by the mitochondrial initiation factor 2 and the post-translational removal of the formyl group are more conserved [323, 324].

1.5.1.3 RNA editing

The mitochondrial genome of *T. brucei* has an unusual bipartite organization containing two types of circular DNA molecules, maxicircles and minicircles. Maxicircles encode a few classical but also some so called protein cryptogenes, while minicircles encode short RNA molecules, the guide RNAs (gRNAs) (see also chapter 1.5.2.1). Highly complex RNA editing reactions, guided by gRNAs, allow the insertion and deletion of uridylates converting transcripts of cryptogenes into translatable protein genes. While the generic process of transcript editing may be employed by many organisms, this RNA editing performed by *T. brucei* and its relatives is excessive and shapes the mitochondrial transcriptome greatly [325, 326].

The maxicircles of *T. brucei* encode six classical protein genes and twelve cryptogenes [49, 327, 328], whose primary transcripts lack translatable open reading frames. To become translatable, these transcripts require insertions and deletions of variable numbers of uridylates at strictly

defined positions. This RNA editing is directed by gRNA molecules and is carried out by a highly specialized protein complex known as the editosome [326, 329, 330].

gRNAs are short ~30-60 nucleotides long molecules. The editing processes require hundreds of distinct gRNAs which are, with only two maxicircle-encoded exceptions, all encoded on minicircles [331-334]. gRNAs base pair with pre-edited transcripts to guide the RNA editing reactions and the non-hybridizing part provides the information of how many uridylates will be inserted or deleted [333, 335]. These reactions are very complex and in total more than 70 proteins have directly or indirectly been associated with RNA editing [326]. Recent structural studies of the active editosome have significantly advanced our understandings of these processes. One key discovery was that the gRNA-transcript recognition is initiated by ribonucleoprotein complex remodelling processes rather than by direct base pairing between the RNA molecules [336].

RNA editing is essential for creating open reading frames in transcripts derived from cryptogenes. In addition, a process known as alternative RNA editing can expand the transcriptome by generating novel open reading frames [337-339]. Six cryptogenes are believed to have the potential for dual coding, and one alternatively edited transcript has been studied in detail (see Chapter 1.5.3.3) [338, 339]. Studying alternative RNA editing is challenging, as it requires *de novo* mRNA or, ideally, protein sequencing. However, recent advances in *de novo* protein sequencing technologies may soon make it possible to investigate the scope and functional relevance of alternative RNA editing [340, 341].

1.5.1.4 Mitochondrial ribosome

Mitochondrial ribosomes (mitoribosomes) have been derived from a bacterial ribosome [342]. However, mitoribosomes have undergone substantial changes and are highly adapted to the translation of the small mitochondrially encoded proteome. Structural insights in mitoribosomes of various organisms revealed not only the many differences to bacterial ribosomes but also the great variability between organisms of different eukaryotic groups [342-346].

The structure determination of the mitoribosome of *T. brucei* revealed an unexpected ribosomal morphology [327]. The trypanosomal mitoribosome contains significantly shortened ribosomal RNAs, the 9S and 12S rRNAs, with a total length of 1’796 nucleotides, compared to total 4’566 nucleotides in *Escherichia coli* [327, 347]. This reduction is likely compensated for by the drastically increased mitoribosomal protein content. In total, the mature trypanosomal

mitoribosome contains 127 proteins, compared to ~55 in *E. coli* [327, 347]. Consequently, the protein to RNA ratio of the *T. brucei* mitoribosome is 6:1, which is significantly higher than the 2:1 ratio in *E. coli* or the 1:2 ratio of mammalian mitoribosomes [327, 347, 348].

The high protein content of the whole mitoribosome, and especially of the small subunit, is responsible for another unexpected structural property; the “small” subunit is larger than the “large” subunit [327, 349]. Some mitoribosomal proteins of *T. brucei* are not typically associated with ribosomes. Furthermore, an additional previously unknown mitochondrially encoded mitoribosomal protein has also been discovered [327].

Overall, the mitoribosome of *T. brucei* is unique and likely highly adapted to the lifestyle and mitochondrial biogenesis of this parasite. The high protein content of the trypanosomal mitoribosome suggests a protein, rather than RNA-based architecture found in other organisms and their mitochondria [327].

1.5.2 Kinetoplast

The kinetoplast and the kDNA are the functional counterparts of mitochondrial nucleoids and the mitochondrial DNA, respectively, of eukaryotes outside the Kinetoplastida lineage. Similar to the classical mitochondrial genomes of other eukaryotes, the kDNA provides all the genetic information coding for a small subset of mitochondrial protein and RNA genes. However, in kinetoplastids, this information is distributed on two types of DNA molecules, maxicircles and minicircles (see also Chapter 1.5.1.3). While the full phylogenetic diversity of the Kinetoplastida remains unresolved, differences in kinetoplast morphology and organization exist at the genus level (Figure 15) [216]. These differences have led to the classification of various kDNA network structures, including the classical disk-shaped eukinetoplast, the prokinetoplast, the pankinetoplast, the megakinetoplast, and the polykinetoplast (Figure 15A) [350].

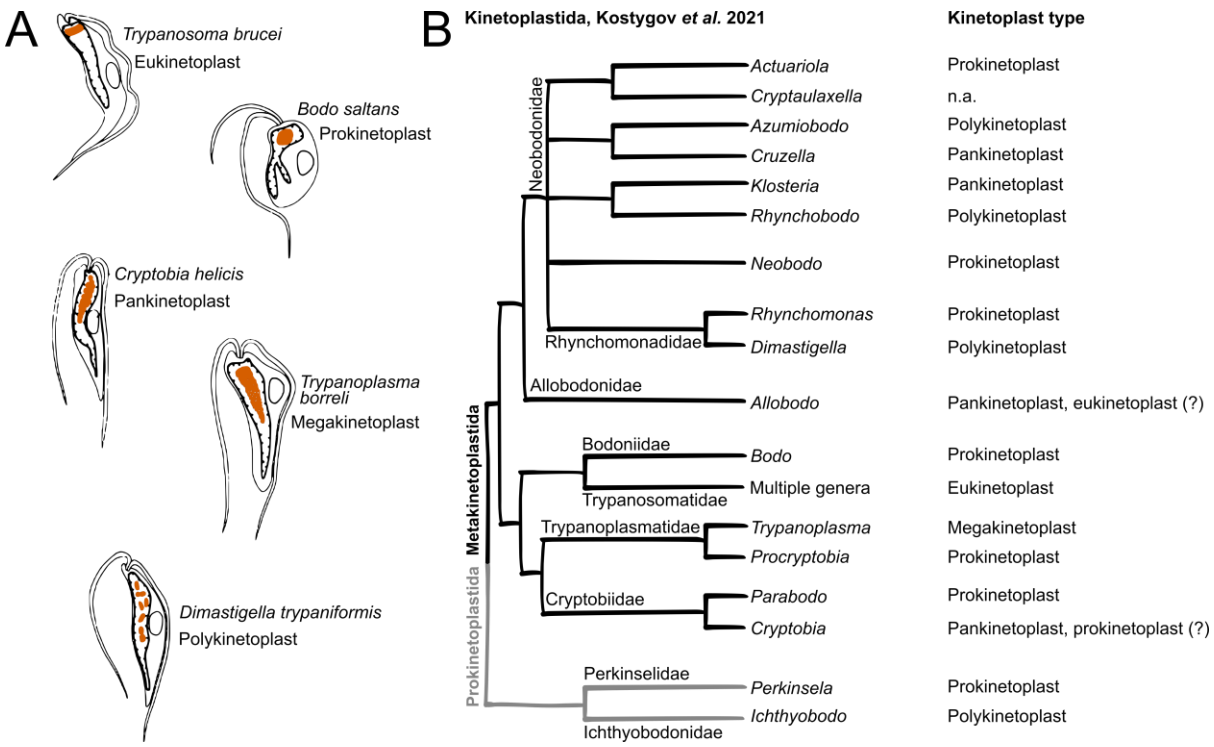

Figure 15. **Kinetoplast diversity**. **(A)** Schematic depictions of the five recognized kinetoplast types (orange). Drawings adapted from [350]. **(B)** Phylogenetic tree of the Pro- and Metakinetoplastida as suggested by Kostygov *et al.* [216]. The kinetoplast types of the genera are indicated on the right side. n.a.: not available or inconclusive. Question marks indicate uncertain groupings which, in the case of *Cryptobia*, might be due to phylogenomic misclassifications and paraphyly in respect to *Parabodo*.

1.5.2.1 Eukinetoplast

The eukinetoplast describes the kDNA network of species of the Trypanosomatidae (Figure 15) [350]. These networks contain, depending on the species, around 25 maxicircles and 5000 minicircles which are interlocked among themselves and with each other to form a single planar elliptical network measuring ~1 µm in diameter [350]. Maxicircles within a species are generally identical, whereas minicircles exhibit significant diversity, with their numbers varying even between strains [351, 352]. The size of maxicircles typically ranges from 20-64 kb [353] and, in *T. brucei,* encode (crypto)genes of 18 mitochondrial proteins, as well as 9S and 12S mitochondrial ribosomal RNAs [49, 327, 328]. In contrast, minicircles are much smaller ranging from 0.5-10 kb with usually constant lengths within one species. They encode one or a few guide RNAs [353, 354]. Hence, despite their small size the minicircles account for ~90% of the kDNA mass making the mitochondrial genome approximately 10 Mb [355]. The kDNA is condensed by histone-like proteins [356]. Unlike other circular DNA molecules, minicircles are not supercoiled [178]. A notable feature of eukinetoplast minicircles is the presence of a conserved twelve nucleotide long sequence known as the “universal minicircle sequence” (UMS). This

sequence is recognized by UMS binding protein 1 (UMSBP1), which is essential for minicircle replication [357]. Minicircle replication involves the release of the molecules from the network and the reattachment at the periphery of the kinetoplast, the so called antipodal sites [178]. However, the mechanisms regulating this process remain poorly understood. A mathematical modelling study suggested that minicircle segregation may occur randomly, accompanied by frequent genetic exchange [358]. Unlike minicircles, maxicircles remain within the network during replication [359]. The eukinetoplast is physically tethered to the basal body of the flagellum, enabling controlled segregation of the kDNA networks after replication. Interestingly, recent research has identified kDNA networks with morphological similarities to the eukinetoplast of trypanosomatids in two species of the Allobodonidae (Figure 15) [360].

1.5.2.2 Prokinetoplast

Kinetoplasts classified as prokinetoplasts have been described in *Bodo saltans*, a species belonging to the Bodonidae, the sister family of the Trypanosomatidae (Figure 15) [216]. Based on the evolutionary history of Kinetoplastida, it is believed that the prokinetoplast of *B. saltans* may represent an ancestral form of the eukinetoplast found in the Trypanosomatidae [350]. Like the eukinetoplast, the prokinetoplast contains both maxicircles and minicircles. However, the prokinetoplast is significantly less concatenated [361]. The maxicircles of *B. saltans* are ~70 kb long and likely encode rRNA genes as well as (crypto)genes of mitochondrial proteins though they have not yet been fully sequenced [362]. The minicircles, which are about 1.4 kb in length, closely resemble those of trypanosomatids and encode two guide RNAs each. Additionally, they contain a ~350 nucleotides long conserved region with a sequence similar to the UMS [361]. However, neither the replication of the maxicircles nor of the minicircles in *B. saltans* have been studied and their sorting and segregation mechanisms are unknown. The prokinetoplast is located near the basal body of the flagellum, but it is unclear whether the two structures are physically tethered, as seen in the eukinetoplast of trypanosomatids [350]. Beyond the Bodonidae, kDNA networks with morphological similarities to the prokinetoplast have also been identified in species from several other groups. These include certain genera within the Neobodonidae, Rhynchomonadinae, Cryptobiidae, Trypanoplasmatidae and the Perkinselidae of the Prokinetoplastida (Figure 15) [216].

The Bodonidae and Trypanosomatidae belong to the orders Eubodonia and Trypanosomatida, respectively, which are sister orders of the Parabodonida. Currently, the Parabodonida contains two families: Cryptobiidae and Trypanoplasmatidae (Figure 15). In each of these families, the kinetoplast architectures of one species have been analyzed, leading to the identification of two

distinct kDNA structures: the pankinetoplast of *Cryptobia helicis* and the megakinetoplast of *Trypanoplasma borreli* (Figure 15) [216, 350].

1.5.2.3 Pankinetoplast

In *C. helicis*, the pankinetoplast occupies most of the mitochondrial matrix [363]. Similar to the prokinetoplast, its kDNA is not arranged in a concatenated network [364]. Instead, the ~8400 minicircles occur mostly as monomeric, and for minicircles unusual, supercoiled molecules. They are ~4.2 kb in size but it is uncertain whether they encode guide RNAs. The replication of the minicircles may, as in the other kinetoplast types, start on conserved UMS-related sequences [364]. The maxicircles of *C. helicis* are approximately 43 kb long, and the only two protein-coding genes identified so far do not require RNA editing [364]. Additionally, kDNA networks with morphological similarity to the pankinetoplast of *C. helicis* were also described in species of some genera of the Allobodonidae and Neobodonidae (Figure 15) [216].

1.5.2.4 Megakinetoplast

The megakinetoplast has so far been exclusively observed in species of the genus *Trypanoplasma* (Trypanoplasmatidae) [216, 350]. In these species, the kDNA is dispersed throughout a large region of the mitochondrial matrix and is likely arranged in a loose network [363]. Interestingly, the “minicircles” in *Trypanoplasma* may be linear molecules of approximately 70 kb length, each encoding an average of 23 putative guide RNAs. In contrast, the maxicircles are ~42 kb and encode rRNAs as well as protein coding (crypto)genes. Hence, the kDNA of the megakinetoplast has a distinctive architecture so far not found in any species outside the genus *Trypanoplasma* [365].

1.5.2.5 Polykinetoplast

The four types of kDNA networks discussed above all may be described as single nucleoid mitochondrial genomes. However, kDNA networks that form multiple globular bundles have also been identified. These were first characterized as polykinetoplasts in two species of the genus *Dimastigella* (Rhynchomonadinae) (Figure 15) [366]. In *Dimastigella* spp. polykinetoplasts are distributed across various discrete locations within the matrix. Similar to the prokinetoplast of *Bodo saltans*, the minicircles, ranging from ~1.2 to 1.5 kb in length, are mostly monomeric and not supercoiled. No data on maxicircles is available to date [366]. Following the initial discovery, polykinetoplasts were also reported in *Cruzella marina* (Neobodonidae) where minicircles are ~2 kb long and exist as relaxed circular molecules. In this species, ~95% of minicircles occur as monomers, ~4% as dimers, and ~1% as tri- or tetramers

[367]. Due to similarities in minicircle organization, it has been proposed that the polykinetoplast represents an ancestral form of the prokinetoplast found in *B. saltans* [350]. Polykinetoplast-like networks have also been described in species of the two genera *Desmomonas* and *Jarrelia* which both have an uncertain phylogenetic origin in the Metakinetoplastida. Additionally, similar kinetoplast architectures have been reported in species belonging to the Ichthyobodonidae in the Prokinetoplastida order [216] and two further prokinetoplastid species with uncertain phylogenetic placement may also possess such kDNA networks [368].

1.5.3 Kinetoplast segregation – tripartite attachment complex

Members of the Kinetoplastida, except for species with polykinetoplasts, have mitochondrial genomes which are condensed in a single structure. This organization resembles the condensation of nuclear DNA within the nucleus, necessitating precise control over kDNA replication and segregation [369, 370]. Unfortunately, in kinetoplastids with pro-, mega-, or pankinetoplasts, the mechanisms for maintaining the mitochondrial genome remain largely unexplored. As a result, little is known about the kinetoplast inheritance in these organisms. Only in the well-studied trypanosomatids, the replication and segregation of the eukinetoplast, hereafter referred to simply as the kinetoplast, have been well characterized. In these organisms, the kDNA replication and segregation are tightly linked to the cell cycle (Figure 16) [350].

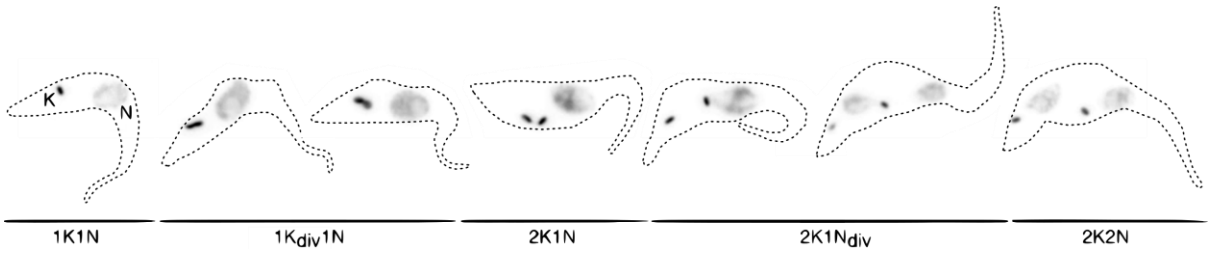

Figure 16. **Temporal coordination of kDNA and nuclear DNA replication and segregation**. Images from left to right display both kDNA and nuclear DNA in *T. brucei* cells during progressive cell cycle stages. Dotted lines mark the periphery of the cell body. K: kDNA, N: nuclear DNA, div: dividing. Images adapted from [371].

Throughout the life cycle and cell cycle of trypanosomatids, the kinetoplast remains physically linked with the basal body of the single flagellum [372]. This linkage is essential for the precise segregation of the replicated kinetoplast to the daughter cells during cytokinesis. The replication of both mini- and maxicircles is coordinated with the nuclear cell cycle through largely unknown pathways [178]. During replication, the minicircles are released from the kDNA

network and the daughter minicircles are reattached at the antipodal sites. The consequence of this process is the complete removal of minicircles from the central region of the kinetoplast which exposes a structure known as the “Nabelschnur” [371]. This structure contains the replicated maxicircles, which are segregated last, and recent discoveries propose that the “Nabelschnur” is a protein-dominated structure [373-375]. The probasal body matures to a basal body with a new flagellum concurrently with kDNA replication. Thereby, the new mature basal body is directly tethered to the replicated kinetoplast, a connection already established in the probasal body stage [369]. Once all cell cycle checkpoints are passed, flagellar motion contributes to the separation of the basal bodies. This separation resolves the “Nabelschnur”, leading to the segregation of the duplicated kDNA networks into daughter cells [178]. However, the exact mechanisms behind basal body separation remain poorly understood. In *T. brucei*, cytokinesis occurs in an unusual manner, with the division plane positioned between the duplicated flagella along the longitudinal axis of the cell [376]. While various of the complex flagellar structures have been linked to the positioning of this division plane [377, 378], the involved proteins and their functions are not yet fully characterized. Recently, a triplet of proteins localizing to the microtubule quartet, a structure associated with the base of the flagellum, was characterized. All three proteins play a critical role in basal body segregation and significantly influence cytokinesis [379-382]. These discoveries underscore the importance of flagellar separation in cytokinesis and highlight the microtubule quartet’s essential role in basal body segregation.

In 1991, researchers demonstrated that kinetoplast segregation in trypanosomes is indirectly controlled by the basal bodies [383]. This is made possible by the TAC, a unique structure that physically tethers the basal and probasal body to the kinetoplast, thereby determining the latter’s position within the cell (Figure 17) [372, 384]. The TAC is a mega-Dalton-sized protein complex likely containing thousands of subunits. The complex appears in electron microscopy as the name giving tripartite structure. Within the cytosol, the TAC region is characterized by a ribosome-depleted zone, where filaments extend from the basal and probasal body toward the OM. The OM and IM appear in closer proximity in the region of the TAC and the IM does not form cristae. On the matrix side of the IM, another set of filaments extends toward the kDNA network. The three substructures were first observed by Ogbadoyi *et al.*, who proposed naming them exclusion zone filaments, differentiated mitochondrial membranes, and unilateral filaments (Figure 17) [384]. More than two decades later, after the identification of most of the subunits, the tripartite nature of the TAC was redefined to reflect its molecular composition and biogenesis. The TAC is now recognized as having three molecular modules: the cytosolic TAC

module, the OM TAC module, and the inner TAC module (Figure 18) [369]. Despite significant progress in understanding the TAC, some fundamental questions remain. While most TAC subunits may have been identified, the exact nature of the connections to both the basal body and the kDNA remain unresolved [369].

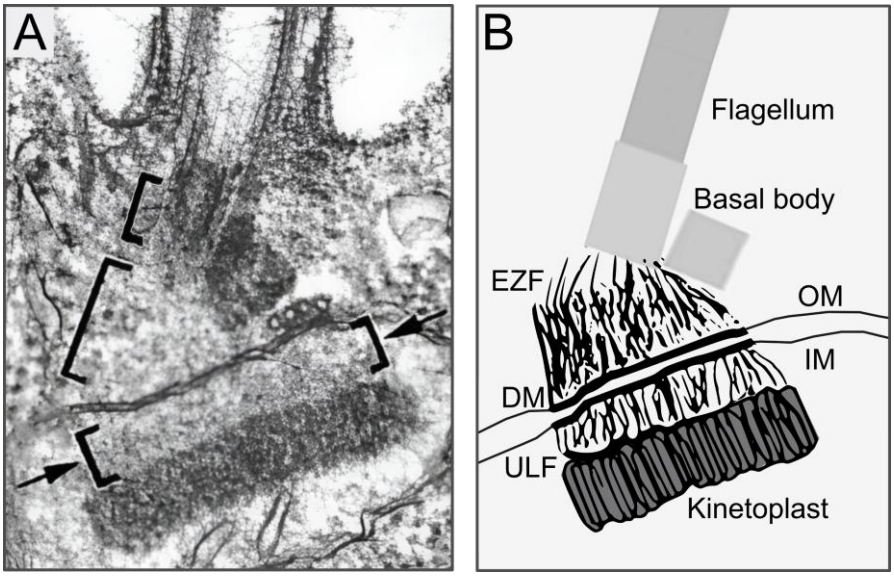

Figure 17. **TAC morphology**. (A) Transmission electron microscopy image of the basal body-kinetoplast interphase of a *T. brucei* cell. Black brackets mark the basal body, the exclusion zone filaments, and the unilateral filaments (top to bottom). The image was adapted from [384]. (B) Structural interpretation of the image in (A) using TAC illustrations by Ogbadoyi *et al*. EZF: exclusion zone filaments, DM: differentiated mitochondrial membranes, ULF: unilateral filaments, OM: mitochondrial outer membrane, IM: mitochondrial inner membrane. Drawings adapted from [384].

The TAC is present throughout the entire cell cycle. As the probasal body matures and the kDNA is replicated, a new TAC assembles to connect these structures [369, 370]. Furthermore, the TAC remains nearly unchanged between the procyclic and bloodstream forms of *T. brucei*, the only two life stages that can be cultured [369, 370]. Interestingly, most TAC subunits are upregulated by up to two folds in the bloodstream form, though the reason and significance remain unknown [239, 240]. The TAC is expected to occur in all life cycle stages without major changes, however this has not yet been thoroughly investigated.

The primary function of the TAC is to connect the basal and probasal body to the kinetoplast, enabling the co-segregation of the latter during cytokinesis [369, 370, 385]. Disrupting TAC integrity significantly impacts kinetoplast segregation. However, TAC absence does not interfere with cytokinesis, suggesting that the TAC is not involved in a cell cycle checkpoint [386]. When the TAC is disrupted, a characteristic mis-segregation pattern occurs: one daughter cell lacks kDNA, while the other retains an over-replicated kinetoplast. Interestingly, this over-replicated

kinetoplast remains attached to the basal body, indicating that the TAC has a low turnover rate. In procyclic *T. brucei*, cells without kDNA can continue proliferating for a few cell cycles, eventually leading to populations where most cells lack kDNA, while a minority accumulates over-replicated kDNA networks, sometimes exceeding the size of the nucleus. In some cases, TAC disruption does not result in complete kinetoplast mis-segregation; instead, daughter cells may retain small fragments of the kDNA network [369, 370, 385]. In some bloodstream form *T. brucei* strains which can tolerate the loss of the mitochondrial genome [233], the TAC is nonessential for cell growth and proliferation [387, 388]. The long-term absence of the TAC in these cells results in populations lacking any detectable kDNA, so called akinetoplastic cells and populations, likely because cells with over-replicated kinetoplasts possess a reduced cell fitness [388].

In addition to its role in kinetoplast segregation, the TAC also passively determines the position of the posterior region of the mitochondrion [264]. Furthermore, some of its subunits may play a direct or indirect role in kDNA maintenance. In TAC-depleted cells, replicated minicircles are not reattached at the antipodal sites but around the periphery of the kDNA network resulting in globular over-replicated kinetoplasts [385, 386]. Additionally, several kDNA maintenance factors have been shown to rely, at least partially, on the TAC for proper localization [389, 390]. However, since the connection between the inner TAC module and the kinetoplast remains unresolved, the significance of these findings has yet to be fully determined.

1.5.3.1 Modules and their subunits

The discovery and morphological characterization of the TAC by Ogbadoyi *et al.* initiated the search for subunits. The first protein formally characterized as a TAC subunit was p166, a subunit of the inner TAC module. Since then, several additional subunits have been characterized and linked to kinetoplast segregation, although some only partially localize to the TAC. To distinguish “core” TAC components, Schneider & Ochsenreiter established a set of criteria. To qualify as a core TAC subunit, a protein must (i) localize between the basal or probasal body and the kDNA in the living cell and on the purified flagellum, (ii) upon depletion cause a kinetoplast segregation but not replication defect in any life cycle stage, (iii) be nonessential for cytokinesis in natural or engineered akinetoplastic strains of bloodstream form *T. brucei* [370]. Currently, nine proteins are classified as core TAC subunits. Of these, one belongs to the cytosolic TAC module, five to the OM TAC module, and three to the inner TAC module (Figure 18) [369, 391].

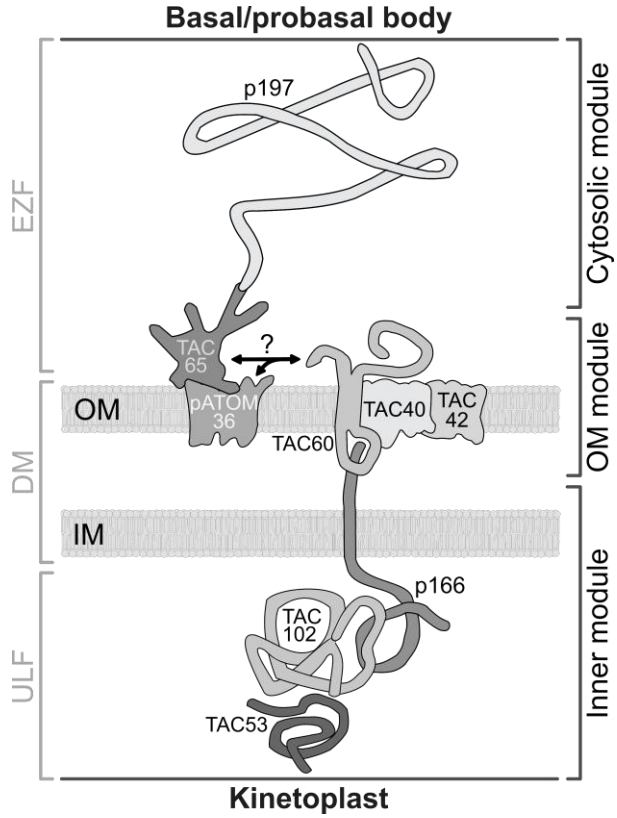

Figure 18. **Composition of molecular TAC modules.** The model does neither represent subunits sizes in relative scale nor their stoichiometry. The range of the molecular TAC modules as defined by Aeschlimann *et al.* are indicated on the right. Morphological subdomains previously defined by Ogbadoyi *et al.* are indicated on the left (EZF: exclusion zone filaments, DM: differentiated mitochondrial membranes, ULF: unilateral filaments). OM: mitochondrial outer membrane, IM: mitochondrial inner membrane.

Cytosolic TAC module

The cytosolic TAC module is a filamentous structure that connects the basal and probasal body to the OM [369]. Surprisingly, p197 is the only core TAC subunit so far identified in this module (Figure 18) [369, 381, 392]. P197 contains three domains: the N-terminal domain, the central (repeat) domain, and the C-terminal domain [392]. The first full genome sequencing of *T. brucei* suggested that the central domain contains approximately 3.5 identical repeats, each 175 residues long, making up a predicted protein size of 197 kDa [393]. However, a later cDNA sequence suggested the presence of more than 26 repeats, though no reads spanning the entire repeat region were found [394]. The most recent genome sequencing, using long-read techniques, identified ~35.3 near-identical repeats in both p197 alleles, increasing the predicted protein size to 880 kDa [395]. Given its large size, it is not surprising that an early ultrastructure expansion microscopy study in *T. brucei* was able to spatially separate the N- and C-terminal domains, localizing them to the OM and basal/probasal body, respectively [392]. This study also showed that the N-terminal domain interacts with TAC65 at the OM, while the C-

terminal domain interacts with as yet unknown protein(s) at the base of the basal and probasal body. Interestingly, phylogenetic comparison of *T. brucei* p197 to orthologs in other trypanosomatids revealed that only the N- and C-terminal domains show some sequence homology while the central domains vary substantially in length and composition [392]. While the N- and C-terminal domains anchor the protein to the OM and basal/probasal body, respectively, the central domain determines the distance between the OM and the basal body [392] and was proposed to function as a molecular spring, allowing dynamic movement of the basal and probasal body relative to the mitochondrion and kinetoplast [396].

Besides p197, a protein likely associated with the cytosolic TAC module is the misleadingly named kinetoplastid-membrane protein-11 (KMP11). KMP11 is well conserved among Kinetoplastida and was initially thought to be a cell membrane protein [397]. However, later studies identified it as a component of the basal body and the flagellum, where it plays a crucial role in cell division, likely by contributing to basal body separation [398]. More recently, KMP11 has been found to associate with p197, particularly with its central repeat domain [399]. However, determining the exact role of KMP11 in kinetoplast segregation remains challenging, as cytokinesis defects occur within a day after its depletion, preceding any detectable kinetoplast mis-segregation [399].

OM TAC module

The N-termini of the p197-filaments of the cytosolic TAC module connect the basal and probasal body to a morphologically unique region of the mitochondrion, known as the OM TAC module [369]. This module exhibits an unexpected complexity, consisting of five unique subunits (Figure 18). Four of these proteins are membrane-embedded, while TAC65 is thought to be a peripheral membrane protein attached to the cytosolic side of the OM [369, 370]. TAC65 interacts with the N-terminal domain of p197, anchoring the cytosolic TAC module filaments to the OM [392]. TAC65 is associated with the OM by interacting with the peripherally associated ATOM36 (pATOM36) [279]. However, the specific domains of TAC65 involved in these interactions, as well as the extent to which TAC65 is associated with or possibly even partially embedded in the OM, remain unknown. pATOM36 is an integral membrane protein with multiple α-helical transmembrane domains and the only core TAC subunit with a dual localization and function [279]. In addition to functioning as an OM TAC module subunit, pATOM36 is an insertase for a subset of OM proteins including some subunits of the ATOM complex (see also Chapter 1.5.1.1). It is therefore essential for ATOM complex assembly [279, 400]. Unlike all other core TAC subunits, pATOM36 is essential for mitochondrial biogenesis in akinetoplastic cells

[279]. It has been reported that pATOM36 has two α-helical transmembrane domains and that the C-terminus faces the cytosol [279, 280]. However, structure predictions with the AlphaFold3 model suggest the presence of five putative transmembrane α-helices. Apart from pATOM36, the OM TAC module contains a second α-helical transmembrane protein, TAC60 [401]. Unlike TAC65 and pATOM36, the secondary and tertiary structures of TAC60 have been studied in detail. TAC60 is anchored in the OM by two transmembrane α-helices (residues ~121-141 and ~238-258), creating a loop exposed to the intermembrane space (residues ~142-237) [401]. Hence, the remaining cytosol-exposed N-terminal as well as C-terminal domains are ~120 and ~295 residues long, respectively. Interestingly, while the N-terminal domain is essential for TAC integration and function, the C-terminal domain, comprising more than half of the protein, is dispensable in procyclic form *T. brucei* [401]. TAC60 was identified due to its stable interaction with TAC40 and TAC42, two β-barrel membrane proteins and subunits of the OM TAC module [387, 401]. TAC40 belongs to the voltage-dependent anion-selective channel (VDAC)-like protein family, while TAC42 is a unique, kinetoplastid-specific β-barrel protein. Interestingly, neither TAC40 nor TAC42 function as essential OM transporters for metabolites, as both are dispensable for the growth of akinetoplastic *T. brucei* strains [387, 401]. This makes them the first known mitochondrial integral membrane β-barrel proteins with a structural rather than a transport role. Their β-barrel structure suggests that they are of bacterial origin [369]. However, no direct orthologs of either of the two proteins could be identified in extant Bacteria.

Inner TAC module

The inner TAC module is a filamentous structure that connects the OM TAC module to the kDNA [369]. The connection between the OM TAC module and the inner TAC module is formed by p166 binding to the intermembrane space-exposed loop of TAC60 (Figure 18) [402]. p166 was the first TAC subunit identified, but it was initially unclear whether the protein is anchored in the IM [386]. However, a later study showed that p166 is targeted to the IM by a presequence and that p166 has a single α-helical transmembrane domain close to the C-terminus (residues ~ 1440–1462) [402]. As a result, most of the protein is exposed to the matrix, while only the ~39 residues of the very C-terminus reach into the intermembrane space, where p166 directly binds to TAC60 [402]. Although the matrix domain of p166 has not been analysed in detail, a yeast two-hybrid screen suggested that a domain of p166 that binds to TAC102 is between residues 71–210 [403]. Together with p166, TAC102 likely contributes to the formation of the filamentous structures of the inner TAC module, which are visible by electron microscopy. Like p166, TAC102 localizes between the basal body and the kinetoplast throughout the cell cycle, though it appears to be positioned closer to the kinetoplast than p166 (Figure 18) [388, 404]. Unlike

p166, TAC102 does not have an N-terminal presequence but may instead contain targeting signals in its C-terminal region. Additionally, the C-terminal domains of TAC102 may interact with TAC53 or a kinetoplast-associated structure, while the N-terminal domain is likely involved in binding to the matrix domain of p166 [404]. TAC53 is a protein that has previously been characterized as a kDNA maintenance factor [405], but the TAC-association has been discovered only recently [391]. TAC53 fulfils all requirements of a core TAC protein, but interestingly, localizes to the TAC in a cell cycle-dependent manner. It has been proposed that TAC53 may be the most basal body distal TAC subunit [391].

1.5.3.2 TAC-kDNA connection

None of the core TAC subunits are DNA-binding proteins, suggesting that the TAC does not directly link the basal body to the kDNA. Instead, it likely connects to an intermediate structure that anchors the kinetoplast. This structure may be referred to as the “kinetochore-like structure” of the kDNA [369].

TAC53 is the core TAC subunit located closest to the kinetoplast, in the region of the postulated kinetochore-like structure [391]. Although the direct interaction partners of TAC53 within this structure remain unknown, several proteins have been associated with the putative kinetochore-like region. One such protein is the TAC-associated protein 110 (TAP110) [406]. Unlike all other core TAC subunits, TAP110 is not essential for cell growth or kinetoplast segregation, suggesting functional redundancy within the kinetochore-like structure. TAP110 localizes to a distinct site between TAC102 and the kinetoplast. Notably, TAP110 remains associated with the TAC even in the absence of the kinetoplast. Whether TAP110 binds directly to DNA is still unknown [406]. Apart from TAP110, an HMG-box-containing protein termed TbmtHMG44 as well as a protein named kDNA-associated protein 68kDa (TbKAP68) have been identified as subunits of the kinetochore-like structure [390]. Unlike TAP110, both TbmtHMG44 and TbKAP68 are essential for kDNA maintenance; however, their deletion leads to the loss of kDNA rather than mis-segregation. These two proteins have been shown to interact *in vitro*, though their functional relationships to TAP110, TAC53, or TAC102 remain unclear. Purified TbKAP68 exhibits nonspecific DNA-binding activity, making it the first TAC-associated protein with a potential role in anchoring the TAC to the kDNA [390]. In summary, the current model of kinetoplast segregation in *T. brucei* describes the TAC as a filamentous structure composed of nine core subunits, connecting the basal and probasal body to a kinetochore-like structure at the kinetoplast. This latter structure includes at least three proteins, TAP110, TbmtHMG44, and

TbKAP68, though further research is needed to fully understand how the TAC is linked to the kDNA.

1.5.3.3 Other proposed TAC-associated proteins

In addition to the TAC subunits introduced in chapter 1.5.3.1, four other proteins have been previously associated with the TAC and/or linked to kinetoplast segregation [370]. However, the TAC association of some of these proteins appears to be life cycle stage-dependent, and none of them were identified in proteomic screens targeting TAC subunits [391]. Additionally, a common characteristic of all core TAC subunits is that kinetoplast segregation defects occur one or a few cell cycles post protein depletion but before the onset of the growth defect [404]. Notably, none of the following proteins exhibit such a phenotype.

One protein previously proposed as a cytosolic TAC module subunit is TBCCD1, a *T. brucei* protein belonging to the tubulin-binding cofactor C family. TBCCD1 has been reported to localize to the basal and/or probasal body, the Golgi bi-lobe, and the anterior end of the cell body [407]. Additionally, weak signals have been detected in the flagellar attachment zone. Depleting TBCCD1 results in a growth defect that begins after one day, with kinetoplast mis-segregation observed two days post depletion [407]. However, it remains unclear whether this mis-segregation is a primary or secondary effect. Typically, core TAC subunits do not cause growth defects until at least three days post depletion, whereas kinetoplast segregation defects appear within the first day.

An enigmatic potential TAC subunit of the IM is the protein product of an alternatively edited transcript of the cytochrome oxidase subunit 3 (Cox3) with the name alternatively edited protein 1 (AEP-1) [339]. The alternative editing generates an open reading frame coding for a 59 residues long novel N-terminal domain followed by the C-terminal 155 residues of Cox3 [408]. AEP-1 was located in the mitochondrion with an enrichment near the kinetoplast. There, it is positioned between the kDNA and the antigen recognized by BBA4, which resides in the cytosolic TAC module, without directly overlapping with either structure [339]. Structural modelling based on bovine Cox3 suggests that AEP-1 may contain up to five transmembrane α-helices, while predictions using the latest AlphaFold model propose four. The nuclear expression of mitochondrion-targeted N-terminal domains of AEP-1 has been shown to cause dominant-negative growth defects, accompanied by kinetoplast segregation defects. Furthermore, *in vitro* studies have demonstrated that AEP-1 can bind DNA. Taken together, these findings suggest that AEP-1 could function as an IM subunit of the TAC [339]. However, the natural occurrence of

T. brucei f. evansi strains with minicircle-only kinetoplasts, so called dyskinetoplastic cells [409], suggest that, if AEP-1 is involved in the TAC, it is not essential for its function [410].

The α-ketoglutarate dehydrogenase component E2 (α-KDE2) is a Krebs cycle enzyme that has been shown to have a moonlighting role in kinetoplast segregation in bloodstream form *Trypanosoma brucei* [411]. In both the procyclic and bloodstream life stages, α-KDE2 localizes to the mitochondrion. However, in the bloodstream form, it is specifically detected at the antipodal sites of the kinetoplast, even in purified flagella [411]. Although the Krebs cycle is inactive in bloodstream form *T. brucei*, and the enzymatic function of α-KDE2 is also inactivated, its depletion is lethal for the parasite. Cells lacking α-KDE2 exhibit a growth retardation starting two days after knockdown induction, with kinetoplast segregation defects appearing three days post induction. Based on these findings, α-KDE2 has been proposed to play a significant role in the TAC [411]. However, its function in the procyclic form remains elusive. Additionally, as with TBCCD1, it cannot be ruled out that the observed kinetoplast segregation defect is a secondary effect since the analysis was conducted one day after the onset of the growth defect.

Finally, the mitochondrial acyl carrier protein (ACP), a protein involved in fatty acid and lipid biogenesis, has been functionally linked to the TAC. In bloodstream form *T. brucei*, ACP depletion is lethal, with kinetoplast mis-segregation occurring before any signs of impaired growth [412]. These findings could imply a possible effect of mitochondrial membrane composition on TAC biogenesis, since ACP depletion affects lipid biogenesis. However, a follow-up study, summarized in the bachelor's thesis of Siri Speck at the University of Bern, found no evidence linking this kinetoplast segregation defect to disruptions in the assembly of TAC40, p166, or TAC102 [413]. While an effect of membrane composition on TAC biogenesis cannot be ruled out, the observed kinetoplast mis-segregation following ACP depletion in bloodstream form parasites is likely a secondary effect.

The four proteins discussed above have been structurally and/or functionally linked to kinetoplast segregation. In addition, several proteins have been proposed as TAC subunits based primarily on their cellular localization. Notably, all of these proteins have been identified and characterized in follow-up studies of the TrypTag project [414, 415].

One of these proteins is TbHD52, an ortholog of the human sterile α motif and histidine–aspartic acid domain-containing protein 1 (SAMHD1) [416]. TbHD52 was proposed as a "TAC middle" subunit, placing it alongside the established subunits of the OM TAC module [417]. However, TbHD52 was characterized previously as an essential enzyme for pyrimidine homeostasis in *T.*

brucei. Cells depleted for TbHD52 were reported to have strong defects in genomic integrity, cell cycle progression, as well as nuclear DNA and kinetoplast segregation. These effects, however, were primarily linked to pyrimidine auxotrophy, as near-normal cell growth could be restored by supplementing 0.6 mM exogenous thymidine [416]. Additionally, while the same study confirmed the mitochondrial localization of TbHD52, no enrichment at the TAC or kinetoplast was observed. Therefore, TbHD52 is unlikely a component of the TAC.

Apart from TbHD52, Pyrih *et al.* proposed 13 subunits for the "TAC proximal to kinetoplast/kinetoplast" region, four of which had not been associated with this region before [417]. While none of the four proteins were studied in detail before, there is currently no strong evidence for their TAC association, as they have not been identified in proteomic screens aiming to identify TAC subunits [391].

The TrypTag project further identified the protein product of Tb927.4.2780 as a putative subunit of the cytosolic TAC module [414]. In a follow up study, the localization of the protein to the TAC was confirmed, and it was named TAC86 [418]. Given its possible localization in the cytosolic TAC module, it was postulated that TAC86 may be one of the hitherto unknown antigens recognized by the BBA4 or Mab22 antibodies, although this was not directly investigated [418]. However, while it is known that the epitopes recognized by BBA4 and Mab22 depend on p197 for TAC localization [388], or may be part of p197 itself, the putative TAC86 has not been detected in p197-based TAC depletion experiments [391]. Therefore, until the biochemical association of the putative TAC86 with the TAC and a role in kinetoplast segregation can be shown, the protein product of Tb927.4.2780 should not be classified as a TAC subunit.

1.5.3.4 Biogenesis and assembly

The discoveries of core TAC subunits over the past two decades have significantly advanced our understanding of this unique structure. In particular, studies on the effects of the depletion of individual subunit have initiated a new area of research focused on TAC assembly and biogenesis.

A key aspect of TAC biogenesis is the sorting of subunits to the structure [369]. Subunits such as p197 and TAC65, whose precursors are synthesized in the cytosol, may reach the TAC through simple diffusion. A similar mechanism might apply to matrix subunits like TAC102 and TAC53, which are also translated in the cytosol and then imported into the mitochondrial matrix before possibly diffusing to the distal end of the inner TAC module. In contrast, membrane-bound subunits face more complex challenges. These proteins must diffuse laterally along the two-

dimensional planes of the mitochondrial membranes to reach the TAC [369]. For the IM-bound p166, this process is complicated by mitochondrial cristae. The β-barrel proteins TAC40 and TAC42 depend on the ATOM complex and Sam50 for OM insertion [387, 401], while TAC60 depends only on the ATOM complex [271]. The mechanism of OM insertion of pATOM36 has not yet been elucidated [369]. The presequence of p166 suggest a mitochondrial import by the ATOM complex, followed by IM insertion through the TIM complex [402]. However, to date, all of these import processes are believed to occur all over the mitochondrial membranes, as no evidence of co-translational or spatially restricted protein import has been observed in *T. brucei*. Elucidating the mechanisms behind the highly specialized sorting processes remains an important topic for future research.

TAC assembly has been studied extensively, revealing that it proceeds (i) *de novo* and (ii) in a polar fashion, from the (pro)basal body toward the kinetoplast (Figure 19) [388]. Evidence for the *de novo* assembly comes from observations in *T. brucei* strains that tolerate the loss of the kDNA [233]. In these strains, the TAC was shown to fully reassemble even after more than 15 generations of p197 depletion [388]. The polar assembly is supported by many experiments showing that the depletion of any TAC subunit has no effect on subunits located closer to the basal body but causes the delocalization of all subunits nearer to the kinetoplast. Interestingly, subunits not integrated into the TAC are not degraded, likely due to their accumulation in stable assembly intermediates. Notably, the polar assembly model does not fully apply to TAC65. Despite its proximity to the basal body and its direct interaction with p197, TAC65 requires the presence of all OM TAC module subunits for proper TAC assembly [388].

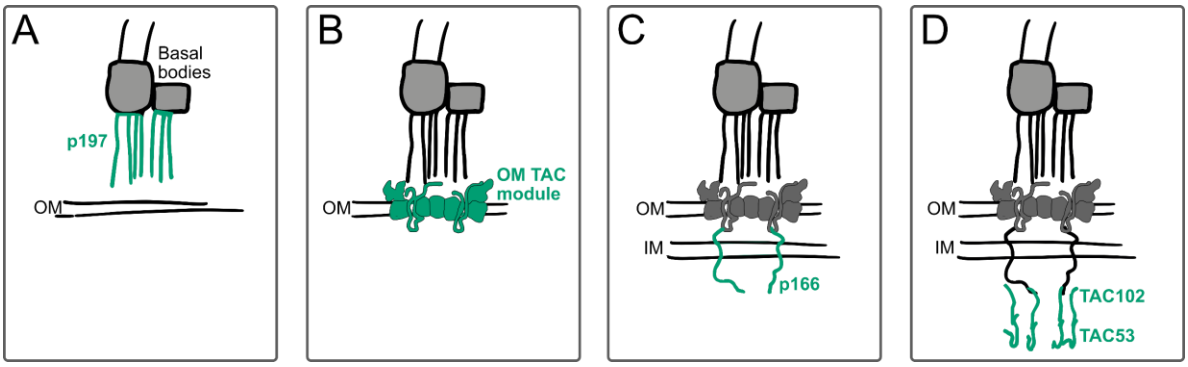

Figure 19. **Hypothetical *de novo* TAC assembly stages**. Illustrations (A-D) show the progressive *de novo* polar assembly of the TAC in a hypothetical setting where no TAC was preexisting on the mature basal body. The structures that are newly assembled in every step are illustrated in green color. OM: mitochondrial outer membrane, IM: mitochondrial inner membrane.

1.5.3.5 Refinement of TAC architecture

Structural features of the TAC have been studied since the complex was discovered. For many years, only electron microscopy images were available to examine its architecture [384]. While these images significantly advanced our understanding of the TAC and its role in kinetoplast segregation, it was not until recent developments in ultrastructure expansion immunofluorescence microscopy that additional structural details became accessible [419].

Ultrastructure expansion microscopy is a technique in which a crosslinked biological sample is embedded in a swellable polymer gel, allowing the sample to physically expand [420]. Unlike conventional approaches that enhance resolution through optical improvements, this method improves resolution by enlarging the sample itself. Although the technique increases resolution by several fold, one potential drawback is the risk of non-physiological sample distortion [420]. However, due to the TAC's resistance to non-ionic detergents, it was proposed that this structure might withstand expansion without significant distortion, making it a good subject for this imaging method [419]. Using ultrastructure expansion microscopy, it was shown that p197 is C-terminally anchored to the basal and probasal body, while the N-terminus connects to the OM TAC module [392]. Furthermore, the same study postulated that the TAC is best described as a hollow cylinder or cone. These observations were confirmed in a recent study that applied ultrastructure expansion microscopy across all TAC modules [391]. Additionally, it was observed that a complete TAC forms on the probasal body even before kinetoplast duplication, suggesting that there are two TACs per kinetoplast [391]. However, future research will be necessary to validate these findings in non-expanded cells.

2. Aim of the Thesis

Mitochondrial genome segregation in trypanosomes is mediated by the TAC which has been best studied in *T. brucei*. Recent research concluded that likely all core TAC subunits have been identified [391]. Nevertheless, apart from a few structural aspects and the basic understanding of its assembly, the biogenesis of the TAC has yet to be thoroughly investigated. Chapter 3.1 highlights the subdomain of the TAC that results in the contact site between the mitochondrial OM and IM. The goal of this chapter was to determine how such a membrane contact site is formed, including the characterization of the molecular interactions. Chapter 3.2 targets the most complex molecular TAC module, the OM TAC module, whose assembly pathways we aimed to elucidate. Chapter 3.3 is an additional, TAC-unrelated chapter, where the aim was to characterize the functions of TbPam16 and TbPam18.

3. Results

3.1 Molecular characterization of the permanent outer-inner membrane contact site of the mitochondrial genome segregation complex in trypanosomes

Philip Stettler [1,2], Bernd Schimanski [1], Salome Aeschlimann [1], André Schneider [1]

[1]Department of Chemistry, Biochemistry and Pharmaceutical Sciences, University of Bern, Switzerland

[2]Graduate School for Cellular and Biomedical Sciences, University of Bern, Switzerland

Published manuscript, first authorship.

Contribution:

- All data shown in figures and supplementary figures.

- Preparation of all cell lines.

- Design of all figures except S1 and contribution to writing of the first draft. Review and editing of the manuscript at all stages.

PLOS PATHOGENS

RESEARCH ARTICLE

Molecular characterization of the permanent outer-inner membrane contact site of the mitochondrial genome segregation complex in trypanosomes

Philip Stettler[1,2], Bernd Schimanski[1], Salome Aeschlimann[1], André Schneider[1]*

1 Department of Chemistry, Biochemistry and Pharmaceutical Sciences, University of Bern, Bern, Switzerland, **2** Graduate School for Cellular and Biomedical Sciences, University of Bern, Bern, Switzerland

* andre.schneider@unibe.ch

Citation: Stettler P, Schimanski B, Aeschlimann S, Schneider A (2024) Molecular characterization of the permanent outer-inner membrane contact site of the mitochondrial genome segregation complex in trypanosomes. PLoS Pathog 20(12): e1012635. https://doi.org/10.1371/journal.ppat.1012635

Editor: Alena Zíková, Biology Centre ASCR, CZECHIA

Received: October 1, 2024

Accepted: November 18, 2024

Published: December 2, 2024

Peer Review History: PLOS recognizes the benefits of transparency in the peer review process; therefore, we enable the publication of all of the content of peer review and author responses alongside final, published articles. The editorial history of this article is available here: https://doi.org/10.1371/journal.ppat.1012635

Data Availability Statement: All relevant data are within the paper and its Supporting Information files.

Abstract

The parasitic protozoan *Trypanosoma brucei* has a single unit mitochondrial genome linked to the basal body of the flagellum via the tripartite attachment complex (TAC). The TAC is crucial for mitochondrial genome segregation during cytokinesis. At the core of the TAC, the outer membrane protein TAC60 binds to the inner membrane protein p166, forming a permanent contact site between the two membranes. Although contact sites between mitochondrial membranes are common and serve various functions, their molecular architecture remains largely unknown. This study elucidates the interaction interface of the TAC60-p166 contact site. Using *in silico*, *in vitro*, and mutational *in vivo* analyses, we identified minimal binding segments between TAC60 and p166. The p166 binding site in TAC60 consists of a short kinked α-helix that interacts with the C-terminal α-helix of p166. Despite the presence of conserved charged residues in either protein, electrostatic interactions are not necessary for contact site formation. Instead, the TAC60-p166 interaction is driven by the hydrophobic effect, as converting conserved hydrophobic residues in either protein to hydrophilic amino acids disrupts the contact site.

Author summary

Mitochondria are surrounded by two membranes and essential for nearly all eukaryotes. Contact sites between the two membranes are important for mitochondrial function. However, most contact sites are dynamic making their molecular architecture challenging to study. The tripartite attachment complex (TAC) of parasitic protozoan *Trypanosoma brucei* connects its compact mitochondrial genome with the basal body of the flagellum. This couples the segregation of the replicated mitochondrial genome to the old and new basal body. The TAC contains permanent contact sites formed by the outer membrane protein TAC60 and the intermembrane space-exposed C-terminus of p166 of the inner membrane. We have used it as a model for a prototypical contact site. AlphaFold predictions and *in vitro* binding assays identified a small region in the intermembrane space

Funding: This study was supported in part by project grant SNF 205200 to A.S. and by a grant of the NCCR RNA & Disease, a National Centre of Competence in Research (grant number 205601) to A.S both funded by the Swiss National Science Foundation (https://www.snf.ch/en). The funders had no role in study design, data collection and analysis, decision to publish, or preparation of the manuscript.

Competing interests: The authors have declared that no competing interests exist.

region of TAC60 that binds p166 forming contact sites. *In vivo* expression of various TAC60 and/or p166 mutants followed by immunoprecipitations demonstrates that contact site formation is driven by the hydrophobic effect and independent of the conserved charged amino acids present at the TAC60-p166 interface. The TAC is unique to Kinetoplastids, understanding the molecular architecture of the TAC60-p166 contact site could therefore inform the development of drugs that disrupt this critical interaction.

Introduction

All organisms need to segregate their replicated genomes to their daughter cells during cell division. Within eukaryotes the same applies for mitochondria and plastids, which evolved from bacteria and have retained an own genome essential for their function [1]. The genome of mitochondria is organized in a number of discrete DNA-protein complexes, termed nucleoids, which in Opisthokonts such as mammals and fungi are distributed all over the organelle and associated with the mitochondrial inner membrane (IM) [2–4]. However, the molecular nature and exact architecture of the nucleoid-IM interactions is still unclear. This is different for the single mitochondrion of the parasitic protozoan *Trypanosoma brucei* and its relatives, which contains a single unit and highly concatenated genome termed kinetoplast DNA (kDNA) [5–7]. It consists of two genetic elements, maxicircles (22 kb, 35 copies each) and minicircles (1 kb, ca. 5000 copies each), which form a single large disk-shaped nucleoid. The kDNA is constitutively linked to the tripartite attachment complex (TAC) - a physical structure which extends across the IM and the outer membrane (OM) to the basal body (BB) of the single flagellum (Figs 1A and S1). The function of the TAC is to link the segregation of two single unit structures, the kDNA and the BB [5,8,9]. Thus, segregation of the replicated kDNAs is coupled to the segregation of the old and the new flagellum prior to cytokinesis. The single unit nature of the kDNA requires that its replication is coordinated with the nuclear cell cycle and BB segregation [10].

The highly unusual trypanosomal TAC can serve as a paradigm for a mitochondrial nucleoid that is constitutively attached to the IM and that extends to a cytoskeletal structure in the cytosol, the BB [11,12]. Intriguingly, the TAC has some resemblance to the mitotic spindles that segregate nuclear chromosomes in both open and closed mitosis [8]. The TAC and the spindle are both filament-based structures and extend, although in opposite directions, from the same type of microtubule (MT)-organizing centers: the BB (in case of the TAC) and the centriole (in case of the spindle). The BB and the centriole are homologous structures sharing many of the same subunits [13]. However, while the spindle filaments consist of MTs, the filaments of the TAC are much smaller, consisting of a single protein (p197) in the cytosol [14–16] and the protein pair (p166/TAC102) in the mitochondrial matrix [17–19]. The nuclear membrane-embedded spindle pole body in organisms showing closed mitosis serves as a platform to link the intranuclear spindle MTs to the cytosolic astral MTs [20]. A conceptually similar platform is formed by the four integral OM TAC subunits which link the cytosolic to the intramitochondrial TAC filaments [8].

The TAC consists of eight known essential subunits and can be subdivided into three molecular modules [8]. The outermost "cytosolic module" links the BB to the "OM module". It is made up of p197, a very large protein of approximately 670 kDa which contains approximately 26 tandem repeats of 175 aa in length [14–16]. The innermost "inner module" links the kDNA disk in the matrix to the IM. It comprises the kDNA-proximal TAC102 which interacts with the region corresponding to aa 71–210 of the α-helical p166 [17,19,21]. p166 forms

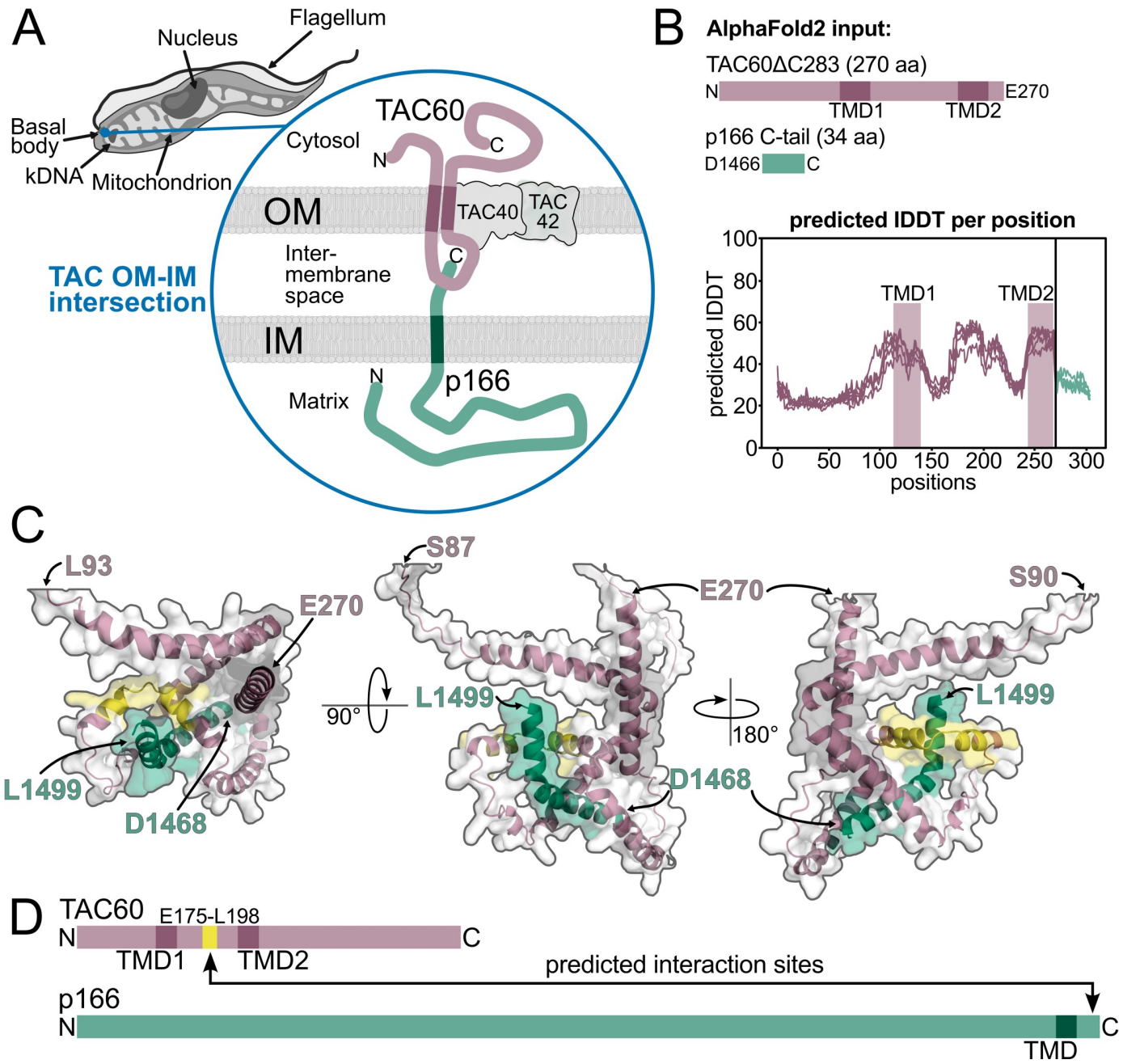

Fig 1. AlphaFold2 predicts TAC60-p166 interaction. (A) Model depicting the OM (outer membrane)-IM (inner membrane) contact site formed by TAC60 and p166 within the TAC (tripartite attachment complex). kDNA, kinetoplast DNA. **(B)** Depiction of the TAC60 (N-terminal 270 aa, purple) and p166 (C-terminal 34 aa, green) segments used as AlphaFold2 inputs. Structure prediction confidence (n = 5) is displayed as the predicted lDDT (local Distance Difference Test) per aa. TMD, transmembrane domain **(C)** Structural prediction of TAC60-p166 interactions from three angles. The following TAC60 regions are depicted in purple: L93-E270 (left), S87- E270 (middle), and S90-E270 (right). The TAC60 region E175-L198 predicted to fold into a kinked α-helix that binds to the C-terminus of p166 is highlighted in yellow. The C-terminal p166 segment D1466-L1499 is shown in green. **(D)** Schematic representation of the predicted interaction sites between TAC60 and p166 based on the AlphaFold2 model.

https://doi.org/10.1371/journal.ppat.1012635.g001

filaments in the matrix, is anchored in the IM via a single C-terminal transmembrane domain (TMD) and contains a 34 aa C-terminal region exposed to the intermembrane space (IMS) [17]. The central and most complex TAC subdomain is the OM module. It comprises the

peripheral OM protein TAC65 which interacts with both p197 of the cytosolic module and the integral OM protein pATOM36 [22,23] (S1 Fig). Intriguingly pATOM36, in addition of being an essential TAC subunit, is required for the biogenesis of a subset of α-helically anchored OM proteins [23,24]. The OM module contains three more integral membrane proteins: two beta barrel proteins, TAC40 and TAC42, as well as TAC60 [22,25]. The latter has two TMDs and its N- and C-termini face the cytosol [22]. The short IMS-exposed loop of TAC60 interacts with the C-terminus of p166 and thus connects the "OM module" with the "Inner module" [17].

The overarching principle of TAC biogenesis is a polar assembly of its subunits starting at the BB. Thus, depletion of a BB-proximal TAC subunit prevents assembly of all downstream TAC components [26]. How the 5 subunits of the "OM TAC module" are assembled is less clear. There is evidence that they form distinct assembly intermediates in the OM membrane independently of all other TAC subunits [8].

Here we have characterized the interaction between p166 and TAC60 on the molecular level. Using a combination of *in silico*, *in vitro*, and *in vivo* assays we identified which amino acids and structural features are critical for this interaction. The p166-TAC60 interaction is central for the understanding of TAC formation as it initiates the polar assembly of the TAC "inner module" that is guided by the "OM membrane module" [8]. Moreover, the p166-TAC60 interaction serves as a rare example of a permanent contact site between the IM and OM [27,28].

Results

AlphaFold2 predicts TAC60-p166 interaction

It has previously been shown that the N- and C-termini of the integral OM TAC subunit TAC60 are exposed to the cytosol, indicating that the sequence segment between the two TMDs (aa 142–237) must face the IMS [22]. Moreover, the only TAC subunit integral to the IM is p166. While most of p166 is exposed to the mitochondrial matrix, the protein has a single TMD near its C-terminus that is followed by a 34 aa C-terminal extension reaching into the IMS (Fig 1A and 1B). Immunoprecipitations have shown that this C-terminal extension is essential for the interaction with TAC60 and thus for cell growth [17]. To characterize the TAC60-p166 interaction in more detail the sequences corresponding to the C-terminal truncated variant of TAC60 (TAC60ΔC283), which was previously shown to be fully functional [22], and the C-terminal 34 aa of p166 (p166 C-tail) were used as inputs for an *in silico* analysis using the AlphaFold2 model (Fig 1B) [29, 30]. The confidence of the structure prediction (predicted local Distance Difference Test, IDDT) for TAC60 was rather mediocre between 20% and 60% (Fig 1B) and the two predicted TMDs did not align very well. However, a one-to-one interaction between the p166 C-tail and TAC60ΔC283 was predicted by the model (Fig 1C). The region interacting with the p166 C-tail corresponded to the TAC60 segment E175-L198. This was a plausible prediction as the interacting segment of TAC60 is located right in the center of the IMS loop (Fig 1D). Moreover, it also included the region where the structure of TAC60 was predicted with highest confidence. The AlphaFold2 model furthermore suggested that only the C-terminal half of the p166 C-tail might be involved in the TAC60 interaction.

Microarray of TAC60 peptides defines p166 C-tail binding site

To confirm the AlphaFold2 prediction experimentally, an *in vitro* protein interaction study was performed using a TAC60 peptide microarray. To that end the p166 C-tail was recombinantly expressed in *E. coli* and purified by immobilized metal affinity chromatography using an N-terminal 6x His tag (S2 Fig). The purified p166 C-tail was directly labelled with a fluorochrome and incubated with the peptide microarray immobilized on a glass surface. The

microarray consisted of 179 overlapping 20 aa long purified synthetic peptides covering the entire TAC60 protein (Fig 2A). The resulting pattern of fluorescent signals was detected by a sensitive microarray scanning system and visualized by heat map analysis (Fig 2B). The heat map showed that the p166 C-tail could bind to five sets of peptides each covering a distinct region of TAC60. Two of these regions corresponded to TAC60 domains that are exposed to the cytosol. Moreover, the C-terminal one locates to a region that is dispensable for TAC function [22]. Two further hotspots for p166 C-tail binding are within, or overlap with, the TMDs. Thus, these four p166 C-tail binding sites cannot be physiologically relevant as *in vivo* they are not accessible for binding to the IMS-exposed C-tail of p166 (Fig 2B). However, one set of peptides that bound to the p166 C-tail, encompassing the TAC60 sequence Q178-M194, mapped to the center of the IMS-exposed loop of TAC60. This is essentially the same region of TAC60 (E175-L198) that was predicted to bind to the p166 C-tail according to the AlphaFold2 analysis (Fig 1C) and is in line with the known topologies of TAC60 and p166 (Fig 1A).

TAC60-p166 interacting regions are conserved within Kinetoplastids

Homologues of TAC subunits, as the TAC itself, are exclusively found within the Kinetoplastids. S3 Fig shows a plot depicting the Shannon's entropy, a measure for the divergence of each position, of a multiple sequence alignment of TAC60 and p166 orthologues from a phylogenetically broad and balanced selection of 12 and 11 Kinetoplastid species, respectively. (*B. saltans* was excluded from the p166 alignment as its orthologue could not be confidentially identified in this species). Low Shannon's entropy values correspond to a high homology, whereas high values indicate high degree of divergence. Overall, the two proteins are only moderately conserved in the different species. However, the *T. brucei* TAC60 region (E175-L198) and the p166 C-tail region (D1466-L1499) which based on structure predictions and biochemical

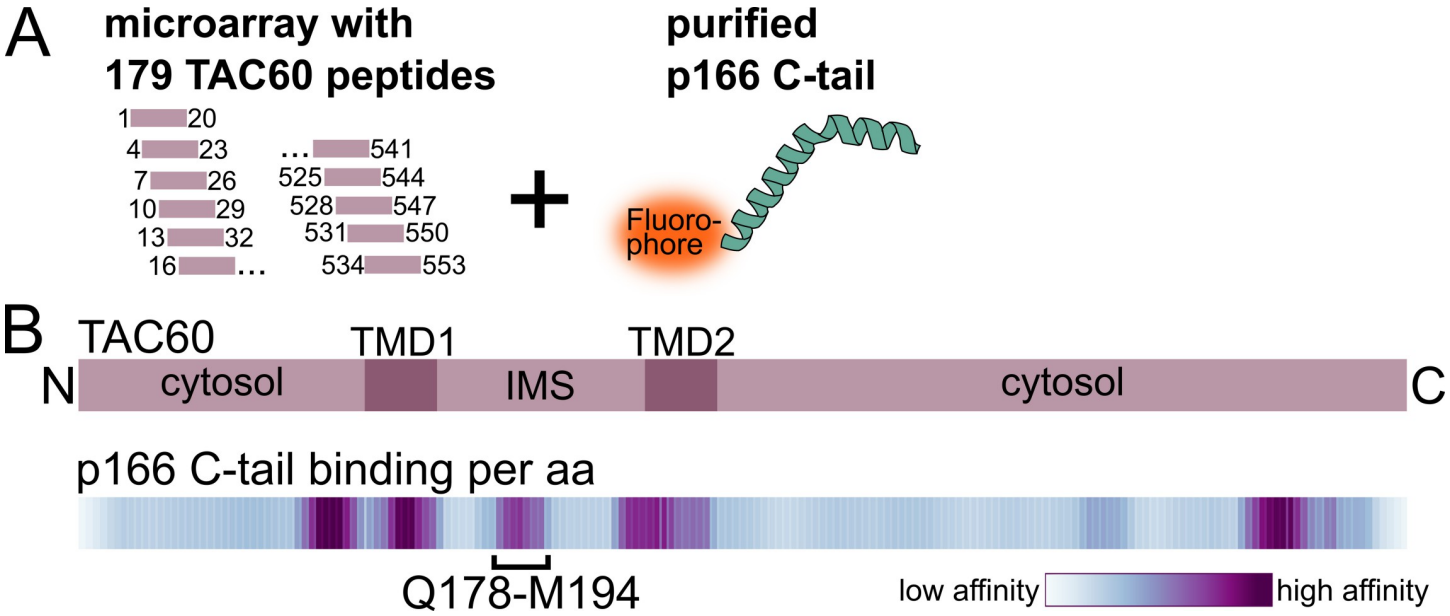

Fig 2. Microarray of TAC60 peptides defines p166 C-tail binding site. (A) Microarray setup for the *in vitro* peptide-protein interaction screen: 179 overlapping 20 aa long peptides of TAC60 were immobilized on a microarray. Interaction with the fluorophore-linked recombinant p166 C-tail was quantified. (For details and purification of the p166 C-tail see S2 Fig). **(B)** Top, domain structure of TAC60. TMD, transmembrane domain; IMS, intermembrane space. Bottom, corresponding heat map depicting the binding affinity of the p166 C-tail protein towards TAC60 peptides. The TAC60 segment Q178-M194 marks the minimal p166 binding site in the IMS domain of TAC60, which is in agreement with the domain identified in the AlphaFold2 structure model.

https://doi.org/10.1371/journal.ppat.1012635.g002

methods (Figs 1C and 2B) interact with each other are highly conserved (S3 Fig, yellow shading). The same is the case for the TMDs of both proteins (S3 Fig, grey shading).

In a next step we zoomed into the putative TAC60 and p166 interacting region of *T. brucei* and compared it with other Kinetoplastid species. The sequence logo in Fig 3A depicts the *T. brucei* TAC60 region (E175-L198) together with the corresponding region of TAC60 orthologues of the same species listed in S3A Fig. The analyzed TAC60 region contains four invariant residues: basic R181, the helix breaker P185, acidic E189, and hydrophobic L196. Moreover, positions 177, 180, 184, 188 and 192 are in all species occupied by hydrophobic amino acids. Thus, the *T. brucei* TAC60 segment interacting with the p166 C-tail is highly conserved across all analyzed Kinetoplastids. In addition, the AlphaFold2 model (Fig 1C) together with helical

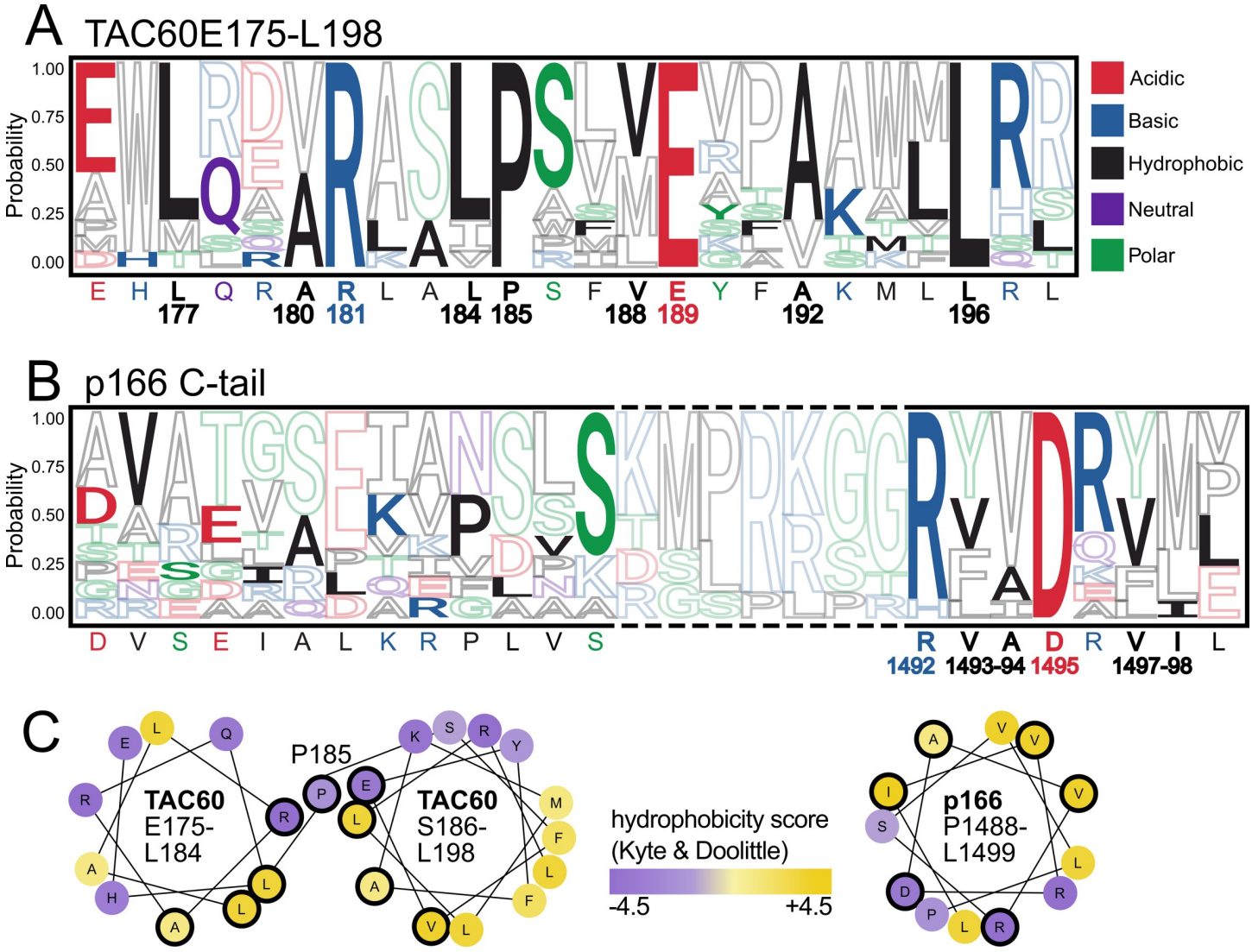

Fig 3. TAC60-p166 interacting regions are conserved within Kinetoplastids. (A) Sequence logo of a multiple sequence alignment (MSA) depicting the *T. brucei* TAC60 region (E175-L198) together with the corresponding region of TAC60 orthologues of 12 Kinetoplastid species (S3A Fig). The *T. brucei* sequence is depicted in filled letters and indicated at the bottom of the logo. Numbers refer to the *T. brucei* TAC60. **(B)** as in (A) but an MSA depicting the *T. brucei* p166 region D1479-L1499 is shown. Broken lines indicate a region containing insertion and or deletions in some Kinetoplastid species. **(C)** Helical wheel projections of the *T. brucei* TAC60 segments E175-L184 (left) and S186-L198 (middle) that are connected by P185. Helical wheel projection of the *T. brucei* p166 segment P1488-L1499 (right). Conserved aa and aa from conserved hydrophobic positions are encircled in black. Hydrophobicity is indicated from violet (hydrophilic) to yellow (hydrophobic).

https://doi.org/10.1371/journal.ppat.1012635.g003

wheel projection analyses (Fig 3C) suggest that a feature shared by all Kinetoplastid TAC60 proteins is that this region folds into two short amphipathic α-helices that are separated by the invariant P185.

The p166 C-tail sequence logo in Fig 3B depicts the *T. brucei* p166 C-tail region (D1479-L1499) aligned with the C-tail regions of p166 orthologues of the same species analyzed in S3B Fig. Overall the p166 C-tail region is less conserved than the TAC60 segment it interacts with. Note that the alignment contains some gaps due to small insertions and deletions relative to the *T. brucei* sequence (S4 Fig). The region mostly affected is indicated by broken lines in Fig 3B. However, the C-terminal 8 aa of *T. brucei* p166 (except for the last one which is absent in some species) are conserved (S4 Fig). This sequence contains a conserved basic amino acid (mostly R) at position 1492 and an invariant D1495. Moreover, positions 1493/1494/1497 and 1498 contain exclusively hydrophobic amino acids in all Kinetoplastids. Similar to what was observed for TAC60, AlphaFold2 and helical wheel analyzes suggest that the C-terminal 12 aa of *T. brucei* p166 fold into a short α-helix, the amphiphilic nature of which is conserved in all Kinetoplastids (Fig 3C).

In vivo system to monitor TAC60-p166 interactions

Which features of the TAC60 region (E175-L198) and the p166 C-tail region (D1466-L1499) are important for their mutual interaction? To find out we devised an *in vivo* system allowing pulldown experiments to test whether mutations in the binding domains of either of the two proteins interfere with the TAC60-p166 C-tail interaction.

The system is based on a tetracycline-inducible RNAi cell line that targets the TAC60 mRNA region (nucleotides 1220–1629) encoding the C-terminal part of the protein (Fig 4A and 4B). Note that the efficiency of the RNAi was monitored in cell lines that in addition to expressing the mutant TAC60 variants also expressed an *in situ* tagged endogenous allele of TAC60 carrying a C-terminal myc-tag (insets in left panels of Fig 4B and 4C). However, growth curves and immunoprecipitations were done in transgenic cell lines having two wild-type alleles of TAC60.

It has previously been shown that tetracycline-inducible, ectopic expression of TAC60 variants results in the essentially complete replacement of the endogenous TAC60 by the ectopically expressed variant [22] (Fig 4C, inset left panel). The TAC60 variant lacking the C-terminal 283 aa and carrying a C-terminal 3x myc-tag, termed TAC60ΔC283-myc, was used as a positive control in our assay. Due to the C-terminal truncation it was not affected by the RNAi. Immunofluorescence analysis of isolated flagella which are still connected to the TAC [25] shows that TAC60ΔC283-myc can be fully integrated into the TAC (Fig 4C, right panel). Moreover, expression of TAC60ΔC283-myc fully complemented the growth inhibition observed in the TAC60 RNAi cell line (Fig 4C, left panel) [22].

Pulldown experiments with TAC subunits are challenging because the fully assembled TAC is insoluble in non-ionic detergents [17]. The OM TAC subunits are an exception because a small fraction of these proteins is found in detergent-soluble subcomplexes representing assembly intermediates [8,22] (Fig 4D). This is different for the full length IM TAC subunit p166 which is essentially insoluble [17]. Thus, we transfected, a C-terminally HA-tagged mini-version of p166 (142 aa in length) which lacks the N-terminal 1357 amino acids but includes the TMD and the IMS-exposed C-tail (mini-p166-HA) into the TAC60 RNAi cell line. To ensure that mini p166-HA was imported into mitochondria it was N-terminally fused to the mitochondrial targeting sequence of trypanosomal mtHsp60 (Fig 4A) [17]. The mini-p166-HA was correctly integrated into the IM, interacted with the IMS domain of TAC60 and

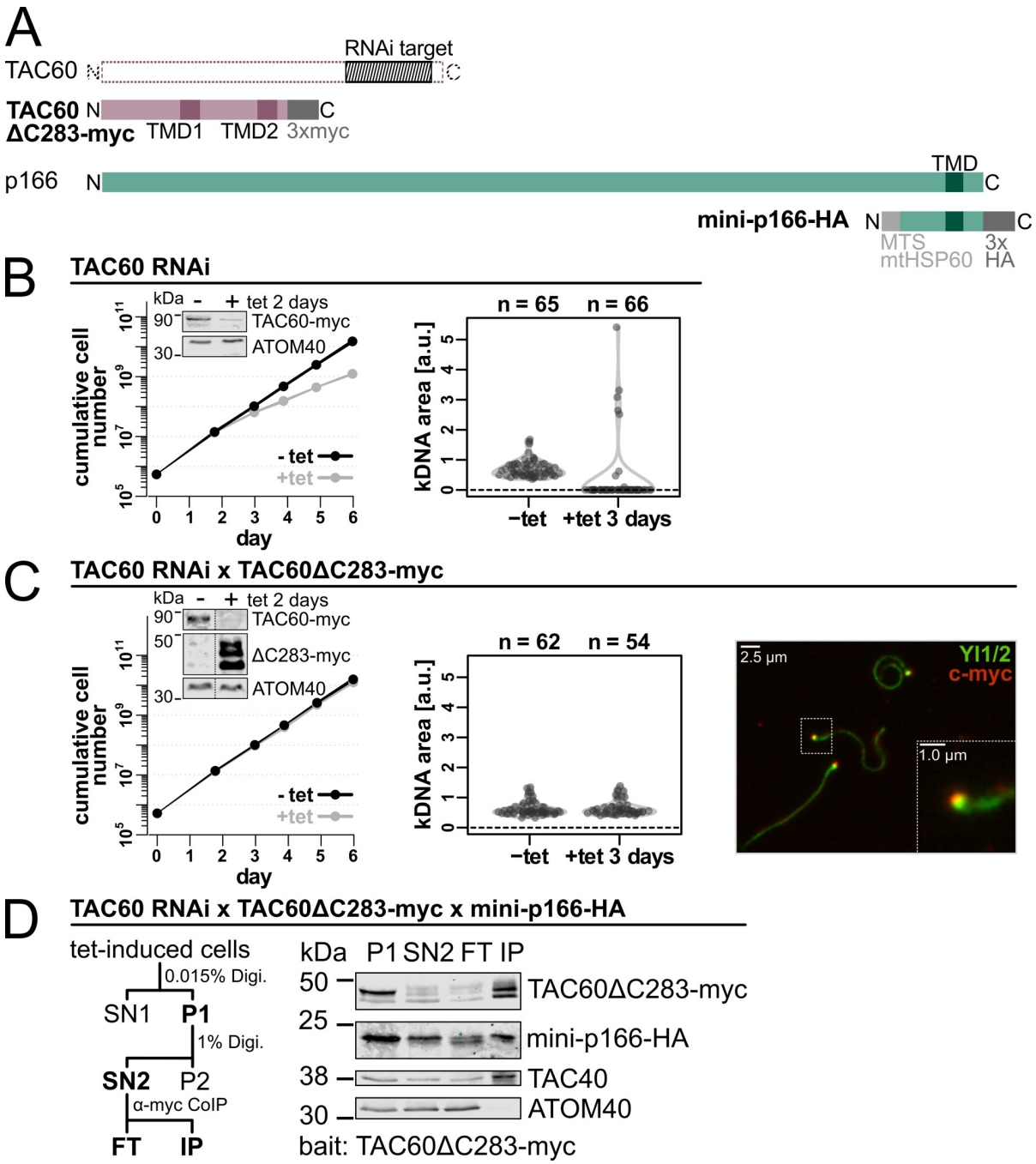

Fig 4. ***In vivo*** **system to monitor TAC60-p166 interactions. (A)** Schematic representations of TAC60ΔC283-myc and mini-p166-HA compared to the corresponding full length proteins. The region targeted by the TAC60 RNAi is shaded in grey and mapped to the full length protein. TMD, transmembrane domain; MTS, mitochondrial targeting sequence **(B)** Left, growth of uninduced (-tet) and induced (+tet) TAC60-RNAi cell line of procyclic *T. brucei*. The linewidth reflects the mean +/- the standard deviation of n = 3 experiments. Inset: Immunoblot of *in situ* 3x myc tagged full length TAC60 levels in uninduced (-) and tet-induced (+) cells. Note that one of the endogenous alleles of TAC60 was in situ tagged with a C-terminal 3x myc-tag to monitor the efficiency of the RNAi. ATOM40 serves as a loading control. Right, combined violin and sina diagrams of DAPI-stained kDNA area measurements, indicated as arbitrary units (a. u.), in the uninduced and induced TAC60 RNAi-cell line. Numbers of analyzed cells are indicated at the top. A kDNA area value of zero means the complete loss of the kDNA. **(C)** As in (A) but a TAC60-RNAi cell line complemented by TAC60ΔC283-myc is shown. Inset as in (A) but expression of TAC60ΔC283-myc is also monitored. Right, Immunofluorescence of extracted flagella of the same cell line probed for TAC60ΔC283-myc (red) shows the TAC60 variant gets integrated into the TAC. Tyrosinated tubulin and TbRP2, detected by YL1/2 (green) serves a marker for the flagellum and basal body. **(D)** Left, workflow of the digitonin (Digi.)- based cell fractionation assay used for pulldown experiments. Right, immunoblot of the pulldown experiment. A cell line shown in (C) induced for two days that also expresses mini-p166-HA was analyzed. P, pellet; SN, supernatant; FT, flow through; IP, eluate of immunoprecipitation. TAC40 and ATOM40 serve as positive and negative controls, respectively.

https://doi.org/10.1371/journal.ppat.1012635.g004

was fully detergent-soluble [17]. However, due the large N-terminal truncation which prevents its interaction with TAC102 and thus the kDNA, it was not functional [17].

Fig 4D shows a pulldown assay in which TAC60ΔC283-myc was used as a bait. TAC60ΔC283-myc is fully functional and serves as a positive control for all tested TAC60 variants. A crude mitochondrial fraction, the pellet (P1) of 0.015% digitonin extracted cells, was further extracted with 1% digitonin, resulting in a supernatant termed SN2. Whereas the fully assembled TAC remained insoluble and was recovered in the P1 pellet, a small fraction of the TAC60ΔC283-myc variants and TAC40, which likely represent assembly intermediates, were solubilized by this treatment. Throughout our study we consistently observe multiple bands for the various TAC60 variants. This is likely mainly due to as yet unknown posttranslational modifications, see [22] for a more detailed discussion. Mini-p166-HA, in contrast to the TAC60ΔC283-myc variants, was essentially completely recovered into the SN2 fraction. Subsequently SN2 was incubated with anti-myc-beads and processed for pulldown (Fig 4D). The result showed that TAC60ΔC283-myc together with the mini-version of p166-HA was recovered in the bound fraction (IP) indicating they interact with each other. TAC40 was also found in the IP fraction because it binds to TAC60 independent of its interaction with p166 and thus serves as a positive control. ATOM40, the integral OM pore subunit of the protein translocase, does not interact with the TAC and serves as a negative control (Fig 4D).

Finally, it has been previously observed that expression of mini p166 in the presence of the endogenous full length p166 caused a slight growth phenotype and a decrease of cells containing normal kDNA [17]. This weak dominant negative effect could be explained because mini-p166-HA likely competes for localization with the wild-type p166 [17]. Thus, to monitor the putative effect of TAC60ΔC283-myc mutants on the kDNA segregation process, they were also expressed in the TAC60-RNAi cell line that did not express the mini-p166-HA. Impairment of TAC function and thus kDNA segregation resulted mainly in kDNA loss. Moreover, over-replication of kDNAs in the few cells that have retained the kDNA was also observed [9] (Fig 4B, right panel and 4C, middle panel).

A kinked helix in TAC60 is necessary but not sufficient for p166 binding

In the first TAC60 mutant tested, termed TAC60-nohelix, we replaced the segment Q178-M194 encompassing the minimal p166-binding site predicted by the TAC60 peptide binding array (Fig 2B). It was exchanged with the peptide (SALQMELIEPTPHILIP) of the same length, which contains three prolines and is predicted to be unable to form an α-helix. The result shows that while the TAC60-nohelix mutant still interacts with the OM TAC subunit TAC40, it cannot pull down mini-p166 (Fig 5A). This was expected considering the entire minimal p166-binding site was replaced and suggests that an α-helical structure of the binding site in TAC60 might be required for the interaction.

Indeed, two short α-helices separated by the invariant P185 is a feature of the *T. brucei* TAC60 p166-binding site that is highly conserved in all Kinetoplastids (Fig 3A). We therefore produced a TAC60 mutant, termed TAC60-P185E, in which the invariant P185 was replaced by an E. This resulting sequence is predicted to form a single α-helix covering the entire TAC60 p166-binding region. Intriguingly, the TAC60-P185E mutant lost the capability to interact with mini-p166 (Fig 5B) suggesting that an α-helix with a kink in the center is required for TAC60-p166 interaction.

In the last mutant of this series, termed TAC60-p197helix, P185 was left unchanged. However, the two short α-helices flanking P185 were replaced by peptides of the same length that were modelled after the α-helical repeat region of the previously characterized TAC subunit p197 [15]. The resulting p166 binding region in the TAC60-p197helix was predicted to fold

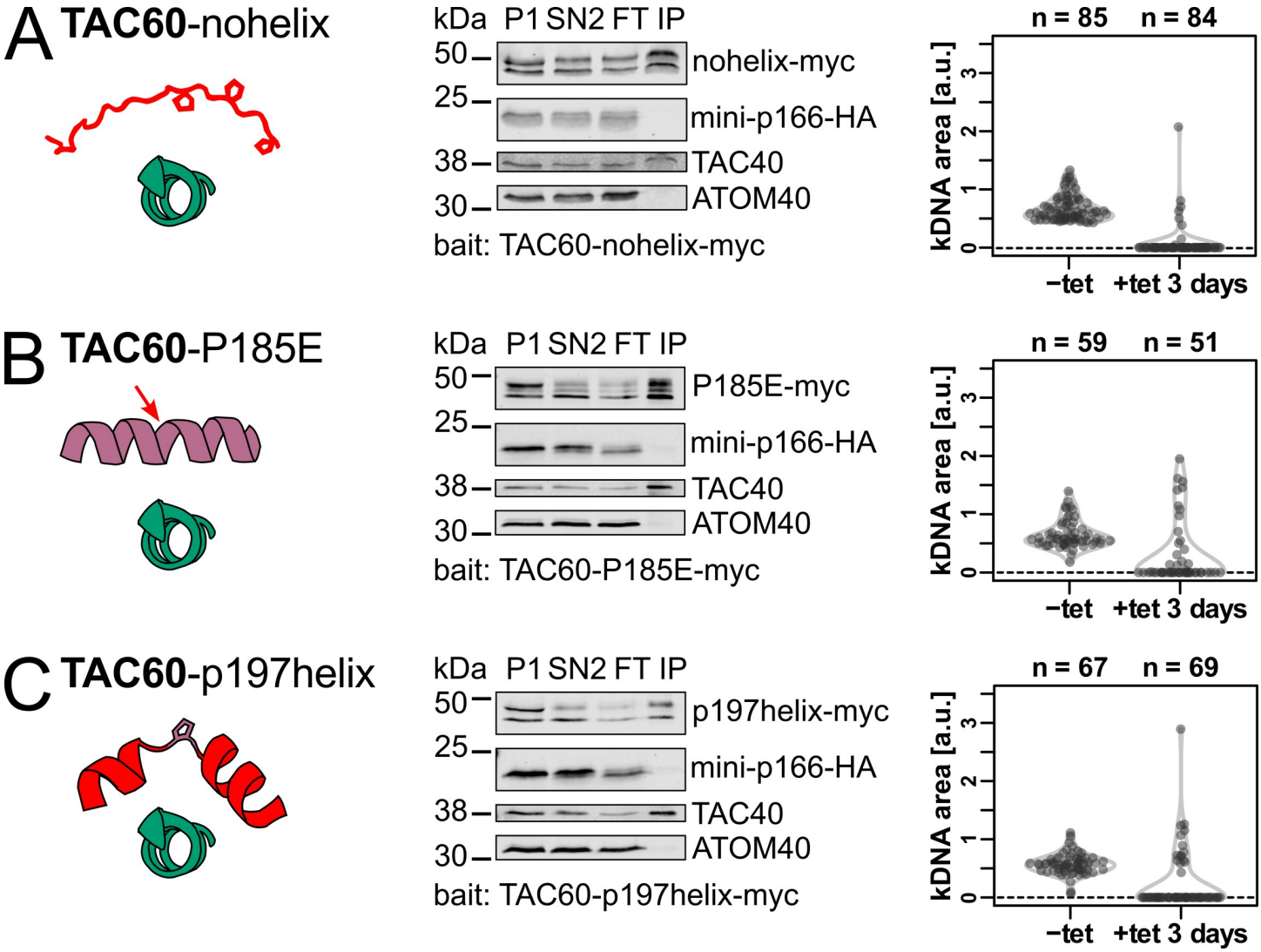

Fig 5. A kinked helix in TAC60 is necessary but not sufficient for p166 binding. (A) Left, schematic structural depiction of the TAC60-p166 interaction for the TAC60-nohelix mutant. Replaced residues of TAC60 are shown in red, the unmodified p166 C-tail is shown in green. Middle, immunoblot analysis of a pulldown experiment of the two days tet-induced TAC60-RNAi cell line complemented by the TAC60-nohelix mutant that also expresses mini-p166-HA. P, pellet; SN, supernatant; FT, flow through; IP, eluate of immunoprecipitation. TAC40 and ATOM40 serve as positive and negative controls, respectively. Right, combined violin and sina diagrams of DAPI-stained kDNA area measurements, indicated as arbitrary units (a. u.), of a tet-induced cell line for TAC60-RNAi and TAC60-nohelix expression. Numbers of analyzed cells are indicated at the top. A kDNA area value of zero means the complete loss of the kDNA. **(B)** and **(C)** as in (A) but the TAC60-P185E and TAC60-p197helix mutants were analyzed. The mutated residues are depicted by the red arrow (B) or by the red helix segments (C).

https://doi.org/10.1371/journal.ppat.1012635.g005

into a kinked α-helix, just as the corresponding wildtype sequence, but has different biochemical properties. The results in Fig 5C show that the TAC60-p197helix mutant was not able to interact with mini-p166, suggesting that a kinked α-helix, while necessary, is not sufficient to mediate binding of TAC60 to p166.

Finally, the panels on the right in Fig 5 show that, as would be expected, exclusive expression of all three TAC60 mutants interfered with kDNA segregation.

Conserved charged amino acids are dispensable for TAC60-p166 interaction

The best-conserved amino acids in the p166-interacting TAC60 α-helix are R181 and E189 which flank the helix-breaking P185. R181 and E189 face the same side of the kinked α-helix and thus may face p166. For the TAC60-interacting α-helix of p166 the best conserved amino acids are the closely spaced R1492 and D1495 located on the same side of the p166 α-helix. Considering the highly conserved nature of the two pairs of charged amino acids in TAC60 and p166, suggests that the TAC60-p166 interactions might be mediated by ionic bonds between opposite charges of R181 (in TAC60) and D1495 (in p166) as well as E198 (in TAC60) and R1492 (in p166), respectively (Fig 6A).

The importance of ionic bonds for TAC60-p166 interactions was experimentally tested by three TAC60 variants in which either R181 and/or E189 were mutated. In the first mutant, termed TAC60-R181A/E189A, both R181 and E189 were each replaced by an uncharged A (Fig 6B, left). In the second mutant, termed TAC60 R181E/E189R, the opposite charges were switched (Fig 6C, left), and in the third mutant, termed TAC60-E189R, E189 was switched to R resulting in a p166-TAC60 interacting kinked α-helix that contains two positive charges (Fig 6D, left). The results of the TAC60 pulldown experiments showed that all three TAC60 mutants still interacted with mini-p166 (Fig 6B, 6C and 6D, middle panels). In line with these results we did not observe impairment of kDNA segregation in cell lines that exclusively express the three mutant TAC60 proteins (Fig 6B, 6C and 6D, right panels).

These experiments were complemented with two p166 mutants, termed p166-R1492A and p166-D1495A, in which either R1492 or D1495 were replaced by a neutral A (Fig 6E and 6F, left). Moreover, a third mutant, termed p166-R1492D/D1495R, was also tested in which R1492 and D1495 were switched (Fig 6G, left). The results showed that in all TAC60 pulldown experiments the mutant p166 versions were recovered in the bound fraction (Fig 6E, 6F and 6G, middle panels).

Our results show that based on the *in vivo* binding assay all positively or negatively charged amino acids, R181/E189 in TAC60 or D1495/R1492 in p166, even though they are highly conserved, are dispensable for the mutual interaction of the two proteins. This excludes that the interaction between TAC60 and p166 is due to ionic bonds.

TAC60-p166 interaction depends on conserved hydrophobic amino acids

Charged amino acids are not required for the TAC60-p166 interaction and the interaction between the two proteins is maintained in the TAC60 R181E/E189R mutant. This strongly suggests that the side of the *T*. *brucei* p166 α-helix containing hydrophobic amino acids faces the kinked TAC60 α-helix, rather than the side with the highly conserved D1492 and E1495 (Fig 7A, top). Thus, we tested whether the interaction between TAC60 and p166 requires the presence of hydrophobic amino acids.

Positions 177, 180, 184, 188, 192 and L196 in TAC60 of *T*. *brucei* are all occupied by hydrophobic amino acids which are oriented to the same side of the kinked TAC60 α-helix, a feature that is highly conserved in all Kinetoplastids (Figs 1C and 3A). Thus, we expressed two TAC60 mutants, in which either all six positions (termed TAC60-fullϕ) (Fig 7B) or all except positions L177 and L196 (termed TAC60-4ϕ) (Fig 7C, left) were replaced by the structurally most similar hydrophilic amino acid (Fig 7A, bottom). The results of the pulldown experiments showed that both the TAC60-fullϕ and the TAC60-4ϕ mutants cannot pull down mini-p166 indicating that at least some of the four amino acids mutated in TAC60-4ϕ are essential for the TAC60-p166 interaction (Fig 7B and 7C, middle panels). In line with these results kDNA

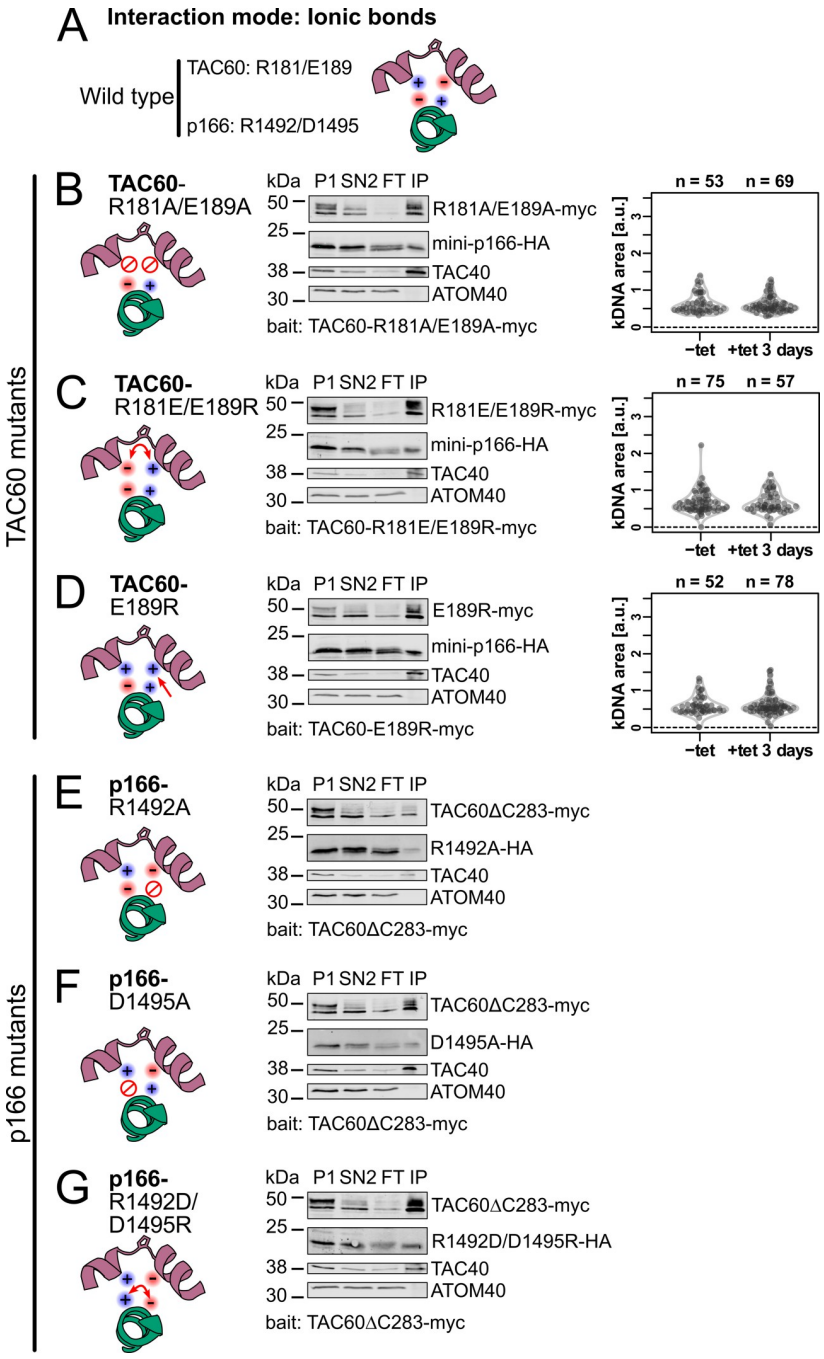

Fig 6. Conserved charged amino acids are dispensable for TAC60-p166 interaction. **(A)** Schematic structural prediction of the model where TAC60 (purple) interacts with p166 (green) via ionic bonds. **(B), (C)** and **(D)** Left, schematic structural depiction of the TAC60-p166 interaction for the indicated TAC60 mutants. Middle, immunoblot analyses of pulldown experiments of the two days tet-induced TAC60-RNAi cell lines complemented by the indicated TAC60 mutants that also express mini-p166-HA. P, pellet; SN, supernatant; FT, flow through; IP, eluate of immunoprecipitation. TAC40 and ATOM40 serve as positive and negative controls, respectively. Right, combined violin and sina diagrams of DAPI-stained kDNA area measurements, indicated as arbitrary units (a. u.), of the same cell lines but without mini-p166-HA expression. Numbers of analyzed cells are indicated at the top. A kDNA area value of zero means the complete loss of the kDNA. **(E)**, **(F)** and **(G)** as above but TAC60-RNAi cell lines complemented by TAC60ΔC283-myc and the indicated mini-p166-HA mutants were analyzed.

https://doi.org/10.1371/journal.ppat.1012635.g006

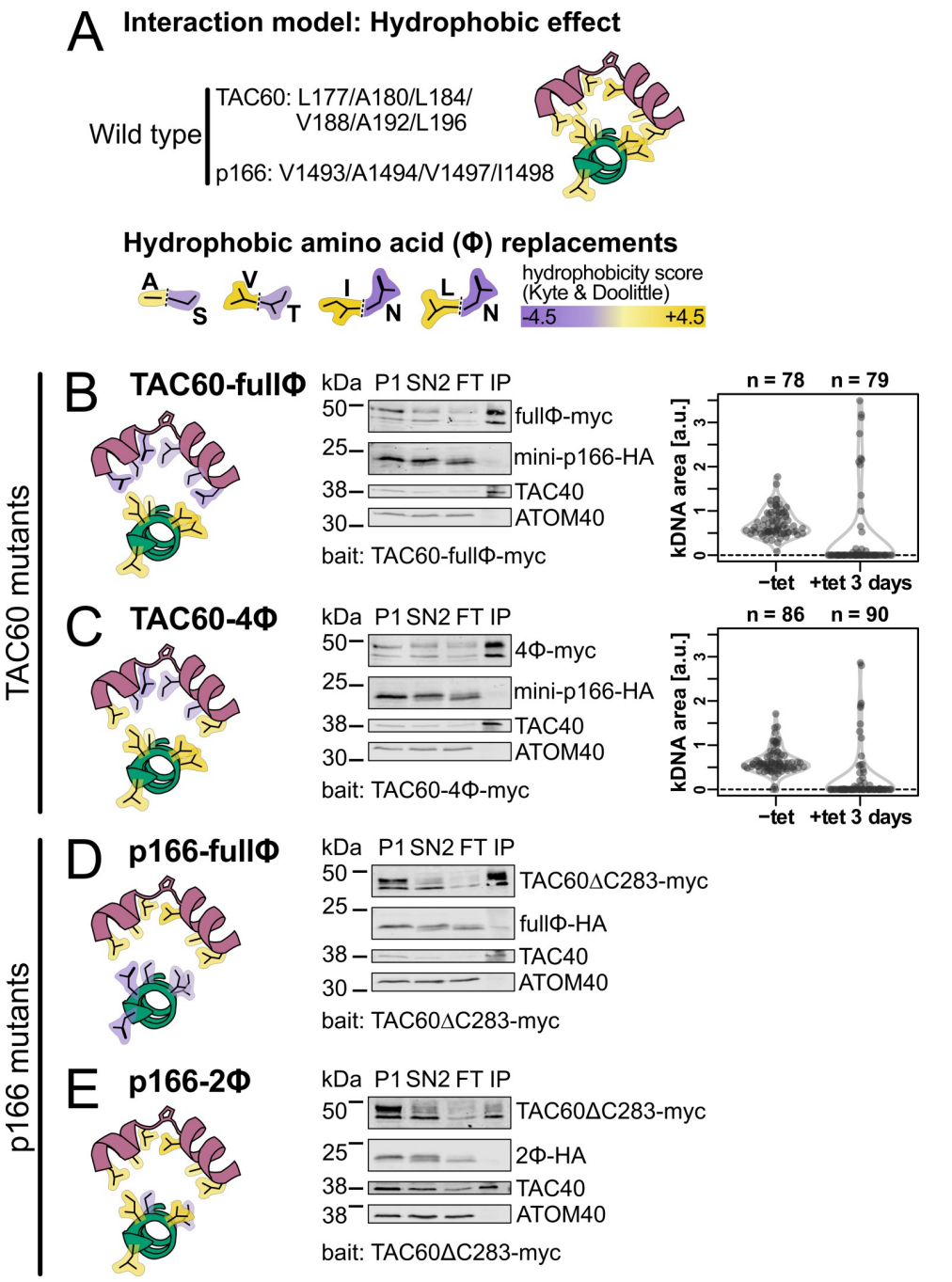

Fig 7. TAC60-p166 interaction depends on conserved hydrophobic amino acids. (A) Top, schematic structural prediction of the model where the TAC60 (purple)-p166 (green) interaction is driven by the hydrophobic effect. Hydrophobic residues are depicted in yellow. Bottom, hydrophobic aa were replaced by the structurally most related hydrophilic aa, as indicated. **(B)** and **(C)** Left, schematic structural depiction of the TAC60-p166 interaction for the indicated TAC60 mutants. Middle, immunoblot analyses of pulldown experiments of the two days tet-induced TAC60-RNAi cell lines complemented by the indicated TAC60 mutants that also express mini-p166-HA. P, pellet; SN, supernatant; FT, flow through; IP, eluate of immunoprecipitation. TAC40 and ATOM40 serve as positive and negative controls, respectively. Right, combined violin and sina diagrams of DAPI-stained kDNA area measurements, indicated as arbitrary units (a. u.), of the same cell lines but without mini-p166-HA expression. Numbers of analyzed cells are indicated at the top. A kDNA area value of zero means the complete loss of the kDNA. **(D)** and **(E)** as above but TAC60-RNAi cell lines complemented by TAC60ΔC283-myc and the indicated mini-p166-HA mutants were analyzed.

https://doi.org/10.1371/journal.ppat.1012635.g007

segregation was impaired in cell lines that exclusively expressed the mutant TAC60 proteins (Fig 7B and 7C, right panels).

The *T. brucei* TAC60 binding region of p166 contains seven hydrophobic amino acids (L1489, V1490, V1493, A1494, V1497, I1498, L1499) all of which are predicted to face the kinked α-helix of TAC60. To test the importance of these amino acids for the TAC60-p166 interaction we produced two mutant mini-p166 variants. In the first one, termed p166-fullϕ (Fig 7D, left), all hydrophobic amino acids were replaced by their most similar hydrophilic counterparts, whereas in the second one, termed p166-2ϕ (Fig 7D, left), only the central V1493 and A1494 were replaced. The presence of hydrophobic amino acids at these two positions is conserved in all Kinetoplastids (Fig 3B). Note that position 1493 and 1497 may be occupied by a Y in some species which is ambiguously classified as either hydrophobic or polar, respectively. The results showed that in TAC60 pulldown experiments both p166-fullΦ and p166-2Φ were not recovered in the bound fraction (Fig 7D and 7E, right panels).

An independent confirmation that the TAC60-p166 interaction is mainly due to hydrophobic rather than ionic interaction is the fact that in a TAC60 pulldown experiment mini-p166 is still recovered in the eluate even in the presence of 0.75 M NaCl which is expected to interfere with electrostatic interactions (Fig 8).

In summary, these results show that the interaction between TAC60 and p166 depends on a kinked α-helix in TAC60, which has a hydrophobic surface on the inside of the bent region, that interacts with the hydrophobic side of the C-terminal α-helix of p166.

Discussion

A detailed knowledge of protein-protein interactions is crucial for the understanding of cellular architecture and for gaining mechanistic insights into biological processes. In this study we have characterized the interaction between the two mitochondrial integral membrane proteins TAC60 (OM) and p166 (IM) of *T. brucei* at the molecular level. The two proteins are subunits of the TAC, which mediates the segregation of the duplicated single-unit mitochondrial nucleoids during the coordinated cell and mitochondrial division in trypanosomes and related organisms [10].

Using a combination of *in silico*, *in vitro*, and *in vivo* analyzes our results suggest a model of how the two proteins interact. For TAC60, the p166-binding site corresponds to the short E175-L198 segment. It contains three conserved charged amino acids and six highly conserved hydrophobic amino acids, forming two short amphiphilic α-helices that are separated by the

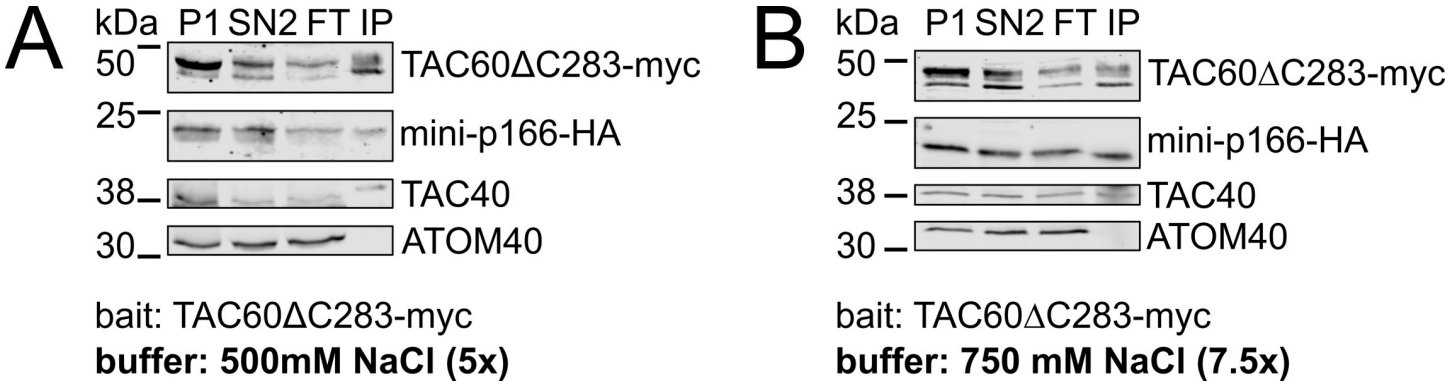

Fig 8. TAC60-p166 interaction is salt resistant. Immunoblot analyses of pulldown experiments of the two days tet-induced TAC60-RNAi cell line complemented by TAC60ΔC283-myc performed in the presence of 500 **(A)** and 750 **(B)** mM NaCl. P, pellet; SN, supernatant; FT, flow through; IP, eluate of immunoprecipitation. TAC40 and ATOM40 serve as positive and negative controls, respectively.

https://doi.org/10.1371/journal.ppat.1012635.g008

P185. The hydrophobic face of each α-helix lines the inside of the bent region, creating a hydrophobic pocket. For p166, the TAC60 binding site corresponds to the C-terminal 11 amino acids of p166. It contains two conserved charged amino acids and four highly conserved hydrophobic amino acids and forms an amphiphilic α-helix. The hydrophobic side of the p166 α-helix faces the hydrophobic pocket formed by the TAC60 E175-L198 segment.

Three key mutants prevented the interaction between TAC60 and p166, supporting the suggested model: i) The TAC60-P185E mutant, which cannot form a kink between the two short α-helices (Fig 5B); ii) The TAC60-4ϕ mutant, in which four conserved hydrophobic amino acids on the inside of the hydrophobic pocket were replaced by hydrophilic ones (Fig 7C), and iii) The p166-2ϕ mutant in which two conserved hydrophobic amino acids on the TAC60-facing side of the p166 α-helix were replaced by hydrophilic ones (Fig 7E). Further corroborating this model, replacing or switching the highly conserved charged amino acids in either TAC60 or p166 in various combinations did not affect TAC60-p166 interactions (Fig 6). This indicates that the conserved charged amino acids are oriented diametrically opposed to the hydrophobic sides of the TAC60 and the p166 α-helices that form the binding interface. We conclude that the TAC60-p166 interaction depends on hydrophobic amino acids at conserved positions in both the TAC60 and the p166 α-helices. Thus, the interaction is ultimately driven by the tendency to minimize the exposure of hydrophobic side chains to water, which is known as the hydrophobic effect. Structural predictions of the TAC60-p166 interaction interface of distantly related Kinetoplastids shows that the model proposed for *T. brucei* likely applies for the whole group (S5 Fig).

If the charged amino acids do not contribute to the TAC60-p166 interaction why are they so highly conserved (Fig 3)? Presently we cannot answer this question. It is possible that they modulate the efficiency of mitochondrial protein import, and that in the cell lines in which the charged amino acids were mutated an import phenotype would be masked because the ectopically expressed mutant TAC60 subunits were overexpressed. Alternatively, as all our experiments were done in procyclic cells, it could be that the charged amino acids and/or the amphiphilic nature of the α-helices have a function in other life cycle stages.

The specific role of TAC60 and p166 within the TAC is to form contact sites between the mitochondrial OM and IM. While the TAC is specific for Kinetoplastids, OM-IM contact sites are an essential feature of mitochondria in all eukaryotes. The most prominent examples are the ones associated with protein translocases [28] and with the mitochondrial contact site and cristae organizing system (MICOS) [31,32].

The translocase of the OM (TOM) complex transiently interacts with the translocase of the inner membrane 23 (TIM23) complex. This interaction is based on a complicated interaction network between the IMS domains of Tom22/Tom40/Tom7 and Tim50/Tim23/Tim21, respectively, and is greatly stabilized by precursor proteins that are being translocated [33,34]. Transient OM-IM contact sites are also formed by the OM protein voltage dependent anion channel (VDAC) which binds to both hydrophobic precursor proteins that are bound to small TIM chaperones in the IMS and to the carrier translocase, the TIM22 complex [35]. In both examples the function of the OM-IM contact sites is to facilitate the transfer of precursor proteins from the TOM complex to the respective protein translocase in the IM.

The hetero-oligomeric MICOS complex forms the cristae junction, a narrow passage in the IM that links the inner boundary membrane, which runs parallel to the OM, with invaginations in the IM termed cristae [31,32]. The MICOS subunit Mic60 is anchored in the IM. It has a large domain exposed into the IMS which is associated with Mic19. The Mic60/Mic19 module forms contact sites with the OM, by interacting with variety of OM proteins including the sorting and assembly machinery (SAM) and the TOM complex, VDAC, and the GTPase Miro [36,37].

Even though OM-IM contact sites are widespread and functionally important, not much is known about the underlying molecular interactions required for their formation and maintenance. The TAC is specific for Kinetoplastids, but it can serve as an example for a prototypical OM-IM contact site. The TAC is a single unit, permanent structure which is precisely localized opposite the single flagellum to which it connects the kDNA. This is different to the OM-IM contact sites described above which are often transient and/or highly dynamic and therefore more challenging to study [38]. The architectural unit of the TAC can be thought of as a cable connecting the BB to the kDNA (S1 Fig) [8]. The cytosolic part of each cable is formed by a single filamentous p197 molecule, which is plugged into the TAC OM module via TAC65 and extends further through other OM module subunits to TAC60. The IMS side of TAC60 then interacts with a single p166 molecule, which extends across the IM, forming a matrix filament that connects to the kDNA. The exact stoichiometry of the TAC subunits within the structure remains unknown. However, the TAC subunits can easily be detected by immunofluorescence. This indicates that the TAC must have a highly repetitive structure consisting of several hundreds of the described TAC cables arranged in a parallel manner. This simplifies *in vivo* studies of the TAC OM-IM contact site because interfering with the TAC60-p166 interaction prevents the formation of each individual TAC cable and thus of the whole structure.

OM-IM contact sites can have multiple functions. The contact sites found in MICOS, besides maintaining the mitochondrial architecture, have been implicated in phospholipid transport and metabolism, protein import, and signaling pathways [36, 37]. However, while the TAC is essential in both procyclic and in bloodstream forms of trypanosomes, its function is restricted to kDNA segregation [26]. The evidence for this comes from the observation that the TAC is dispensable for normal growth of the L262P bloodstream form cell line, which due to a mutation in the γ-subunit of the ATP synthase, can grow in the absence of the kDNA [39]. This is perhaps surprising because for an exclusive tethering function, the OM TAC module consisting of four essential integral OM membrane proteins, appears to be unnecessarily complex.

In contrast to most other mitochondrial OM-IM contact sites, the trypanosomal TAC is a permanent structure. What could be the explanation for this? The kDNA disk, the flagellum and the BB are single unit structures in non-dividing cells and the BB is the master organizer of cellular architecture [10]. Proper BB duplication, maturation, segregation, and its positioning within the cell, ensures correct segregation of flagella, the replicated kDNAs and other structures during cytokinesis [40]. Thus, proper kDNA segregation in the cell is achieved, i) by coordinating kDNA replication with BB duplication and maturation, and ii) by the evolution of a physical tether that permanently hardwires the kDNA to the BB. In short, because the overarching principle of kDNA segregation is "physically coupled co-segregation with basal bodies" [12], this necessitates a permanent OM-IM contact site formed by TAC60 and p166.

The TAC60-p166 contact site must not only be temporally stable but also physically robust because the TAC makes the connection between two huge structures: the kDNA and the BB with the flagellum. Moreover, during mitochondrial fission and cytokinesis the old and the newly formed kDNA-TAC-BB supercomplexes are segregated within the highly viscous matrix and cytosol, respectively. Hence, the TAC60-p166 interaction must be strong enough, and the number of single unit TAC cables high enough, to bear this load.

Our study defined the binding interface of the OM-IM contact site formed by TAC60-p166 interaction in the trypanosomal TAC. Furthermore, we have shown that the formation and maintenance of the contact site does not rely on electrostatic interactions but is driven by the hydrophobic effect. Even though it is presently beyond the scope of our study, this knowledge may in the future allow to engineer synthetic OM-IM contact sites in organisms other than trypanosomes and thus open new ways to manipulate mitochondrial architecture.

Finally, knowing the critical features of the TAC60-p166 contact sites may help to find compounds that interfere with their formation. Because TAC60 and p166 are conserved in Kinetoplastids (Figs 3 and S4) but absent in mammals, such substances may form the basis of new drugs to combat the diseases that are caused by *T. brucei* and its relatives.

Material and methods

Protein structure predictions

Protein and protein complex structures were predicted using the AlphaFold2 model [29], implemented in ColabFold [30,41], and visualized with PyMol (version 2.5, Schrödinger, LLC). Input sequences for the predicted structures in Fig 1C were TAC60 (Tb427.07.1400, aa 1–270) and p166 (Tb427tmp.02.0800, aa 1466–1499). Predictions were made using the pdb100 template data base. Default settings were used where applicable and all structures were relaxed using amber.

Protein purification

The coding sequence of a 6x His tag-3x myc tag was cloned upstream of the sequence coding for the C-terminal 34 aa of p166 by PCR and the coding sequence of the resulting fusion protein was inserted into an *E. coli* expression vector derived from the "parallel" expression vector family [42]. *E. coli* BL21 [43] was transformed with the resulting construct and expression of the fusion protein was induced for 3 hours by 1 mM isopropyl-β-D-thiogalactopyranosid (IPTG). Cells were harvested by centrifugation at 5'000 g and washed with phosphate-buffered saline (PBS) (137 mM NaCl, 2.7 mM KCl, 10 mM Na_2HPO_4, and 1.8 mM KH_2PO_4, pH 7.4) before cell lysis. Cell lysis was done using a high pressure homogenizer (HPL6, Maximator GmbH) in cell lysis buffer (20 mM 3-(N-morpholino) propanesulfonic acid (MOPS) at pH 7.5 containing 150 mM NaCl, 10% glycerol, 10 mM imidazole) supplemented with 1 mM phenylmethanesulfonyl fluoride (PMSF). Cell debris was removed by centrifugation (20 minutes, 13'000 g at 4˚C). The resulting supernatant was incubated with Ni-NTA agarose beads (Cube Biotech) for 3 hours at 4˚C. Beads were washed in cell lysis buffer supplemented with 40 mM imidazole, and cell lysis buffer supplemented with 200 mM imidazole was used for elution of the fusion protein. The final eluate was concentrated using a 3 kDa size filter (Millipore) to approximately 1 μg/μl as determined by the BCA test (Thermo Scientific) [44].

In vitro peptide-protein interaction screening

The *in vitro* peptide-protein interaction assay was conducted by JPT Peptide Technologies GmbH (Germany). TAC60 peptides 20 aa in length with a 3 aa shift relative to the preceding peptides covering the whole TAC60 sequence were synthesized and immobilized on microarray slides yielding a total of 179 different peptides. The purified p166 fusion protein was labelled using the DyLight microscale antibody labeling kit (Thermo Scientific). The immobilized TAC60 peptides were incubated with 10, 1, 0.1, 0.01 and 0.001 μg/ml of the labelled fusion protein for 1 hour at 30˚C. Bound proteins were detected by fluorescence emitted after excitation with a high-resolution laser scanner at 635 nm. The resulting signals for all peptides were extrapolated to scores for each aa of the TAC60 sequence by summing up the scores of all overlapping peptide regions (Fig 3B).

Multiple sequence alignments and helical wheel projections

Sequences of TAC60 and p166 orthologs of Kinetoplastids were obtained from the TriTrypDB database [45]. The following orthologs were used for the analyses: *T. brucei* (TAC60:

Tb427.07.1400, p166: Tb427tmp.02.0800), *T. cruzi* (TAC60: TcCLB.508209.30, p166: TcCLB.509589.40), *Angomonas deanei* (TAC60: ADEAN_000333400, p166: ADEAN_000718300), *Blechomonas ayalai* (TAC60: Baya_042_0220, p166: Baya_075_0150), *Bodo saltans* (TAC60: BSAL_45895), *Crithidia fasciculata* (TAC60: CFAC1_290011300, p166: CFAC1_220045700), *Endotrypanum monterogeii* (TAC60: EMOLV88_260009700, p166: EMOLV88_130019600), *Leishmania aethiopica* (TAC60: LAEL147_000431100, p166: LAEL147_000188600), *L. amazonensis* (TAC60: LAMA_000507700, p166: LAMA_000208900), *L. donovani* (TAC60: LdBPK_260530.1, p166: LdBPK_131340.1), *L. major* (TAC60: LmjF.26.0560, p166: LmjF.13.1600), *Leptomonas pyrrhocoris* (TAC60: LpyrH10_01_8410, p166: LpyrH10_20_0130), *Paratrypanosoma confusum* (TAC60: PCON_0005540, p166: PCON_0032280). Multiple sequence alignments (msa) were calculated with the R (version 4.3.2) package msa (version 1.36.1) [46] from Bioconductor (version 3.17) and visualized as sequence logos (Fig 3A and 3B) or as an msa (S4 Fig) using the ggseqlogo (version 0.2) [47] and ggmsa (Bioconductor, version 1.10.0) [47] packages, respectively. Shannon's entropy [48] for msa (S3 Fig) was calculated only for positions with <50% gaps using the base two logarithm version. Phylogenetic trees (S3 Fig) were created using the neighbour joining algorithm [49] implemented in the R package ape (version 5.8) [49] with distance tables calculated by the SeqinR package (version 4.2–36) [50]. Helical wheel projections (Fig 3C) were created with the helixvis package (version 1.0.1) [51] in R. Hydrophobicity values were taken from Kyte and Doolittle [52].

Transgenic cell lines

All cell lines derive from a single marker *T. brucei* 427 cell line [15] grown at 27˚C in SDM-79 supplemented with 5% (v/v) fetal calf serum. Tetracycline-inducible RNAi of TAC60 (Tb927.7.1400/Tb427.07.1400) targets nucleotides 1220–1629 of the open reading frame [22]. To monitor TAC60 RNAi efficiency in Figs 4B, 4C and S6, one of the alleles of TAC60 was C-terminally tagged with 3x myc using a PCR construct based on plasmids of the pMOtag series [53]. C-terminally 3x myc-tagged TAC60 mutants are based on a C-terminally truncated TAC60 version termed TAC60ΔC283 [22] and were cloned into modified pLEW100 vectors [54] for tetracycline-inducible expression. S1 Table summarizes all TAC60 mutants. The C-terminally 3x HA-tagged N-terminally truncated version of p166 (Tb927.11.3290/Tb427tmp.02.0800) was previously described as "mini-p166-HA" [17]. A full list of all mutants of mini-p166 is given in S1 Table. Note, the protein lengths of Tb927.11.3290 and Tb427tmp.02.0800 differ by two aa (Tb927.11.3290 Q998 and S999 are missing in Tb427tmp.02.0800), we therefore exclusively refer to residue numbers of the Tb427tmp.02.0800 aa sequence. The control experiments that the TAC60 mutants used in our study completely replace the endogenous TAC60 and are fully integrated into the TAC are provided in S6 and S7 Figs, respectively.

Flagella extraction and immunofluorescence microscopy

Flagella extraction was performed as described previously [55]. In summary, two days tetracycline-induced cell cultures were supplemented with EDTA (5 mM final) before harvesting. Harvested cells were lysed on ice for 10 minutes with extraction buffer (10mM NaH_2PO_4, 150mM NaCl, 1mM $MgCl_2$, pH 7.2) supplemented with 0.5% (v/v) Triton X-100 and centrifuged (3'000 g, 3 minutes, 4˚C). The resulting cytoskeletal pellet was resuspended in extraction buffer without Triton X-100 and centrifuged as above. The resulting pellet was resuspended in 200 μl containing 10^8 cell equivalents extraction buffer containing 1 mM $CaCl_2$, incubated on ice for 30 minutes and centrifuged (10'000 g, 10 minutes, 4˚C). Finally the extracted flagellar

pellet was washed twice with PBS and resuspended in PBS at 10^7 cell equivalents/50 μl. Subsequently, the flagellar fraction was processed for immunofluorescence microscopy. 50 μl of isolated flagella were allowed to settle on glass slides before fixation with 4% paraformaldehyde for 10 minutes. Fixed flagella were washed with PBS, chilled on ice and blocked with PBS containing 2% (w/v) bovine serum albumin (BSA) before incubation with two rounds of primary (anti myc, YL1/2) and the corresponding secondary antibodies diluted in PBS containing 2% BSA. For more information about the antibodies used see below. Pictures were acquired on a DMI6000B microscope equipped with a DFC360 FX monochrome camera and LAS X software (Leica Microsystems). Images were processed using Fiji software.

kDNA area quantification

kDNA area measurements were performed on three days tetracycline-induced cells. Cells were harvested by a low spin centrifugation and after washing with PBS allowed to settle on glass slides. Settled cells were fixed with 4% paraformaldehyde and Vectashield, containing 4′,6-diamidino-2-phenylindole (DAPI) for DNA visualization, was added to the final samples before mounting the cover slides. Z-stack images were acquired and projected to one plane using Fiji software. All images were processed with identical contrast settings and were converted to binary files for kDNA area quantification. kDNA area was only measured when the entire cell was visible and where the kDNA was in the focal plane. The absence of the kDNA was determined by eye. Violin [56] and sina [57] graphs were generated using the R packages vioplot (version 0.5.0, https://github.com/TomKellyGenetics/vioplot) and SinaPlot (version 1.1.0).

Immunoprecipitations

The TAC60-myc pulldown experiments were performed as described previously [17]. Solubilized mitochondria-enriched fractions of two days tetracycline-induced cells were generated by a two-step digitonin extraction. First, washed cells were lysed in SoTE buffer (20 mM Tris HCl pH 7.5, 0.6 M sorbitol, 2 mM ethylenediaminetetraacetic acid (EDTA)) containing 0.015% (w/v) digitonin and 1x cOmplete, Mini, EDTA-free protease-inhibitor-cocktail (Roche). Following a centrifugation step (6'700 g, 5 minutes, 4˚C) the mitochondria-enriched pellet fraction (P1) was resuspended in a 20 mM Tris HCl pH 7.4, 100 mM NaCl, 10% glycerol, 0.1 mM EDTA, containing 1% (w/v) digitonin and 1x of cOmplete protease-inhibitor-cocktail as above. After another centrifugation (20'000 g, 15 minutes, 4˚C) the resulting supernatant (SN2) was processed for immunoprecipitations and incubated with anti-c myc beads (Sigma) for 2 hours at 4˚C. Subsequently the beads were washed in the same buffer containing only 0.1% (w/v) digitonin. For elution the beads were boiled in SDS-PAGE sample loading buffer lacking β-mercaptoethanol. Samples were collected for the P1, SN2, FT, and IP fractions (Fig 4D) and $5x10^6$ (P1, SN2, and FT) or $5x10^7$ (IP) cell equivalents were used for SDS-PAGE and subsequent immunoblot analysis.

Antibodies

The following non-commercial antibodies were used. The dilutions of the antibodies are indicated in parentheses for immunoblots (IB) and immunofluorescence (IF) analyses, respectively. The polyclonal rabbit antisera against TAC40 (Tb927.4.1610) (IB 1:100) and ATOM40 (Tb927.9.9660) (IB 1:10'000) were described before in [15] and [58], respectively. The monoclonal rat antibody YL1/2 (IF 1:1'000) that recognizes tyrosinated α-tubulin [59] and the basal body protein TbRP2 [60] was a gift from Keith Gull. Commercially available antibodies were used as follows: monoclonal mouse anti-myc antibody (Invitrogen, 132500; IB 1:2'000, IF

1:50), monoclonal mouse anti-HA antibody (Enzo Life Sciences AG, CO-MMS-101 R-1000; IB 1:5'000).

Secondary antibodies for immunoblot analyses were IRDye 680LT goat anti-mouse and IRDye 800CW goat anti-rabbit (both from LI-COR Biosciences; IB 1:20'000). Secondary antibodies for immunofluorescence microscopy were goat anti-mouse Alexa Fluor 596, goat anti-rat Alexa Fluor 488 (both from Thermo Scientific; IF 1:1'000).

Supporting information

S1 Fig. Architectural unit of the tripartite attachment complex (TAC). Single unit TAC cable connecting the basal body to the kinetoplast DNA (kDNA). The three molecular TAC modules and the individual TAC subunits are indicated. The TAC consists of several hundreds of TAC cables arranged in a parallel manner. OM, outer membrane; IM, inner membrane.
(TIF)

S2 Fig. His-tag affinity purification of the p166 C-tail. (A) Depiction of the intermembrane space exposed C-terminus of p166 (D1466-L1499) that was N-terminally fused to 6x His and 3x myc tags and recombinantly expressed in *E. coli*. **(B)** Workflow for the His-tag affinity purification of the fusionprotein. **(C)** Left, Ponceau S stain of a blotted SDS-gel monitoring the purification of the recombinant fusion protein. Right, immunoblot staining of the purified protein fraction (Reten.) using an anti-myc antiserum.
(TIF)

S3 Fig. TAC60 and p166 are conserved in Kinetoplastids. (A) Multiple sequence alignment of TAC60 orthologues from the Kinetoplastid species shown in the phylogenetic tree on the left was analyzed using a Shannon's entropy plot. **(B)** Multiple sequence alignment of p166 orthologues from the Kinetoplastid species shown in the phylogenetic tree on the left was analyzed using a Shannon's entropy plot. The right graph shows a magnification of the C-terminal p166 region depicted by the dashed red line.
(TIF)

S4 Fig. Multiple sequence alignment of p166. Sequence alignment of the C-terminal region of p166 orthologues of the same Kinetoplastid species as were used for Fig 3B.
(TIF)

S5 Fig. AlphaFold2 predictions of the TAC60-p166 interaction for diverse kinetoplastid species. Models depicting the predicted TAC60- p166 interaction interface in *T. brucei*, *T. cruzi*, *L. donovani*, and *A. deanei*. The predicted structure for *T. brucei* is identical to the model shown in Fig 1. For the predictions in the other species the following input sequence segments were used: *T. cruzi* TAC60 (1–233 aa), p166 (1349–1384 aa); *L. donovani* TAC60 (1–312 aa), p166 (1160–1204 aa); *A. deanei* TAC60 (1–239 aa), p166 (986–1017 aa). The models display the conserved kinked α-helix of TAC60 beginning 10 aa upstream and ending 12 aa downstream of the conserved P (see Fig 3). The sidechains of the conserved hydrophobic aa are shown as sticks. While the predicted local Distance Difference Test (IDDT) scores were low for all predictions, a hydrophobic pocket is predicted for all the interaction interfaces.
(TIF)

S6 Fig. Expression of TAC60 mutants in the TAC60-RNAi cell line replaces the endogenous TAC60 with its mutated counterparts. (A) Immunoblots showing that TAC60 RNAi results in efficient depletion of the endogenous *in situ* tagged TAC60-myc and the exclusive expression of the ectopically expressed TAC60ΔC283-myc variants analyzed in Fig 4. (B) and (C) as in (A) but TAC60ΔC283-myc mutants of Figs 6 and 7 were analyzed. ATOM40 serves

as a loading control.
(TIF)

S7 Fig. Immunofluorescence analysis of isolated flagella with TAC60 mutants. Immunofluorescence images of extracted flagella of the indicated mutant TAC60 cell lines show that the mutant proteins (red) co-fractionate with flagella and colocalize with or very close to the basal body. This indicates that the mutant proteins are integrated into the TAC. Tyrosinated tubulin and TbRP2, detected by YL1/2 (green) serves a marker for the flagellum and basal body. Broken line mark original and enlarged insets.
(TIF)

S1 Table. Summary of TAC60 and p166 variants. The control experiments that the TAC60 mutants used in our study completely replace the endogenous TAC60 and are fully integrated into the TAC are provided in S6 and S7 Figs, respectively
(PDF)

S1 Data. Numerical data for all graphs presented in the study.
(XLSX)

S1 Raw images. Original images for all gels and blots.
(PDF)

Acknowledgments

We thank Elke Horn for excellent technical assistance.

Author Contributions

Conceptualization: Philip Stettler, André Schneider.

Formal analysis: Philip Stettler, Salome Aeschlimann.

Funding acquisition: André Schneider.

Investigation: Philip Stettler, Bernd Schimanski, Salome Aeschlimann.

Methodology: Philip Stettler.

Supervision: Bernd Schimanski, André Schneider.

Validation: Philip Stettler.

Visualization: Philip Stettler, André Schneider.

Writing – original draft: Philip Stettler, André Schneider.

Writing – review & editing: Philip Stettler, Bernd Schimanski, Salome Aeschlimann, André Schneider.

References

1. Archibald JM. Endosymbiosis and Eukaryotic Cell Evolution. Curr Biol. 2015; 25(19):R911–21. https://doi.org/10.1016/j.cub.2015.07.055 PMID: 26439354.
2. Lee SR, Han J. Mitochondrial Nucleoid: Shield and Switch of the Mitochondrial Genome. Oxid Med Cell Longev. 2017; 2017:8060949. Epub 20170607. https://doi.org/10.1155/2017/8060949 PMID: 28680532; PubMed Central PMCID: PMC5478868.
3. Bonekamp NA, Larsson NG. SnapShot: Mitochondrial Nucleoid. Cell. 2018; 172(1–2):388– e1. https://doi.org/10.1016/j.cell.2017.12.039 PMID: 29328920.

4. Falkenberg M, Larsson NG, Gustafsson CM. Replication and Transcription of Human Mitochondrial DNA. Annu Rev Biochem. 2024. Epub 20240409. https://doi.org/10.1146/annurev-biochem-052621-092014 PMID: 38594940.
5. Povelones ML. Beyond replication: division and segregation of mitochondrial DNA in kinetoplastids. Mol Biochem Parasitol. 2014; 196:53–60. https://doi.org/10.1016/j.molbiopara.2014.03.008 PMID: 24704441.
6. Amodeo S, Bregy I, Ochsenreiter T. Mitochondrial genome maintenance - the kinetoplast story. FEMS Microbiol Rev. 2022. Epub 20221130. https://doi.org/10.1093/femsre/fuac047 PMID: 36449697.
7. Jensen RE, Englund PT. Network news: the replication of kinetoplast DNA. Annu Rev Microbiol. 2012; 66:473–91. https://doi.org/10.1146/annurev-micro-092611-150057 PMID: 22994497
8. Aeschlimann S, Stettler P, Schneider A. DNA segregation in mitochondria and beyond: insights from the trypanosomal tripartite attachment complex. Trends Biochem Sci. 2023; 48(12):1058–70. Epub 20230927. https://doi.org/10.1016/j.tibs.2023.08.012 PMID: 37775421.
9. Schneider A, Ochsenreiter T. Failure is not an option - mitochondrial genome segregation in trypanosomes. J Cell Sci. 2018;131(18). https://doi.org/10.1242/jcs.221820 PMID: 30224426.
10. Wheeler RJ, Gull K, Sunter JD. Coordination of the Cell Cycle in Trypanosomes. Annual review of microbiology. 2019; 73:133–54. Epub 2019/09/11. https://doi.org/10.1146/annurev-micro-020518-115617 PMID: 31500537.
11. Ogbadoyi EO, Robinson DR, Gull K. A high-order trans-membrane structural linkage is responsible for mitochondrial genome positioning and segregation by flagellar basal bodies in trypanosomes. Mol Biol Cell. 2003; 14:1769–79. https://doi.org/10.1091/mbc.e02-08-0525 PMID: 12802053
12. Robinson DR, Gull K. Basal body movements as a mechanism for mitochondrial genome segregation in the trypanosome cell cycle. Nature. 1991; 352:731–3. https://doi.org/10.1038/352731a0 PMID: 1876188
13. Carvalho-Santos Z, Azimzadeh J, Pereira-Leal JB, Bettencourt-Dias M. Evolution: Tracing the origins of centrioles, cilia, and flagella. J Cell Biol. 2011; 194(2):165–75. https://doi.org/10.1083/jcb.201011152 PMID: 21788366; PubMed Central PMCID: PMC3144413.
14. Gheiratmand L, Brasseur A, Zhou Q, He CY. Biochemical characterization of the bi-lobe reveals a continuous structural network linking the bi-lobe to other single-copied organelles in Trypanosoma brucei. J Biol Chem 2013; 288:3489–99. https://doi.org/10.1074/jbc.M112.417428 PMID: 23235159
15. Aeschlimann S, Kalichava A, Schimanski B, Berger BM, Jetishi C, Stettler P, et al. Single p197 molecules of the mitochondrial genome segregation system of Trypanosoma brucei determine the distance between basal body and outer membrane. Proc Natl Acad Sci U S A. 2022; 119(40):e2204294119. Epub 20220926. https://doi.org/10.1073/pnas.2204294119 PMID: 36161893; PubMed Central PMCID: PMC9546609.
16. Bregy I, Radecke J, Noga A, Hoek Hvd, Kern M, Haenni B, et al. Cryo-electron tomography sheds light on the elastic nature of the Trypanosoma brucei tripartite attachment complex. Biorvix. 2023. https://doi.org/10.1101/2023.03.06.531305
17. Schimanski B, Aeschlimann S, Stettler P, Kaser S, Gomez-Fabra Gala M, Bender J, et al. p166 links membrane and intramitochondrial modules of the trypanosomal tripartite attachment complex. PLoS Pathog. 2022; 18(6):e1010207. Epub 20220616. https://doi.org/10.1371/journal.ppat.1010207 PMID: 35709300.
18. Zhao Z, Lindsay ME, Chowdhury AR, Robinson DR, Englund PT. p166, a link between the trypanosome mitochondrial DNA and flagellum, mediates genome segregation. EMBO J. 2008; 27:143–54. https://doi.org/10.1038/sj.emboj.7601956 PMID: 18059470
19. Trikin R, Doiron N, Hoffmann A, Haenni B, Jakob M, Schnaufer A, et al. TAC102 Is a Novel Component of the Mitochondrial Genome Segregation Machinery in Trypanosomes. PLoS Pathog. 2016; 12(5): e1005586. https://doi.org/10.1371/journal.ppat.1005586 PMID: 27168148; PubMed Central PMCID: PMC4864229.
20. Seybold C, Schiebel E. Spindle pole bodies. Curr Biol. 2013; 23(19):R858–60. https://doi.org/10.1016/j.cub.2013.07.024 PMID: 24112974.
21. Baudouin HCM, Pfeiffer L, Ochsenreiter T. A comparison of three approaches for the discovery of novel tripartite attachment complex proteins in Trypanosoma brucei. PLoS Negl Trop Dis. 2020; 14(9): e0008568. Epub 2020/09/17. https://doi.org/10.1371/journal.pntd.0008568 PMID: 32936798; PubMed Central PMCID: PMC7521757.
22. Käser S, Willemin M, Schnarwiler F, Schimanski B, Poveda-Huertes D, Oeljeklaus S, et al. Biogenesis of the mitochondrial DNA inheritance machinery in the mitochondrial outer membrane of Trypanosoma brucei. PLoS Pathog. 2017; 13(12):e1006808. https://doi.org/10.1371/journal.ppat.1006808 PMID: 29287109.

23. Käser S, Oeljeklaus S, Tyc J, Vaughan S, Warscheid B, Schneider A. Outer membrane protein functions as integrator of protein import and DNA inheritance in mitochondria. Proc Natl Acad Sci USA. 2016; 113:E4467–75. https://doi.org/10.1073/pnas.1605497113 PMID: 27436903.

24. Vitali DG, Käser S, Kolb A, Dimmer KS, Schneider A, Rapaport D. Independent evolution of functionally exchangeable mitochondrial outer membrane import complexes. eLife. 2018; 7:e34488. https://doi.org/10.7554/eLife.34488 PMID: 29923829

25. Schnarwiler F, Niemann M, Doiron N, Harsman A, Kaser S, Mani J, et al. Trypanosomal TAC40 constitutes a novel subclass of mitochondrial beta-barrel proteins specialized in mitochondrial genome inheritance. Proc Natl Acad Sci U S A. 2014; 111(21):7624–9. Epub 2014/05/14. https://doi.org/10.1073/pnas.1404854111 PMID: 24821793; PubMed Central PMCID: PMC4040615.

26. Hoffmann A, Käser S, Jakob M, Amodeo S, Peitsch C, Tyc J, et al. Molecular model of the mitochondrial genome segregation machinery in Trypanosoma brucei. Proc Natl Acad Sci U S A. 2018; 115(8): E1809–E18. https://doi.org/10.1073/pnas.1716582115 PMID: 29434039; PubMed Central PMCID: PMC5828607.

27. Tamura Y, Kawano S, Endo T. Lipid homeostasis in mitochondria. Biological chemistry. 2020; 401(6–7):821–33. https://doi.org/10.1515/hsz-2020-0121 PMID: 32229651.

28. Horvath SE, Rampelt H, Oeljeklaus S, Warscheid B, van der Laan M, Pfanner N. Role of membrane contact sites in protein import into mitochondria. Protein Sci. 2015; 24(3):277–97. Epub 20150212. https://doi.org/10.1002/pro.2625 PMID: 25514890; PubMed Central PMCID: PMC4353355.

29. Jumper J, Evans R, Pritzel A, Green T, Figurnov M, Ronneberger O, et al. Highly accurate protein structure prediction with AlphaFold. Nature. 2021; 596(7873):583–9. Epub 20210715. https://doi.org/10.1038/s41586-021-03819-2 PMID: 34265844; PubMed Central PMCID: PMC8371605.

30. Mirdita M, Schutze K, Moriwaki Y, Heo L, Ovchinnikov S, Steinegger M. ColabFold: making protein folding accessible to all. Nat Methods. 2022; 19(6):679–82. Epub 20220530. https://doi.org/10.1038/s41592-022-01488-1 PMID: 35637307; PubMed Central PMCID: PMC9184281.

31. Huynen MA, Muhlmeister M, Gotthardt K, Guerrero-Castillo S, Brandt U. Evolution and structural organization of the mitochondrial contact site (MICOS) complex and the mitochondrial intermembrane space bridging (MIB) complex. Biochim Biophys Acta. 2016; 1863(1):91–101. https://doi.org/10.1016/j.bbamcr.2015.10.009 PMID: 26477565.

32. Schorr S, van der Laan M. Integrative functions of the mitochondrial contact site and cristae organizing system. Semin Cell Dev Biol. 2018; 76:191–200. https://doi.org/10.1016/j.semcdb.2017.09.021 PMID: 28923515.

33. Busch JD, Fielden LF, Pfanner N, Wiedemann N. Mitochondrial protein transport: Versatility of translocases and mechanisms. Mol Cell. 2023; 83(6):890–910. https://doi.org/10.1016/j.molcel.2023.02.020 PMID: 36931257.

34. Gomkale R, Linden A, Neumann P, Schendzielorz AB, Stoldt S, Dybkov O, et al. Mapping protein interactions in the active TOM-TIM23 supercomplex. Nat Commun. 2021; 12(1):5715. Epub 20210929. https://doi.org/10.1038/s41467-021-26016-1 PMID: 34588454; PubMed Central PMCID: PMC8481542.

35. Ellenrieder L, Dieterle MP, Doan KN, Martensson CU, Floerchinger A, Campo ML, et al. Dual Role of Mitochondrial Porin in Metabolite Transport across the Outer Membrane and Protein Transfer to the Inner Membrane. Mol Cell. 2019; 73(5):1056–65 e7. Epub 20190206. https://doi.org/10.1016/j.molcel.2018.12.014 PMID: 30738704.

36. Khosravi S, Harner ME. The MICOS complex, a structural element of mitochondria with versatile functions. Biological chemistry. 2020; 401(6–7):765–78. https://doi.org/10.1515/hsz-2020-0103 PMID: 32229686.

37. Eramo MJ, Lisnyak V, Formosa LE, Ryan MT. The 'mitochondrial contact site and cristae organising system' (MICOS) in health and human disease. J Biochem. 2020; 167(3):243–55. https://doi.org/10.1093/jb/mvz111 PMID: 31825482.

38. Tamura Y, Kawano S, Endo T. Organelle contact zones as sites for lipid transfer. J Biochem. 2019; 165 (2):115–23. https://doi.org/10.1093/jb/mvy088 PMID: 30371789.

39. Dean S, Gould MK, Dewar CE, Schnaufer AC. Single point mutations in ATP synthase compensate for mitochondrial genome loss in trypanosomes. Proc Natl Acad Sci USA 2013; 110:14741–6. https://doi.org/10.1073/pnas.1305404110 PMID: 23959897

40. Vaughan S, Gull K. Basal body structure and cell cycle-dependent biogenesis in Trypanosoma brucei. Cilia. 2015; 5:5. Epub 2016/02/11. https://doi.org/10.1186/s13630-016-0023-7 PMID: 26862392; PubMed Central PMCID: PMC4746817.

41. Evans R, O'Neill M, Pritzel A, Antropova N, Senior A, Green T, et al. Protein complex prediction with AlphaFold-Multimer. bioRxiv. 2022. https://doi.org/10.1101/2021.10.04.463034

42. Sheffield P, Garrard S, Derewenda Z. Overcoming expression and purification problems of RhoGDI using a family of "parallel" expression vectors. Protein Expr Purif. 1999; 15(1):34–9. https://doi.org/10.1006/prep.1998.1003 PMID: 10024467.

43. Studier FW, Moffatt BA. Use of bacteriophage T7 RNA polymerase to direct selective high-level expression of cloned genes. Journal of molecular biology. 1986; 189(1):113–30. https://doi.org/10.1016/0022-2836(86)90385-2 PMID: 3537305.

44. Smith PK, Krohn RI, Hermanson GT, Mallia AK, Gartner FH, Provenzano MD, et al. Measurement of protein using bicinchoninic acid. Anal Biochem. 1985; 150(1):76–85. https://doi.org/10.1016/0003-2697(85)90442-7 PMID: 3843705.

45. Aslett M, Aurrecoechea C, Berriman M, Brestelli J, Brunk BP, Carrington M, et al. TriTrypDB: a functional genomic resource for the Trypanosomatidae. Nucleic acids research. 2010;38(Database issue): D457-62. Epub 20091020. https://doi.org/10.1093/nar/gkp851 PMID: 19843604; PubMed Central PMCID: PMC2808979.

46. Bodenhofer U, Bonatesta E, Horejs-Kainrath C, Hochreiter S. msa: an R package for multiple sequence alignment. Bioinformatics. 2015; 31(24):3997–9. Epub 20150826. https://doi.org/10.1093/bioinformatics/btv494 PMID: 26315911.

47. Wagih O. ggseqlogo: a versatile R package for drawing sequence logos. Bioinformatics. 2017; 33 (22):3645–7. https://doi.org/10.1093/bioinformatics/btx469 PMID: 29036507.

48. Shannon CE. A Mathematical Theory of Communication. The Bell System Technical Journal. 1948; 27:379–423.

49. Saitou N, Nei M. The neighbor-joining method: a new method for reconstructing phylogenetic trees. Mol Biol Evol. 1987; 4(4):406–25. https://doi.org/10.1093/oxfordjournals.molbev.a040454 PMID: 3447015.

50. Charif D, Lobry JR. SeqinR 1.0–2: A Contributed Package to the R Project for Statistical Computing Devoted to Biological Sequences Retrieval and Analysis. Structural Approaches to Sequence Evolution, Springer. 2007:207–32. https://doi.org/10.1007/978-3-540-35306-5_10

51. Wadhwa RR, Subramanian V, Stevens-Truss R. Visualizing alpha-helical peptides in R with helixvis. JOSS. 2018; 3:1008. https://doi.org/10.21105/joss.01008

52. Kyte J, Doolittle RF. A simple method for displaying the hydropathic character of a protein. Journal of molecular biology. 1982; 157(1):105–32. https://doi.org/10.1016/0022-2836(82)90515-0 PMID: 7108955.

53. Oberholzer M, Morand S, Kunz S, Seebeck T. A vector series for rapid PCR-mediated C-terminal in situ tagging of Trypanosoma brucei genes. Mol Biochem Parasitol. 2006; 145:117–20. https://doi.org/10.1016/j.molbiopara.2005.09.002 PMID: 16269191

54. Wirtz E, Leal S, Ochatt C, Cross GA. A tightly regulated inducible expression system for conditional gene knock-outs and dominant-negative genetics in Trypanosoma brucei. Mol Biochem Parasitol. 1999; 99:89–101. https://doi.org/10.1016/s0166-6851(99)00002-x PMID: 10215027

55. Sasse R, Gull K. Tubulin posttranslational modifications and the construction of microtubular organelles in Trypanosoma brucei. J Cell Sci. 1988; 90:577–89. https://doi.org/10.1242/jcs.90.4.577 PMID: 3075618

56. Hintze JL, Nelson RD. Violin Plots: A Box Plot-Density Trace Synergism. The American Statistician. 1998; 52:181–4. https://doi.org/10.1080/00031305.1998.10480559

57. Sidiropoulos N, Sohi SH, Pedersen TL, Porse BT, Winther O, Rapin N, et al. SinaPlot: An Enhanced Chart for Simple and Truthful Representation of Single Observations Over Multiple Classes. Journal of Computational and Graphical Statistics. 2018; 27(3):673–6. https://doi.org/10.1080/10618600.2017.1366914

58. Niemann M, Wiese S, Mani J, Chanfon A, Jackson C, Meisinger C, et al. Mitochondrial outer membrane proteome of Trypanosoma brucei reveals novel factors required to maintain mitochondrial morphology. Mol Cell Proteomics. 2013; 12:515–28. https://doi.org/10.1074/mcp.M112.023093 PMID: 23221899

59. Kilmartin JV, Wright B, Milstein C. Rat monoclonal antitubulin antibodies derived by using a new nonsecreting rat cell line. J Cell Biol. 1982; 93(3):576–82. https://doi.org/10.1083/jcb.93.3.576 PMID: 6811596; PubMed Central PMCID: PMC2112140.

60. Harmer J, Qi X, Toniolo G, Patel A, Shaw H, Benson FE, et al. Variation in Basal Body Localisation and Targeting of Trypanosome RP2 and FOR20 Proteins. Protist. 2017; 168(4):452–66. Epub 20170713. https://doi.org/10.1016/j.protis.2017.07.002 PMID: 28822909.

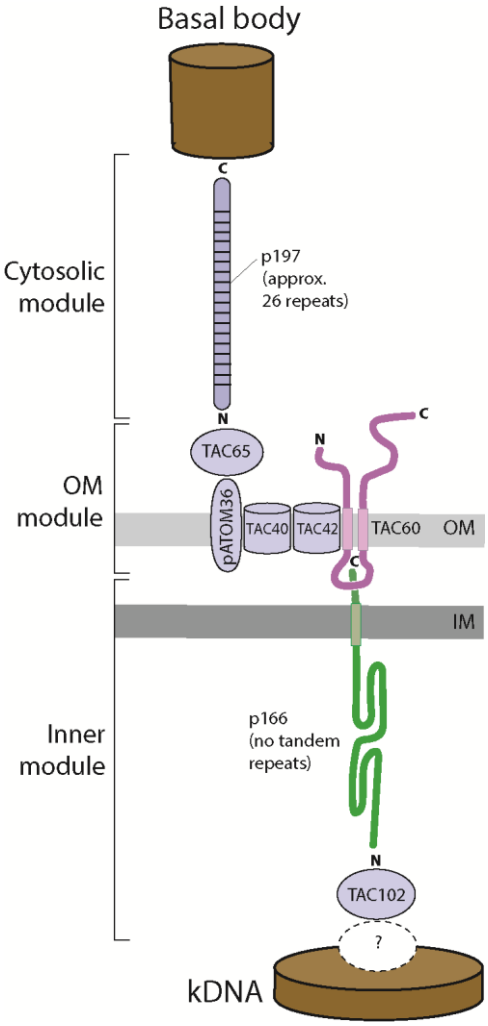

S1 Fig. Architectural unit of the tripartite attachment complex (TAC).

Single unit TAC cable connecting the basal body to the kinetoplast DNA (kDNA). The three molecular TAC modules and the individual TAC subunits are indicated. The TAC consists of several hundreds of TAC cables arranged in a parallel manner. OM, outer membrane; IM, inner membrane.

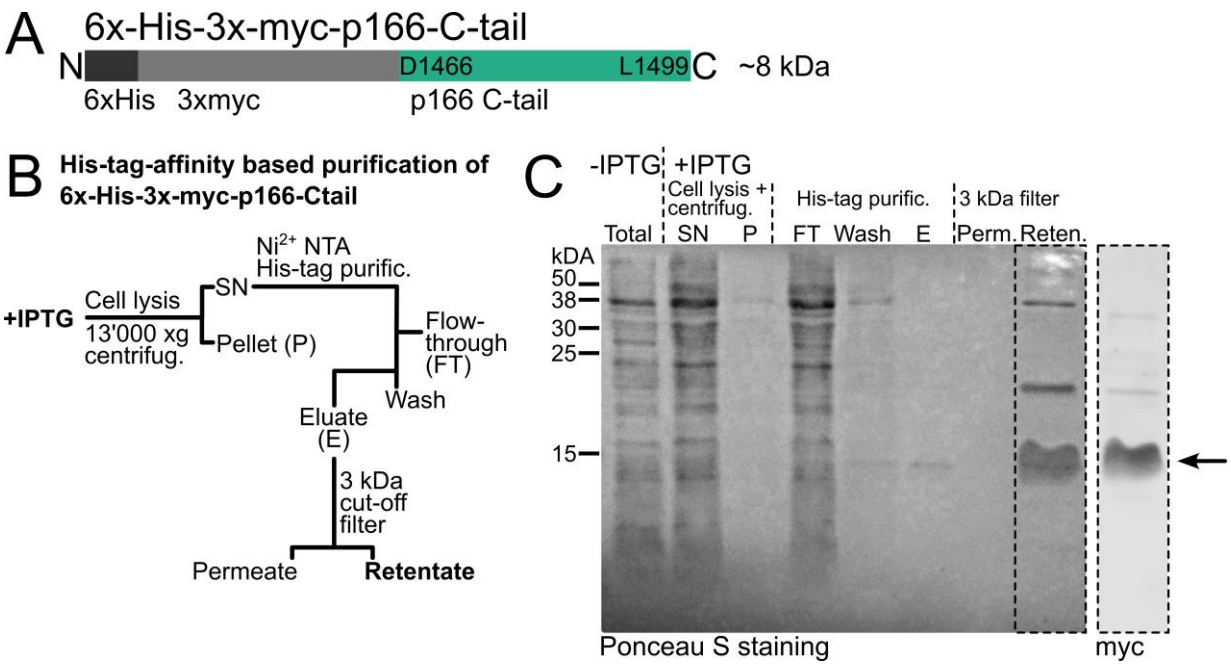

S2 Fig. His-tag affinity purification of the p166 C-tail.

(A) Depiction of the intermembrane space exposed C-terminus of p166 (D1466-L1499) that was N-terminally fused to 6x His and 3x myc tags and recombinantly expressed in *E. coli*. **(B)** Workflow for the His-tag affinity purification of the fusionprotein. **(C)** Left, Ponceau S stain of a blotted SDS-gel monitoring the purification of the recombinant fusion protein. Right, immunoblot staining of the purified protein fraction (Reten.) using an anti-myc antiserum.

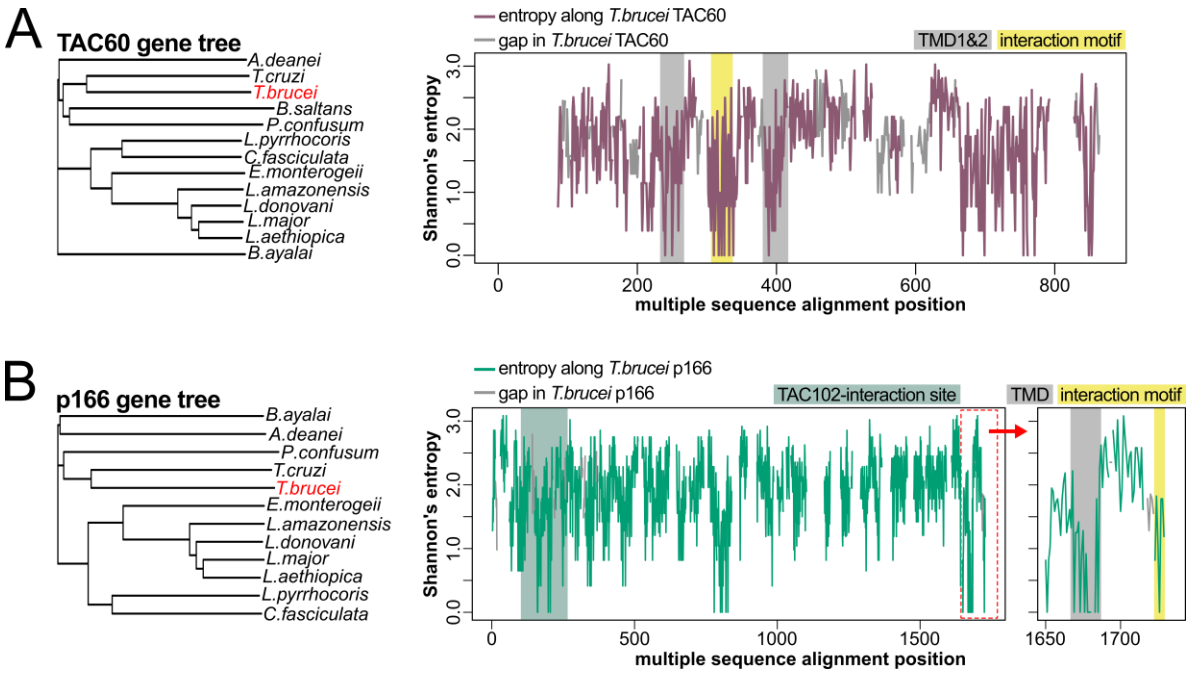

S3 Fig. TAC60 and p166 are conserved in Kinetoplastids.

(A) Multiple sequence alignment of TAC60 orthologues from the Kinetoplastid species shown in the phylogenetic tree on the left was analyzed using a Shannon's entropy plot. **(B)** Multiple sequence alignment of p166 orthologues from the Kinetoplastid species shown in the phylogenetic tree on the left was analyzed using a Shannon's entropy plot. The right graph shows a magnification of the C-terminal p166 region depicted by the dashed red line.

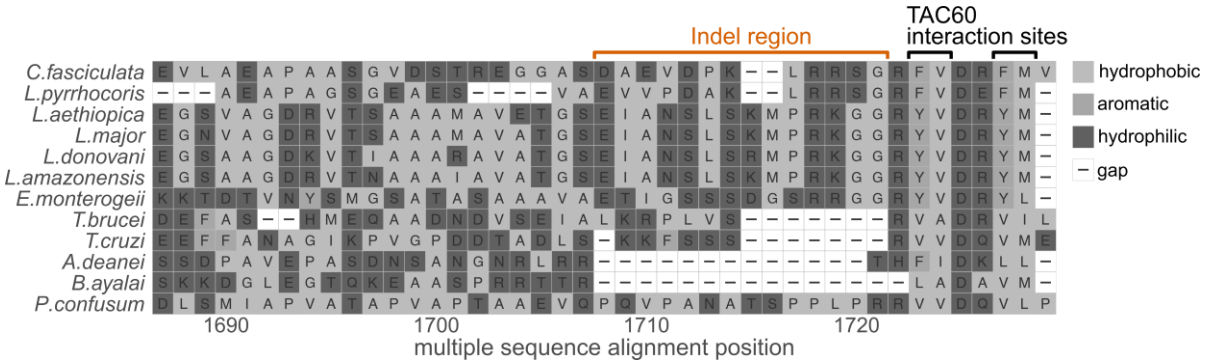

S4 Fig. Multiple sequence alignment of p166.

Sequence alignment of the C-terminal region of p166 orthologues of the same Kinetoplastid species as were used for Fig 3B.

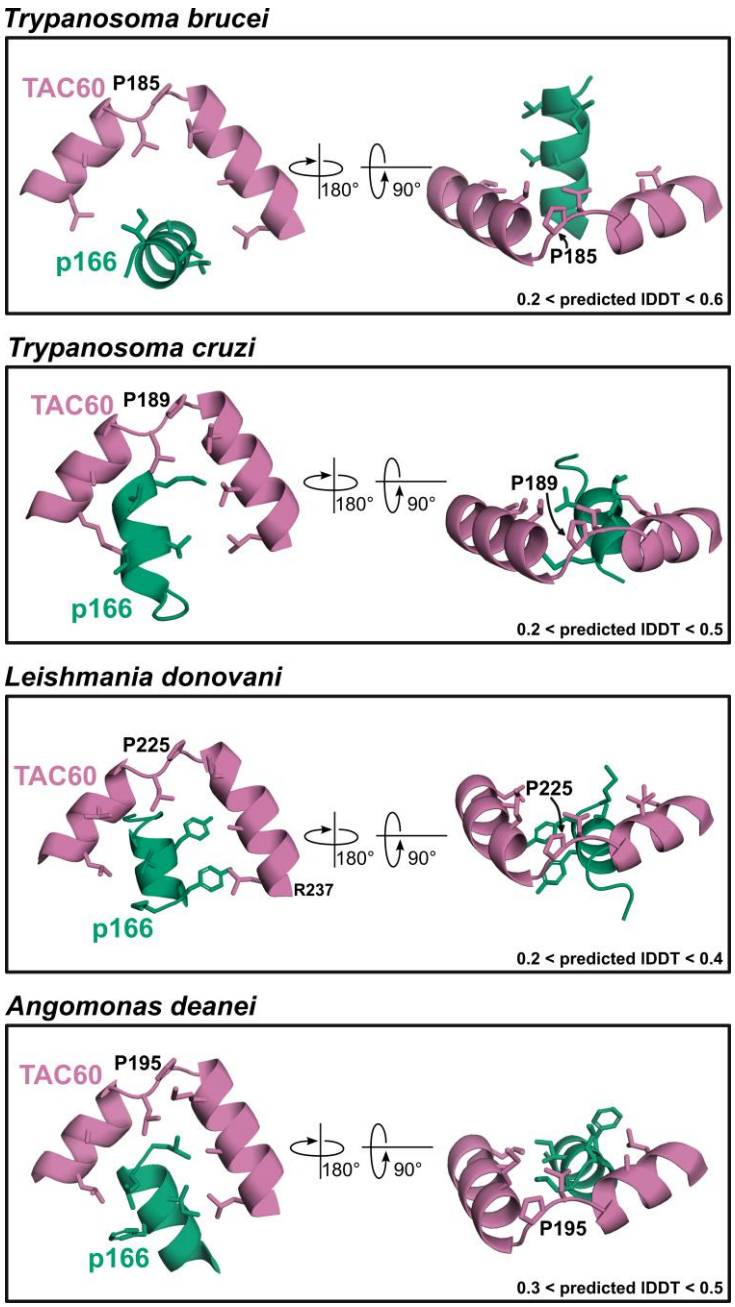

S5 Fig. AlphaFold2 predictions of the TAC60-p166 interaction for diverse kinetoplastid species.

Models depicting the predicted TAC60- p166 interaction interface in *T. brucei*, *T. cruzi*, *L. donovani*, and *A. deanei*. The predicted structure for *T. brucei* is identical to the model shown in Fig 1. For the predictions in the other species the following input sequence segments were used: *T. cruzi* TAC60 (1–233 aa), p166 (1349–1384 aa); *L. donovani* TAC60 (1–312 aa), p166 (1160–1204 aa); *A. deanei* TAC60 (1–239 aa), p166 (986–1017 aa). The models display the conserved kinked α-helix of TAC60 beginning 10 aa upstream and ending 12 aa downstream of the conserved P (see Fig 3). The sidechains of the conserved hydrophobic aa are shown as sticks. While the predicted local Distance Difference Test (IDDT) scores were low for all predictions, a hydrophobic pocket is predicted for all the interaction interfaces.

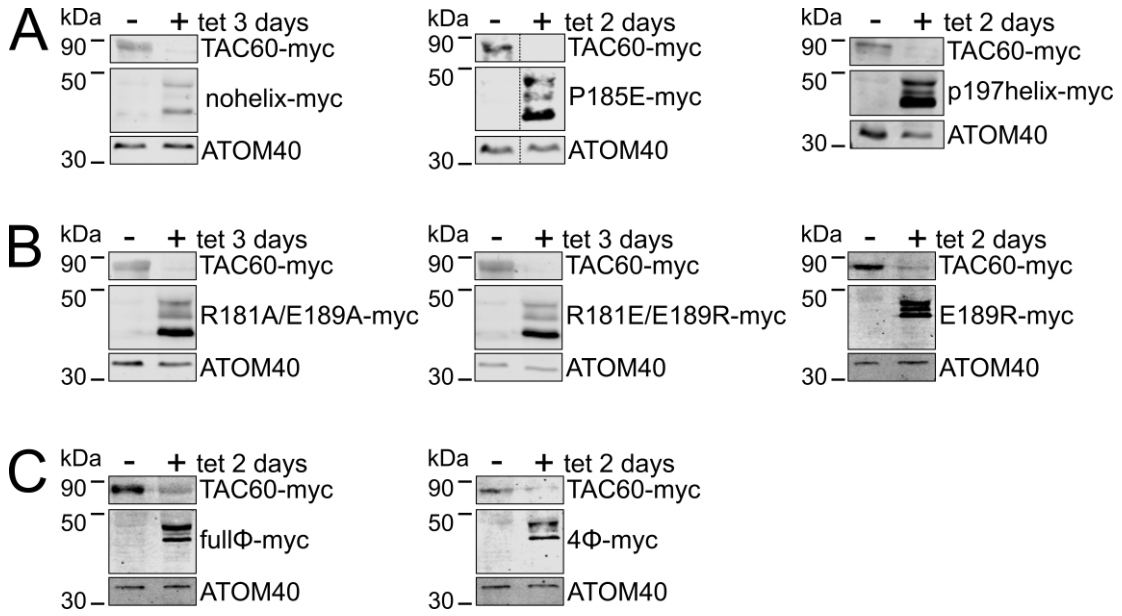

S6 Fig. Expression of TAC60 mutants in the TAC60-RNAi cell line replaces the endogenous TAC60 with its mutated counterparts.

(A) Immunoblots showing that TAC60 RNAi results in efficient depletion of the endogenous *in situ* tagged TAC60-myc and the exclusive expression of the ectopically expressed TAC60ΔC283-myc variants analyzed in Fig 4. (B) and (C) as in (A) but TAC60ΔC283-myc mutants of Figs 6 and 7 were analyzed. ATOM40 serves as a loading control.

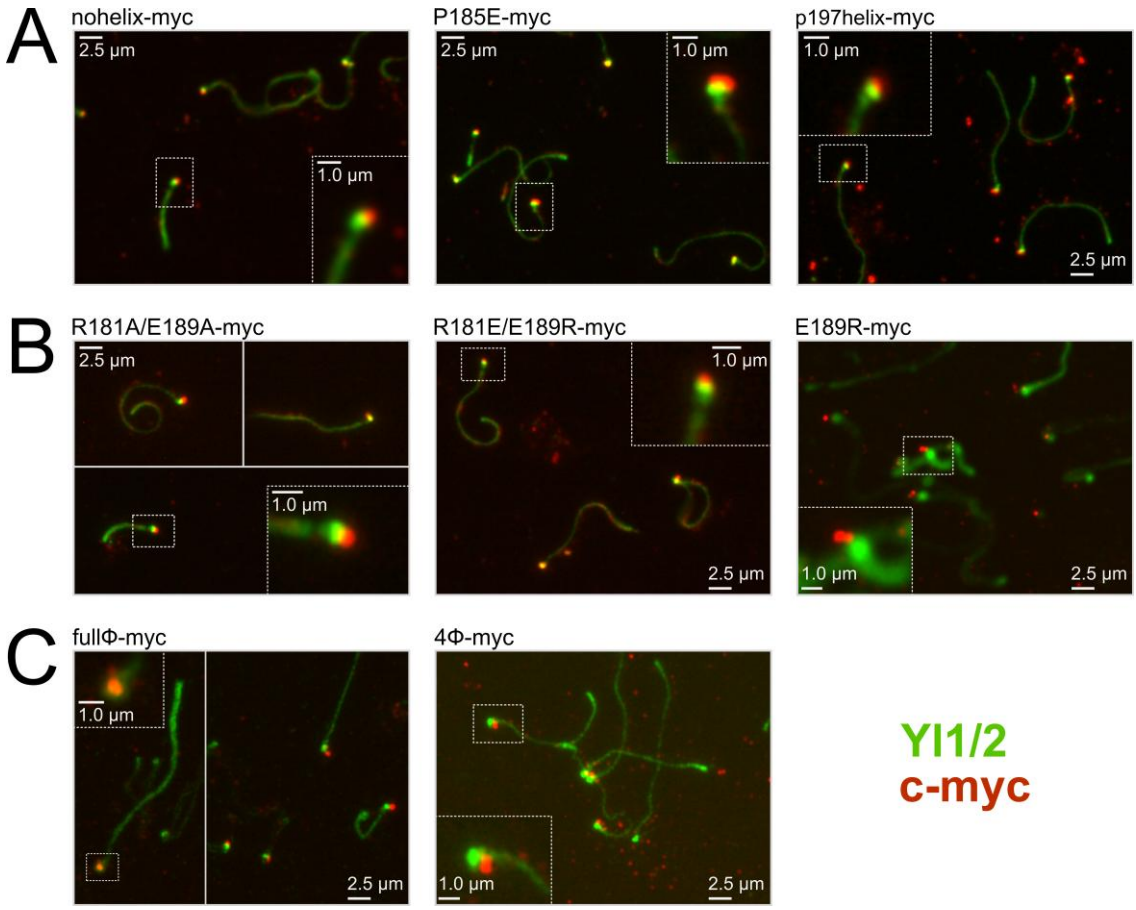

S7 Fig. Immunofluorescence analysis of isolated flagella with TAC60 mutants.

Immunofluorescence images of extracted flagella of the indicated mutant TAC60 cell lines show that the mutant proteins (red) co-fractionate with flagella and colocalize with or very close to the basal body. This indicates that the mutant proteins are integrated into the TAC. Tyrosinated tubulin and TbRP2, detected by YL1/2 (green) serves a marker for the flagellum and basal body. Broken line mark original and enlarged insets.

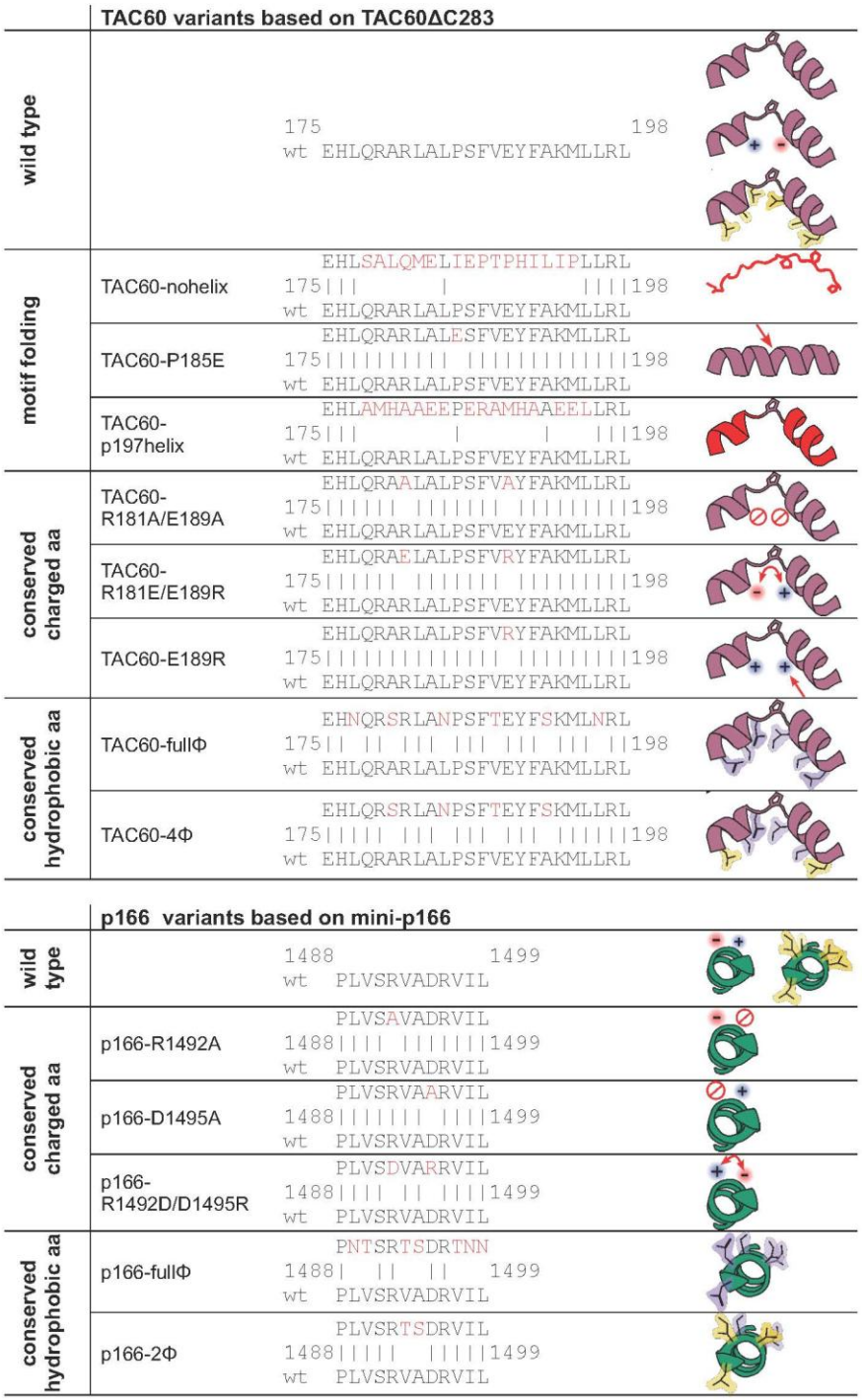

S1 Table. Summary of TAC60 and p166 variants.

The control experiments that the TAC60 mutants used in our study completely replace the endogenous TAC60 and are fully integrated into the TAC are provided in S6 and S7 Figs, respectively.

3.2 Assembly of the mitochondrial outer membrane module of the trypanosomal tripartite attachment complex

Philip Stettler [1,2], Salome Aeschlimann [1], Bernd Schimanski [1], André Schneider [1]

[1]Department of Chemistry, Biochemistry and Pharmaceutical Sciences, University of Bern, Switzerland

[2]Graduate School for Cellular and Biomedical Sciences, University of Bern, Switzerland

Contribution:

- All data shown in figures and supplementary figures.

- All cell lines except previously published cell lines and the cell lines used in figures 5 and S3 and in figures 7AB.

- Design of all figures and writing of the first draft. Review and editing of the manuscript at all stages.

Assembly of the mitochondrial outer membrane module of the trypanosomal tripartite attachment complex

Philip Stettler[1,2], Salome Aeschlimann[1], Bernd Schimanski[1], and André Schneider[1]*

[1]Department of Chemistry, Biochemistry and Pharmaceutical Sciences, University of Bern, Bern, Switzerland

[2]Graduate School for Cellular and Biomedical Sciences, University of Bern, Bern, Switzerland.

*Corresponding author: andre.schneider@unibe.ch

Abstract

The parasitic protozoan *Trypanosoma brucei* has a single mitochondrial nucleoid, anchored to the basal body of the flagellum via the tripartite attachment complex (TAC). The detergent-insoluble TAC is essential for mitochondrial genome segregation during cytokinesis. The TAC assembles de novo in a directed way from the probasal body towards the kDNA. However, the OM TAC module which is composed of five subunits, has previously been suspected to follow more complicated assembly pathways. Here, we identified four detergent-soluble OM TAC module subcomplexes that we assign to two classes. One class contains an oligomeric TAC40 complex that according to AlphaFold contains 6-8 subunits, as well as two subcomplexes of different sizes comprising TAC40, TAC42, and TAC60. The second class consists of a single complex composed of TAC65 and pATOM36. We show that the two subcomplex classes form independently and accumulate upon impairment of TAC assembly. The expression of an N-terminally truncated TAC60 variant causes the accumulation of the larger TAC40/TAC42/TAC60 complex and blocks completion of OM TAC module assembly. This suggests the following assembly pathway: i) TAC40 oligomerizes, ii) TAC42 and TAC60 bind the TAC40 oligomer forming two discrete larger intermediates, where iii) the larger subcomplex merges with the pATOM36/TAC65 subcomplex subsequently forming the OM TAC module.

Introduction

Genome replication and faithful segregation of the replicated genomes to daughter cells during cell division are arguably the most central processes of life. The most complex situation is found in eukaryotes which have up to three different genomes localized in the nucleus, in mitochondria, and in plastids.

How replicated organellar genomes are segregated during organellar fission processes is an understudied subject. Mitochondrial genome segregation processes have mainly been studied in *Saccharomyces cerevisiae* and humans [1-3] which both belong to the eukaryotic supergroup of the Opisthokonts [4]. Both species contain many mitochondria (in human up to several hundred per cell) that form highly dynamic networks which are constantly remodeled by fission and fusion processes [5-7]. The mitochondrial genome is organized in nucleoids, each consisting of a few copies of the mitochondrial genome associated with numerous DNA binding and other proteins [8, 9]. Nucleoids outnumber mitochondria, appear to be associated with the mitochondrial inner membrane (IM) and can be transported actively within the network. The processes ensuring proper segregation of nucleoids during mitochondrial fission appear to involve mitochondria-associated ER domains but how they work in detail remains to be elucidated [10-12].

In the present study we were studying mitochondrial genome segregation in the parasitic protozoan *Trypanosoma brucei* which belongs to the Discoba group [4]. *T. brucei* is an experimentally highly accessible model system and has arguably the best studied mitochondrion outside the Opisthokonts [13-21].

T. brucei and its relatives, most of which are parasites, are famous for having a single mitochondrion with a single nucleoid only [22]. The structure of the trypanosomal mitochondrial genome, termed kinetoplast DNA (kDNA), is very complicated. It consists of two genetic elements: approximately 25 maxicircles (22 kb in length) and approximately 5'000 minicircles (1 kb in length). Maxicircles and minicircles are highly concatenated among themselves and between each other forming a large disk-shaped kDNA network [19, 20, 23]. Maxicircles encode mainly subunits of the respiratory complexes [24]. Many of their genes represent cryptogenes, thus their transcripts must be edited by multiple uridine insertions and/or deletions to become functional mRNAs. Minicircles, on the other hand, encode guide RNAs that provide the information for RNA editing [18, 25, 26].

The kDNA is permanently tethered, across the two mitochondrial membranes, with the basal body of the flagellum by a unique structure called the tripartite attachment complex (TAC) (S1 Fig) [27-29]. The function of the mega-Dalton-sized TAC is to allow the coupled segregation of the single kDNA disk and the single flagellum [27, 30]. This implies that the kDNA network needs to be replicated in coordination with the nuclear cell cycle [19, 22].

In *T. brucei* nine TAC subunits each present in several hundred to a few thousand copies have identified so far [30, 31] (S1 Fig). The TAC subunits and the TAC architecture are conserved within Kinetoplastids [19, 31]. Traditionally, the TAC has been divided into three morphological domains based on transmission electron microscopy: the cytosolic exclusion zone filaments, the differentiated mitochondrial membranes, and the unilateral filaments in the matrix [28]. However, characterization of the nine TAC subunits, which likely represent the nearly complete set of TAC components, now allows to define three TAC modules based on their molecular composition: the cytosolic, the outer membrane (OM), and the inner TAC modules [31] (S1 Fig.).

The "cytosolic TAC module" connects the basal body to the OM TAC module and consists of the single subunit p197 [32, 33]. The C- and N-termini of p197 interact with the basal body and TAC65 of the OM module, respectively. The large central part of p197, making up approximately 84% of the protein, consists of 35 or more near-identical α-helical repeats of 175 aa in length [34] and determines the distance between the basal body and the OM [32]. Thus, the predicted molecular mass of p197 is more than 880 kDa making it the largest protein of *T. brucei*.

The "OM TAC module" consists of the five subunits TAC65, pATOM36, TAC40, TAC42 and TAC60 [31]. The globular TAC65 is a peripheral OM protein which faces the cytosol [35, 36]. It interacts with the N-terminus of p197 [32] and binds to pATOM36, one of four integral OM proteins of the OM module [36]. pATOM36 has a dual function, it is an essential subunit of the TAC structure, whereas outside of the TAC it mediates biogenesis of the atypical protein translocase of the OM (ATOM) complex [36]. Reciprocal complementation experiments between yeast and *T. brucei* have shown that pATOM36 and the yeast MIM complex have identical functions in the biogenesis of a subset of OM proteins [37]. TAC40 and TAC42 are β-barrel membrane proteins that form a complex with TAC60 which has two α-helical transmembrane domains [38, 39]. Both the N- and C-termini of TAC60 face the cytosol, but in contrast to the N-terminus, the cytosolically exposed C-terminus of TAC60 is dispensable for TAC function [38]. The 142 aa long intermembrane (IMS) -exposed loop of TAC60 contains the binding site for the interaction with the C-terminus of p166 [40].

p166 is a subunit of the “inner TAC module” and contains a single transmembrane domain close to its C-terminus [31, 41, 42]. The IMS-exposed loop of TAC60 binds to the IMS-exposed C-terminus of p166 and forms a stable contact site between the OM and IM. It was shown that the minimal p166 binding site of TAC60 consists of a short kinked α-helix that via hydrophobic interactions binds to the C-terminal α-helix of p166 [40]. The large soluble domain of p166 is exposed to the matrix and binds to TAC102, a soluble matrix protein [41, 43, 44]. While TAC102 localizes close to the kDNA it does not bind to it directly. Four proteins, TAC53, TAP110, KAP68, and mtHMG44, which localize between TAC102 and the kinetoplast have been identified [45-47]. Of these only TAC53 behaves like a classical TAC subunit [47]. KAP68 can bind to DNA at least in vitro [45]. However, what precise functions these proteins have and how they are arranged relative to each other is not known. Thus, how exactly the TAC is anchored to the kDNA remains unclear [31].

An interphase trypanosomal cell has a single flagellum and a single kDNA that is connected to the TAC [28]. The coordinated assembly and duplication of the TAC during the cell cycle represents one of the most extreme sorting and assembly events seen in any mitochondria [30, 31]. It is known that the overarching principle of TAC formation is based on a *de novo* and hierarchical assembly of its subunits [35]. Starting with p197 at the pro basal body the assembly proceeds towards the kDNA. Generally, depletion of basal body-proximal TAC subunits results in the delocalization of all distal subunits. However, there are hints that the complex OM TAC module behaves differently. Although TAC65 is the direct interaction partner of p197 and a cytosolically exposed peripheral OM protein, it cannot assemble into the TAC after ablation of TAC40 or TAC60 [35].

Using a combination of RNAi cell lines and blue native (BN)-PAGE analyses we have studied the biogenesis of the OM TAC module. We could show that it involves the independent formation of various detergent-soluble assembly intermediates consisting of either TAC40/TAC42/TAC60 and TAC65/pATOM36, respectively.

Results

OM TAC module subunits form detergent-soluble subcomplexes

The fully assembled TAC structure is insoluble in non-ionic detergents [32, 41, 42]. However, pulldown experiments of digitonin-solubilized crude mitochondrial fractions using tagged OM TAC subunits demonstrated the existence of two main classes of detergent soluble complexes consisting of either (i) TAC40, TAC42 and TAC60 or (ii) TAC65 and pATOM36, respectively [36, 38]. Together with RNAi analyses these experiments suggested that the OM TAC module may not strictly adhere to the hierarchical assembly model described above [35]. Thus, we decided to investigate the detergent-soluble protein complexes of the OM TAC module in the procyclic form (PCF) of *T. brucei* in more detail using BN-PAGE and immunoblot analyses, with the ultimate aim to gain insight into its assembly process (Fig 1).

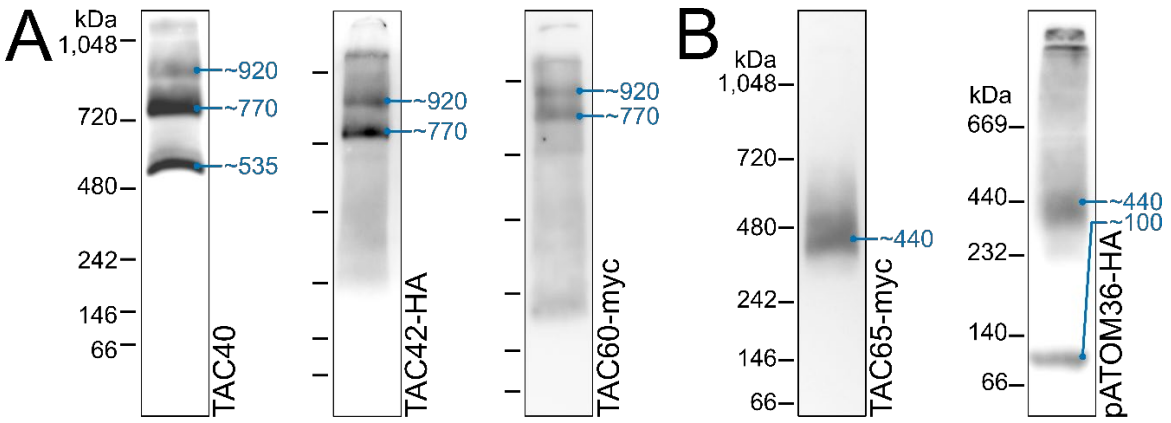

Fig 1: OM TAC module subunits form detergent-soluble subcomplexes.

(A) Immunoblots of BN-PAGE experiments probed for TAC40, TAC42-HA, or TAC60-myc with protein (TAC40) or tag specific (TAC42, TAC60) antibodies. The positions of marker proteins with their size in kDa are indicated on the left of each lane. Based on these markers, the sizes of the detected protein complexes were estimated (blue numbers) (see Material and methods). **(B)** As in (A) but immunoblots were probed for TAC65-myc and pATOM36-HA with tag specific antibodies.

Using a polyclonal antiserum recognizing TAC40, we detected three different TAC40-containing subcomplexes with estimated sizes of ~535, ~770, and ~920 kDa, respectively (Fig 1A, left panel). The bands corresponding to the ~535 and ~770 kDa subcomplexes contained similar amounts of TAC40, whereas the band corresponding to the ~920 kDa subcomplex contained

much less of the protein. To detect the OM TAC module subunits TAC42 and TAC60, we prepared transgenic cell lines expressing C-terminally HA or myc-tagged versions of the proteins (Fig. 1A, middle and right panels). Immunoblot analyses showed that tagged TAC42 and TAC60 were exclusively detected in the ~770 and ~920 kDa TAC40-containing subcomplexes, respectively. The two subcomplexes displayed similar signal intensities when probed for TAC60 whereas the ~920 kDa subcomplex gave a slightly less intense signal relative to the ~770 kDa subcomplex when probed for TAC42.

Thus, our results confirm the previous immunoprecipitations experiments [38] and show that TAC40 is mainly present in three distinct subcomplexes. The lowest one of ~535 kDa consists exclusively of TAC40 whereas the ~770 and ~920 kDa subcomplexes likely in addition contain variable amounts of TAC42 and TAC60.

Reciprocal immunoprecipitations have shown that TAC65 interacts with pATOM36 and vice versa [36]. BN-PAGE analysis of cell lines expressing myc-tagged TAC65 revealed a diffuse TAC65-containing complex of ~440 kDa (Fig. 1B, left panel). An analogous experiment indicated that HA-tagged pATOM36 appears to be present in the same ~440 kDa subcomplex but also in a smaller subcomplex migrating at approximately ~100 kDa (Fig. 1B, right panel). The latter subcomplex was reported previously [36, 48]. The fact that this subcomplex is also detected when pATOM36 is expressed in *S. cerevisiae* shows that it represents the fraction of pATOM36 that functions in OM protein biogenesis [37]. Thus, the ~440 kDa complex, likely consisting of TAC65 and pATOM36, is the one relevant for assembly of the OM TAC module. The signals near the top of the gel represent complexes that accumulate at the stacking gel-separating gel interface.

In summary, our results are in line with previous analyses [36, 38] and show that TAC65 together with pATOM36 is present in a single protein subcomplex of ~440 kDa, whereas pATOM36 in addition forms an ~100 kDa subcomplex.

Depletion of OM TAC module subunits alters subcomplex formation

To investigate the effects of depletion of OM TAC module subunits on subcomplex compositions, we used a combination of RNAi, BN-PAGE, and immunoblot analyses. The left panel of Fig. 2A shows that depletion of either TAC60 or TAC42 prevents the formation of the larger TAC40-containing subcomplexes (~770 and ~920 kDa) and concomitantly causes the accumulation of the smaller ~535 kDa subcomplex containing only TAC40. This suggests that

neither a TAC40/TAC60 nor a TAC40/TAC42 pair can independently form discrete complexes detectable by BN-PAGE in the absence of the third subunit. Similarly, depletion of either TAC40 or TAC60 eliminates the two discrete TAC42-containing subcomplexes (~770 and ~920 kDa) (Fig. 2A, middle panel). Instead, TAC42 is dispersed into a poorly resolved smear representing complexes with a large spread of molecular weights. This indicates that TAC42 alone cannot form defined subcomplexes with either TAC40 or TAC60. Additionally, unlike TAC40, TAC42 does not assemble into a stable oligomeric subcomplex. TAC60 behaves differently: in the absence of TAC42, it forms very large subcomplexes of >1'000 kDa, while after TAC40 depletion, it is found in two discrete groups of subcomplexes of ~320-400 kDa and of ~710-850 kDa, respectively (Fig. 2A, right panel). The composition of these aberrant TAC60-containing subcomplexes remains unknown.

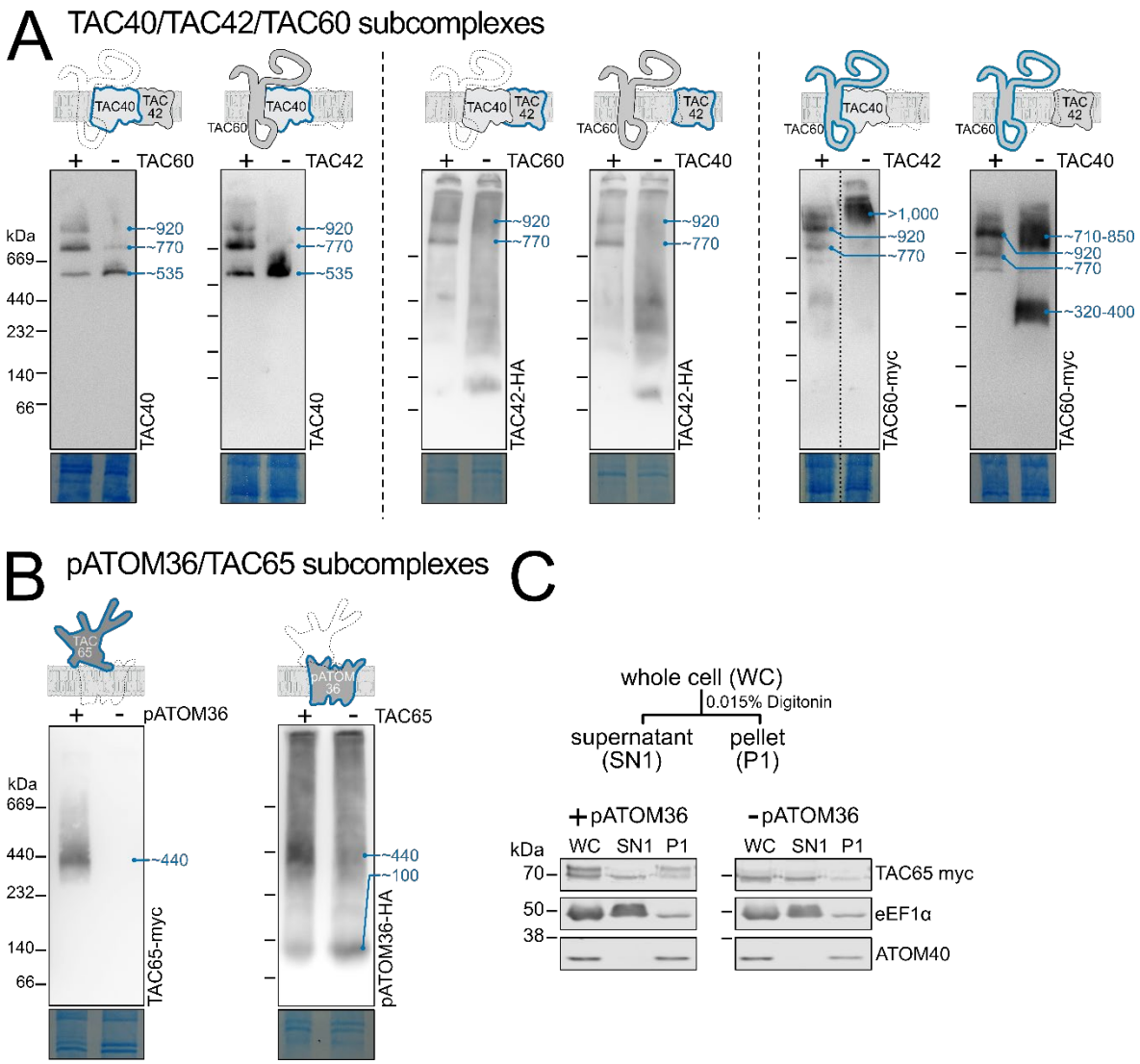

Fig 2: Depletion of OM TAC module subunits alters subcomplex formation.

(A) Left panel: Immunoblots of BN-PAGE gels were probed with a TAC40 antiserum. Inducible RNAi knock down cell lines for TAC60 or TAC42 were analyzed. The approximate sizes in kDa of detected subcomplexes are indicated with blue numbers. Schematics on top indicate which TAC subunits were detected by the immunoblot (blue) and which TAC subunits were the targets of the knockdown (dashed line). Bottom panels show sections of Coomassie blue-stained gels and serve as loading controls. Immunoblots of BN-PAGE gels shown in all following panels and figures are presented in an analogous way. **(B)** as in (A) detected proteins and targets of depletion are indicated. **(C)** Top panel: Scheme depicting the one-step 0.015% digitonin fractionation. Bottom panel: Immunoblots of an SDS-PAGE gel of a one-step digitonin fractionation of cells expressing TAC65-myc in the presence of (left) or depleted for (right) pATOM36. Eukaryotic elongation factor 1 alpha (eEF1α) and the atypical translocase of the outer membrane 40 (ATOM40) serve as cytosolic and mitochondrial markers, respectively.

In summary, our analysis reveals that TAC40, TAC42, and TAC60 form three subcomplexes: one of ~535 kDa consisting of a TAC40 oligomer and two of ~770 and ~920 kDa, respectively, which are likely exclusively composed of various amounts of TAC40, TAC42 and TAC60.

Fig. 2B shows that pATOM36 and TAC65 are both present in a ~440 kDa complex. Depleting either protein causes the dissociation of this complex, suggesting that it consists solely of pATOM36 and TAC65 (Fig. 2B). As expected, the ~100 kDa pATOM36 complex, which functions in OM protein biogenesis, still assembles in the absence of TAC65. However, TAC65 alone does not form a complex, and no monomeric TAC65 signal is detected in crude mitochondrial extracts analyzed by BN-PAGE. The bottom right panel of Fig. 2C further reveals that after pATOM36 depletion, TAC65 levels are drastically reduced in the crude mitochondrial pellet fraction obtained by 0.015% digitonin extraction. This is expected, as TAC65 is a peripheral OM protein without predicted transmembrane domains, and its association with the OM depends on pATOM36. Note: similar to TAC60, TAC65 appears as a double band on denaturing gels [36]. The upper band likely results from an unknown post-translational modification and serves as a marker for proper TAC integration [38] (Fig. 2C, bottom left panel).

The two classes of OM TAC module subcomplexes form independently

As shown above the OM TAC module subunits form two classes of detergent-soluble subcomplexes. The first class consists of a TAC40 oligomer of ~535 kDa and two subcomplexes (~770 and ~920 kDa) that contain various amounts of TAC40, TAC42 and TAC60. The second class includes a ~440 kDa complex composed of pATOM36 and TAC65 as well as the OM protein biogenesis complex of ~100 kDa that contains pATOM36.

According to the hierarchical model of TAC formation, the different TAC subunits are expected to assemble in a strict stepwise manner, beginning at the (pro)basal body and extending toward the kDNA [35]. Based on this model, the more basal body-proximal 440 kDa subcomplex, consisting of pATOM36 and TAC65, should be required for the formation of the three more basal body-distal TAC40-, TAC42- and TAC60-containing subcomplexes (~535 kDa, ~770, ~920 kDa).

However, our results contradict this expectation. Even after depletion of pATOM36 or TAC65, resulting in the absence of the ~440 kDa subcomplex, the TAC40-, TAC42-, and TAC60-containing subcomplexes (~535 kDa, ~770 kDa, and ~920 kDa) still form (Fig. 3A). In addition,

depletion of the TAC40-containing subcomplexes does not disrupt the more basal-body-proximal ~440 kDa subcomplex composed of pATOM36 and TAC65 (Fig. 3B).

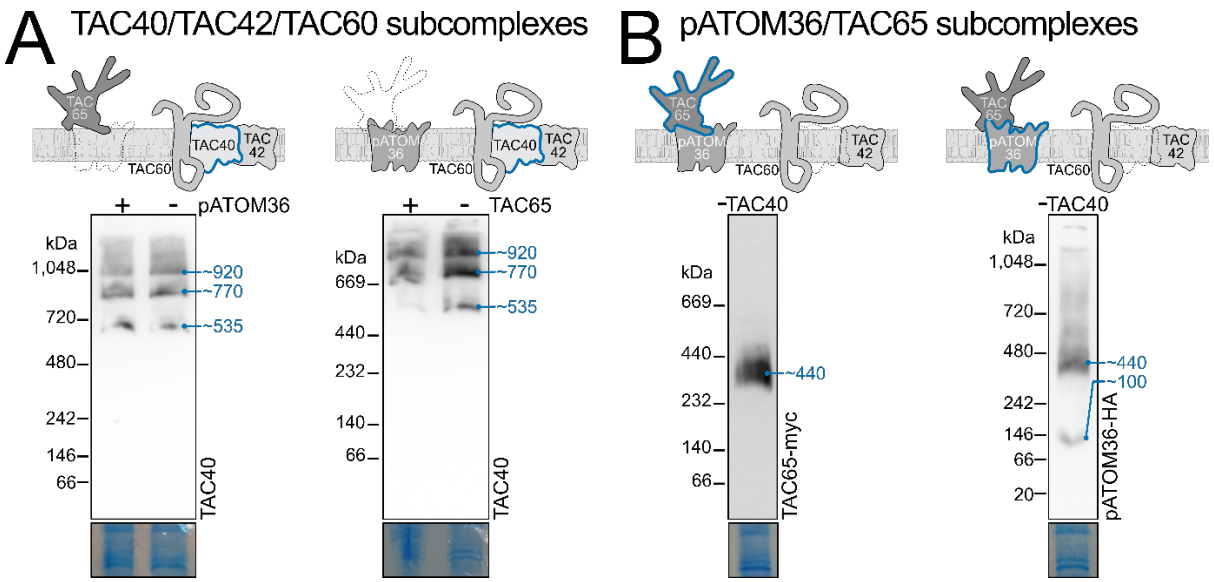

Fig 3: The two classes of OM TAC module subcomplexes form independently.

(A) Immunoblots of BN-PAGE experiments probed for TAC40 of cell lines with inducible pATOM36 (left) or TAC65 (right) knockdown. **(B)** As in (A) but immunoblots of TAC40 depleted cells probed for TAC65-myc (left) and pATOM36-HA (right) with anti-tag antibodies are shown.

These findings are surprising, as previous immunofluorescence analysis has shown that depletion of any of the tested OM TAC module subunits (TAC40, TAC60, TAC65) leads to the dispersion of the entire module [35]. Despite this, the subunits are not degraded, as they remain detectable on denaturing gels [35]. Instead, their dispersal across the OM prevents their detection via immunofluorescence.

TAC OM module subcomplexes form independently of cytosolic and inner TAC modules

The cytosolic and the inner TAC modules are both anchored at the OM TAC module. Thus, we examined the fate of OM TAC subcomplexes upon depletion of either the cytosolic TAC module alone or both the cytosolic and inner TAC modules simultaneously.

In contradiction to the hierarchical assembly model, depletion of the cytosolic TAC module subunit p197, which connects to the OM TAC module subunit TAC65, did not disrupt the

formation of either class of OM TAC module subcomplexes (Fig 4A, left). Instead, the two TAC40-, TAC42-, and TAC60-containing subcomplexes (~770 and ~920 kDa) accumulated in the absence of p197, while the amount of the TAC40 oligomer of ~535 kDa remained constant (Fig. 4A, left panel). Similarly, simultaneous depletion of p197 and p166 led to an accumulation of the largest ~920 kDa TAC40-, TAC42-, and TAC60-containing subcomplex and a concomitant depletion of the small ~535 kDa TAC40 oligomer. The intermediate ~770 kDa subcomplex, however, remained unchanged (Fig 4A, right). - Additionally, p197 depletion resulted in an accumulation of the pATOM36- and TAC65-containing subcomplexes (~440 and ~100 kDa) when compared to wild-type cells (Fig 4B).

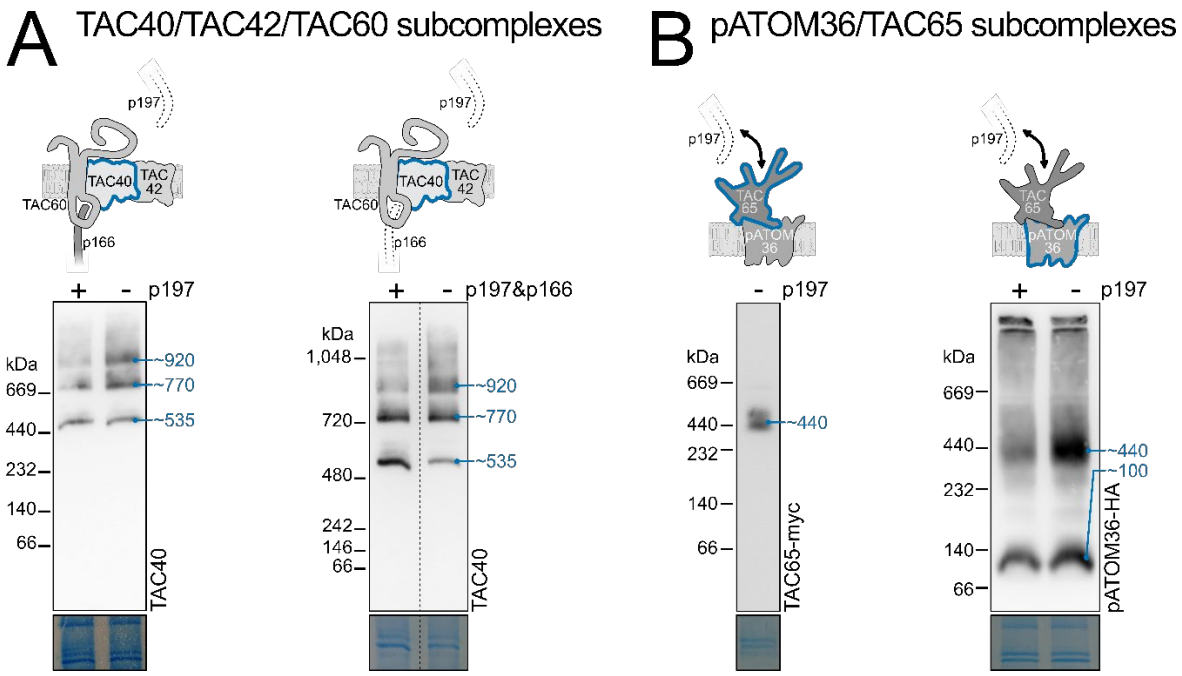

Fig 4: TAC OM module subcomplexes form independently of cytosolic and inner TAC modules.

(A) Immunoblots of BN-PAGE experiments from cells with inducible knockdown of p197 (left), or the simultaneously inducible knockdown of p197 and p166 (right) were probed for TAC40. For confirmation of the knockdowns see S2 Fig. **(B)** as in (A) but immunoblots of a cell line expressing TAC65-myc in an induced p197 knockdown (left) and a cell line expressing pATOM36-HA in an inducible p197 knockdown (right) are shown.

These results suggest that the two classes of detergent-soluble OM TAC module subcomplexes represent distinct assembly intermediates. The observed relative changes in the amounts of the three TAC40-containing subcomplexes (~535, ~770, and ~920 kDa), after p197 and p197/p166 depletion, support a model in which the ~535 kDa TAC40 oligomer assembles first and then sequentially incorporates TAC42 and TAC60 to form the two larger subcomplexes (~770, and

~920 kDa). The accumulation of the largest ~920 kDa TAC40-, TAC42- and TAC60-containing subcomplex, along with the ~440 kDa pATOM36- and TAC65-containing subcomplex, is therefore a direct consequence of the p197 depletion-induced disruption of the cytosolic TAC module, which prevents their integration into the insoluble TAC structure.

Rapid *de novo* formation of TAC40-containing subcomplexes

The *T. brucei* γL262P mutant bloodstream form (BSF), carrying an L262P mutation in the γ -subunit of the ATPase, can grow in the absence of kDNA and does not require the TAC [49]. To investigate TAC assembly, we generated a TAC40 double-knockout γL262P-cell line. While these cells lacked both the OM and inner TAC modules, resulting in the complete loss of kDNA, they exhibited normal growth.

Based on findings in PCFs [35], we expected that other OM TAC module subunits, though delocalized, would still be present within the OM. A limitation of the RNAi analyses shown in Fig 3 and Fig 4 was that small amounts of the targeted proteins, and thus of residual TAC structures that may act as assembly seeds, were still present. However, in the γ L262P TAC40 double-knockout cells, TAC40 and thus the OM and the inner TAC modules were completely absent. Consequently, tetracycline-induced ectopic re-expression of tagged TAC40 in this cell line triggered *de novo* formation of the two modules.

It had previously been shown that TAC subunits are generally expressed at a higher level in BSFs compared to PCF cells [50, 51]. Fig 5 shows that wildtype BSFs of *T. brucei* have three TAC40-containing subcomplexes (~535, ~770 and ~920 kDa). Except for the ~920 kDa band, which appears to have a lower relative intensity, this is identical to what was observed in PCFs (Fig 1B and Fig 2A). Thus, BSFs formed the same TAC40-, TAC42- and TAC60-containing subcomplexes than PCFs. Triggering re-expression of tagged TAC40 in the TAC40-lacking γL262P cell line results in a time-dependent *de novo* formation of the three tagged TAC40-containing subcomplexes with a similar pattern than was observed in wild-type BSFs (Fig 5). The migration of these subcomplexes was slightly slower than in wild-type cells, which was likely because they consisted exclusively of tagged TAC40. All three tagged TAC40-containing complexes were already detected after four hours, indicating that their de novo formation was rapid. Moreover, their relative amounts remained the same over time. This is expected because unlike in the experiments shown in Fig. 4, p197 was still expressed in the γ L262P cells, which allowed continuous integration of the newly formed ~920 kDa TAC-containing subcomplex into the insoluble TAC structure.

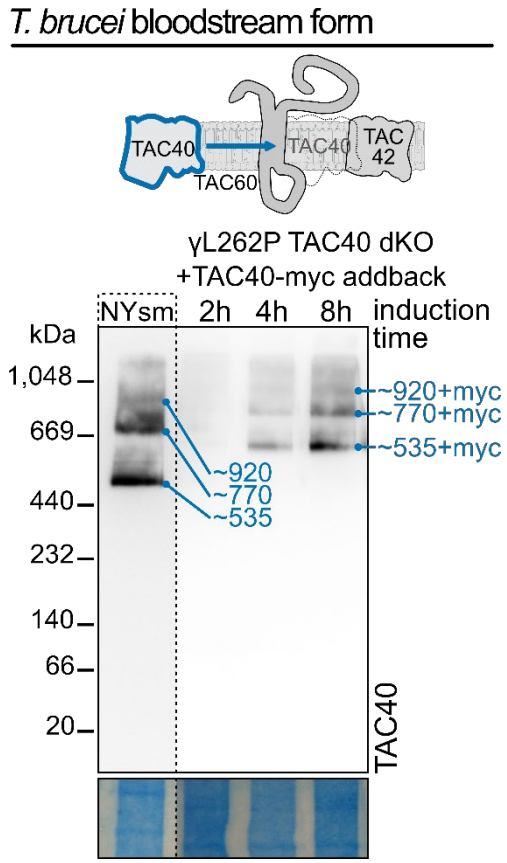

Fig 5: Rapid de novo formation of TAC40-containing subcomplexes.

Immunoblot of a BN-PAGE gel from experiments with BSF *T. brucei* cells probed for TAC40. The left lane shows the detergent-soluble TAC40-containing subcomplexes in wildtype NYsm cells. The three lanes on the right show detergent-soluble complexes extracted from a TAC40 dKO γL262P BSF cell line induced for TAC40-myc addback expression for 2, 4, and 8 hours. The scheme (top) visualizes the conditional addback expression of TAC40 and complex formation with TAC42 and TAC60. For additional controls of this cell line see S3 Fig.

The TAC60 N-terminus is essential for the integrity of the OM TAC module

TAC60 has two α-helical transmembrane domains and both its N- and C-termini face the cytosol [38]. The short IMS-exposed loop contains the binding site for the C-terminus of p166, the only integral IM TAC subunit of the inner TAC module [40, 41]. Previous *in vivo* deletion studies revealed that a tagged TAC60 variant lacking the cytosolic C-terminal 283 aa (TAC60-ΔC283-myc) remained functional. However, a TAC60 variant lacking both the N- and C-terminal domains (TAC60-ΔN97ΔC283-myc) was non-functional despite showing TAC localization [38].

To study the subcomplexes formed by these truncated TAC60 variants, we used previously established RNAi cell lines allowing tetracycline-inducible replacement of full length TAC60 by TAC60-Δ283-myc or TAC60-ΔN97ΔC28-myc, respectively. BN-PAGE analyses showed that TAC60-ΔC283-myc and TAC60-ΔN97ΔC283-myc formed two subcomplexes each (Fig 6A),

similar to full-length TAC60. However, as expected, their estimated molecular weights (~735/815 kDa and ~670/750 kDa, respectively) were lower than those formed by full-length TAC60 (~770/920 kDa). Moreover, while the abundance of TAC60-ΔC283-myc is similar in both bands, the band corresponding to the larger subcomplex formed by TAC60-ΔN97ΔC283-myc (750 kDa) was much more intense, suggesting accumulation of a non-productive assembly intermediate.

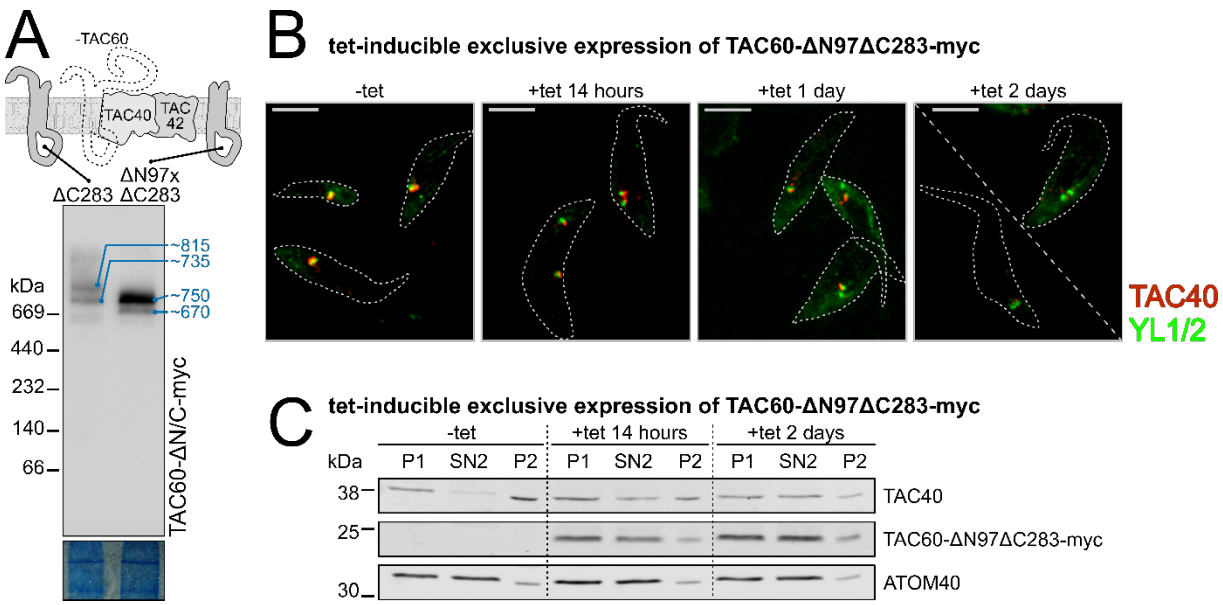

Fig 6: The TAC60 N-terminus is essential for the integrity of the OM TAC module.

(A) Immunoblot of a BN-PAGE experiment of cells expressing the TAC60 truncation variants TAC60-ΔC283-myc and TAC60-ΔN97ΔC283-myc under TAC60 knockdown probed for the TAC60 variants. The scheme at the top depicts the truncated TAC60 variants. **(B)** Immunofluorescence microscopy images of cytoskeletons isolated at indicated time points after tetracycline (tet)-induction of the TAC60-ΔN97ΔC283-myc exclusive expressor cell line. TAC40 (red) and tyrosinated α-tubulin which stains basal bodies (YL1/2, green) were detected using specific antisera. Scale bar: 5 µm. **(C)** Immunoblot of an SDS-PAGE gel of an experiment performed with the identical cell line as in (B) induced for the indicated time with tetracycline. Samples of the organellar fraction (P1), the soluble organellar fraction (SN2) and the insoluble organellar fraction (P2) were collected as described in the Material and methods. TAC40 and TAC60-ΔN97ΔC283-myc were detected using a anti TAC40 antiserum and a myc specific antibody, respectively. ATOM40 serves as a marker for the soluble organellar fraction.

To confirm these findings, we monitored the morphology of the OM TAC module in the cell line allowing for tetracycline-inducible exclusive expression of TAC60-ΔN97ΔC28-myc. Immunofluorescence analysis of this cell line showed a progressive TAC40 delocalization from newly formed basal bodies, culminating in a complete mislocalization after two days of

induction (Fig 6B). The same cells were also analyzed biochemically. In uninduced cells, the majority of TAC40 is integrated into the detergent-resistant insoluble TAC structure recovered in the pellet fractions after a two-step (0.015 and 1%) digitonin fractionation (Fig 6C, P1 and P2). However, in line with the microscopy results, the TAC40 signal shifted from the P2 to the SN2 fraction, indicating that after exclusive expression of TAC60-ΔN97ΔC28-myc much of TAC40 became detergent-soluble. Moreover, also TAC60-ΔN97ΔC28-myc was mostly detergent soluble.

We conclude that despite forming assembly intermediates with TAC40 and TAC42, TAC60-ΔN97ΔC283-myc failed to integrate into the detergent-insoluble TAC structure, blocking the formation of a functional TAC. Since the C-terminus of TAC60 is dispensable for protein function, these findings demonstrate the essential role of the N-terminus of TAC60 (1-97 aa) for OM TAC module assembly, possibly by facilitating interactions with the pATOM36- and TAC65-containing subcomplex.

Predicted structure of the TAC40 oligomer

TAC40 independently forms a stable ~535 kDa subcomplex, detectable as a sharp band on BN-PAGE. It also serves as the core subunit of two larger assembly subcomplexes (~770 and ~920 kDa) that incorporate TAC42 and TAC60. Notably, TAC42 and TAC60 cannot form detectable subcomplexes on their own and instead must assemble onto the preexisting TAC40-only complex.

The existence of the TAC40 oligomer is strongly supported by the results shown in Fig 1 and Fig 2. Moreover, BN-PAGE analysis of an anti-HA pulldown experiment, performed on extracts from a TAC42-depleted cell line expressing both untagged and HA-tagged TAC40 alleles, exclusively recovered the ~535 kDa TAC40 oligomer under native elution conditions (Fig 7A). Finally, when analyzed by denaturing SDS-PAGE both HA-tagged and wild-type TAC40 are detected, confirming that TAC40 molecules interact with each other within this complex (Fig 7B).

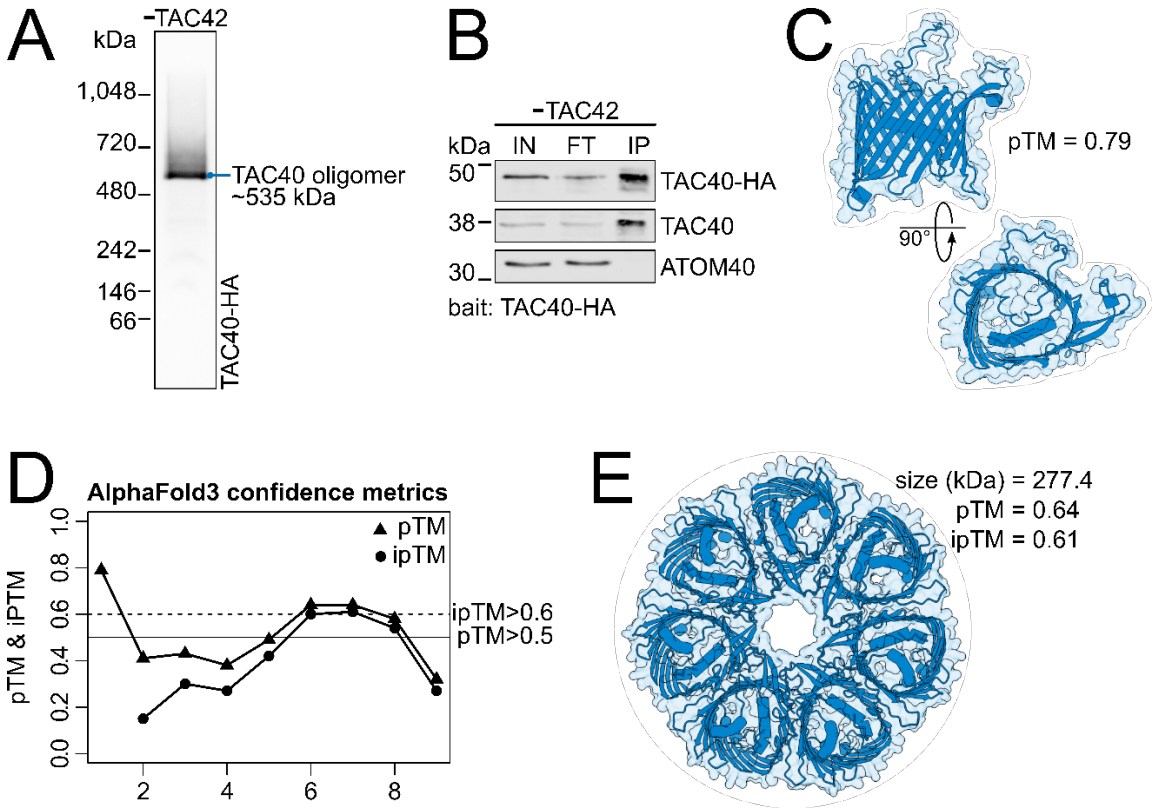

Figure 7: Predicted structure of the TAC40 oligomer.

(A) BN-PAGE immunoblot probed for TAC40-HA of the TAC40-HA oligomer-containing eluate of an HA-pulldown experiment. The TAC40-HA oligomer was pulled down from the extract of a cell line depleted for TAC42 that expressed one HA-tagged TAC40 allele. **(B)** Fractions of the same HA-pulldown experiment shown in (A) were analyzed by an SDS-PAGE immunoblot and probed for TAC40-HA, TAC40, and ATOM40. IN: input (digitonin-solubilized mitochondria enriched fraction) $5x10^6$ cell equivalents; FT: Flow through, $5x10^6$ cell equivalents; IP: eluate, $1x10^8$ cell equivalents. ATOM40 serves as a negative control. **(C)** AlphaFold3 predicted structure model of the TAC40 monomer. The model of the predicted structure is shown from the side (top) and from IMS side (bottom). pTM: predicted template modelling score. **(D)** Graph showing the pTM and the interference pTM (ipTM) scores of AlphaFold3 predicted structures of complexes formed by TAC40 containing 1-9 monomers. Threshold lines for the pTM (>0.5) and ipTM (>0.6) are indicated with a solid and dashed line, respectively. **(E)** Top view of an Alphafold3 predicted structure model of the heptameric TAC40 complex.

To determine the number and arrangement of TAC40 molecules within the ~535 kDa oligomer, we performed an *in silico* analysis using AlphaFold3 [52]. The predicted template modeling score (pTM) for a single TAC40 molecule was 0.79, indicating a highly accurate prediction of its structure (Fig 7C). Since AlphaFold3 can also predict protein complexes, we modeled TAC40 oligomers containing 1 to 9 TAC40 molecules (Fig 7D). In the resulting predictions, TAC40 molecules consistently formed symmetrical ring-like structures. In all cases, the proteins maintained a consistent topology in a planar arrangement, in line with their integral membrane localization.

The most confident structural prediction was obtained for the TAC40 heptamer, which had a pTM score of 0.64 and an interface pTM (ipTM) score of 0.61 (Fig 7E). The hexamer and octamer showed slightly lower scores, while other oligomeric states were predicted with low confidence only.

Discussion

The fully assembled TAC is a very large, permanent structure that is insoluble in non-ionic detergents [32, 41, 42]. However, subunits of the OM TAC module are not only present in the final TAC structure but are also recovered in two groups of detergent-soluble subcomplexes. The first group consists of three subcomplexes of ~535, ~770, and ~920 kDa that contain variable amounts of TAC40, TAC42 and TAC60, whereas the second group consists of a ~440 kDa subcomplex formed by pATOM36 and TAC65 (Fig 1 and Fig 2).

AlphaFold3 predicts with high confidence (pTM/ipTM scores > 0.6) that the ~535 kDa subcomplex of the first group consists of an oligomer containing 6 to 8 molecules of TAC40 that are arranged in a planar ring (Fig 7DE). This prediction is consistent with the BN-PAGE and immunoblots analyses which showed a sharp band of ~535 kDa that contained TAC40 but neither TAC42 nor TAC60. Moreover, it also fits with the known integral membrane localization of TAC40 and could explain how it can assembly into such a well-defined subcomplex. However, the molecular weight of the TAC40 subcomplex of ~535 kDa, as determined by BN-PAGE, is much higher than the calculated 240-320 kDa for the TAC40 hexa- to octamer. A possible explanation for this discrepancy is that the TAC40 oligomer forms a planar ring with a central cavity rather than a globular complex, leading to aberrant migration on BN-PAGE. Additionally, the TAC oligomer is membrane-embedded and solubilized by detergents which likely causes a shift towards a higher molecular weight on a BN-PAGE.

TAC40 is a kinetoplastid-specific β-barrel protein that belongs to the VDAC-like protein family [39]. It has been reported that mammalian VDAC is present in a dynamic equilibrium between dimers and oligomers [53, 54]. The function of these VDAC oligomers appear to be connected to apoptosis-related cytochrome c release from the IMS [54]. Moreover, in oxidatively stressed mitochondria VDAC1 oligomers have been implicated in the release of short mtDNA fragments to the cytosol where they cause inflammation [53]. It is therefore not surprising that TAC40 also appears to oligomerize. However, whereas mammalian VDAC oligomers are stress-induced and form large pores in the OM, the trypanosomal TAC40 is present exclusively in the oligomeric

form and its function is restricted to the organization of the TAC architecture, which to our knowledge does not require pore formation. This is evidenced by the fact that TAC40 is dispensable in the γL262P cell line, that can grow in the absence of kDNA [49] (Fig 5 and S4 Fig).

Six lines of evidence suggest that the three TAC40-containing subcomplexes (~535, ~770, ~920 kDa), as well as the subcomplex consisting of pATOM36 and TAC65 (~440 kDa), are assembly intermediates of the OM TAC module:

(i) Unlike in the fully assembled TAC, the OM TAC module subunits are detergent-soluble when present in the four subcomplexes (Fig 1).

(ii) The smallest subcomplex (~535 kDa) has the simplest composition consisting of TAC40-only, whereas the two larger subcomplexes (~770, ~920 kDa) in addition to TAC40 also contain TAC42 and TAC60 (Fig 2A).

(iii) Neither TAC42 nor TAC60 form subcomplexes on their own, or with each other, suggesting that TAC42 and TAC60 are incorporated into the preexisting TAC40-only subcomplex (Fig 2A).

(iv) The four subcomplexes (~535, ~770, ~920 and ~440 kDa) form independently of the cytosolic and the inner TAC modules (Fig 4).

(v) Depletion of p197 results in the accumulation of the two higher TAC40-containing subcomplexes (~770, ~920 kDa), likely because the 920 kDa subcomplex cannot be properly linked to the nascent TAC structure. The pATOM36- and TAC65-containing subcomplex (~440 kDa) likely accumulates for the same reason (Fig 4).

(vi) Deleting the N-terminal 97 aa of TAC60, which prevent its incorporation into the nascent TAC structure [38] - similar to what was observed after depletion of p197 (Fig 4) - causes a massive accumulation of the largest TAC40-, TAC42- and TAC60-containing subcomplex (corresponding to 920 kDa in wild-type cells) (Fig 6A).

Based on these results we propose the following working model for the assembly pathway of the OM TAC module.
In the first step, TAC40 is inserted into the OM mediated by the ATOM complex and by the β-barrel protein insertion pore Sam50 [39, 55]. TAC40 then oligomerizes into a ring-like structure likely composed of 6-8 molecules, forming a platform that provides binding sites for TAC42 and TAC60 (Fig 8A).

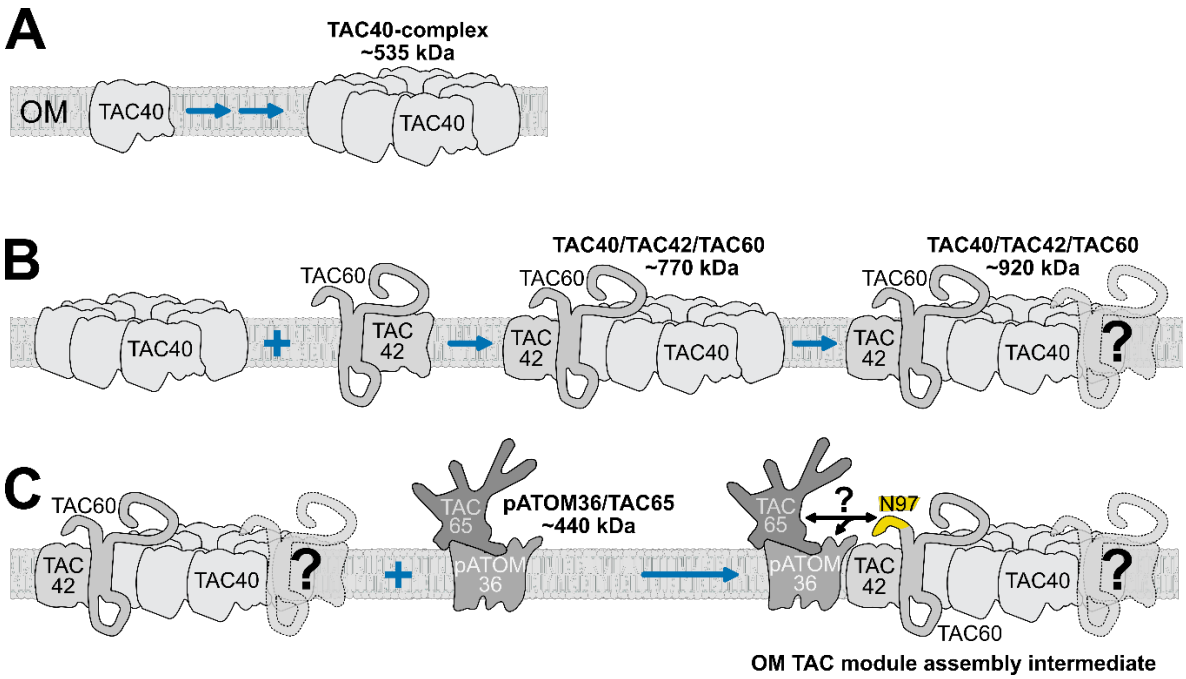

Figure 8: Assembly model of the OM TAC module.

(A) Oligomerization of TAC40 into a ~535 kDa TAC40 subcomplex. OM: mitochondrial outer membrane**. (B)** The TAC40 oligomer binds to either a dimer or monomers of TAC42 and TAC60 forming the ~770 kDa and subsequently the ~920 kDa TAC40/TAC42/TAC60 subcomplex. **(C)** The ~920 kDa TAC40/TAC42/TAC60 subcomplex interacts with pATOM36/TAC65 subcomplex (~440 kDa) resulting in a putative OM TAC modules assembly intermediate.

In the second step, TAC42 and TAC60 associate with the preformed TAC40 oligomer in two stages, forming first the ~770 and subsequently the ~920 kDa subcomplexes (Fig 8B). The two proteins may be incorporated individually or as a dimer. The existence of a TAC42-TAC60 dimer is predicted by AlphaFold3 with good confidence (pTM = 0.42, ipTM = 0.68) (S4A Fig). Moreover, consistent with our working model, AlphaFold3 predictions using seven TAC40 molecules and one or two TAC42-TAC60 pairs as templates generate structures that potentially correspond to two subcomplexes with pTM/ipTM scores > 0.36 (S4BC Fig). These structures appear plausible, as the two transmembrane domains of TAC60 align within the OM plane with the correct topology ($N_{Cytoslic}$, $C_{Cytosolic}$) relative to the β-barrel proteins TAC40 (N_{IMS}, C_{IMS}) and TAC42 (N_{IMS}, C_{IMS}).

Much of the third step remains speculative. Since TAC65 interacts with p197 [32], the ~440 kDa subcomplex containing pATOM36 and TAC65 should be able to interact with the cytosolic TAC module subunit p197 on its own. However, TAC65 fails to assemble into the TAC after depletion of either TAC40 or TAC60 [35]. While the molecular mechanism underlying the crosstalk between the two subcomplex classes remains unclear the N-terminal 97 aa of TAC60 are essential for the formation of the TAC OM module (Fig 6BC). This suggests that merging of the

~920 kDa subcomplex (TAC40, TAC42, TAC60) with the ~440 kDa complex (pATOM36, TAC65) (Fig 8C) is a prerequisite for linking the OM TAC module to p197 and, consequently, to the cytosolic TAC module. Notably, the complex corresponding to the fully assembled OM TAC module assembly intermediate could not be detected by BN PAGE, likely due to its transient nature and/or instability in digitonin.

After its integration in the nascent TAC structure the OM TAC module interacts with the matrix-localized p166 via TAC60. If the fully formed OM TAC module is considered as a single unit, formation of the TAC follows the hierarchical assembly model, which implies a strict sequential assembly of TAC subunits from the (pro)basal body to the kDNA [35]. However, formation of the OM TAC module itself is independent of the cytosolic and the inner TAC modules. It follows a unique pathway involving at least four membrane-embedded subcomplexes. The first one consists of the TAC40 oligomer, two further subcomplexes are formed by adding various amounts of TAC42 and TAC60 to the oligomer. Subsequently, the largest of TAC40-containing subcomplex merges with the separately formed pATOM36- and TAC65-containing subcomplex forming the fully assembled OM TAC module.

It is not surprising that the assembly of the OM TAC module is so complicated, since with five different subunits it is the most intricate of all three TAC modules. Moreover, except for TAC65, all of its subunits are integral membrane proteins that need to be inserted into the OM, a process mediated by at least two different insertases: the ATOM complex and Sam50 [14].

It is important to acknowledge the limitations of our assembly model. While the composition of various assembly subcomplexes is known, the stoichiometry of their subunits remains to be determined. The proposed TAC40 oligomer structure is predicted by AlphaFold with high confidence and supported by experimental evidence. However, the same confidence does not extend to the predicted structures of the other subcomplexes. A deeper understanding of the OM TAC module assembly pathway will require experimental determination of the atomic structure of its subcomplexes, which is beyond the scope of this study. Despite these limitations, our model provides a valuable framework that can guide future experiments aimed at elucidating the assembly pathway of the TAC structure, the unique mitochondrial genome segregation system of trypanosomes.

Material and Methods

Transgenic cell lines

Procyclic cell lines are based on the *T. brucei* 29-13 [56] and a single marker *T. brucei* 427 strain [32] and were grown at 27°C in SDM-79 supplemented with 10% or 5% (v/v) fetal calf serum, respectively. BSF cell lines are based on the NYsm strain [56] or on the γL262P variant [49] and were cultivated in HMI-9 containing 10% (v/v) fetal calf serum at 37°C in a 5% (v/v) CO_2 atmosphere. RNAi cell lines of the TAC proteins used in the study were created using modified pLEW100 vectors [56] which contain stem loops allowing the expression of double stranded RNAs corresponding to open reading frames (ORF) or to the 3' untranslated regions (UTR) of the target mRNAs, respectively. An overview of all used cell lines is given in Table 1. The p166/p197 double RNAi cell line was produced by the stable transfection of a p197 3'UTR RNAi cell line [32] with a p166 3'UTR RNAi stem loop vector [41].

C-terminal *in situ* 3xHA tags for TAC40, TAC42, and pATOM36 were introduced using PCR products amplified from vectors of the pMOtag series [57]. Transfection of these PCR products allowed the tagging of one of the endogenous alleles (Table 1).

C-terminally tagged variants of TAC65 as well as the wild type TAC60 and truncated variants thereof were expressed under tetracycline control from ectopic genes. The constructs used for stable transfection are based on modified pLEW100 vectors [56] and have been used before (Table 1).

To generate a double allele knockout of TAC40 in the γL262P cell line, 500 base pairs of 5' and 3' flanking regions of TAC40 were cloned upstream and downstream of the resistance cassettes of vectors of the pMOtag series [57]. This way, a blasticidine and a phleomycine resistance gene were used to produce a single and double allele knockout of TAC40, respectively. For inducible addback expression, we used a modified pLEW100 vector [56] allowing the stable integration into the rDNA locus of a TAC40 gene with a C-terminal 3x myc tag whose expression is regulated by tetracycline [39].

Description	Parental cell line	Additional information	Reference	Figure
TAC42 3x HA		C-term 3x HA (*in situ*, single allele)	Cell line: [38]	1A middle
TAC60 3x myc		C-term 3x myc (ectopic allele)	Cell line: [38]	1A right, 2A right
TAC65 3x myc		C-term 3x myc (ectopic allele)	Cell line: [36]	1B left, 2B left, 2C left
pATOM36 3x HA		C-term 3x HA (*in situ*, single allele)	Cell line: [36]	1B right
TAC60 ORF RNAi			Cell line: [38]	2A left
TAC42 ORF RNAi			Cell line: [38]	2A left
TAC42 3x HA x TAC60 ORF RNAi	TAC60 ORF RNAi [38]	C-term 3x HA (*in situ*, single allele) (PCR based, [38])	This study	2A middle
TAC42 3x HA x TAC40 ORF RNAi	TAC40 ORF RNAi [39]	C-term 3x HA (*in situ*, single allele) (PCR based, [38])	This study	2A middle
TAC60 3x myc x TAC42 ORF RNAi	TAC42 ORF RNAi [38]	C-term 3x myc (ectopic allele) [38]	This study	2A right
TAC60 3x myc x TAC40 ORF RNAi	TAC40 ORF RNAi [39]	C-term 3x myc (ectopic allele) [38]	This study	2A right
TAC65 3x myc x pATOM36 ORF RNAi	pATOM36 ORF RNAi [48]	C-term 3x myc (ectopic allele) [36]	This study	2B left, 2C right
pATOM36 3x HA x TAC65 ORF RNAi	TAC65 ORF RNAi [36]	C-term 3x HA (*in situ*, single allele) (PCR based, [48])	This study	2B right
pATOM36 ORF RNAi			Cell line: [48]	3A left
TAC65 ORF RNAi			Cell line: [36]	3A right
TAC65 3x myc x TAC40 ORF RNAi	TAC40 ORF RNAi [39]	C-term 3x myc (ectopic allele) [36]	This study	3B left
pATOM36 3x HA x TAC40 ORF RNAi	TAC40 ORF RNAi [39]	C-term 3x HA (*in situ*, single allele) (PCR based, [48])	This study	3B right
p197 3'UTR RNAi			Cell line: [32]	4A left
p197 3'UTR RNAi x p166 3'UTR RNAi	p197 3'UTR RNAi [32]	2nd RNAi: p166 3'UTR RNAi (Vector: [41])	This study	4A right
TAC65 3x myc x p197 3'UTR RNAi	p197 3'UTR RNAi [32]	C-term 3x myc (ectopic allele) [36]	This study	4B left
pATOM36 3x HA x p197 3'UTR RNAi	p197 3'UTR RNAi [32]	C-term 3x HA (*in situ*, single allele) (PCR based, [48])	This study	4B right
Bloodstream form NYsm			Cell line: [56]	5
γL262P mutant bloodstream form			Cell line: [49]	S3
Bloodstream form TAC40 dKO x TAC40 3x myc	γL262P mutant bloodstream form [49]	C-term 3x myc (ectopic allele) [38]	This study	5, S3
TAC60-ΔC283 3x myc x TAC60 ORF RNAi			Cell line: [38]	6A
TAC60-ΔN97ΔC283 3x myc x TAC60 ORF RNAi			Cell line: [38]	6A, 6B, 6C
TAC40 3x HA x TAC42 ORF RNAi	TAC42 ORF RNAi [38]	C-term 3x HA (*in situ*, single allele) (PCR based, [39])	This study	7A, 7B

Table 1: Summary of transgenic *T. brucei* cell lines used in this study.

Cell fractionation

One or two step digitonin extractions were used to isolate mitochondria-enriched fractions and to prepare solubilized mitochondrial extracts, respectively [32]. To study the subcellular localization of TAC65 (Fig 2C), $5x10^7$ cells were collected and washed twice in PBS (137 mM NaCl, 2.7 mM KCl, 10 mM Na_2HPO_4, and 1.8 mM KH_2PO_4, pH 7.4). After resuspension in 0.25 ml of SoTE buffer (20 mM Tris HCl pH 7.5, 0.6 M sorbitol, 2 mM ethylenediaminetetraacetic acid (EDTA), 1x cOmplete, Mini, EDTA-free protease-inhibitor-cocktail (Roche)) 0.25 ml of SoTE containing 0.03% (w/v) digitonin was added at room temperature. After a 10 min incubation on ice, a mitochondria-enriched pellet (P1) was separated from the cytosolic fraction (SN1) by centrifugation (6'700 g, 5 minutes, 4°C).

For BN-PAGE analysis the P1 fraction of a digitonin extraction corresponding to 10^8 cell equivalents was resuspended in 100 µl 20 mM Tris HCl pH 7.4, 100 mM NaCl, 10% glycerol, 0.1 mM EDTA, 1% (w/v) digitonin and 1x of cOmplete protease-inhibitor-cocktail. The sample was kept on ice for 15 minutes before the final centrifugation (20'000 g, 15 minutes, 4°C) resulting in the SN2 fraction containing solubilized mitochondria and the P2 pellet.

BN-PAGE

BN-PAGE was used to study native protein complexes. 90 µl of the SN2 supernatant of the two-step digitonin extraction (see above) was mixed with 10 µl 10x loading dye (300 µM Coomassie brilliant blue G-250 (Sigma), 500 mM 6-amino n-caproic acid, 100 mM Bis-Tris pH 7.0) and protein complexes were separated on 4-13% (or in Fig 4A, right panel 4-10%) polyacrylamide gradient gels. For immunoblotting. gels were incubated for 5 minutes in 25 mM Tris, 190 mM glycine, 1 mM EDTA, 0.05% sodium dodecyl sulfate (SDS) and subsequently electrophoretically transferred in 20 mM Tris, 150 mM glycine, 0.02% SDS, 20% methanol onto polyvinylidene fluoride membranes (Immobilon-FL).

Proteins of interest were detected by protein-specific or tag-specific primary antibodies followed by horseradish peroxidase (HRP)-coupled secondary antibodies (see below). Finally, the SuperSignal™ West Pico Plus and Femto chemiluminescent substrate detection kits (Thermo Fisher Scientific) were used for image acquisition.

Subcomplex size estimation on BN-PAGE gels

Migration distances of marker proteins on BN-PAGE gels used in this study revealed a very strong correlation (Pearson's r > 0.99) between the relative migration distances (defined as distance between the upper edge of the gel and the band of interest, relative to the distance between the upper edge of the gel and the lowest molecular weight marker) and the square root (sqrt) of the protein weight in kDa (S5 Fig). The estimated molecular weights of the TAC subcomplexes presented here were calculated by linear models based on marker protein migration patterns. All models and their coefficients of determination are shown in S5 Fig.

RNA extraction and reverse transcription PCR

To determine RNAi efficiency in the p166/p197 double RNAi cell line, total RNA of uninduced and two days tetracycline-induced cells was extracted using guanidinium thiocyanate-phenol-chloroform and dissolved in milli-Q water as described in [58]. Total RNA extracts were first treated with DNase to remove the genomic DNA (DNA-free Kit, Ambion). For the reverse transcription, first-strand cDNA synthesis was performed using oligo(dT)20 primers (SuperScript First Strand, Invitrogen). Control reactions without reverse transcriptase were performed simultaneously. Quantitative PCR was done with identical amounts of each cDNA sample and with primer pairs for the amplification of a α-tubulin segment (ORF nt 546-1'249) using primers described in [32], the p197 3'UTR, primer as in [32] and a p166 segment (ORF 3'601-4'189; forward: CAGAAAGCGGTAGAGCACTTTGC; reverse: GCACAGGCGACAATACTTGAACC). PCR products were separated on a 1% agarose gel and stained with ethidium bromide.

Immunofluorescence microscopy

10^6 cells of an exponentially growing cell culture were harvested by centrifugation (2'700 g, 1 minute, room temperature) and washed with PBS. The cells were resuspended in 50 µl PBS and distributed on glass slides where they were allowed to settle before lysis for 30 seconds using PBS containing 0.2% Triton X-100. Following cell lysis, the samples were washed with PBS and fixed in 4% paraformaldehyde for 10 minutes. Fixed samples were washed with PBS and blocked with PBS containing 2% (w/v) bovine serum albumin (BSA) before incubation with two rounds of the corresponding primary and secondary antibodies diluted in PBS containing 2% BSA. For more information on the antibodies used see below. After antibody incubation, slides

were washed with PBS, air-dried, and mounted with Vectashield containing 4',6-diamidine-2-phenylindole dihydrochloride (DAPI) (Vectorlabs). The slides were imaged on a DMI6000B microscope equipped with a DFC360 FX monochrome camera and LAS X software (Leica Microsystems). Images were processed using Fiji software.

Immunoprecipitations

For immunoprecipitation purification of TAC40-HA complexes, 3 x 10^8 exponentially growing cells were harvested and washed twice with PBS. Cells were subjected to a two-step digitonin cell fractionation as described above. The SN2 fraction was incubated with an anti-HA affinity matrix (Roche) for 2 hours at 4°C. Beads were washed five times with a wash buffer (20 mM Tris HCl pH 7.4, 100 mM NaCl, 10% glycerol, 0.1 mM EDTA, and 0.1% (w/v) digitonin). Bound proteins and protein complexes were eluted under native conditions with elution buffer (20 mM Tris HCl pH 7.4, 100 mM NaCl, 25 mM KCl, and 0.1 mM EDTA containing 0.25% (w/v) digitonin and 1mg/ml HA peptide (Sigma)) at 30°C for 15 minutes and further analysed by BN-PAGE. Alternatively, elution was done under denaturing conditions with SDS-PAGE sample buffer without β-mercaptoethanol for SDS-PAGE analysis.

Antibodies

Dilutions used for immunoblot (IB) and immunofluorescence (IF) analyses are indicated in brackets. The polyclonal rabbit antisera against TAC40 (IB 1:100, IF 1:50) and ATOM40 (IB 1:10’000) were described before [32] [59]. The monoclonal rat anti-YL1/2 antibody (IF 1:1’000) that recognizes tyrosinated α-tubulin [60] and the basal body protein TbRP2 [61] was a kind gift from Keith Gull. Commercially available antibodies were used as follows: monoclonal mouse anti-myc antibody (Invitrogen, 132500; IB 1:2’000), monoclonal mouse anti-HA antibody (Sigma, H9658; IB 1:5’000), monoclonal mouse anti-eEF1α antibody (Merck Millipore, 05–235; WB 1:10’000).

Secondary antibodies used for SDS-PAGE immunoblot analyses were IRDye 680LT goat anti-mouse (LI-COR Biosciences, 926-68020; IB 1:20,000) and IRDye 800CW goat anti-rabbit (LI-COR Biosciences, 926-32211; IB 1:20’000), and secondary antibodies used for BN-PAGE immunoblot analyses were HRP-coupled goat anti-mouse antibodies (Sigma, 12-349; IB 1:5’000) as well as goat anti-rabbit antibodies (Sigma, AP307P; IB 1:5’000). Secondary antibodies used for immunofluorescence analyses were goat anti-rat Alexa Fluor 488 (Thermo Fisher Scientific, A-Z1006; IF 1:1’000), goat anti-rabbit Alexa Fluor 596 (Thermo Fisher Scientific, A-11012; IF 1:1’000).

References

1. Gustafsson, C.M., M. Falkenberg, and N.G. Larsson, *Maintenance and Expression of Mammalian Mitochondrial DNA*. Annu Rev Biochem, 2016. **85**: p. 133-60.
2. Kraus, F., et al., *Function and regulation of the divisome for mitochondrial fission*. Nature, 2021. **590**(7844): p. 57-66.
3. Westermann, B., *Mitochondrial inheritance in yeast*. Biochim Biophys Acta, 2013.
4. Burki, F., et al., *The New Tree of Eukaryotes*. Trends in Ecology & Evolution, 2020/01/01. **35**(1).
5. Adebayo, M., et al., *Mitochondrial fusion and fission: The fine-tune balance for cellular homeostasis*. The FASEB Journal, 2021/06/01. **35**(6).
6. Bliek, A.M.v.d., Q. Shen, and S. Kawajiri, *Mechanisms of Mitochondrial Fission and Fusion*. Cold Spring Harbor Perspectives in Biology, 2013-06-01. **5**(6).
7. Labbe, K., A. Murley, and J. Nunnari, *Determinants and functions of mitochondrial behavior*. Annu Rev Cell Dev Biol, 2014. **30**: p. 357-91.
8. Bogenhagen, D.F., *Mitochondrial DNA nucleoid structure*. Biochimica et Biophysica Acta (BBA) - Gene Regulatory Mechanisms, 2012/09/01. **1819**(9-10).
9. Bonekamp, N.A. and N.G. Larsson, *SnapShot: Mitochondrial Nucleoid*. Cell, 2018. **172**(1-2): p. 388-388 e1.
10. Qin, J., et al., *ER-mitochondria contacts promote mtDNA nucleoids active transportation via mitochondrial dynamic tubulation*. Nat Commun, 2020. **11**(1): p. 4471.
11. Miyakawa, I., *Organization and dynamics of yeast mitochondrial nucleoids*. Proc Jpn Acad Ser B Phys Biol Sci, 2017. **93**(5): p. 339-359.
12. Lewis, S.C., L.F. Uchiyama, and J. Nunnari, *ER-mitochondria contacts couple mtDNA synthesis with mitochondrial division in human cells*. Science, 2016. **353**(6296): p. aaf5549.
13. Lukeš, J., et al., *Trypanosomes as a magnifying glass for cell and molecular biology*. Trends in Parasitology, 2023/11/01. **39**(11).
14. Harsman, A. and A. Schneider, *Mitochondrial protein import in trypanosomes: Expect the unexpected*. Traffic, 2017. **18**(2): p. 96-109.
15. Schneider, A., *Evolution of mitochondrial protein import - lessons from trypanosomes*. Biol Chem, 2020. **401**(6-7): p. 663-676.
16. Schneider, A., *Unique aspects of mitochondrial biogenesis in trypanosomatids*. Int J Parasitol, 2001. **31**(13): p. 1403-15.
17. Zikova, A., *Mitochondrial adaptations throughout the Trypanosoma brucei life cycle*. J Eukaryot Microbiol, 2022. **69**(6): p. e12911.
18. Read, L.K., J. Lukes, and H. Hashimi, *Trypanosome RNA editing: the complexity of getting U in and taking U out*. Wiley Interdiscip Rev RNA, 2016. **7**(1): p. 33-51.
19. Povelones, M.L., *Beyond replication: division and segregation of mitochondrial DNA in kinetoplastids*. Mol Biochem Parasitol, 2014. **196**(1): p. 53-60.
20. Jensen, R.E. and P.T. Englund, *Network news: the replication of kinetoplast DNA*. Annu Rev Microbiol, 2012. **66**: p. 473-91.
21. Verner, Z., et al., *Malleable mitochondrion of Trypanosoma brucei*. Int Rev Cell Mol Biol, 2015. **315**: p. 73-151.
22. Tyler, K.M., K.R. Matthews, and K. Gull, *Anisomorphic Cell Division by African Trypanosomes*. Protist, 2001/12/01. **152**(4).
23. Amodeo, S., I. Bregy, and T. Ochsenreiter, *Mitochondrial genome maintenance—the kinetoplast story*. FEMS Microbiology Reviews, 2023/11/01. **47**(6).
24. Shapiro, T.A. and P.T. Englund, *The structure and replication of kinetoplast DNA*. Annu Rev Microbiol, 1995. **49**: p. 117-43.

25. Hajduk, S. and T. Ochsenreiter, *RNA editing in kinetoplastids.* RNA Biol, 2010. **7**(2): p. 229-36.
26. Schneider, A., *A short history of guide RNAs: The intricate path that led to the discovery of a basic biological concept.* EMBO Rep, 2020. **21**(12): p. e51918.
27. Robertson, M., *Notes on the Life-History of Trypanosoma gambiense, with a Brief Reference to the Cycles of Trypanosoma nanum and Trypanosoma pecorum in Glossina palpalis.* Philosophical Transactions of the Royal Society B, 1913. **203**(294-302).
28. Ogbadoyi, E.O., D.R. Robinson, and K. Gull, *A high-order trans-membrane structural linkage is responsible for mitochondrial genome positioning and segregation by flagellar basal bodies in trypanosomes.* Mol Biol Cell, 2003. **14**(5): p. 1769-79.
29. Robinson, D.R. and K. Gull, *Basal body movements as a mechanism for mitochondrial genome segregation in the trypanosome cell cycle.* Nature, 1991. **352**: p. 731-733.
30. Schneider, A. and T. Ochsenreiter, *Failure is not an option - mitochondrial genome segregation in trypanosomes.* J Cell Sci, 2018. **131**(18).
31. Aeschlimann, S., P. Stettler, and A. Schneider, *DNA segregation in mitochondria and beyond: insights from the trypanosomal tripartite attachment complex.* Trends in Biochemical Sciences, 2023/12/01. **48**(12).
32. Aeschlimann, S., et al., *Single p197 molecules of the mitochondrial genome segregation system of Trypanosoma brucei determine the distance between basal body and outer membrane.* Proc Natl Acad Sci U S A, 2022. **119**(40): p. e2204294119.
33. Gheiratmand, L., et al., *Biochemical characterization of the bi-lobe reveals a continuous structural network linking the bi-lobe to other single-copied organelles in Trypanosoma brucei.* J Biol Chem, 2013. **288**(5): p. 3489-99.
34. Rabuffo, C., et al., *Inter-chromosomal transcription hubs shape the 3D genome architecture of African trypanosomes.* Nat Commun, 2024. **15**(1): p. 10716.
35. Hoffmann, A., et al., *Molecular model of the mitochondrial genome segregation machinery in Trypanosoma brucei.* Proc Natl Acad Sci U S A, 2018. **115**(8): p. E1809-E1818.
36. Kaser, S., et al., *Outer membrane protein functions as integrator of protein import and DNA inheritance in mitochondria.* Proc Natl Acad Sci U S A, 2016. **113**(31): p. E4467-75.
37. Vitali, D.G., et al., *Independent evolution of functionally exchangeable mitochondrial outer membrane import complexes.* Elife, 2018. **7**.
38. Kaser, S., et al., *Biogenesis of the mitochondrial DNA inheritance machinery in the mitochondrial outer membrane of Trypanosoma brucei.* PLoS Pathog, 2017. **13**(12): p. e1006808.
39. Schnarwiler, F., et al., *Trypanosomal TAC40 constitutes a novel subclass of mitochondrial beta-barrel proteins specialized in mitochondrial genome inheritance.* Proc Natl Acad Sci U S A, 2014. **111**(21): p. 7624-9.
40. Stettler, P., et al., *Molecular characterization of the permanent outer-inner membrane contact site of the mitochondrial genome segregation complex in trypanosomes.* PLoS Pathog, 2024. **20**(12): p. e1012635.
41. Schimanski, B., et al., *p166 links membrane and intramitochondrial modules of the trypanosomal tripartite attachment complex.* PLoS Pathog, 2022. **18**(6): p. e1010207.
42. Zhao, Z., et al., *p166, a link between the trypanosome mitochondrial DNA and flagellum, mediates genome segregation.* EMBO J, 2008. **27**(1): p. 143-54.
43. Baudouin, H.C.M., L. Pfeiffer, and T. Ochsenreiter, *A comparison of three approaches for the discovery of novel tripartite attachment complex proteins in Trypanosoma brucei.* PLoS Negl Trop Dis, 2020. **14**(9): p. e0008568.
44. Trikin, R., et al., *TAC102 Is a Novel Component of the Mitochondrial Genome Segregation Machinery in Trypanosomes.* PLoS Pathog, 2016. **12**(5): p. e1005586.

45. Amodeo, S., et al., *Characterization of two novel proteins involved in mitochondrial DNA anchoring in Trypanosoma brucei.* PLoS Pathog, 2023. **19**(7): p. e1011486.
46. Amodeo, S., et al., *Characterization of the novel mitochondrial genome segregation factor TAP110 in Trypanosoma brucei.* J Cell Sci, 2021. **134**(5).
47. Jetishi, C., et al., *Beyond a Linear Structure: The Tubular Organization of the Tripartite Attachment Complex and the Functional Role of TAC53.* bioRxiv, 2025: p. 2025.05.14.653994.
48. Pusnik, M., et al., *An essential novel component of the noncanonical mitochondrial outer membrane protein import system of trypanosomatids.* Mol Biol Cell, 2012. **23**(17): p. 3420-8.
49. Dean, S., et al., *Single point mutations in ATP synthase compensate for mitochondrial genome loss in trypanosomes.* Proc Natl Acad Sci U S A, 2013. **110**(36): p. 14741-6.
50. Urbaniak, M.D., M.L. Guther, and M.A. Ferguson, *Comparative SILAC proteomic analysis of Trypanosoma brucei bloodstream and procyclic lifecycle stages.* PLoS One, 2012. **7**(5): p. e36619.
51. Gunasekera, K., et al., *Proteome remodelling during development from blood to insect-form Trypanosoma brucei quantified by SILAC and mass spectrometry.* BMC Genomics, 2012. **13**: p. 556.
52. Abramson, J., et al., *Accurate structure prediction of biomolecular interactions with AlphaFold 3.* Nature, 2024. **630**(8016): p. 493-500.
53. Keinan, N., D. Tyomkin, and V. Shoshan-Barmatz, *Oligomerization of the mitochondrial protein voltage-dependent anion channel is coupled to the induction of apoptosis.* Mol Cell Biol, 2010. **30**(24): p. 5698-709.
54. Kim, J., et al., *VDAC oligomers form mitochondrial pores to release mtDNA fragments and promote lupus-like disease.* Science, 2019. **366**(6472): p. 1531-1536.
55. Peikert, C.D., et al., *Charting organellar importomes by quantitative mass spectrometry.* Nat Commun, 2017. **8**: p. 15272.
56. Wirtz, E., et al., *A tightly regulated inducible expression system for conditional gene knock-outs and dominant-negative genetics in Trypanosoma brucei.* Mol Biochem Parasitol, 1999. **99**(1): p. 89-101.
57. Oberholzer, M., et al., *A vector series for rapid PCR-mediated C-terminal in situ tagging of Trypanosoma brucei genes.* Mol Biochem Parasitol, 2006. **145**(1): p. 117-20.
58. Chomczynski, P. and N. Sacchi, *Single-step method of RNA isolation by acid guanidinium thiocyanate-phenol-chloroform extraction.* Anal Biochem, 1987. **162**(1): p. 156-9.
59. Mani, J., et al., *Mitochondrial protein import receptors in Kinetoplastids reveal convergent evolution over large phylogenetic distances.* Nat Commun, 2015. **6**: p. 6646.
60. Kilmartin, J.V., B. Wright, and C. Milstein, *Rat monoclonal antitubulin antibodies derived by using a new nonsecreting rat cell line.* J Cell Biol, 1982. **93**(3): p. 576-82.
61. Harmer, J., et al., *Variation in Basal Body Localisation and Targeting of Trypanosome RP2 and FOR20 Proteins.* Protist, 2017. **168**(4): p. 452-466.

Supplementary figures

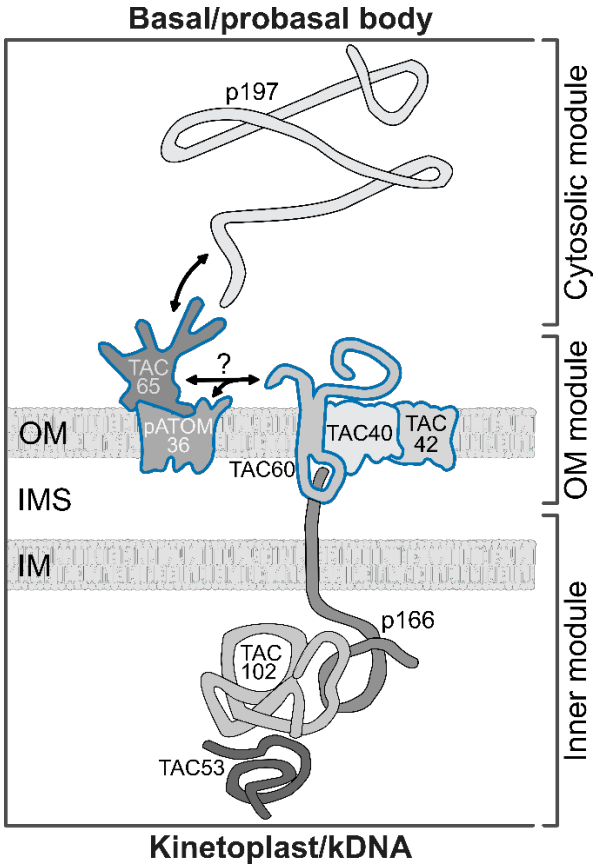

S1 Fig: Molecular model of the tripartite attachment complex (TAC).

On the molecular level the TAC can be divided into three modules: (i) the cytosolic TAC module, (ii) the OM TAC module, and (iii) the inner TAC module. The cytosolic TAC module consists exclusively of p197, a protein anchored at the basal body which connects to an unknown domain of TAC65 at the OM. The OM TAC module contains the peripheral membrane protein (TAC65), two integral membrane proteins (pATOM36, TAC60) with α-helical transmembrane domains, and two β-barrel membrane proteins (TAC40, TAC42). TAC65 and pATOM36 interact, the same is the case for TAC40, TAC42, and TAC60. How the two groups of proteins interact with each other is unclear (?). TAC60 interacts with p166, an integral IM protein with a single α-helical transmembrane domain. As a part of the inner TAC module, p166 interacts with TAC102 in the mitochondrial matrix. TAC53 is the inner TAC module subunit that is most proximal to the kDNA.

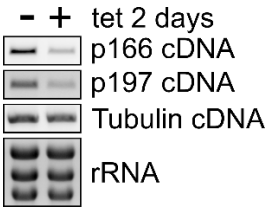

S2 Fig: Controls for the inducible p166/p197 double RNAi cell line. Ethidium bromide-stained agarose gels of PCR amplified cDNA segments corresponding to p166, p197, and tubulin mRNAs, as well as non-amplified cytosolic rRNA of the uninduced and induced p166/p197 double RNAi cell line. Tubulin cDNA and rRNA signals serve as loading controls.

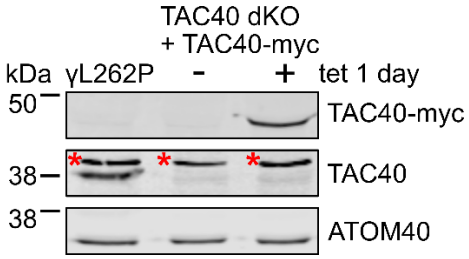

S3 Fig: Controls for the TAC40 dKO γL262P BSF cell line allowing inducible ectopic expression of TAC40-myc.

Immunoblots comparing whole cell protein levels of TAC40-myc (top panel), TAC40 (middle panel), and ATOM40 (bottom panel). The parent γL262P BSF cell line (left lane) and TAC40 dKO γL262P BSF uninduced (middle lane) and induced (right lane) for ectopic expression of TAC40-myc were analyzed. The ATOM40 signals serve as a loading control. Numbers on the left indicate protein size markers in kDa. Asterisk, unspecific band recognized by the polyclonal TAC40 antiserum.

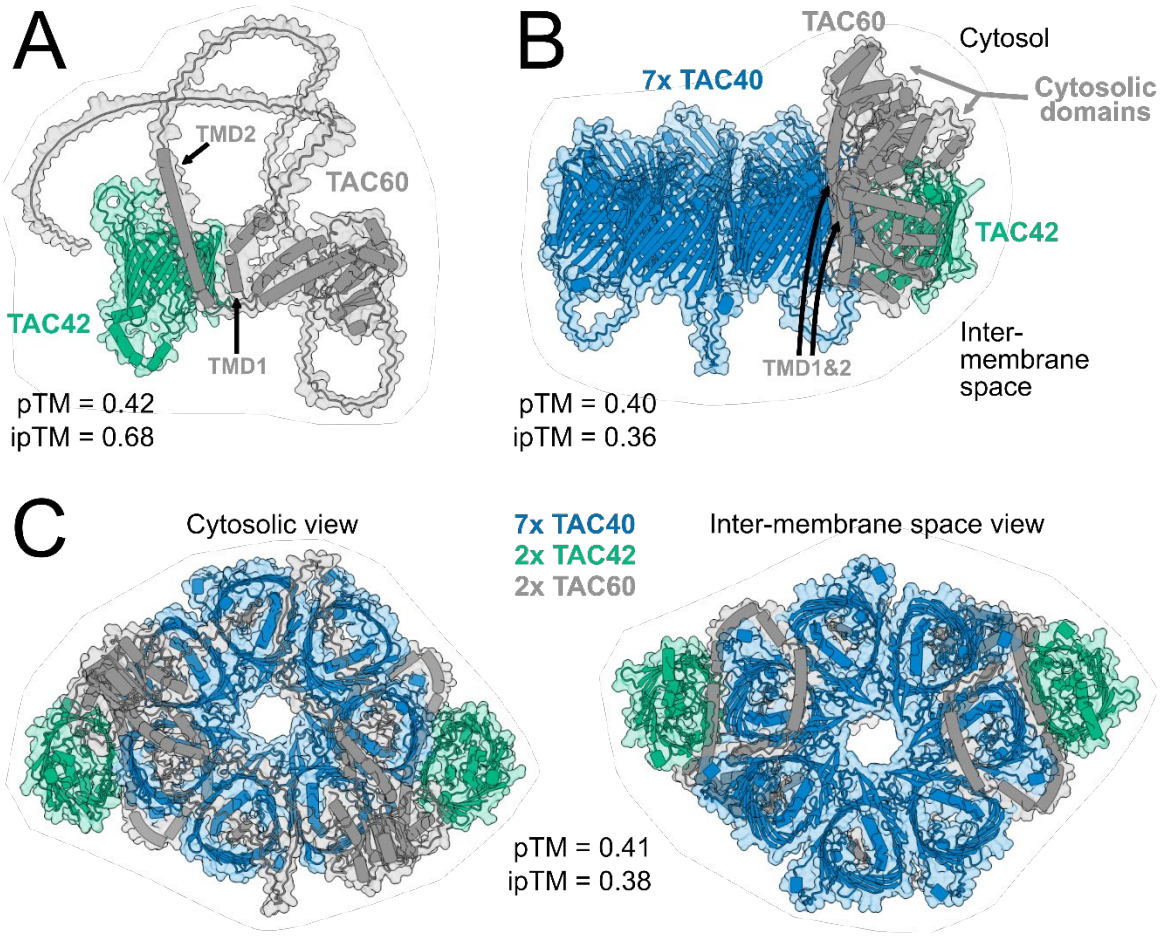

S4 Fig: AlphaFold3 structure predictions for the TAC40/TAC42/TAC60 subcomplexes.

(A) Model of an AlphaFold3 structure prediction for a TAC42/TAC60 dimer shown from the side of the membrane. TMD: α-helical transmembrane domain; pTM: predicted template modelling score; ipTM: interference pTM. **(B)** Model of an AlphaFold3 structure prediction for a complex possibly matching the ~770 kDa TAC40/TAC42/TAC60 subcomplex shown from the side of the membrane. **(C)** Model of an AlphaFold3 structure predictions for a complex possibly matching the ~920 kDa TAC40/TAC42/TAC60 subcomplex shown from the cytosolic (left) and the inter-membrane space (right) side.

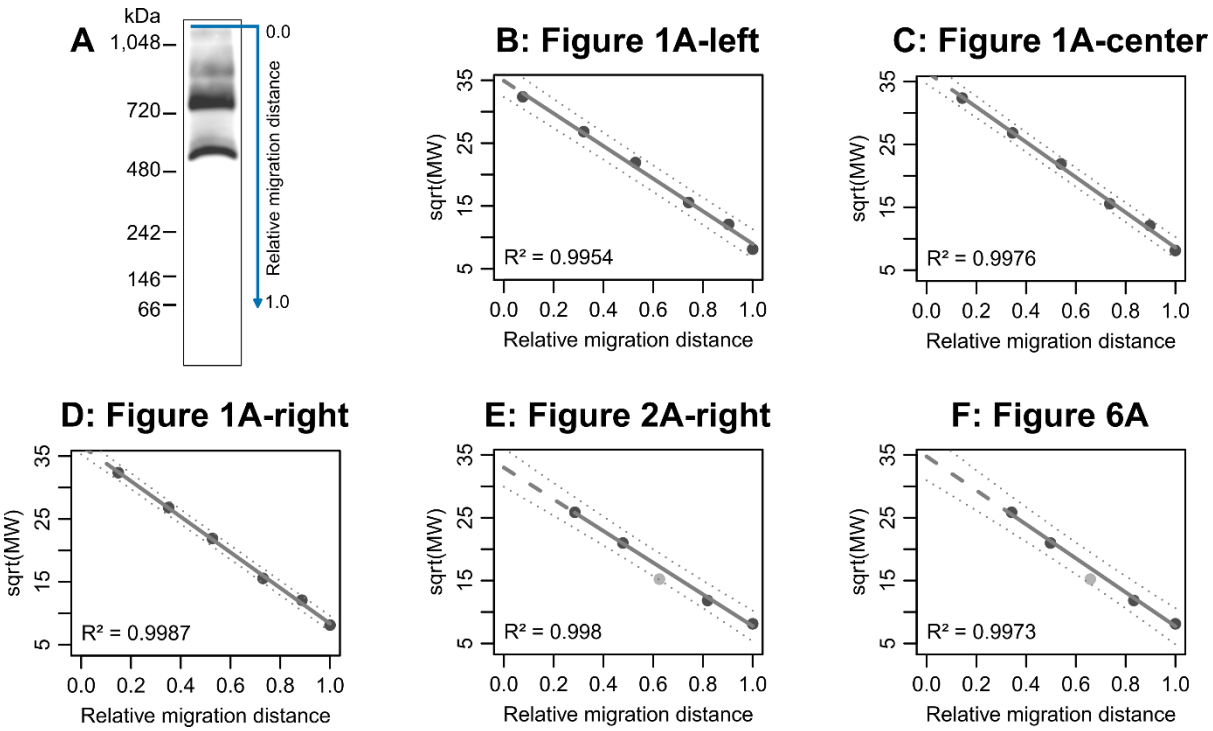

S5 Fig: BN-PAGE complex size estimation and extrapolation. (A) Definition of "relative migration distance": distance between the upper edge of the gel and the band of interest divided by the distance between the upper edge of the gel and the lowest molecular weight marker. The shown lane is identical to the panel in Fig 1A (left). **(B-F)** Graphs depicting the linear models of the relative migration distance of marker proteins versus the square root (sqrt) of the molecular weight in kDa. Dark gray datapoints represent marker protein data used for the linear models. Light gray datapoints in (E) and (F) show marker measurements which were omitted for calculation of linear models. The solid and dashed gray lines show the inter- and extrapolated linear models, respectively. Dotted lines show the 90% prediction confidence intervals. The coefficient of determination (R^2) of the linear model is shown at the bottom left of each graph.

3.3 Pam16 and Pam18 were repurposed during *Trypanosoma brucei* evolution to regulate the replication of mitochondrial DNA

Corinne von Känel [1], Philip Stettler [1,2], Carmela Esposito [1,2], Stephan Berger [1,2], Simona Amodeo [1], Silke Oeljeklaus [3], Salvatore Calderaro [1], Ignacio M Durante [4], Vendula Rašková [4,5], Bettina Warscheid [3], André Schneider [1]

[1]Department of Chemistry, Biochemistry and Pharmaceutical Sciences, University of Bern, Switzerland

[2]Graduate School for Cellular and Biomedical Sciences, University of Bern, Switzerland

[3]Faculty of Chemistry and Pharmacy, Biochemistry II, Theodor Boveri-Institute, University of Würzburg, Würzburg, Germany.

[4]Institute of Parasitology, Biology Centre, České Budějovice, Czech Republic.

[5]Faculty of Science, University of South Bohemia, České Budějovice, Czech Republic.

Published manuscript, second authorship.

Contribution:

- Data shown in figures 4CD, S4B, S6B right panels and S6C, S9/S10/S11 (sample generation), S11 (statistical analysis and figure design), data tables S1-3 (update for gene annotations), data table S3 (sample generation).

- Contribution to additional experiments required for the revision process and contribution to final revision of the manuscript.

PLOS BIOLOGY

RESEARCH ARTICLE

Pam16 and Pam18 were repurposed during *Trypanosoma brucei* evolution to regulate the replication of mitochondrial DNA

Corinne von Känel[1], Philip Stettler[1], Carmela Esposito[1], Stephan Berger[1], Simona Amodeo[1], Silke Oeljeklaus[2], Salvatore Calderaro[1], Ignacio M. Durante[3], Vendula Rašková[3,4¤], Bettina Warscheid[2]*, André Schneider[1]*

1 Department of Chemistry, Biochemistry and Pharmaceutical Sciences, University of Bern, Bern, Switzerland, **2** Faculty of Chemistry and Pharmacy, Biochemistry II, Theodor Boveri-Institute, University of Würzburg, Würzburg, Germany, **3** Institute of Parasitology, Biology Centre, České Budějovice, Czech Republic, **4** Faculty of Science, University of South Bohemia, České Budějovice, Czech Republic

¤ Current address: CEITEC–Central European Institute of Technology, Brno, Czech Republic
* bettina.warscheid@uni-wuerzburg.de (BW); andre.schneider@unibe.ch (AS)

Citation: von Känel C, Stettler P, Esposito C, Berger S, Amodeo S, Oeljeklaus S, et al. (2024) Pam16 and Pam18 were repurposed during *Trypanosoma brucei* evolution to regulate the replication of mitochondrial DNA. PLoS Biol 22(8): e3002449. https://doi.org/10.1371/journal.pbio.3002449

Academic Editor: Michael Duffy, University of Melbourne, AUSTRALIA

Received: November 13, 2023

Accepted: July 23, 2024

Published: August 15, 2024

Peer Review History: PLOS recognizes the benefits of transparency in the peer review process; therefore, we enable the publication of all of the content of peer review and author responses alongside final, published articles. The editorial history of this article is available here: https://doi.org/10.1371/journal.pbio.3002449

Data Availability Statement: The mass spectrometry proteomics data have been deposited to the ProteomeXchange Consortium via the PRIDE partner repository and are accessible using

Abstract

Protein import and genome replication are essential processes for mitochondrial biogenesis and propagation. The J-domain proteins Pam16 and Pam18 regulate the presequence translocase of the mitochondrial inner membrane. In the protozoan *Trypanosoma brucei*, their counterparts are TbPam16 and TbPam18, which are essential for the procyclic form (PCF) of the parasite, though not involved in mitochondrial protein import. Here, we show that during evolution, the 2 proteins have been repurposed to regulate the replication of maxicircles within the intricate kDNA network, the most complex mitochondrial genome known. TbPam18 and TbPam16 have inactive J-domains suggesting a function independent of heat shock proteins. However, their single transmembrane domain is essential for function. Pulldown of TbPam16 identifies a putative client protein, termed MaRF11, the depletion of which causes the selective loss of maxicircles, akin to the effects observed for TbPam18 and TbPam16. Moreover, depletion of the mitochondrial proteasome results in increased levels of MaRF11. Thus, we have discovered a protein complex comprising TbPam18, TbPam16, and MaRF11, that controls maxicircle replication. We propose a working model in which the matrix protein MaRF11 functions downstream of the 2 integral inner membrane proteins TbPam18 and TbPam16. Moreover, we suggest that the levels of MaRF11 are controlled by the mitochondrial proteasome.

Introduction

The parasitic protist *Trypanosoma brucei* has a unique mitochondrial biology. As in other eukaryotes, more than 95% of its mitochondrial proteins are encoded in the nucleus, synthesized in the cytosol, and imported into and across the mitochondrial membranes [1]. However, the trypanosomal mitochondrial protein import machineries show significant differences to

the dataset identifiers PXD046840 (TbPam16 SILAC RNAi data), PXD046845 (TbPam18 SILAC RNAi data), PXD046849 (TbPam16 SILAC CoIP data), and PXD053251 (MaRF11 SILAC RNAi data).

Funding: This study was supported in part by NCCR RNA & Disease, a National Centre of Competence in Research (grant number 205601 to A.S.) and by project grant SNF 205200 to A.S. both funded by the Swiss National Science Foundation (https://www.snf.ch/en). The funders had no role in study design, data collection and analysis, decision to publish, or preparation of the manuscript.

Competing interests: AS is a member of the PLOS Biology Editorial Board.

Abbreviations: BSF, bloodstream form; dKO, double knockout; FCS, fetal calf serum; gRNA, guide RNA; IM, inner membrane; kDNA, kinetoplast DNA; LC–MS, liquid chromatography–mass spectrometry; MCP, mitochondrial carrier protein; mHsp70, mitochondrial heat shock protein 70; MRP, mitoribosomal protein; MS, mass spectrometry; MTS, mitochondrial targeting sequence; mtRNAP, mitochondrial RNA polymerase; NYsm, New York single marker; ORF, open reading frame; OXPHOS, oxidative phosphorylation; PAM, presequence translocase-associated motor; PCF, procyclic form; sKO, single knockout; TAC, tripartite attachment complex; TMD, transmembrane domain; UTR, untranslated region; WB, western blot.

the prototypical systems of yeast and mammals [2–6]. The largest differences are found in the translocase of the inner mitochondrial membrane (IM), the TIM complex (S1A Fig). Essentially all eukaryotes have 2 TIM complexes, termed TIM22 and TIM23 [7,8]. The TIM22 complex mediates insertion of proteins into the IM that have multi-spanning membrane domains, such as mitochondrial carrier proteins (MCPs) [9,10]. The TIM23 complex imports presequence-containing proteins across or into the IM [11]. To import its substrates into the mitochondrial matrix, TIM23 associates with the matrix-exposed presequence translocase-associated motor (PAM). The PAM consists of 5 essential and highly conserved subunits [7]: the mitochondrial heat shock protein 70 (mHsp70) [12,13], its J-domain-containing co-factors Pam18 [14–16] and Pam16 [17], Tim44 [18] and the nucleotide exchange factor Mge1 [19–21].

In contrast, *T. brucei* has a single TIM complex only, which with minor compositional variations, imports both types of substrates [22]. Interestingly, the only trypanosomal TIM component sharing homology to a subunit of TIM complexes in yeast or mammals is TbTim17. TbTim17 is an orthologue of the Tim22 subunit of the TIM22 complex [7,8,23,24].

To import presequence-containing proteins, the trypanosomal TIM complex associates with a PAM module [42] containing the trypanosomal mHsp70 orthologue (TbmHsp70), which is essential for the import of presequence-containing proteins [25,26]. *T. brucei* contains bona fide orthologues of Pam18 and Pam16, termed TbPam18 and TbPam16. However, while they are essential for normal growth of procyclic form trypanosomes, they are not involved in mitochondrial protein import [26]. Instead, the function of Pam18, and likely Pam16, in the trypanosomal PAM is carried out by the non-orthologous, essential, J-domain-containing integral IM protein TbPam27 [26].

The evidence for this has been described in detail in a previous publication [26]. In short, TbPam27 is: (i) stably associated with the TIM complex; (ii) required for import of presequence-containing proteins in vivo; (iii) essential for the formation of an import-arrested presequence-containing but not for an import-arrested carrier substrate; and (iv) recovered in the pulldown of the import-arrested presequence-containing but not in the pulldown of the import-arrested carrier substrate. In contrast, TbPam18 and TbPam16 are not associated with any known constellation of the trypanosomal TIM complex. Furthermore, their depletion does not affect mitochondrial protein import nor the formation of the 2 import-arrested intermediates.

Based on these observations, an evolutionary scenario was proposed that aims to explain the transition from 2 ancestral TIM complexes, found in most eukaryotes, to the single TIM complex of trypanosomes [26]. It posits that in the ancestor of kinetoplastids, TbPam27 fortuitously interacted with TbTim17. This allowed mHsp70 to bind to the resulting TbTim17/TbPam27 complex forming a rudimentary PAM. As a consequence, the TbTim17-containing, TIM22-like TIM complex acquired the capability to import both, presequence-containing proteins and MCPs. Thus, the previously essential TIM23 complex became redundant and its subunits were lost. However, the proposed scenario cannot explain why TbPam18 and TbPam16 were retained during evolution and why they are essential for the growth of PCF *T. brucei* [26].

The single mitochondrion of trypanosomes contains a single nucleoid containing all mitochondrial DNA. This DNA forms the most complex mitochondrial genome known in nature and is termed kinetoplast DNA (kDNA) (S1B Fig). It consists of 2 types of DNA rings: maxicircles (ca. 25 copies, 23 kb each) and heterogenous minicircles (ca. 5,000 copies, 1 kb each), which are arranged in a large intercatenated network [27,28]. Maxicircles encode 16 subunits of the oxidative phosphorylation (OXPHOS) complexes, 2 mitoribosomal proteins (MRPs), and 2 rRNAs [27–29]. Twelve of their transcripts require RNA editing to become functional mRNAs. This process is mediated by small guide RNAs (gRNAs), which are the only genes encoded on the minicircles [30–33]. Minicircles are highly topologically interlocked and

comprise 90% of the kDNA network [34]. Maxicircles are also interlocked with each other [35], and in addition, interwoven into the minicircle network [36]. The resulting kDNA disk in the mitochondrial matrix is physically connected to the flagellum's basal body in the cytosol via the tripartite attachment complex (TAC) [37,38].

Minicircle replication begins with their release into the kinetoflagellar zone, located between the kDNA disk and the IM [39]. It occurs unidirectionally via theta structures [40]. Replicated minicircles migrate to the antipodal sites, which are protein complexes at opposing sites of the kDNA disk, where gaps are repaired and minicircles are reattached to the periphery of the network [41,42]. Maxicircles replicate like minicircles, but always remain interlocked with the kDNA. However, the details of the process and the factors required for it are not well understood [28,43]. Minicircle release and reattachment causes concentration of the catenated maxicircles in the center of the disk [35]. The concomitant replication and segregation of the kDNA network, mediated by the TAC and the basal bodies, results in the formation of a maxicircle-containing filament between the 2 minicircles networks, termed Nabelschnur. Completion of kDNA segregation requires cleavage of this Nabelschnur, to unlink the daughter kDNAs [44,45].

Altogether, replication of the single kDNA network involves up to 150 different proteins and is tightly coordinated with the nuclear cell cycle [27,28]. However, the mechanism of this coordination is presently unknown. What has been shown is that the mitochondrial proteasome TbHslVU, composed of the 2 subunits TbHslV and TbHslU, acts a negative regulator of minicircle and maxicircle copy numbers and its depletion thus causes accumulation of giant kDNAs [46,47]. Intriguingly, up to date, only a single TbHslVU substrate has been identified, the maxicircle replication factor TbPIF2, whose levels are increased in TbHslVU depleted cells [47].

Here, we show that TbPam18 and TbPam16, while not involved in mitochondrial protein import, are required for the replication of the maxicircle component of the kDNA. Strikingly, this function is mediated by a soluble TbPam16-interacting protein whose levels appear to be controlled by TbHslVU.

Results

Depletion of TbPam18 or TbPam16 mainly affects MRPs and OXPHOS complexes

TbPam18 and TbPam16 are not required for protein import, but the fact that they are essential integral IM proteins indicates that they have another function linked to mitochondria [26]. To identify what this function might be, we quantified global changes in the mitochondrial proteome caused by the depletion of either of the 2 proteins. Previously established tetracycline-inducible TbPam18 and TbPam16 RNAi cell lines [26] were analyzed by stable isotope labeling by amino acids in cell culture (SILAC)-based quantitative mass spectrometry (MS). Surprisingly, neither TbPam18 nor TbPam16 were detected in the 2 SILAC RNAi experiments. However, using a TbPam16 antibody, we found that after only 1 day of RNAi induction, TbPam16 levels were strongly reduced in both cell lines (Fig 1A). Thus, we conclude that (i) the stability of TbPam16 depends on TbPam18, in line with the idea that the 2 proteins form a heterodimer as in yeast; and (ii) that RNAi against TbPam16 is very efficient.

The 916 and 893 mitochondrial proteins [1,29,48] were detected in the SILAC RNAi data sets and the levels of 12% and 13% of them were reduced more than 1.5-fold in the TbPam18 and TbPam16 RNAi cell lines, respectively (Fig 1B). The most affected proteins included MRPs [29] of which 59% and 63% were depleted more than 1.5-fold in the 2 cell lines (Fig 1B, top panels). Furthermore, we found that 15% and 16% of all detected components of the

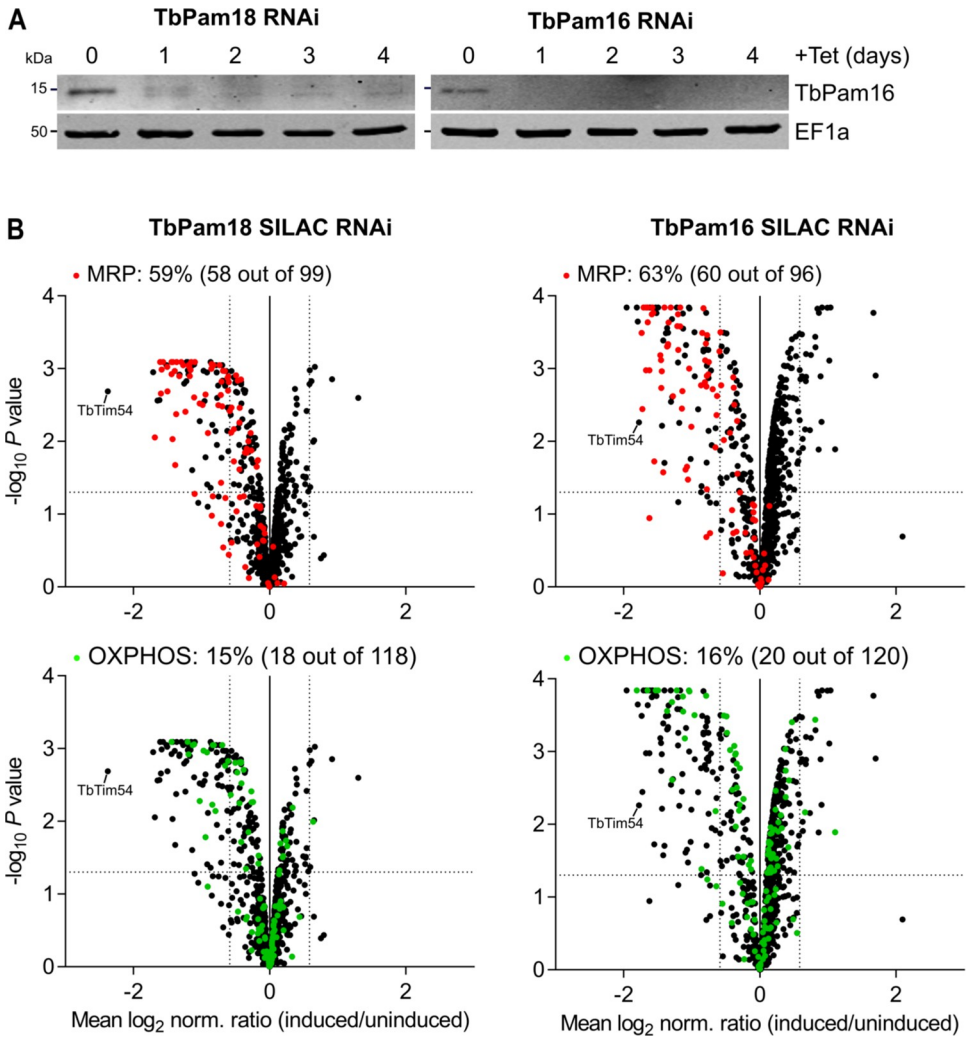

Fig 1. TbPam18 and TbPam16 RNAi predominantly affects MRPs and OXPHOS components. (A) Immunoblot analysis of steady-state protein levels of TbPam16 in whole-cell extracts of TbPam16 or TbPam18 RNAi cell lines over 4 days of induction. EF1a serves as loading control. **(B)** Global mitochondrial proteome changes upon ablation of TbPam18 (left panels) or TbPam16 (right panels). Mitochondria-enriched fractions of uninduced and 4 days induced TbPam18 and TbPam16 RNAi cells were analyzed by SILAC-based quantitative MS. Data sets were filtered for mitochondrial proteins and the mean $\log_2$ of normalized ratios (induced/uninduced) was plotted against the corresponding negative $\log_{10}$ of the adjusted *P* value (limma test). Highlighted are MRPs (red) and components of the OXPHOS pathway (green). The horizontal dotted line in each volcano plot marks an adjusted *P* value of 0.05. The vertical dotted lines indicate a fold-change in protein abundance of ±1.5. The percentages of all detected MRPs or OXPHOS proteins that are depleted more than 1.5-fold are indicated at the top of each panel. The number of all more than 1.5-fold depleted MRPs or OXPHOS proteins and the total number of all detected MRPs or OXPHOS proteins are shown in parentheses. Numerical data for panel (B) are available in S1 Table. MRP, mitoribosomal protein; MS, mass spectrometry; OXPHOS, oxidative phosphorylation.

https://doi.org/10.1371/journal.pbio.3002449.g001

OXPHOS pathway [48] were reduced more than 1.5-fold in the 2 cell lines (Fig 1B, bottom panels). In both experiments, complex IV was affected the most, followed by complexes I and III, whereas the levels of complex II and V subunits were not or only marginally decreased.

A common feature of the mitoribosome and the OXPHOS complexes I, III, and IV is that some of their subunits are encoded on the kDNA [27,29,49]. For mitoribosomes, these are the 12S and 9S rRNAs as well as 2 MRPs [29]. For complexes I, III, and IV, the number of maxicircle-encoded subunits is 6, 3, and 3, respectively. In contrast, only a single complex V subunit is

encoded on the kDNA and all complex II subunits are encoded in the nuclear genome [49]. In total, 67% (TbPam18) and 68% (TbPam16) of all more than 1.5-fold depleted mitochondrial proteins were either MRPs or subunits of the OXPHOS complexes I, III, IV, and V, all of which contain mitochondrially encoded RNAs and/or proteins (Fig 1B).

For protein categories consisting exclusively of nucleus-encoded proteins, the situation is very different. Neither of the 33 (TbPam18) and 30 (TbPam16) proteins detected in the category "kDNA replication factors" [43] were more than 1.5-fold depleted (S2A and S3A Figs). Essentially, the same results were obtained for 6 other major previously defined subgroups of mitochondrial proteins [48], which exclusively consist of nucleus-encoded proteins (S2B–S2F and S3B–S3F Figs). In all these subgroups combined, only 3 out of 279 detected proteins (TbPam18 RNAi) and not a single protein out of 274 (TbPam16 RNAi) were depleted more than 1.5-fold.

The observed phenotypes after depletion of TbPam18 or TbPam16 are notably different from RNAi cell lines targeting components of the protein import system, such as ATOM40 [1] or TbTim17 [50], in which depletion of members of all subgroups of mitochondrial proteins was observed. The SILAC RNAi results therefore confirm that TbPam18 and TbPam16 are not involved in mitochondrial protein import and suggest that the 2 proteins might be required for maintenance or replication of the kDNA.

Depletion of TbPam18 and TbPam16 leads to shrinkage of the kDNA disk

To investigate the fate of the kDNA upon TbPam18 or TbPam16 depletion, we analyzed DAPI-stained RNAi cells by fluorescence microscopy. In line with the SILAC-RNAi analyses (Fig 1B), we found that after 4 days of RNAi induction, many TbPam18 and TbPam16 RNAi cells had smaller kDNAs compared to uninduced cells (Fig 2A, upper panels). A quantification of the experiments (Fig 2A, lower panels) showed in both cell lines a time-dependent decrease of the kDNA size to 90% and about 60% after 3 (prior to the onset of the growth retardation) to 5 days of RNAi induction, respectively. Shrinkage of the kDNA disk has been observed previously when proteins involved in kDNA replication were ablated [47,51–55].

However, there is an alternative explanation. The most depleted protein upon TbPam18 RNAi and the fourth most depleted one upon TbPam16 RNAi was TbTim54 (Fig 1B). TbTim54 is unrelated to the yeast TIM22 complex subunit Tim54, but was proposed to mediate import of a subset of mitochondrial proteins with internal targeting sequences [56]. Thus, we wanted to exclude that the loss of maxicircles observed in the TbPam18 and TbPam16 RNAi cell lines could be a consequence of the co-depletion of TbTim54 (Fig 1B). Since RNAi depletion of TbTim54 did not affect growth [56], we produced a conditional double knock out cell line. In this cell line, depletion of the ectopically expressed copy of TbTim54 caused a growth arrest starting 4 days after tetracycline removal (S4A Fig). However, even after 6 days of tetracycline removal, no shrinkage of the kDNA was observed (S4B Fig). Thus, while TbTim54 is essential for normal growth, its depletion did not interfere with import of kDNA replication factors.

This is in line with the fact that even though TbTim54 has been reported to interact with TbTim17 [24], it was not enriched in any of our previously published pulldowns of TIM complex subunits or associated proteins (TbTim17, TbTim42, ACAD, TbTim13, TbPam27) [26,50,57]. These results, together with the observation that TbPam18 and TbPam16 are neither associated with the single trypanosomal TIM complex nor involved in mitochondrial protein import [26] (Figs 1B S2, and S3), suggest that TbPam18 and TbPam16 are more directly involved in kDNA replication or maintenance.

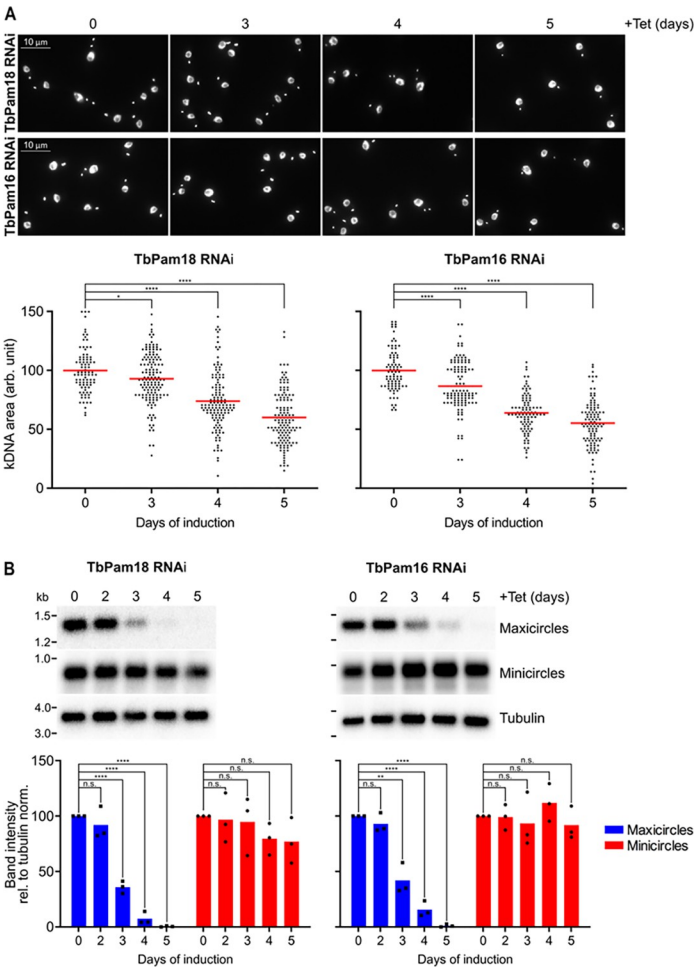

Fig 2. TbPam18 and TbPam16 ablation causes the loss of maxicircles. (A) Upper panels: Fluorescence microscopy analysis of DAPI-stained uninduced and 3 to 5 days induced TbPam18 and TbPam16 RNAi cells. Lower panels: Quantification of kDNA areas in 86 to 140 DAPI-stained RNAi cells induced for the indicated amount of time. The red line indicates the mean of the kDNA areas at each time point. The mean of the uninduced cells was set to 100%. *: *P* value <0.05, ****: *P* value <0.0001, as calculated by an unpaired two-tailed *t* test. **(B)** Southern blot analysis of steady-state levels of mini- and maxicircles in the TbPam18 and TbPam16 RNAi cell lines. Upper panels: Total DNA from uninduced or 3 to 5 days induced cells was isolated and digested with HindIII and XbaI. Probes specifically recognizing mini- or maxicircles were used. A probe detecting a 3.6-kb fragment of the tubulin intergenic region serves as loading control. Lower panels: Densitometric quantification of mini- and maxicircle abundance on Southern blots. The ratio of the mini- or maxicircle abundance and the respective loading control (tubulin) was normalized (norm.) to the ratios of uninduced cells. Blue (maxicircles) and red (minicircles) bars represent the mean of 3 independent biological replicates. n.s.: not significant, **: *P* value <0.01, ****: *P* value <0.0001, as calculated by an unpaired two-tailed *t* test. Numerical data for panels (A) and (B) are available in S1 Data. kDNA, kinetoplast DNA.

https://doi.org/10.1371/journal.pbio.3002449.g002

Depletion of TbPam18 and TbPam16 leads to a selective loss of maxicircles

To study the effects of TbPam18 and TbPam16 depletion on the kDNA in more detail, we performed Southern blot analysis (Fig 2B). Total DNA was extracted from uninduced and induced RNAi cells, digested by restriction enzymes and separated on an agarose gel. The resulting blot was hybridized with mini- and maxicircle specific probes. Already after 3 days of RNAi induction, maxicircle levels were significantly reduced to about 39% in both cell lines. After 5 days, they were almost undetectable. In contrast, the levels of minicircles were not significantly changed over 5 days of RNAi induction. The same experiment (Fig 2B) was repeated

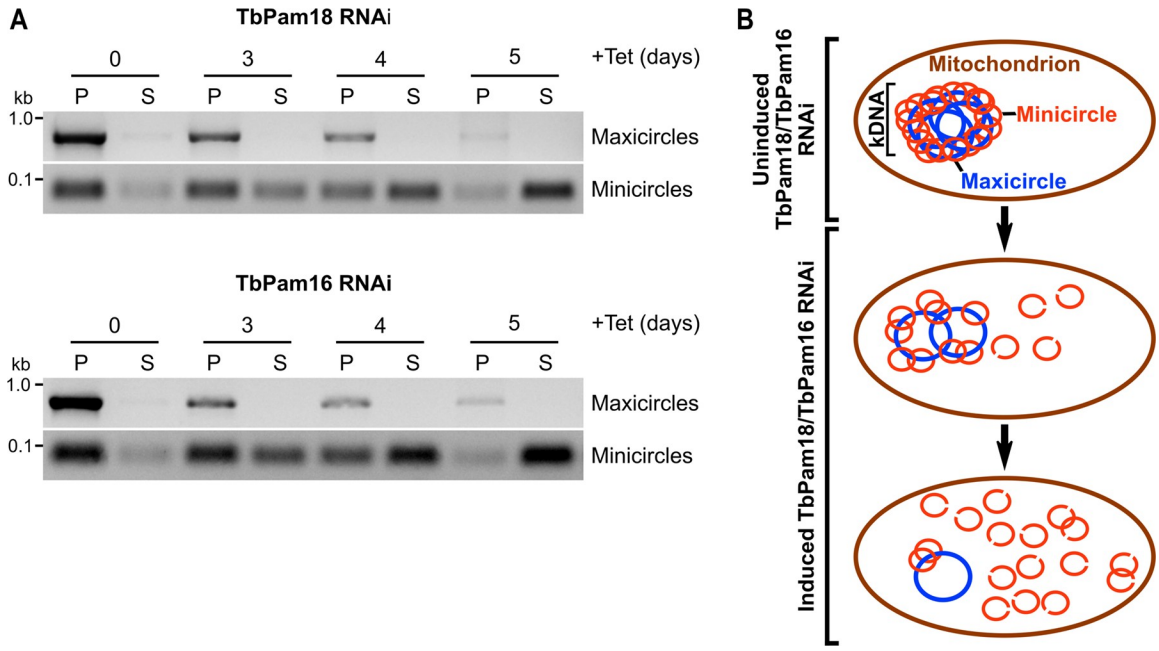

Fig 3. Ablation of TbPam18 and TbPam16 causes accumulation of free minicircles. (A) A quantitative PCR-based method was used to analyze steady-state levels of kDNA-bound or free mini- and maxicircles. Digitonin-extracted, mitochondria-enriched pellets from uninduced and 3 to 5 days induced TbPam18 and TbPam16 RNAi cells were solubilized in 1% digitonin. Subsequent centrifugation resulted in a pellet fraction (P) containing intact kDNA networks and a soluble fraction (S) containing free minicircles. DNA extracted from both fractions was used as template for PCR reactions amplifying specific mini- or maxicircle regions. PCR products were analyzed on agarose gels. **(B)** Schematic illustration of the putative sequence of effects on mini- and maxicircles upon RNAi-induced knockdown of TbPam18 and TbPam16. The ablation of TbPam18 and TbPam16 and the concomitant loss of maxicircles does not seem to inhibit the release of minicircles from the kDNA nor their replication. However, it appears to prevent the reattachment of free minicircles to the kDNA network. Consequently, free minicircles accumulate in the mitochondrial matrix. kDNA, kinetoplast DNA.

https://doi.org/10.1371/journal.pbio.3002449.g003

using PCR, to detect the changes in mini- and maxicircle levels and the same results were obtained (S5 Fig). The observation that the depletion of maxicircles is detected prior to the onsets of growth retardations (which occur at day 4) [26] suggests that TbPam18 and TbPam16 are directly involved in maxicircle replication or maintenance.

Since minicircles make up 90% of the kDNA [34], the massive network shrinkage seen in the DAPI stains of Fig 2A cannot be explained by a selective loss of maxicircles only [1,8]. One way to explain the constant levels of minicircles during TbPam18 and TbPam16 depletion (Fig 2B) is that they are released from the kDNA disk that progressively gets depleted from maxicircles.

To detect potential changes in free minicircle levels, digitonin-extracted, mitochondria-enriched pellets from uninduced and induced TbPam18 and TbPam16 RNAi cells were solubilized in 1% digitonin. Subsequent centrifugation resulted in pellets containing kDNA networks and supernatants containing free minicircles. PCR analysis of the DNA extracted from these fractions showed that maxicircles were only present in the pellets and that their levels decreased over time of induction as expected (Fig 3A). Minicircles behaved very differently. In uninduced cells, they were almost exclusively found in pellet fractions and thus in the kDNA networks. However, during the course of the RNAi, the amount of detected minicircles completely shifted to the supernatant (Fig 3A). Thus, ablation of TbPam18 and TbPam16, and the accompanying loss of maxicircles, does not inhibit the release of minicircles from the remaining kDNA network, nor their replication. But it appears to prevent their reattachment to the maxicircle-depleted networks (Fig 3B).

TbPam18 and TbPam16 have procyclic form-specific functions

T. brucei has a complex life cycle alternating between an insect vector, the Tsetse fly, and a mammalian host. One of the replicative stages in the insect vector is the procyclic form (PCF), which contains an extensively reticulated mitochondrion that is capable of OXPHOS. The replicative stage in the mammalian host is the bloodstream form (BSF), which has a less reticulated mitochondrion that cannot perform OXPHOS [27,48]. The BSF produces its energy exclusively by glycolysis. But because the mitochondrial membrane potential in BSFs is maintained by the F_1F_o ATP synthase working in reverse, a subunit of which is encoded on the kDNA, an intact kDNA network is essential not only in the PCF but also for the BSF [58,59].

It was therefore surprising that RNAi-mediated ablation of TbPam18 in the New York single marker (NYsm) BSF strain [60] did not affect growth (Fig 4A). However, the interpretation of this result is complicated, because even efficient RNAi never eliminates all mRNAs. It could be that the small amount of TbPam18 still present in these cells is sufficient for growth. To not run into the same issue with TbPam16, we established a TbPam16 NYsm double knockout (dKO) cell line, whose growth was indistinguishable from its parent cell line (Fig 4B). (For unknown reason, we were not able to produce a dKO cell line for TbPam18, not even a conditional one.)

In line with the lack of growth phenotypes there was no significant change in the size of the kDNA networks (Fig 4C) in neither the TbPam18-depleted RNAi cell line nor in the TbPam16 dKO cell line. Moreover, Southern blot analysis showed that the mean of mini- and maxicircle abundance was even higher in the 2 depleted cell lines; however, this change was not statistically significant (Fig 4D). This demonstrates that the function of TbPam16 is indeed specific for PCF trypanosomes and that its role in maxicircle replication is redundant in BSF cells or taken over by another protein. Moreover, based on the results of the TbPam18 RNAi cell line (Fig 4A) and the observation that TbPam16 and TbPam18, as Pam18 and Pam16 in yeast, likely form a heterodimer (Fig 1A), we conclude that the function of TbPam18 is also probably redundant in the BSF.

Integral membrane localization of TbPam18 and TbPam16 is functionally relevant

TbPam18 and TbPam16 are integral IM proteins [26], which raises the question whether this feature is essential for their function. To find out, we expressed RNAi-resistant TbPam18 and TbPam16 variants lacking their predicted transmembrane domains (TMDs) [61], as well as their short IMS-exposed N-termini (4 aa for TbPam18 and 33 aa for TbPam16) (Fig 5A) [55]. This was achieved by ectopically expressing the RNAi-resistant variants of the 2 proteins under tetracycline control in the background of the corresponding RNAi cell lines. In the complemented cell lines tetracycline addition therefore simultaneously induces RNAi and expression of the RNAi-resistant variants of the 2 proteins. Note that whereas the TbPam16 variants could be C-terminally HA-tagged, in the case of TbPam18, both N- and C-terminal tags abolished the function of the protein (Figs 5A and S6A). Expression of full-length TbPam18 or TbPam16-HA in RNAi cells ablated for the corresponding endogenous proteins, restored normal growth as expected (Fig 5B and 5C, left panels). However, the same was not the case for the ΔN-TbPam18 and ΔN-TbPam16-HA variants that lack the predicted N-terminal TMDs (Fig 5B and 5C, right panels). Both truncated variants were N-terminally fused to the mitochondrial targeting sequence (MTS) of trypanosomal TbmHsp60 to ensure their import into mitochondria. Since the TbPam16-HA and ΔN-TbPam16-HA variants were tagged, their expression and import could be verified biochemically using digitonin extractions (S6B Fig). The abundance of ΔN-TbPam16-HA is approximately 1.5-fold higher than the one of the full-

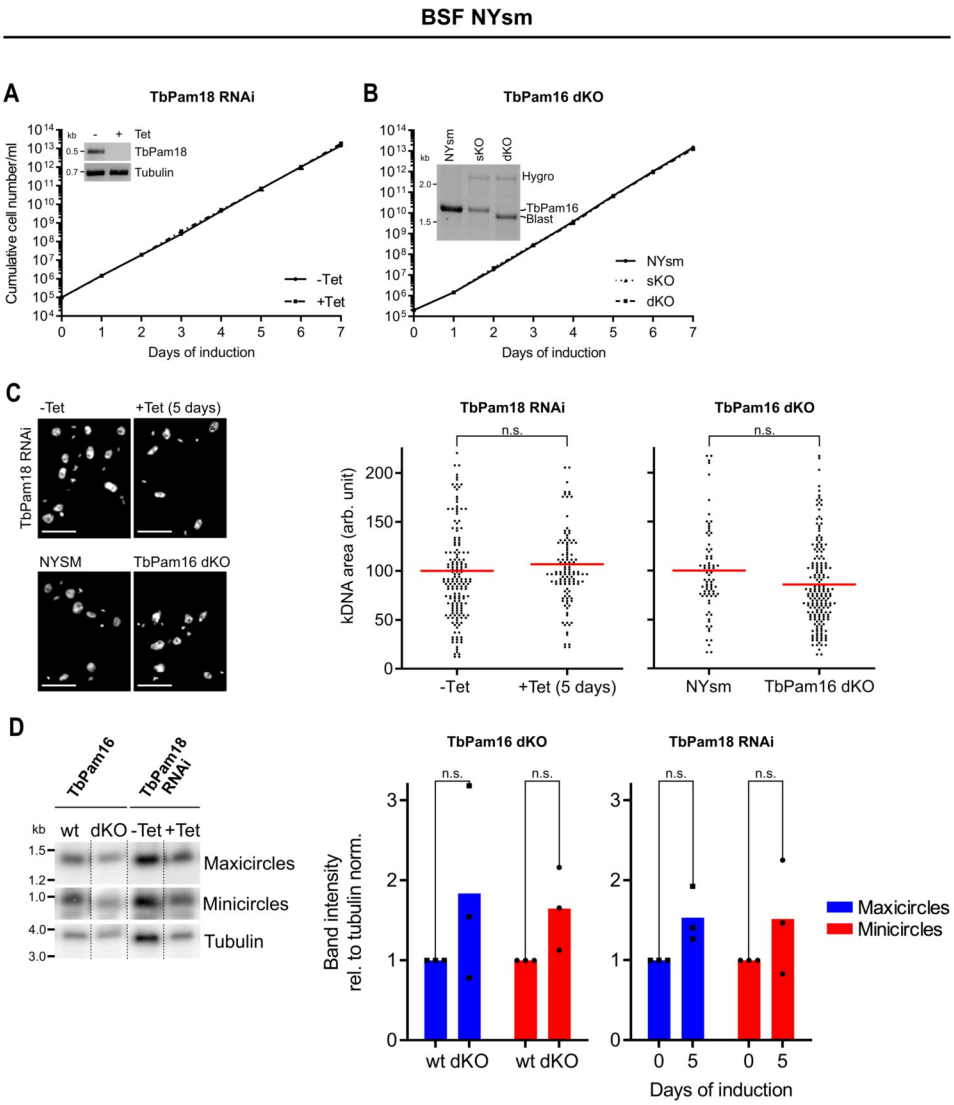

Fig 4. TbPam18 and TbPam16 are not essential in BSF trypanosomes. (A) Growth curve of uninduced (-Tet) and induced (+Tet) BSF NYsm RNAi cell line ablating TbPam18. Error bars correspond to the standard deviation ($n = 3$, error bars are too small to be visible). Inset: RT-PCR product of the wt TbPam18 mRNA in uninduced (-) or 2 days induced (+) cells. Tubulin mRNA serves as loading control. **(B)** Growth curve of NYsm, TbPam16 sKO, and dKO BSF cell lines. Inset: Verification of sKO and dKO by PCR using 1 primer pair to amplify the TbPam16 ORF (approximately 1.7 kilobases (kb)), the hygromycin (hygro, approximately 2.3 kb), or blasticidin (blast, approximately 1.6 kb) resistance cassettes at the same time. Hygro was used to replace the first allele and blast was used to replace the second allele. **(C)** Left: Comparison of DAPI-stained uninduced and 5 days induced BSF TbPam18 RNAi cells as well as BSF NYsm (parental cell line) and BSF TbPam16 dKO cells by fluorescence microscopy analysis. Right: Quantification of kDNA areas in 78 to 191 DAPI-stained cells. The red line indicates the mean of the kDNA areas. The mean of the uninduced TbPam18 RNAi cells and the NYsm cells was set to 100%. n.s.: not significant (P value >0.05) as calculated by a permutation test. **(D)** Southern blot analysis of mini- and maxicircles in NYsm (wt) cells, TbPam16 dKO cells as well as uninduced (-Tet) and 5 days induced (+Tet) BSF TbPam18 RNAi cells. Left: Total DNA from the indicated cell lines was isolated and digested with HindIII and XbaI. Probes specifically recognizing mini- or maxicircles were used. A probe detecting a 3.6-kb fragment of the tubulin intergenic region serves as loading control. Right: Densitometric quantification of mini- and maxicircle abundance on Southern blots. The ratio of the mini- or maxicircle abundance and the respective loading control (tubulin) was normalized (norm.) to the ratios of uninduced cells. Blue (maxicircles) and red (minicircles) bars represent the mean of 3 independent biological replicates. n.s.: not significant as calculated by an unpaired two-tailed t test. Numerical data for panels (A) to (D) are available in S1 Data. BSF, bloodstream form; dKO, double knockout; kDNA, kinetoplast DNA; NYsm, New York single marker; ORF, open reading frame; sKO, single knockout.

https://doi.org/10.1371/journal.pbio.3002449.g004

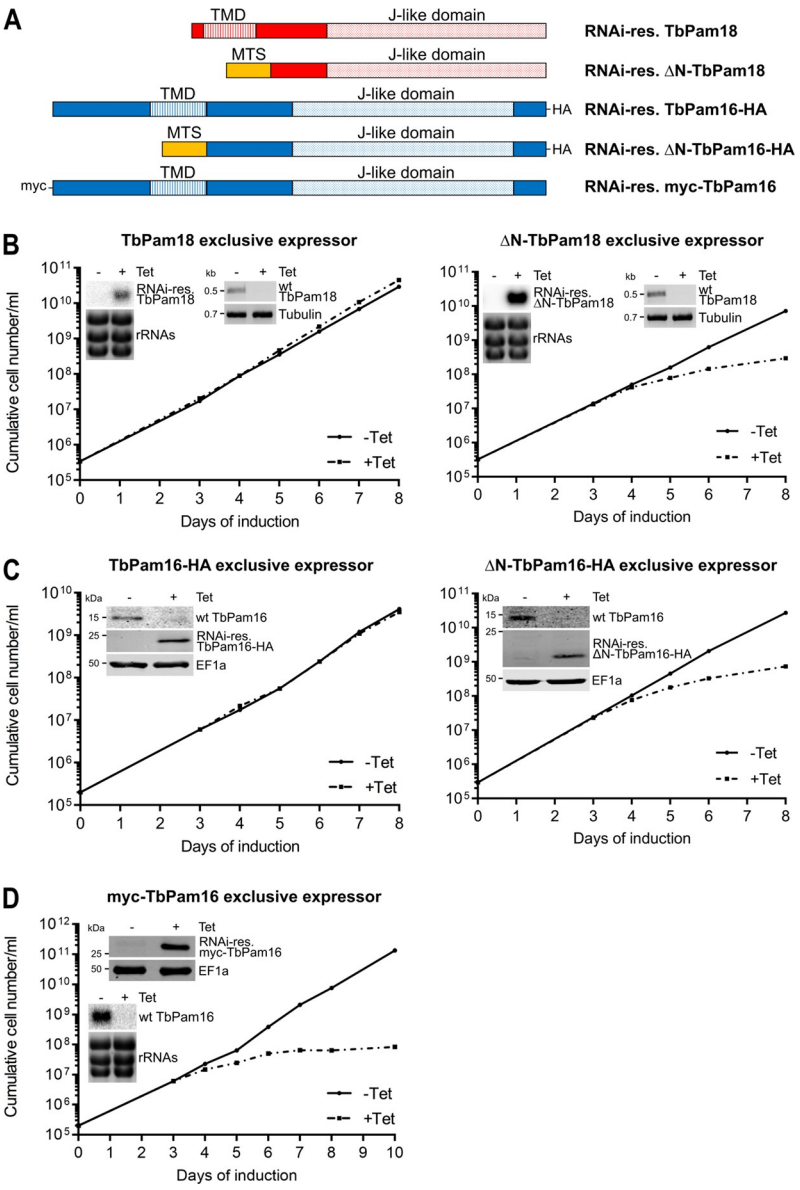

Fig 5. Integral membrane localization of TbPam18 and TbPam16, as well as the IMS-exposed N-terminus of TbPam16 are functionally relevant. (A) Schematic representation of RNAi-resistant (RNAi-res.) full-length and N-terminally truncated variants of TbPam18 and TbPam16. TbPam18 constructs are untagged, while TbPam16 constructs carry an N-terminal myc-tag or a C-terminal HA-tag. Predicted TMDs and J-like domains are indicated. Predicted TMDs and J-like domains are indicated. To ensure mitochondrial localization, the N-terminally truncated variants were expressed carrying the MTS of trypanosomal mitochondrial heat shock protein 60. **(B)** Growth curves of uninduced (-Tet) and induced (+Tet) cell lines ectopically expressing RNAi-res., full-length TbPam18 (left), or ΔN-TbPam18 (right) in the background of RNAi targeting the wild-type (wt) TbPam18 (TbPam18 and ΔN-TbPam18 exclusive expressors). Insets on the left: Northern blots of total RNA isolated from uninduced (-) and 2 days induced (+) cells probed for the mRNAs of RNAi-res. TbPam18 or ΔN-TbPam18 to confirm efficient inducible ectopic expression. Ethidium bromide-stained rRNAs serve as loading control. Insets on the right: RT-PCR products of the wt TbPam18 mRNA in uninduced (-) or 2 days induced (+) cells. Tubulin mRNA serves as loading control. **(C)** Growth curve of uninduced (-Tet) and induced (+Tet) cells ectopically expressing RNAi-res. TbPam16-HA (left) or ΔN-TbPam16-HA (right) in the background of RNAi targeting the wt TbPam16 (TbPam16-HA and ΔN-TbPam16-HA exclusive expressors). Insets: Immunoblot analysis of whole-cell extracts of uninduced (-) and 2 days induced (+) cells probed for wt TbPam16, RNAi-res. TbPam16-HA or ΔN-TbPam16-HA and EF1a as loading control. **(D)** Growth curve of uninduced (-Tet) and induced (+Tet) cells ectopically expressing RNAi-res. HA-TbPam16 in the background of RNAi targeting the wt TbPam16. Top inset: Immunoblot analysis of whole-cell extracts of uninduced (-) and 2 days induced (+) cells probed for myc-TbPam16 and EF1a as loading control. Bottom

inset: Northern blot of total RNA isolated from uninduced (-) and 2 days induced (+) cells probed for the mRNA of wt TbPam16. Ethidium bromide-stained rRNAs serve as loading control. Numerical data for panel (B) to (D) are available in S1 Data. MTS, mitochondrial targeting sequence; TMD, transmembrane domain.

https://doi.org/10.1371/journal.pbio.3002449.g005

length variant indicating that the lack of complementation is not due to insufficient expression of the protein (S6C Fig).

Alkaline carbonate extractions furthermore showed that as expected for an integral membrane protein, full-length TbPam16-HA is exclusively recovered in the pellet. In contrast, the major fraction of the truncated ΔN-TbPam16-HA is recovered in the supernatant indicating it is soluble.

In summary, the results in Fig 5A–5C suggest that the integration of TbPam18 and TbPam16 into the IM is essential for their function and thus link maxicircle replication to the IM.

The IMS-exposed N-terminus of TbPam16 is functionally relevant

To find out, whether the very N-terminus of the 33 aa IMS-exposed domain is required for TbPam16 function, we expressed an N-terminally myc-tagged version of RNAi-resistant TbPam16 in the background of the TbPam16-RNAi cell line (Fig 5A). As in the case of the ΔN-TbPam16-HA variant, the myc-TbPam16 was not able to complement growth (Fig 5D). The myc-TbPam16 was highly expressed and a small amount was recovered in the crude mitochondrial fraction in a digitonin extraction. Moreover, essentially all myc-TbPam16 in this fraction was recovered in the pellet after an alkaline carbonate extraction as would be expected for an integral membrane protein (S6B Fig). These results suggest that the N-terminal myc-tag interferes with TbPam16 function indicating that at least part the IMS-exposed domain of TbPam16 is essential for its function.

The J-domain of yeast Pam18 cannot complement the loss of the TbPam18 J-like domain

Classic Pam18 homologues involved in mitochondrial protein import contain the highly conserved tripeptide HPD in their J-domain (S7A Fig) [57], which is essential for the stimulation of the ATPase activity of their Hsp70 partners [62,63]. In contrast, TbPam18 has a degenerate J-domain containing the tripeptide HSD making it a J-like protein [63], a feature that is highly conserved within kinetoplastids (S7B Fig). Thus, we wondered (i) whether the HSD motif of TbPam18 is important for its function; and (ii) if the J-domain of yeast Pam18 (ScPam18) can take over the function of the J-like domain of TbPam18.

To that end, we generated a cell line allowing the exclusive expression of a TbPam18 variant in which the tripeptide HSD was mutated to HPD (TbPam18-S98P, Fig 6A). Intriguingly, this variant can fully complement the growth retardation caused by the RNAi-mediated depletion of TbPam18 (Fig 6B). Thus, TbPam18 can function with both, J or J-like domains.

To find out whether the intact J-domain of ScPam18 can replace the J-like domain of TbPam18, we used a chimeric protein consisting of the TMD of TbPam18 and the J-domain of ScPam18 (Tb/ScPam18) (Fig 6A). Expression of Tb/ScPam18 in TbPam18 RNAi background delayed the onset of the growth phenotype by 1 day but could not rescue the growth retardation at later time points (Fig 6C).

Because tagged versions of TbPam18 are not functional (S6A Fig), the variants tested above were untagged. Nevertheless, we analyzed the localization of N-terminally myc-tagged TbPam18 and Tb/ScPam18, which showed that about half of each variant is recovered in the

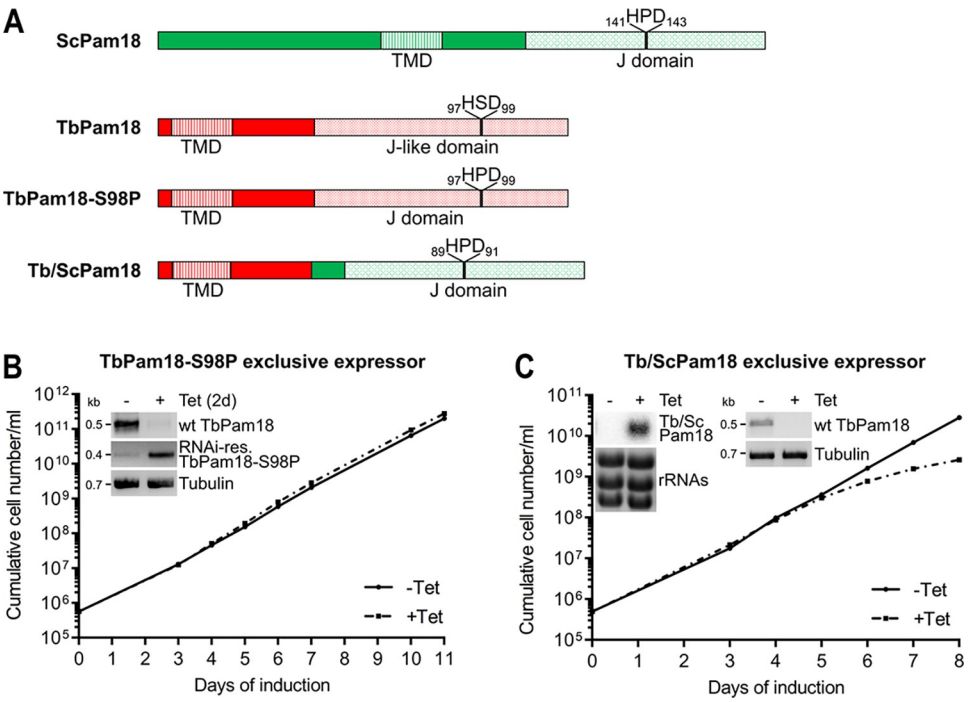

Fig 6. The J-domain of ScPam18 cannot complement the loss of the J-like domain of TbPam18. (A) Schematic representations of yeast (Sc) Pam18, TbPam18, and a mutated TbPam18 version, in which the J-like domain was altered to a J-domain by changing the serine residue at position 98 to a proline residue (TbPam18-S98P). Finally, a Tb/Sc fusion Pam18 (Tb/ScPam18), in which the J-like domain of TbPam18 was replaced by the J-domain of ScPam18 is shown. **(B)** Growth curve of uninduced (-Tet) and induced (+Tet) cells ectopically expressing RNAi-res. TbPam18-S98P in the background of RNAi targeting the endogenous wt TbPam18 (TbPam18-S98P exclusive expressor). Inset: RT-PCR products of wt TbPam18 and TbPam18-S98P mRNAs in uninduced (-) or 2 days induced (+) cells. Tubulin mRNA serves as loading control. **(C)** Growth curve of uninduced (-Tet) and induced (+Tet) cells ectopically expressing RNAi-resistant (RNAi-res.) Tb/ScPam18 in the background of RNAi targeting the endogenous wild-type (wt) TbPam18 (Tb/ScPam18 exclusive expressor). Inset on the left: Northern blot of total RNA extracted from uninduced (-) and 2 days induced (+) cells, probed for Tb/ScPam18, to confirm inducible ectopic expression. Inset on the right: RT-PCR product of the wt TbPam18 mRNA in uninduced (-) or 2 days induced (+) cells. Tubulin mRNA serves as loading control. Numerical data for panel (B) and (C) are available in S1 Data. TMD, transmembrane domain.

https://doi.org/10.1371/journal.pbio.3002449.g006

mitochondria-enriched fraction of a digitonin extraction (S7C Fig). Moreover, in an alkaline carbonate extraction, both TbPam18 versions present in the mitochondria-enriched fraction are exclusively recovered in the pellet indicating they are integrated into the IM. This strongly suggest that also untagged TbPam18 and Tb/ScPam18 are correctly localized.

In summary, these results show that some feature of the ScPam18 J-domain, other than the HSD or HPD tripeptide, is incompatible with the function of TbPam18.

TbPam16 interacts with TbPam18 and 2 additional essential proteins

We have previously used TbPam18-HA and TbPam16-HA for SILAC co-immunoprecipitations experiments (CoIP) [26]. However, tagged TbPam18 is not functional (S6A Fig). Moreover, in the TbPam16-HA CoIP experiment, the only interactor identified was TbPam18 [26]. Thus, in hindsight, these experiments are difficult to interpret. Therefore, we repeated the TbPam16 SILAC CoIP with 2 modifications. First, we used the newly generated cell line allowing exclusive expression of functional TbPam16-HA (Fig 5C), and second, we analyzed both premix as well as postmix samples. Premix conditions means that differentially labeled

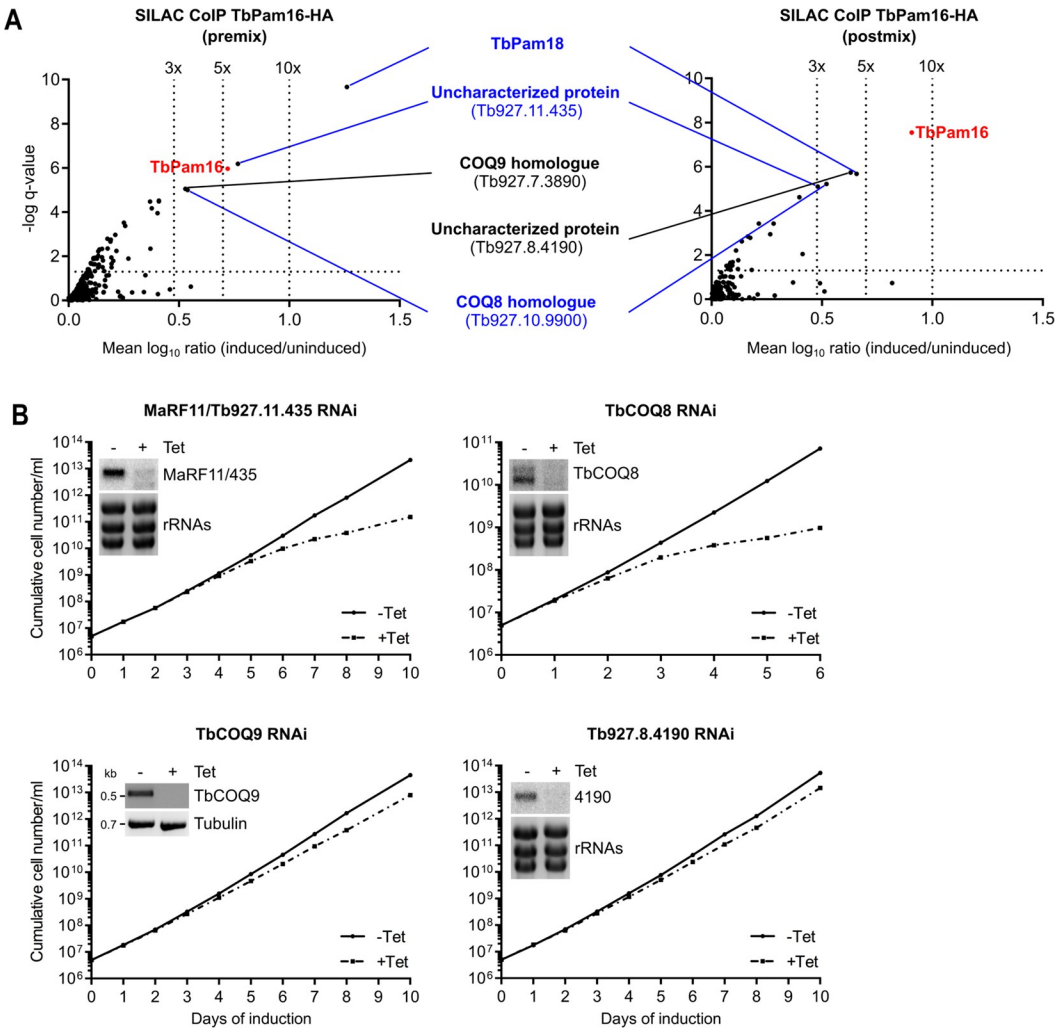

Fig 7. TbPam16 interacts with TbPam18 and 2 other essential proteins. (A) Volcano plots depicting proteins detected in SILAC-based quantitative MS analysis of TbPam16-HA CoIPs. In the experiment on the left, differentially labeled uninduced and induced cells were mixed and the resulting mixture was subjected to CoIP (premix). In the experiment on the right, CoIPs with uninduced and induced cells were done separately and the resulting eluates were mixed afterwards (postmix). The vertical dotted lines in the volcano plots indicate the specified enrichment factors. The horizontal dotted line indicates a rank-sum test significance level of 0.05. The bait TbPam16 is highlighted in red. Proteins that were significantly detected and enriched more than 3-fold in the pre- as well as the postmix experiments are labeled in blue. Proteins enriched more than 3-fold in either the pre- or the postmix experiment are labeled in black. **(B)** Growth curves of uninduced (-Tet) and induced (+Tet) MaRF11/Tb927.11.435, TbCOQ8, TbCOQ9, and Tb927.8.4190 RNAi cells. Insets in the MaRF11/Tb927.11.435, TbCOQ8, and Tb927.8.4190 RNAi growth curves: Northern blots of total RNA extracted from uninduced (-) and 2 days induced cells (+), probed for the respective mRNAs. Ethidium bromide-stained ribosomal RNAs (rRNAs) serve as loading controls. Inset in the TbCOQ9 RNAi growth curve: RT-PCR product of the TbCOQ9 mRNA in uninduced (-) or 2 days induced (+) cells. Tubulin mRNA serves as loading control. Numerical data for panel (A) and (B) are available in S2 Table and S1 Data, respectively. MS, mass spectrometry.

https://doi.org/10.1371/journal.pbio.3002449.g007

uninduced and induced cells are mixed prior to the CoIP, which preferentially detects stable interaction partners. In contrast, in the postmix sample, the eluates from separately generated, differentially labeled CoIPs are mixed, allowing the detection of both stable and more transient interaction partners [64].

In the premix experiment, TbPam16 was enriched 5.3-fold and in the postmix experiment 8.1-fold demonstrating that both CoIPs were successful (Fig 7A). Importantly, apart from the

bait TbPam16, the most enriched protein in both experiments was TbPam18 confirming the interaction between the 2 proteins.

Interestingly, in addition to TbPam18, 2 other proteins were enriched more than 3-fold in both experiments (Fig 7A). The first one is a trypanosome-specific, uncharacterized protein (Tb927.11.435) with a molecular weight of only 10.6 kDa and a remarkably high isoelectric point (pI = 10.6). This is interesting because a high pI is a characteristic often found in DNA-binding proteins. An AlphaFold structure prediction of Tb927.11.435 reveals that it consists of 4 consecutive in part amphiphilic α-helices (S8 Fig) [65]. The second protein, Tb927.10.9900 (Fig 7A), is homologous to yeast and human COQ8 and thus was termed TbCOQ8. COQ8 is a subunit of the coenzyme Q biosynthetic complex (complex Q), located on the matrix face of the IM [66]. While COQ8 appears to be required for coenzyme Q synthesis, its exact role is not known. Sequence homology suggests COQ8 might be a protein kinase; however, it likely does not function as a canonical kinase but may use its ATPase activity to stabilize complex Q [66]. Intriguingly, in the TbPam16-HA premix SILAC CoIP, Tb927.7.3890, a protein orthologous to complex Q subunit 9 (COQ9) was detected. COQ9 is a lipid-binding protein associated with COQ7 [66]. The presence of TbCOQ8 and TbCOQ9 among the most enriched proteins in the TbPam16-HA SILAC CoIPs is striking. However, only little is known about ubiquinone biosynthesis in *T. brucei* and neither of the 2 subunits have been previously analyzed. In the postmix experiment, the fifth protein enriched more than 3-fold was Tb927.8.4190, another trypanosome-specific, uncharacterized protein.

To further study the 4 newly identified TbPam16 interaction partners, we generated PCF RNAi cell lines. Growth curves revealed that knockdowns of Tb927.11.435 and TbCOQ8 cause a retardation in growth starting after 5 and 2 days of induction, respectively (Fig 7B). In contrast, RNAi against TbCOQ9 and Tb927.8.4190 only marginally affected growth. Hence, we focused on Tb927.11.435 and TbCOQ8 in further experiments.

Tb927.11.435 ablation phenocopies the depletions of TbPam18 and TbPam16

Next, we investigated the fate of the kDNA upon Tb927.11.435 or TbCOQ8 depletion using the methods that were applied for TbPam16 and TbPam18 (Figs 2A, 3, and S5).

Quantification of DAPI-stained RNAi cells using fluorescence microscopy showed that in the Tb927.11.435 RNAi cell line the kDNA size was significantly reduced to 80% and 36% after 3 (prior to the onset of the growth retardation at day 4) to 6 days of RNAi induction, respectively (Fig 8A). On the contrary, ablation of TbCOQ8 was not found to significantly change the size of the kDNA over 4 days of RNAi induction. The kDNA network in the Tb927.11.435 RNAi cell line was further analyzed by quantitative PCR, which showed a decrease in the amount of maxicircles to 31% and less than 10% after 3 to 4 days of RNAi induction, respectively. In contrast, there was no significant change in the amount of minicircles for at least 6 days (Fig 8B). However, while the total amount of minicircles remained constant, they were progressively and essentially completely released from the kDNA network within 5 days of induction (Fig 8C).

Finally, we analyzed the Tb927.11.435 RNAi cell line using SILAC-based quantitative MS (S9 and S10 Figs), as was done for TbPam18 and TbPam16 RNAi cell lines (Figs 1B, S2, and S3). A total of 904 mitochondrial proteins [1,29,48] were detected. The most affected proteins were MRPs and OXPHOS subunits, of which 58% and 17% were depleted more than 1.5-fold, making up for 60% of all 1.5-fold depleted mitochondrial proteins (S9 Fig). For 7 protein categories consisting exclusively of nucleus-encoded proteins only 2 out of 205 proteins were more than 1.5-fold depleted (S10 Fig). These results are very similar to what has been observed in TbPam18 or TbPam16 depleted cells (Figs 1B, S2, and S3).

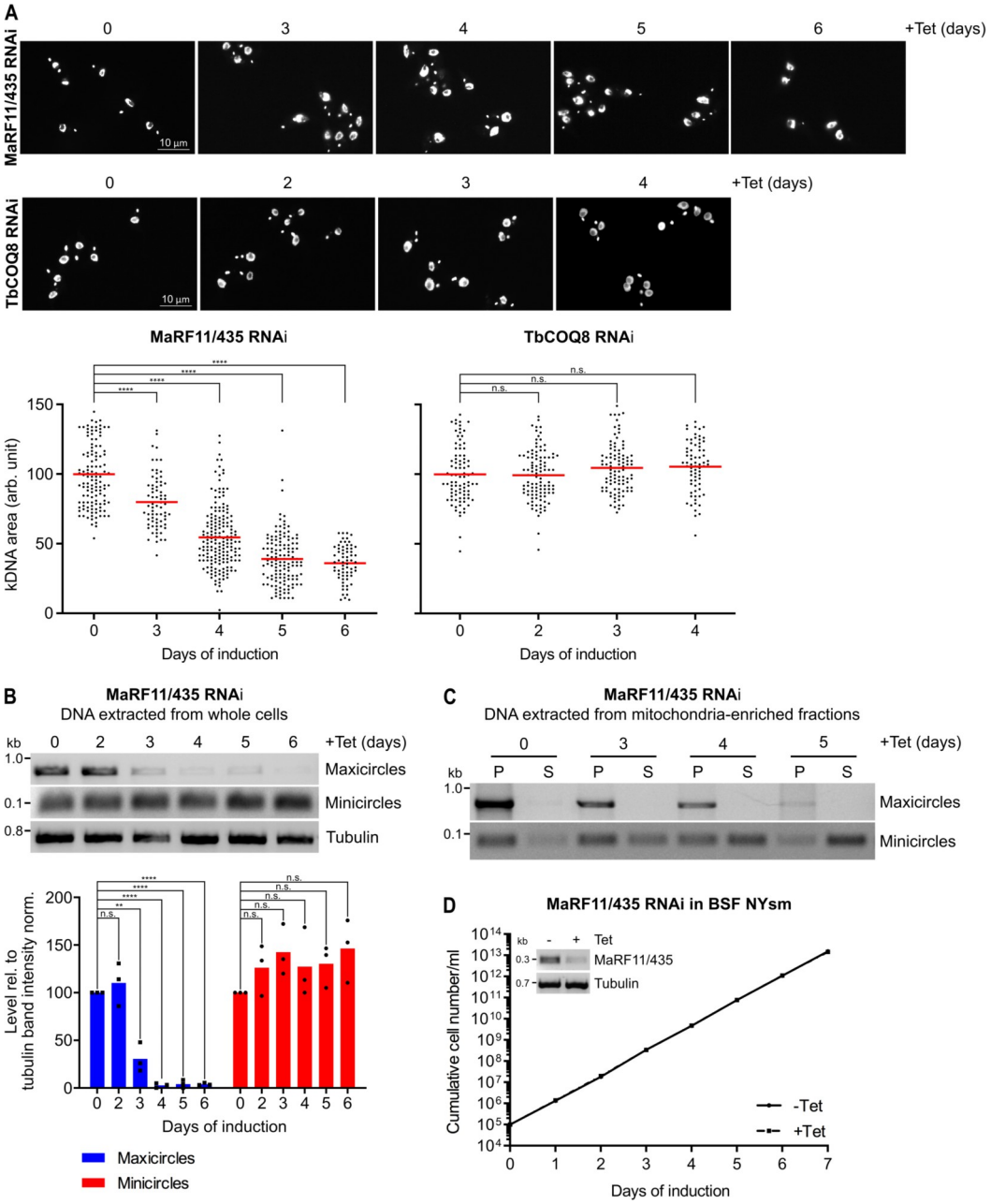

Fig 8. Ablation of MaRF11/Tb927.11.435 phenocopies the depletions of TbPam18 and TbPam16 in PCF and BSF. (A) Upper panels: Fluorescence microscopy analysis of DAPI-stained uninduced and 3 to 6 days induced MaRF11/Tb927.11.435 (435) RNAi cells as well as uninduced and 2 to 4 days induced TbCOQ8 RNAi cells. Lower panels: Quantification of kDNA areas in 65 to 175 DAPI-stained RNAi cells. Red line indicates the mean of the kDNA size at each time point. The mean of the uninduced cells was set to 100%. n.s. = not significant, ****: *P* value <0.0001, as calculated by an unpaired two-tailed *t* test. **(B)** Upper panel: A quantitative PCR-based (qPCR) method was used to detect changes in steady-state levels of total mini- and maxicircles. Total DNA was extracted from uninduced and 2 to 6 days induced MaRF11/435 RNAi cells. This DNA was used as the template in PCRs amplifying specific mini- and maxicircle regions or the intergenic region of tubulin. PCR products were analyzed on agarose gels. Lower panels: Densitometric quantification of mini- and maxicircle abundance as detected by qPCR. The ratio of the mini- or maxicircle band intensity and the respective loading control (tubulin band intensity) was normalized (norm.) to the ratios of uninduced cells. Blue (maxicircles) and red (minicircles) bars represent the mean of 3 independent biological replicates. n.s.: not significant, **: *P* value <0.05, ****: *P* value <0.0001, as calculated by an unpaired two-tailed *t* test. **(C)** A quantitative PCR-based method used to analyze steady-state levels of kDNA-bound or free mini- and maxicircles. A digitonin-extracted, mitochondria-enriched pellet from uninduced and 3 to 5 days induced MaRF11/435 RNAi cells was solubilized in 1% digitonin. A subsequent centrifugation

step resulted in a pellet fraction (P) containing intact kDNA networks and a soluble fraction (S) containing free minicircles. DNA extracted from both fractions was used as template for PCR reactions amplifying specific mini- or maxicircle regions. PCR products were analyzed on agarose gels. **(D)** Growth curve of uninduced (-Tet) and induced (+Tet) BSF NYsm RNAi cell line ablating MaRF11/435. Inset: RT-PCR product of MaRF11/435 mRNA in uninduced (-) or 2 days induced (+) cells. Tubulin mRNA serves as loading control. Numerical data for panel (A), (B), and (D) are available in S1 Data. BSF, bloodstream form; kDNA, kinetoplast DNA; NYsm, New York single marker; PCF, procyclic form.

https://doi.org/10.1371/journal.pbio.3002449.g008

To quantify the similarities the depletion of TbPam18, TbPam16, and Tb927.11.435 caused on the mitochondrial proteome, we performed a correlation analysis comparing all 3 data sets. Moreover, we included a previously published SILAC RNAi data set for TbTim17, the core component of the single trypanosomal TIM complex (S11 Fig) [22]. This allowed to compare how the mitochondrial proteome reacted to depletion of a general IM import factor versus factors involved in maxicircle replication. The results showed that the Spearman's rank correlation factors among the TbPam18, TbPam16, and Tb927.11.435 data sets were between 0.69 and 0.73 (S11 Fig), which is very high considering the maximal possible correlation is 1.0. In contrast, the correlation between the TbTim17 data set and the 3 other data sets was much lower ranging from 0.21 to 0.3 (S11 Fig).

These results show that depletion of TbPam18, TbPam16, and Tb927.11.435 caused the same proteomic phenotypes, strongly suggesting that the 3 proteins are involved in the same biological process. Moreover, the results also confirm that depletion of TbTim17, a general IM import factor, results in different changes to the mitochondrial proteome than were observed for the 3 other factors.

Thus, depletion of Tb927.11.435 exactly phenocopied the results observed in induced TbPam16 and TbPam18 PCF RNAi cells, which is why we named it maxicircle replication factor of 11 kDa (MaRF11) (Figs 2, 3, and 8). Moreover, RNAi-induced knockdown of MaRF11 in BSF NYsm cells does not cause a change in the growth rate, which is identical to what is observed in BSF TbPam18 RNAi or TbPam16 dKO cells (Figs 4 and 8D).

TbHslV controls the level of MaRF11

One way in which TbPam18 and TbPam16 could regulate the activity of MaRF11 would be by controlling its degradation, reminiscent of TbPIF2, the levels of which are controlled by the mitochondrial protease TbHsIVU [47]. Indeed, RNAi-mediated ablation of the TbHslV subunit of TbHslVU results in a growth retardation (Fig 9A) and a concomitant accumulation of giant kDNAs as observed previously (Fig 9B) [47]. Under the same conditions, analogous to TbPIF2, a continuous increase in the levels of MaRF11 for up to 6 days after induction was observed, whereas the levels of TbPam16 and EF1a remained constant (Fig 9C).

Discussion

Our study has shown that TbPam18 and TbPam16 are essential for replication of the maxicircle component of the kDNA (Fig 2). This observation closes an important gap in the previously proposed evolutionary scenario explaining why trypanosomes have a single bifunctional TIM complex only [26]. Our finding is unexpected, because neither Pam18 nor Pam16 orthologues have ever been associated with the biogenesis of the mitochondrial genome before. Thus, while phylogenomics classifies TbPam18 and TbPam16 as bona fide Pam18 and Pam16 orthologues [26], the 2 proteins have switched their function during evolution, from protein import to mitochondrial genome replication. It is worth noting that this change in function could only be discovered experimentally and was not predicted in silico. Interestingly, yeast Pam18 has also been associated with another function than mitochondrial protein import. It

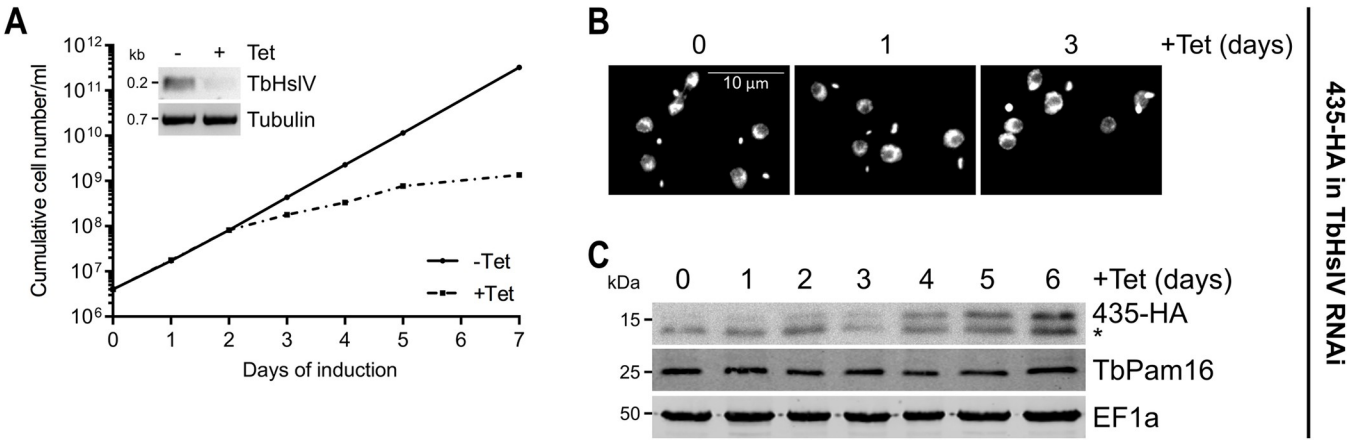

Fig 9. TbHslV controls the level of MaRF11/Tb927.11.435. (A) Growth curve of uninduced (-Tet) and induced (+Tet) cells expressing MaRF11/435-HA in the background of TbHslV RNAi. Inset shows the RT-PCR product of the TbHslV mRNA in uninduced (-) or 2 days induced (+) cells. Tubulin mRNA serves as loading control. **(B)** Fluorescence microscopy analysis of the DAPI-stained uninduced and 1 or 3 days induced cell line explained in (A). **(C)** Immunoblot analysis of steady-state protein levels of MaRF11/435-HA and TbPam16 in TbHslV RNAi background over 6 days of induction. EF1a serves as loading control. Asterisk indicates an unspecific band. Numerical data for panel (A) are available in S1 Data.

https://doi.org/10.1371/journal.pbio.3002449.g009

can stimulate the mHsp70-dependent assembly of respiratory super-complexes, when present as a homodimer [67]. However, in contrast to TbPam18, yeast Pam18 is still an essential component of the PAM and thus has a dual function.

Among all proteins known to be involved in kDNA maintenance and replication, depletion of only 4 preferentially affects the maxicircles: the mitochondrial RNA polymerase (mtRNAP) [68], the mitochondrial DNA primase 1 (TbPRI1) [52], the mitochondrial DNA helicase (TbPIF2) [47], and the mitochondrial heat shock proteins TbmHsp70/TbmHsp40 [53]. We have now discovered 3 additional factors: TbPam18, TbPam16, and the TbPam16-interacting MaRF11. Each of them is essential for normal growth of PCF *T. brucei* [26] (Fig 7B) and their depletion specifically affects replication of the maxicircles prior to the onset of the growth arrest (Figs 2B and 8B). Interestingly, similar to what has been observed upon ablation of the maxicircle replication factors mentioned above, total minicircle levels remain constant after the loss of maxicircles upon TbPam18, TbPam16, and MaRF11 depletion (Figs 2B and 8B). Moreover, depletion of TbPRI1 [52] and TbmHsp70/TbmHsp40 [53], but not of TbPIF2 [47], causes a rapid shrinkage of kDNA disks. The same was observed after TbPam18, TbPam16, and MaRF11 ablation (Figs 2A and 8A). A reduction in maxicircles alone, which make up only 10% of the kDNA network, cannot explain this shrinkage. In fact, while maxicircles are selectively depleted in the TbPIF2 RNAi cell line, its kDNA network remains intact [47]. It has been suggested for TbPRI1 [52] and TbmHsp70/TbmHsp40 [53] depletion that the shrinkage of the kDNA network is due to the detachment of minicircles from the kDNA disk. The free minicircles are then replicated but cannot reattach to the maxicircle-depleted kDNA network. As a consequence, the kDNA network shrinks and free minicircles accumulate in the mitochondrial matrix [52,53], which is exactly what is also observed in the TbPam18, TbPam16, and the MaRF11 RNAi cell lines (Figs 3 and 8C).

How can we explain that TbPam16, TbPam18, and MaRF11 are dispensable in the BSF of *T. brucei*? The 2 life cycle stages show many differences, including optimal growth temperatures (27˚C for PCF/37˚C for BSF) and generation times (10 to 12 h for PCF/5 to 6 h for BSF). Moreover, the PCF can undergo cytokinesis without completion of mitosis, whereas in the BSF a mitotic block inhibits cytokinesis but not kDNA replication [69]. Thus, it would not be

surprising if these differences may require some life cycle stage-specific adaptations in the regulation of kDNA replication.

TbPam18 and TbPam16 are integral IM proteins, each containing a single TMD [26] that is essential for their function (Fig 5). This contrasts with yeast, where the TMD of Pam18 is dispensable and where Pam16 does not even have a TMD [70]. Our results functionally connect maxicircle replication to the IM. This is unexpected as maxicircles are replicated while remaining interlocked with the kDNA network and proteins involved in their replication generally localize to the kDNA disk [71]. The only known integral IM protein associated with kDNA inheritance is p166, a subunit of the TAC [72,73]. The TAC is essential for kDNA segregation but not for its replication [37,74]. Knockdown of TAC subunits leads to enlarged, overreplicated kDNAs in a few cells [37,74], which is not what is observed upon TbPam16, TbPam18, and MaRF11 depletion. It is therefore unlikely that these 2 proteins are involved in kDNA segregation and their IM localization must be explained in a different way.

J-domain family proteins are known regulators of a plethora of biological processes by selecting client proteins for Hsp70-type chaperones [62,75,76]. Interestingly, *T. brucei* has a greatly expanded mitochondrial J-domain protein family consisting of at least 38 members [1,77–81]. One reason for this could be that they may be required for functional differentiation of the single TbmHsp70.

TbPam16, just as its yeast counterpart, is a J-like protein. However, while Pam18 in yeast contains an intact J-domain with a conserved HPD motif [70], TbPam18 is a J-like protein containing an HSD tripeptide. Expression of a chimeric protein, in which the J-like domain of endogenous TbPam18 was replaced by the J-domain of yeast Pam18, failed to restore growth in a TbPam18 RNAi cell line (Fig 6A and 6C). Surprisingly, the change of TbPam18's HSD to an HPD does not affect the functionality of the protein (Fig 6A and 6B). Thus, the divergence that prevents the functional interchangeability of the TbPam18 J-like domain with the J-domain of yeast Pam18 must have occurred outside the tripeptide motif.

Since the HPD motif is essential for the interaction of J-domains with their Hsp70 partners [82], the J-like domains of TbPam18 and TbPam16 likely cannot stimulate the ATPase activity of TbmHsp70, at least not directly. Thus, the change in function of TbPam18 during evolution must have allowed the inactivation of the conserved tripeptide from HPD to HSD indicating that TbPam18 and TbPam16 function independently of mHsp70. This is reminiscent to what has been suggested for *Arabidopsis thaliana*, which has 21 J-like proteins involved in various processes, most of which function independently of Hsp70 [83,84]. In line with this, pulldown experiments of TbPam16 prominently recover TbPam18, but neither TbmHsp70 nor other J-domain protein family members (Fig 7A). Instead, the SILAC CoIPs recovered the 2 essential proteins MaRF11 and TbCOQ8 indicating they might be client proteins (Fig 7A). This implies that the TbPam18/TbPam16 heterodimer binds to a few clients only. Ablation of TbCOQ8 inhibits growth of PCF trypanosomes, but does not affect the size of the kDNA (Figs 7B and 8A). However, ablation of the soluble, basic protein MaRF11 phenocopies what is observed in TbPam18 and TbPam16 RNAi cell lines (Figs 7B, 8A, and 8B). We have also shown that MaRF11 is a substrate of the mitochondrial proteasome orthologue TbHslVU, since depletion of the TbHslVU subunit TbHslV increases MaRF11 levels (Fig 9C). Thus, both MaRF11 and the previously characterized TbPIF2, the only 2 TbHsIVU substrates known to date, are essential maxicircle replication factors explaining the three to 4-fold accumulation of maxicircles in the absence of TbHslV [28]. However, the TbHsIVU substrate(s) causing the previously reported 20-fold accumulation of minicircles in the absence of TbHslVU remain unknown [28]. In summary, the identification of MaRF11 as a second substrate of TbHslVU underscores the central role the mitochondrial proteasome plays in controlling kDNA replication.

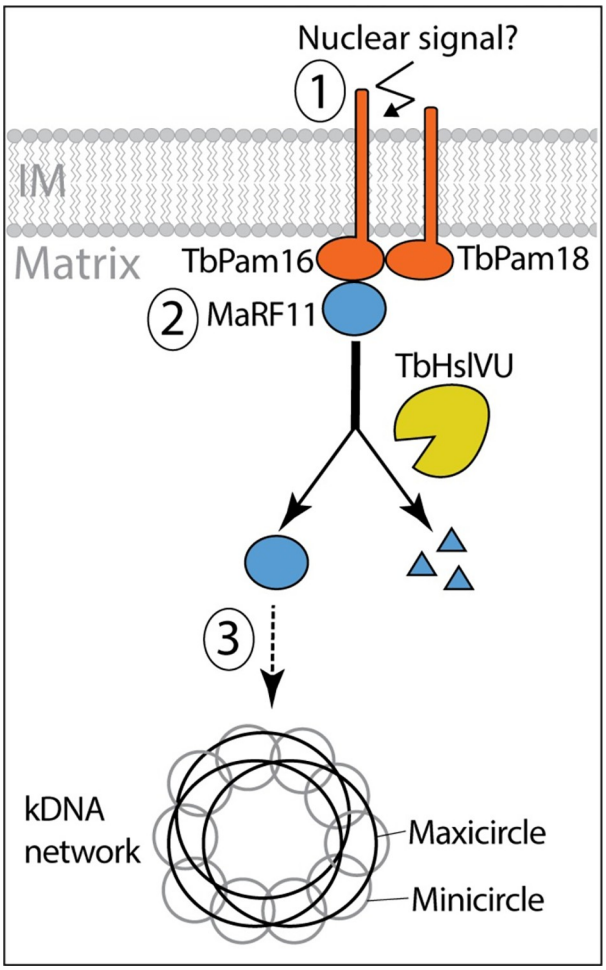

Fig 10. Working model of maxicircle replication control by MaRF11. The integral membrane proteins TbPam18 and TbPam16, together with the soluble matrix protein MaRF11, are part of membrane-bound complex required for maxicircle replication. MaRF11 acts downstream of TbPam18 and TbPam16. The levels of MaRF11 are regulated by proteolytic degradation via TbHsIVU. Outstanding questions are highlighted. These include the identity of a putative nuclear signal (1), how such a signal may regulate the binding of MaRF11 to TbPam18 and TbPam16 (2) and whether MaRF11 directly mediates maxicircle replication or whether it activates other as yet unknow replication factors (3). kDNA, kinetoplast DNA; IM, inner membrane.

https://doi.org/10.1371/journal.pbio.3002449.g010

Based on the results described above, we propose the following working model for a mitochondrial inner membrane-bound protein complex involved in the replication of the maxicircle portion of the kDNA (Fig 10). The complex includes the soluble protein MaRF11 and the integral IM proteins TbPam18 and TbPam16. The latter 2 probably form a heterodimer and have their J-like domains exposed to the matrix. All 3 proteins are individually essential for maxicircle replication in procyclic trypanosomes. The fact that MaRF11 is a soluble matrix protein suggests that it may function downstream of the integral IM proteins TbPam18 and TbPam16. Furthermore, we have shown that MaRF11 levels are controlled by proteolytic degradation by TbHslVU.

In *T. brucei*, the mitochondrial S-phase is precisely coordinated with the nuclear S-phase by an as yet unknown signal [85]. Since not only the TMDs of TbPam18 and TbPam16 but also the IMS-exposed N-terminus of TbPam16 are essential for normal growth, it is tempting to speculate that the TbPam18/TbPam16/MaRF11 complex may play a role in this coordination.

However, some aspects of the model remain speculative. For example, how MaRF11 controls maxicircle replication is still unknown. Its high pI would be consistent with a direct binding to the kDNA, but it is also possible that MaRF11 is only one component of a more elaborate maxicircle replication pathway that involves other factors further downstream. However, pulldown experiments aimed at identifying such factors in a cell line exclusively expressing tagged MaRF11 were not successful. Spatial proteomic analyses of the procyclic and bloodstream forms of *T. brucei* showed that at steady-state TbPam18, TbPam16, and MaRF11 co-fractionate with IM marker proteins, consistent with the TbPam16 pulldown experiment (Fig 7A) [86]. It would support our model if the 3 proteins were concentrated in the IM around the kDNA region. Unfortunately, despite the use of signal enhancement protocols, we were unable to detect any of the 3 tagged proteins by immunofluorescence microscopy. This suggests that, consistent with our inability to detect any of the 3 proteins by MS in our global SILAC proteomics studies, they are of too low abundance to be detected by immunofluorescence microscopy. Despite these limitations the proposed model can serve as a guide for future experiments aimed at providing more insights into the intricate process of how maxicircles and the kDNA in general are replicated.

Materials and methods

Transgenic cell lines

Transgenic *T. brucei* cell lines are either based on the PCF strain 29–13 or the BSF strain NYsm [60]. PCF cells were grown in SDM-79 [87] supplemented with 10% (v/v) fetal calf serum (FCS) at 27˚C. BSF cells were cultivated in HMI-9 [88] containing 10% (v/v) FCS at 37˚C.

RNAi against TbPam18 (Tb927.8.6310) and TbPam16 (Tb927.9.13530) has been described previously [26]. For complementation experiments, synthetic genes (Biomatik) were used. The codons in regions of the open reading frame (ORF) that are targeted by RNAi were changed such that their transcripts are RNAi resistant (RNAi-res.) but still translate into the same amino acid sequence as in the endogenous proteins. To produce constructs allowing expression of N-terminally truncated TbPam18 (ΔN-TbPam18) and TbPam16 (ΔN-TbPam16), the corresponding DNA fragments were amplified from the synthetic genes. To ensure targeting to mitochondria, the MTS of trypanosomal mitochondrial Hsp60 (TbmHsp60, Tb927.10.6510) was cloned in front of the truncated constructs. For the RNAi-res. Tb/ScPam18 fusion protein and RNAi-res. TbPam18-S98P, additional synthetic genes (Biomatik) were used. To generate RNAi-res. Tb/ScPam18, the first 138 nucleotides of RNAi-res. TbPam18 were fused to the last 213 nucleotides of wild-type yeast Pam18 (YLR008C). To generate TbPam18-S98P, the cytosine at position 292 of the nucleotide sequence of RNAi-res. TbPam18 was exchanged against a thymine. Sequences of all synthetic genes are shown in S12 Fig.

To generate plasmids for ectopic expression of untagged, N- or C-terminally triple c-myc- or HA-tagged, RNAi-res., full-length or N-terminally truncated TbPam18 or TbPam16 variants, Tb/ScPam18, TbPam18-S98P, MaRF11 and TbTim54 (Tb927.6.2470) the complete or truncated ORFs of the respective genes were amplified by PCR. The PCR products subsequently were cloned into a modified pLew100 vector [60,89], which contains a puromycin resistance cassette and either no epitope tag or triple c-myc- or HA-tags [90].

MaRF11, TbCOQ8, TbCOQ9, Tb927.8.4190, and TbHslV (Tb927.11.10240) RNAi cell lines were generated using the same pLew100-derived vector described above. This vector allows the generation of a stem-loop construct by the insertion of the RNAi target regions in opposite directions and a 460 nucleotide (nt) spacer fragment forming the loop. The RNAi targets the

indicated nts of the ORFs of MaRF11 (Tb927.11.435, nt 14–255) and TbCOQ8 (nt 353–536) or the 3′ untranslated regions (UTRs) of TbCOQ9 (nt (+49)—(+543)), Tb927.8.4190 (nt (+253)—(+458)), and TbHslV (nt (+114)—(+609)). To ensure efficient transcription of the RNAi construct in the NYsm BSF strain, the procyclin promotor in the above described MaRF11 RNAi plasmid was exchanged against the rRNA promotor.

To generate the TbTim54 conditional dKO cell line, 90 nts up- and downstream of the TbTim54 alleles were fused to either a hygromycin (hygro) or a neomycin (neo) resistance cassette. The first TbTim54 allele was replaced by hygro resulting in the single knockout (sKO). To generate the dKO, the second TbTim54 allele was replaced by neo. In a third cloning step, this TbTim54 dKO cell line was transfected with the plasmid for ectopic expression of TbTim54-HA described above.

The NYsm BSF cell line containing the TbPam16 dKO was generated by fusing the 500 nts up- and downstream of the TbPam16 alleles to the N- or C-terminus of hygro or the blasticidin (blast) resistance cassette, respectively. The first TbPam16 allele was replaced by hygro and the second TbPam16 allele was replaced by blast.

Antibodies

Polyclonal rabbit antiserum against TbPam16 was commercially produced (Eurogentec, Belgium) using amino acids 153–167 (VKDSHGNSRGNDAMW) as antigen. For western blots (WB), the TbPam16 antiserum was used at a 1:500 dilution. Commercially available antibodies used in this study were: Mouse anti-c-myc (Invitrogen, dilution WB 1:2'000), mouse anti-HA (Sigma-Aldrich, dilution WB 1:5'000), and mouse anti-EF1a (Merck Millipore, dilution WB 1:10'000). Polyclonal rabbit anti-ATOM40 (dilution WB 1:10'000) and polyclonal rabbit anti-Cyt C (dilution WB 1:100) were previously produced in our laboratory [81,91]. Secondary antibodies used: Goat anti-mouse IRDye 680LT conjugated (LI-COR Biosciences, dilution WB 1:20'000) and goat anti-Rabbit IRDye 800CW conjugated (LI-COR Biosciences, dilution WB 1:20'000). For detection of 435-HA on immunoblots, HRP-coupled anti-mouse secondary antibodies (Sigma) were used.

Digitonin extraction

Cell lines were induced with tetracycline for 1 day prior to the experiment to ensure expression of epitope-tagged proteins. To selectively solubilize the plasma membrane, 1×10^8 cells were incubated at 4˚C for 10 min in a buffer containing 0.6 M sorbitol, 10 mM Tris-HCl (pH 7.5), 1 mM EDTA (pH 8.0), and 0.015% (w/v) digitonin. A mitochondria-enriched pellet was separated from a supernatant that is enriched in cytosolic proteins by centrifugation (6'800 g, 5 min, 4˚C). Equivalents of 2×10^6 cells of each fraction were analyzed by SDS-PAGE and western blotting.

Alkaline carbonate extraction

A digitonin-extracted, mitochondria-enriched pellet was resuspended in 100 mM Na_2CO (pH 11.5) and incubated at 4˚C for 10 min. Centrifugation (100'000 g, 10 min, 4˚C) yielded in a pellet enriched in integral membrane proteins and a supernatant enriched in soluble or loosely membrane-associated proteins. Equivalents of 2×10^6 cells of each fraction were analyzed by SDS-PAGE and western blotting.

Fluorescence microscopy and kDNA area quantification

TbPam18 and TbPam16 RNAi cells were fixed with 4% paraformaldehyde in PBS, postfixed in cold methanol, and mounted using VectaShield containing 4′,6-diamidino-2-phenylindole

(DAPI) (Vector Laboratories). Images were acquired by a DMI6000B microscope and a DFC360 FX monochrome camera (both Leica Microsystems).

Images were analyzed using ImageJ [92]. The kDNA size analysis was performed on binarized 8-bit format images. The size of particles was measured in arbitrary units (a.u.) and kDNA particles >0.0 a.u. and <0.75 a.u. were included in the analysis. Boomerang shaped, dividing kDNAs and randomly picked up particles were manually removed from the analysis. Significance of these results was calculated by an unpaired two-tailed *t* test.

RNA extraction, RT-PCR, and northern blotting

Acid guanidinium thiocyanate-phenol-chloroform extraction to isolate total RNA from uninduced and 2 days induced RNAi cells was done as described elsewhere [93]. To determine RNAi efficiency, the extracted RNA was either utilized for RT-PCR or separated on a 1% agarose gel in MOPS buffer containing 0.5% formaldehyde for subsequent northern blotting. Northern probes were generated from gel-purified PCR products corresponding to the RNAi inserts or the overexpressed proteins described above, and radiolabeled by means of the Prime-a-Gene labeling system (Promega).

DNA extraction, Southern blotting, and quantitative PCR

For DNA isolation, 5×10^7 cells were resuspended in NTE buffer (100 mM NaCl, 10 mM Tris (pH 7.5), and 5 mM EDTA) containing 0.5% SDS for cell lysis and 0.2 mg/ml RNase A to degrade RNA. After incubation for 1 h at 37˚C, 1 mg/ml proteinase K was added, followed by 2 h of incubation at 37˚C. DNA was isolated by phenol-chloroform extraction and subsequent ethanol precipitation.

For Southern blotting, 5 μg of DNA were digested overnight at 37˚C with HindIII and XbaI. Digested DNA was separated in a 1% agarose gel in 1× TAE buffer. Gel processing and blotting was done as described elsewhere [51,94]. For kDNA detection, sequence-specific mini- and maxicircle probes were generated by PCR. The minicircle probe was a 0.1 kb stretch of the conserved minicircle sequence [94]. A 1.4 kb fragment served as the maxicircle probe [51,95]. For normalization, a tubulin probe binding to a 3.6 kb stretch within the intergenic region between α- and β-tubulin was used [94]. Probes were radiolabeled by means of the Prime-a-Gene labeling system (Promega).

To determine total mini- and maxicircles or free minicircle levels by quantitative PCR, DNA was either isolated from whole cells or from fractionated digitonin-extracted, mitochondria-enriched pellets and used as the template in a PCR utilizing the same primers as for the Southern blot probes.

SILAC RNAi and SILAC CoIP experiments

TbPam18, TbPam16, and MaRF11 RNAi cells or cells exclusively expressing TbPam16-HA were washed in PBS and resuspended in SDM-80 [96] containing 5.55 mM glucose, 10% dialyzed FCS (BioConcept, Switzerland) and either light ($^{12}C_6/^{14}N_x$) or heavy ($^{13}C_6/^{15}N_x$) isotopes of arginine (1.1 mM) and lysine (0.4 mM) (Euroisotope). The cells were grown in SILAC medium for 6 to 10 doubling times to ensure a complete labeling of all proteins with heavy amino acids. For the SILAC RNAi and the premix SILAC CoIP, uninduced and induced (4 days for SILAC RNAi, 2 days for SILAC CoIP) cells were mixed in a one-to-one ratio. For the postmix SILAC CoIP, uninduced and induced cells were kept separately. From all samples, digitonin-extracted, mitochondria-enriched pellets were generated. For the SILAC RNAi experiments, these pellets were processed as described previously including tryptic in solution digestion [97] and then analyzed by liquid chromatography–mass spectrometry (LC–MS).

TbPam18 and TbPam16 SILAC RNAi experiments were done in 4 biological replicates including a label-switch.

For the SILAC CoIP experiments, mitochondria-enriched digitonin pellets were solubilized in a buffer containing 20 mM Tris-HCl (pH 7.4), 0.1 mM EDTA, 100 mM NaCl, 10% glycerol, 1X Protease Inhibitor mix (Roche, EDTA-free), and 1% (w/v) digitonin for 15 min at 4˚C. After centrifugation (21'000 g, 15 min, 4˚C), the lysate was transferred to HA bead slurry (anti-HA affinity matrix, Roche), which had been equilibrated in wash buffer (20 mM Tris-HCl (pH 7.4), 0.1 mM EDTA, 1 mM NaCl, 10% glycerol, 0.2% (w/v) digitonin). Incubation in an end-over-end shaker for 2 h at 4˚C was followed by removal of the supernatant containing the unbound proteins. After washing the bead slurry 3 times with wash buffer, the bound proteins were eluted by boiling the resin for 5 min in 2% SDS in 60 mM Tris-HCl (pH 6.8). In case of the postmix SILAC CoIP, eluates of uninduced and induced cells were now mixed in a one-to-one ratio. All eluates were further prepared for analysis by LC–MS as has been described in detail elsewhere [98]. TbPam16-HA pre- and postmix SILAC CoIP experiments were done in 4 biological replicates including label-switches.

LC–MS and data analysis

LC–MS analyses of tryptic peptide mixtures from all experiments were performed using a Q Exactive Plus mass spectrometer connected to an UltiMate 3000 RSLCnano HPLC system (Thermo Fisher Scientific, Germany) as described before [26] with minor modifications. The software package MaxQuant [99,100] (version 1.6.3.4 for TbPam18 and TbPam16 SILAC RNAi, 2.0.2.0 for TbPam16 SILAC IP, and 2.5.1.0 for MaRF11 SILAC RNAi data) was used for protein identification and SILAC-based relative quantification. Mass spectrometric raw data were searched against a database containing the protein sequences for *T*. *brucei* TREU927 as provided by the TriTrypDB (https://tritrypdb.org; version 8.1 for TbPam18/TbPam16 SILAC RNAi and TbPam16 SILAC IP experiments, and version 55 for MaRF11 SILAC RNAi samples). Protein identification and quantification was based on $\geq$1 unique peptide and $\geq$1 ratio count, respectively. For all other parameters, MaxQuant default settings were used, including carbamidomethylation of cysteine as fixed modification, N-terminal acetylation and oxidation of methionine as variable modifications, and Lys8/Arg10 as heavy labels. The options "requantify" and "match between runs" were enabled.

MaxQuant result files were processed with python using pandas (version 1.5.3; https://pandas.pydata.org) as well as numpy (version 1.24.2; https://numpy.org/), seaborn (version 0.11.2; https://seaborn.pydata.org), scipy (version 1.10.0; https://www.scipy.org/), and matplotlib (version 3.6.3; https://matplotlib.org/) for data analysis and visualization. Data analysis of all experiments was based on protein abundance ratios calculated by MaxQuant.

To identify proteins affected by ablation of TbPam16 and TbPam18 following RNAi induction, MaxQuant protein ratios were first normalized replicate-wise by adjusting the summed ratios to the highest value, followed by cyclic loess normalization [101] of $\log_2$-transformed protein ratios as implemented in the R Bioconductor (version 3.17) package "affy" [102] (version 1.78.2). Values missing in 1 or 2 out of 4 replicates were imputed using the DIMA package [103] (https://github.com/kreutz-lab/DIMAR). To identify proteins with significantly altered abundance upon RNAi induction, the "linear models for microarray data" (limma) approach) [104,105] (version 3.28.14) was applied. *P* values were corrected for multiple testing following the Benjamini–Hochberg method [106]. Proteins affected by the RNAi-induced ablation of MaRF11 were identified based on normalized protein abundance ratios determined by MaxQuant using the limma approach and corrected *P* values as described above.

To identify proteins significantly enriched in TbPam16 pre- and postmix SILAC CoIP experiments, the rank sum method [107,108] as implemented in the R package "RankProd" [109] (version 3.24.0) was applied. The rank sum, defined as the arithmetic mean of the ranks of a protein in all replicates, was converted into FDR-controlled q-values.

For information about proteins identified and quantified, see S1–S3 Tables.

Supporting information

S1 Fig. Schematic depiction of mitochondrial inner membrane protein translocases and organization of the mitochondrial genome, termed kinetoplast DNA (kDNA) in T. brucei. **(A)** Schematic depiction of the yeast TIM23 and TIM22 complexes (left) and the single trypanosomal TIM complex (right). In the trypanosomal TIM complex, the subunits specifically associated with presequence pathway are indicated in broken lines. Subunits of the presequence-associated import motor (PAM) are indicated in bold red lines. Unique and homologous subunits between the 2 species are indicated in gray and orange, respectively. The non-homologous J domain proteins Pam18/16 and TbPam27 are indicated in bold. (B) Organization of the single unit kDNA of *T. brucei*. The kDNA is a disk consisting of an intercalated network of maxi- and minicircles, which is physically connected, across the outer and the inner membrane, with the basal body of the flagellum via the tripartite attachment complex (TAC). Minicircles are replicated via theta structures after they have been released from the center of the network into the kinetoflagellar zone. After replication, they are reattached to the kDNA disk at the antipodal sites. Maxicircles in contrast are replicated while remaining attached to the kDNA disk.
(TIF)

S2 Fig. TbPam18 RNAi does not affect protein subgroups exclusively consisting of nucleus-encoded proteins. Mitochondria-enriched fractions of uninduced and 4 days induced TbPam18 RNAi cells were analyzed by SILAC-based quantitative mass spectrometry (same data set as in Fig 1B). **(A–F)** The indicated subgroups of mitochondrial proteins are highlighted in the indicated colors. The number of all more than 1.5-fold depleted proteins and the total number of all detected proteins for each subgroup are indicated in parentheses at the top of each panel. Numerical data for panel (A) to (F) are available in S1 Table.
(TIF)

S3 Fig. TbPam16 RNAi does not affect protein subgroups exclusively consisting of nucleus-encoded proteins. Mitochondria-enriched fractions of uninduced and 4 days induced TbPam16 RNAi cells were analyzed by SILAC-based quantitative mass spectrometry (same data set as in Fig 1B). **(A–F)** The indicated subgroups of mitochondrial proteins are highlighted in the indicated colors. The number of all more than 1.5-fold depleted proteins and the total number of all detected proteins for each subgroup are indicated in parentheses at the top of each panel. Numerical data for panel (A) and (F) are available in S1 Data.
(TIF)

S4 Fig. TbTim54 is not required to maintain kDNA integrity. **(A)** Growth curve of a TbTim54 conditional double knockout (cond. dKO) cell line. While both TbTim54 alleles are knocked out in uninduced (-Tet) as well as induced (+Tet) cells, TbTim54-HA is only ectopically expressed when tetracycline is present. Inset: Verification of single knockout (sKO) and dKO by PCR using a primer pair to amplify the TbTim54 ORF (approximately 2.0 kilobases (kb)), the hygromycin (hygro, approximately 1.5 kb), or the neomycin (neo, approximately 1.3 kb) resistance cassettes at the same time. Hygro was used to replace the first and neo was used to replace the second allele. **(B)** Left: DAPI-stained TbTim54 cond. dKO cell line grown in the

presence of tetracycline (+Tet) and 3 or 6 days after the removal of tetracycline from the medium (-Tet). Right: Quantification of kDNA areas in 69 to 90 DAPI-stained cells. The red line indicates the mean of the kDNA areas for each time point. The mean of the control cells (+Tet) was set to 100%. n.s.: not significant (P value >0.05) as calculated by an unpaired two-tailed t test. Numerical data for panel (A) and (B) are available in S1 Data.
(TIF)

S5 Fig. Changes in mini- and maxicircle levels can be detected by quantitative PCR. Upper panels: A quantitative PCR-based (qPCR) method was used to detect changes in steady-state levels of total mini- and maxicircles. Total DNA was extracted from uninduced and 2 to 5 days induced TbPam18 and TbPam16 RNAi cell lines. This DNA was used as the template in PCRs amplifying specific mini- and maxicircle regions or the intergenic region of tubulin. PCR products were analyzed on agarose gels. Lower panels: Densitometric quantification of mini- and maxicircle abundance as detected by qPCR. The ratio of the mini- or maxicircle band intensity and the respective control (tubulin band intensity) was normalized (norm.) to the ratios of uninduced cells. Blue (maxicircles) and red (minicircles) bars represent the mean of 3 independent biological replicates. n.s.: not significant, **: P value <0.05, ***: P value <0.005, ****: P value <0.0001, as calculated by an unpaired two-tailed t test. Numerical data are available in S1 Data.
(TIF)

S6 Fig. Functional analysis of tagged TbPam18 and subcellular localization of TbPam16 variants. (A) Growth curve of uninduced (-Tet) and induced (+Tet) cells expressing RNAi-resistant (RNAi-res.) TbPam18-HA (left) or myc-TbPam18 (right) in the background of RNAi against the wild type (wt) TbPam18 (TbPam18-HA and myc-TbPam18 exclusive expressors). Insets, top: Immunoblot analysis of whole cell extracts of uninduced (-) and 2 days induced (+) cells, probed for RNAi-res. TbPam18-HA or myc-TbPam18 and EF1a as loading control. Insets, bottom: RT-PCR products of the wt TbPam18 mRNA in uninduced (-) or 2 days induced (+) cells. Tubulin mRNA serves as loading control. **(B)** Upper panels: Immunoblot analysis of total cells (T), digitonin-extracted, mitochondria-enriched (M), and soluble cytosolic (C) fractions of TbPam16-HA, ΔN-TbPam16-HA, and myc-TbPam16 exclusive expressor cell lines. Blots were probed with anti-HA antibodies and antisera against ATOM40 and EF1a, which serve as mitochondrial and cytosolic markers, respectively. Lower panels: digitonin-extracted, crude mitochondrial fractions (M) were subjected to an alkaline carbonate extraction resulting in a pellet enriched in integral membrane proteins (P) and a soluble supernatant fraction (S). Immunoblots were probed with anti-HA and antisera against ATOM40 and cytochrome C (Cyt C), which serve as marker for integral membrane and soluble proteins, respectively. All immunoblots derive from the same gel. **(C)** Quantification of the expression levels in total cells, lanes T in (B), of TbPam16-HA and ΔN-TbPam16-HA normalized to ATOM40. Numerical data for panel (A) and (C) are available in S1 Data.
(TIF)

S7 Fig. Multiple sequence alignments of Pam18 homologues and subcellular localization of TbPam18 variants. (A) Sequence alignment of N-terminal regions of Pam18 homologues of 13 representative eukaryotes. **(B)** Sequence alignment of N-terminal regions of Pam18 homologues of 9 representative trypanosomatids. In (A) and (B) Histidine-Proline-Aspartate (HPD) motifs are highlighted in red and Histidine-Serine-Aspartate (HSD) motifs in green. **(C)** Upper panels: Immunoblot analysis of total cells (T), digitonin-extracted mitochondria-enriched (M), and soluble cytosolic (C) fractions of cell lines expressing N-terminally myc-tagged TbPam18 or Tb/ScTbPam18. Blots were probed with anti-myc antibodies and antisera

against ATOM40 and EF1a, which serve as mitochondrial and cytosolic markers, respectively. Lower panels: digitonin-extracted crude mitochondrial fractions (M) were subjected to an alkaline carbonate extraction resulting in a pellet enriched in integral membrane proteins (P) and a soluble supernatant fraction (S). Immunoblots were probed with anti-myc and antisera against ATOM40 and Cyt C, which serve as makers for integral membrane and soluble proteins, respectively.
(TIF)

S8 Fig. AlphaFold prediction of MaRF11/Tb927.11.435.
(TIF)

S9 Fig. Effect of MaRF11/Tb927.11.435 RNAi on the mitochondrial proteome. Mitochondria-enriched fractions of uninduced and 4 days induced MaRF11 RNAi cells were analyzed by SILAC-based quantitative mass spectrometry. The data set was filtered for mitochondrial proteins and the mean $\log_2$ of normalized ratios (induced/uninduced) was plotted against the corresponding negative $\log_{10}$ of adjusted *P* value (limma test). Highlighted are mitochondrial ribosomal proteins (MRPs, red) and components of the oxidative phosphorylation pathway (OXPHOS, green) as well as TbPam16 (pink). The horizontal dotted line in each volcano plot marks an adjusted *P* value of 0.05. The vertical dotted lines indicate a fold-change in protein abundance of ±1.5. The percentages of all detected MRPs or OXPHOS proteins that are depleted more than 1.5-fold is indicated at the top of each panel. The number of all more than 1.5-fold depleted MRPs or OXPHOS proteins and the total number of all detected MRPs or OXPHOS proteins is shown in parentheses. MaRF11/Tb927.11.435 was not detected. Numerical data are available in S3 Table.
(TIF)

S10 Fig. MaRF11/Tb927.11.435 RNAi does not affect protein subgroups exclusively consisting of nucleus-encoded proteins. Mitochondria-enriched fractions of uninduced and 4 days induced MaRF11 RNAi cells were analyzed by SILAC-based quantitative mass spectrometry (same data set as in S9 Fig). **(A–F)** The indicated subgroups of mitochondrial proteins are highlighted in the indicated colors. The number of all more than 1.5-fold depleted proteins and the total number of all detected proteins for each subgroup are indicated in parentheses at the top of each panel. Numerical data for panel are available in S3 Table.
(TIF)

S11 Fig. Correlation analysis of TbPam18, TbPam16, MaRF11/Tb927.11.435, and TbTim17 SILAC RNAi data sets. The mitochondrial proteins detected in the data sets of the indicated SILAC RNAi analyses were quantitatively compared in a pairs diagram created with R (version 4.2.1). The $\log_2$-normalized foldchanges of all detected mitochondrial proteins of 1 SILAC experiment were compared to each of the other experiments in individual scatter graphs. Yellow clouds indicate the range in which 50% (inner cloud) and 90% (outer cloud) of the data points are located. The correlation between the data sets was calculated using the Spearman's rank correlation algorithm and is indicated as r_s. *N* indicates the total number of proteins that could be compared between 2 data sets. The 4 panels along the diagonal axis contain histograms combined with density graphs displaying the overall data point distribution in each experiment. As all 4 data sets have a left-skewed distribution, the Spearman's rank correlation was used as the statistical measure. Numerical data are available in S1 and S3 Tables.
(TIF)

S12 Fig. Synthetic TbPam18 and TbPam16 genes. RNAi-resistant (RNAi-res.) TbPam18 and TbPam16 DNA sequences in black with changed nucleotides highlighted in red. In the

ΔN-TbPam18 and ΔN-TbPam16 constructs, the first 81 and 156 nucleotides, respectively, were replaced by the first 45 nucleotides of TbmHsp60, which encode the mitochondrial targeting sequence of the protein (green). To generate the Tb/ScPam18 fusion protein, the first 295 nucleotides of RNAi-res. TbPam18 were fused to the last 213 nucleotides of yeast (Sc) Pam18 (blue). To generate RNAi-res. TbPam18-S98P, the cytosine at position 292 of the nucleotide sequence was exchanged against a thymine (highlighted in yellow).
(TIF)

S1 Table. SILAC RNAi TbPam18 and TbPam16.
(XLSX)

S2 Table. SILAC CoIPs TbPam16.
(XLSX)

S3 Table. TbMaRF11 SILAC RNAi.
(XLSX)

S1 Data. Numerical data for all graphs presented in the study.
(XLSX)

S1 Raw Images. Original images for all gels and blots.
(PDF)

Acknowledgments

We thank Julian Bender and Johannes Zimmermann for assistance in bioinformatics data analysis.

Author Contributions

Conceptualization: Corinne von Känel, Philip Stettler, Bettina Warscheid, André Schneider.

Data curation: Silke Oeljeklaus.

Formal analysis: Corinne von Känel, Philip Stettler, Carmela Esposito, Stephan Berger, Simona Amodeo, Silke Oeljeklaus, Salvatore Calderaro, Bettina Warscheid, André Schneider.

Funding acquisition: Bettina Warscheid, André Schneider.

Investigation: Corinne von Känel, Philip Stettler, Carmela Esposito, Stephan Berger, Simona Amodeo, Silke Oeljeklaus, Salvatore Calderaro, Ignacio M. Durante, Vendula Rašková.

Methodology: Corinne von Känel.

Project administration: Bettina Warscheid, André Schneider.

Supervision: Bettina Warscheid, André Schneider.

Validation: Corinne von Känel, Philip Stettler.

Visualization: Corinne von Känel, Philip Stettler, Silke Oeljeklaus, André Schneider.

Writing – original draft: Corinne von Känel, Philip Stettler, André Schneider.

Writing – review & editing: Corinne von Känel, Philip Stettler, Carmela Esposito, Stephan Berger, Simona Amodeo, Silke Oeljeklaus, Salvatore Calderaro, Ignacio M. Durante, Vendula Rašková, Bettina Warscheid, André Schneider.

References

1. Peikert CD, Mani J, Morgenstern M, Käser S, Knapp B, Wenger C, et al. Charting organellar importomes by quantitative mass spectrometry. Nat Commun. 2017; 8:15272. https://doi.org/10.1038/ncomms15272 PMID: 28485388
2. Schneider A. Evolution and diversification of mitochondrial protein import systems. Curr Opin Cell Biol. 2022; 75:102077.
3. Schneider A. Mitochondrial protein import in trypanosomatids: Variations on a theme or fundamentally different? PLoS Pathog. 2018; 14:e1007351.
4. Schneider A. Evolution of mitochondrial protein import—Lessons from trypanosomes. Biol Chem. 2020; 401:663–676. https://doi.org/10.1515/hsz-2019-0444 PMID: 32142472
5. Harsman A, Schneider A. Mitochondrial protein import in trypanosomes: Expect the unexpected. Traffic. 2017; 18:96–109. https://doi.org/10.1111/tra.12463 PMID: 27976830
6. Mani J, Meisinger C, Schneider A. Peeping at TOMs—Diverse entry gates to mitochondria provide insights into the evolution of eukaryotes. Mol Biol Evol. 2016; 33:337–351. https://doi.org/10.1093/molbev/msv219 PMID: 26474847
7. Fukasawa Y, Oda T, Tomii K, Imai K. Origin and evolutionary alteration of the mitochondrial import system in eukaryotic lineages. Mol Biol Evol. 2017; 34:1574. https://doi.org/10.1093/molbev/msx096 PMID: 28369657
8. Žárský V, Doležal P. Evolution of the Tim17 protein family. Biol Direct. 2016;11.
9. Ferramosca A, Zara V. Biogenesis of mitochondrial carrier proteins: Molecular mechanisms of import into mitochondria. Biochim Biophys Acta. 2013; 1833:494–502. https://doi.org/10.1016/j.bbamcr.2012.11.014 PMID: 23201437
10. Zimmermann R, Neupert W. Transport of proteins into mitochondria: Posttranslational transfer of ADP/ATP carrier into mitochondria in vitro. Eur J Biochem. 1980; 109:217–229.
11. Schulz C, Schendzielorz A, Rehling P. Unlocking the presequence import pathway. Trends Cell Biol. 2015; 25:265–275.
12. Kang PJ, Ostermann J, Shilling J, Neupert W, Craig EA, Pfanner N, et al. Requirement for Hsp70 in the mitochondrial matrix for translocation and folding of precursor proteins. Nature. 1990; 348:137–143. https://doi.org/10.1038/348137a0 PMID: 2234077
13. Horst M, Oppliger W, Rospert S, Schönfeld HJ, Schatz G, Azem A. Sequential action of two Hsp70 complexes during protein import into mitochondria. EMBO J. 1997; 16:1842. https://doi.org/10.1093/emboj/16.8.1842 PMID: 9155010
14. D'Silva PD, Schilke B, Walter W, Andrew A, Craig EA. J protein cochaperone of the mitochondrial inner membrane required for protein import into the mitochondrial matrix. Proc Natl Acad Sci U S A. 2003; 100:13839–13844. https://doi.org/10.1073/pnas.1936150100 PMID: 14605210
15. Truscott KN, Voos W, Frazier AE, Lind M, Li Y, Geissler A, et al. A J-protein is an essential subunit of the presequence translocase–associated protein import motor of mitochondria. J Cell Biol. 2003; 163:707.
16. Mokranjac D, Sichting M, Neupert W, Hell K. Tim14, a novel key component of the import motor of the TIM23 protein translocase of mitochondria. EMBO J. 2003; 22:4945–4956. https://doi.org/10.1093/emboj/cdg485 PMID: 14517234
17. Frazier AE, Dudek J, Guiard B, Voos W, Li Y, Lind M, et al. Pam16 has an essential role in the mitochondrial protein import motor. Nat Struct Mol Biol. 2004; 11:226–233.
18. Banerjee R, Gladkova C, Mapa K, Witte G, Mokranjac D. Protein translocation channel of mitochondrial inner membrane and matrix-exposed import motor communicate via two-domain coupling protein. Elife. 2015;4. https://doi.org/10.7554/eLife.11897 PMID: 26714107
19. Laloraya S, Gambill BD, Craig EA. A role for a eukaryotic GrpE-related protein, Mge1p, in protein translocation. Proc Natl Acad Sci U S A. 1994; 91:6481–6485. https://doi.org/10.1073/pnas.91.14.6481 PMID: 8022808
20. Laloraya S, Dekker PJT, Voos W, Craig EA, Pfanner N. Mitochondrial GrpE modulates the function of matrix Hsp70 in translocation and maturation of preproteins. Mol Cell Biol. 1995; 15:7098–7105. https://doi.org/10.1128/MCB.15.12.7098 PMID: 8524277
21. Schneider HC, Westermann B, Neupert W, Brunner M. The nucleotide exchange factor MGE exerts a key function in the ATP-dependent cycle of mt-Hsp70-Tim44 interaction driving mitochondrial protein import. EMBO J. 1996; 15:5796–5803. PMID: 8918457
22. Harsman A., Oeljeklaus S., Wenger C, Huot JH, Warscheid BSchneider A. The non-canonical mitochondrial inner membrane presequence translocase of trypanosomatids contains two essential

rhomboid-like proteins. Nat Commun 2016; 7:1–13. https://doi.org/10.1038/ncomms13707 PMID: 27991487

23. Pyrihová E, Motyková A, Voleman L, Wandyszewska N, Fišer R, Seydlová G, et al. A single TIM translocase in the mitosomes of Giardia intestinalis illustrates convergence of protein import machines in anaerobic eukaryotes. Genome Biol Evol. 2018; 10:2813–2822. https://doi.org/10.1093/gbe/evy215 PMID: 30265292

24. Singha UK, Hamilton V, Duncan MR, Weems E, Tripathi MK, Chaudhuri M. Protein translocase of mitochondrial inner membrane in Trypanosoma brucei. J Biol Chem. 2012; 287:14480.

25. Tschopp F, Charrière F, Schneider A. In vivo study in Trypanosoma brucei links mitochondrial transfer RNA import to mitochondrial protein import. EMBO Rep. 2011; 12:825–832.

26. von Känel C, Muñoz-Gómez SA, Oeljeklaus S, Wenger C, Warscheid B, Wideman JG, et al. Homologue replacement in the import motor of the mitochondrial inner membrane of trypanosomes. Elife. 2020;9. https://doi.org/10.7554/eLife.52560 PMID: 32105215

27. Verner Z, Basu S, Benz C, Dixit S, Dobáková E, Faktorová D, et al. Malleable mitochondrion of Trypanosoma brucei. Int Rev Cell Mol Biol. 2015; 315:73–151. https://doi.org/10.1016/bs.ircmb.2014.11.001 PMID: 25708462

28. Jensen RE, Englund PT. Network News: The replication of kinetoplast DNA. Annu Rev Microbiol. 2012; 66:473–491. https://doi.org/10.1146/annurev-micro-092611-150057 PMID: 22994497

29. Ramrath DJF, Niemann M, Leibundgut M, Bieri P, Prange C, Horn EK, et al. Evolutionary shift toward protein-based architecture in trypanosomal mitochondrial ribosomes. Science. 2018; 362(6413): eaau7735 https://doi.org/10.1126/science.aau7735 PMID: 30213880

30. Schneider A. A short history of guide RNAs. EMBO Rep. 2020; 21:e51918.

31. Read LK, Lukeš J, Hashimi H. Trypanosome RNA editing: The complexity of getting U in and taking U out. Wiley Interdiscip Rev RNA. 2016; 7:33–51. https://doi.org/10.1002/wrna.1313 PMID: 26522170

32. Stuart KD, Schnaufer A, Ernst NL, Panigrahi AK. Complex management: RNA editing in trypanosomes. Trends Biochem Sci. 2005; 30:97–105.

33. Hajduk S, Ochsenreiter T. RNA editing in kinetoplastids. RNA Biol. 2010; 7:229–236. https://doi.org/10.4161/rna.7.2.11393 PMID: 20220308

34. Cooper S, Wadsworth ES, Ochsenreiter T, Ivens A, Savill NJ, Schnaufer A. Assembly and annotation of the mitochondrial minicircle genome of a differentiation-competent strain of Trypanosoma brucei. Nucleic Acids Res. 2019; 47:11304–11325. https://doi.org/10.1093/nar/gkz928 PMID: 31665448

35. Shapiro TA. Kinetoplast DNA maxicircles: networks within networks. PNAS. 1993; 90:7809–7813. https://doi.org/10.1073/pnas.90.16.7809 PMID: 8395055

36. Chen J, Rauch CA, White JH, Englund PT, Cozzarelli NR. The topology of the kinetoplast DNA network. Cell. 1995; 80:61–69.

37. Schneider A, Ochsenreiter T. Failure is not an option—mitochondrial genome segregation in trypanosomes. J Cell Sci. 2018;131.

38. Ogbadoyi EO, Robinson DR, Gull K. A high-order trans-membrane structural linkage is responsible for mitochondrial genome positioning and segregation by flagellar basal bodies in trypanosomes. Mol Biol Cell. 2003; 14:1769–1779. https://doi.org/10.1091/mbc.e02-08-0525 PMID: 12802053

39. Drew ME, Englund PT. Intramitochondrial location and dynamics of Crithidia fasciculata kinetoplast minicircle replication intermediates. J Cell Biol. 2001; 153:735–744.

40. Ryant KA, Englund PT. Synthesis and processing of kinetoplast DNA minicircles in Trypanosoma equiperdum. Mol Cell Biol. 1989; 9:3212. https://doi.org/10.1128/mcb.9.8.3212-3217.1989 PMID: 2552285

41. Melendy T, Sheline C, Ray DS. Localization of a type II DNA topoisomerase to two sites at the periphery of the kinetoplast DNA of Crithidia fasciculata. Cell. 1988; 55:1083–1088. https://doi.org/10.1016/0092-8674(88)90252-8 PMID: 2849507

42. Ryan KA, Englund PT. Replication of kinetoplast DNA in Trypanosoma equiperdum: Minicircle H strand fragments which map at specific locations. J Biol Chem. 1989; 264:823–830.

43. Amodeo S, Bregy I, Ochsenreiter T. Mitochondrial genome maintenance—the kinetoplast story. FEMS Microbiol Rev. 2022. https://doi.org/10.1093/FEMSRE/FUAC047 PMID: 36449697

44. Povelones ML. Beyond replication: Division and segregation of mitochondrial DNA in kinetoplastids. Mol Biochem Parasitol. 2014; 196:53–60. https://doi.org/10.1016/j.molbiopara.2014.03.008 PMID: 24704441

45. Gluenz E, Povelones ML, Englund PT, Gull K. The kinetoplast duplication cycle in Trypanosoma brucei is orchestrated by cytoskeleton-mediated cell morphogenesis. Mol Cell Biol. 2011; 31:1012–1021. https://doi.org/10.1128/MCB.01176-10 PMID: 21173163

46. Li Z, Lindsay ME, Motyka SA, Englund PT, Wang CC. Identification of a bacterial-like HslVU protease in the mitochondria of Trypanosoma brucei and its role in mitochondrial DNA replication. PLoS Pathog. 2008;4.

47. Liu B, Wang J, Yaffe N, Lindsay M, Zhao Z, Zick A, et al. Trypanosomes have six mitochondrial DNA helicases with one controlling kinetoplast maxicircle replication. Mol Cell. 2009; 35:490–501. https://doi.org/10.1016/j.molcel.2009.07.004 PMID: 19646907

48. Zíková A, Verner Z, Nenarokova A, Michels PAM, Lukeš J. A paradigm shift: The mitoproteomes of procyclic and bloodstream Trypanosoma brucei are comparably complex. PLoS Pathog. 2017; 13: e1006679. https://doi.org/10.1371/journal.ppat.1006679 PMID: 29267392

49. Clement SL, Mingler MK, Koslowsky DJ. An Intragenic Guide RNA Location Suggests a Complex Mechanism for Mitochondrial Gene Expression in Trypanosoma brucei. Eukaryot Cell. 2004; 3:862.

50. Harsman A, Oeljeklaus WC, Huot JL, Warscheid B, Schneider A. The non-canonical mitochondrial inner membrane presequence translocase of trypanosomatids contains two essential rhomboid-like proteins. Nat Commun. 2016; 7:1–13.

51. Amodeo S, Jakob M, Ochsenreiter T. Characterization of the novel mitochondrial genome replication factor MiRF172 in Trypanosoma brucei. J Cell Sci. 2018;131. https://doi.org/10.1242/jcs.211730 PMID: 29626111

52. Hines JC, Ray DS. A mitochondrial DNA primase is essential for cell growth and kinetoplast DNA replication in Trypanosoma brucei. Mol Cell Biol. 2010; 30:1319–1328. https://doi.org/10.1128/MCB.01231-09 PMID: 20065037

53. Týč J, Klingbeil MM, Lukeš J. Mitochondrial heat shock protein machinery hsp70/hsp40 is indispensable for proper mitochondrial DNA maintenance and replication. MBio. 2015;6. https://doi.org/10.1128/mBio.02425-14 PMID: 25670781

54. Beck K, Acestor N, Schulfer A, Anupama A, Carnes J, Panigrahi AK, et al. Trypanosoma brucei Tb927.2.6100 is an essential protein associated with kinetoplast DNA. Eukaryot Cell. 2013; 12:970–978.

55. Grewal JS, McLuskey K, Das D, Myburgh E, Wilkes J, Brown E, et al. PNT1 is a C11 cysteine peptidase essential for replication of the trypanosome kinetoplast. J Biol Chem. 2016; 291:9492–9500. https://doi.org/10.1074/jbc.M116.714972 PMID: 26940875

56. Singha UK, Tripathi A, Smith JJ, Quinones L, Saha A, Singha T, et al. Novel IM-associated protein Tim54 plays a role in the mitochondrial import of internal signal-containing proteins in Trypanosoma brucei. Biol Cell. 2021; 113:39–57. https://doi.org/10.1111/boc.202000054 PMID: 33084070

57. von Känel C, Oeljeklaus S, Wenger C, Stettler P, Harsman A, Warscheid B, et al. Intermembrane space-localized TbTim15 is an essential subunit of the single mitochondrial inner membrane protein translocase of trypanosomes. Mol Microbiol. 2024. https://doi.org/10.1111/mmi.15262 PMID: 38622999

58. Bhat GJ, Koslowsky DJ, Feagin JE, Smiley BL, Stuart K. An extensively edited mitochondrial transcript in kinetoplastids encodes a protein homologous to ATPase subunit 6. Cell. 1990; 61:885–894. https://doi.org/10.1016/0092-8674(90)90199-o PMID: 2140530

59. Dean S, Gould MK, Dewar CE, Schnaufer AC. Single point mutations in ATP synthase compensate for mitochondrial genome loss in trypanosomes. Proc Natl Acad Sci U S A. 2013; 110:14741–14746.

60. Wirtz E, Lea S, Ochatt C, Cross GAM. A tightly regulated inducible expression system for conditional gene knock-outs and dominant-negative genetics in Trypanosoma brucei. Mol Biochem Parasitol. 1999; 99:89–101. https://doi.org/10.1016/s0166-6851(99)00002-x PMID: 10215027

61. Krogh A, Larsson B, von Heijne G, Sonnhammer ELL. Predicting transmembrane protein topology with a hidden Markov model: application to complete genomes. J Mol Biol. 2001; 305:567–580. https://doi.org/10.1006/jmbi.2000.4315 PMID: 11152613

62. Kampinga HH, Andreasson C, Barducci A, Cheetham ME, Cyr D, Emanuelsson C, et al. Function, evolution, and structure of J-domain proteins. Cell Stress Chaperones. 2018; 24:7–15.

63. Walsh P, Bursać D, Law YC, Cyr D, Lithgow T. The J-protein family: modulating protein assembly, disassembly and translocation. EMBO Rep. 2004; 5:567–571.

64. Oeljeklaus S, Reinartz BS, Wolf J, Wiese S, Tonillo J, Podwojski K, et al. Identification of core components and transient interactors of the peroxisomal importomer by dual-track stable isotope labeling with amino acids in cell culture analysis. J Proteome Res. 2012; 11:2567–2580.

65. Wheeler RJ. A resource for improved predictions of Trypanosoma and Leishmania protein three-dimensional structure. PLoS ONE. 2021; 16:e0259871. https://doi.org/10.1371/journal.pone.0259871 PMID: 34762696

66. Stefely JA, Pagliarini DJ. Biochemistry of Mitochondrial Coenzyme Q Biosynthesis. Trends Biochem Sci. 2017; 42:824–843.

67. Priesnitz C, Böttinger L, Zufall N, Gebert M, Guiard B, van der Laan M, et al. Coupling to Pam16 differentially controls the dual role of Pam18 in protein import and respiratory chain formation. Cell Rep. 2022; 39:110619. https://doi.org/10.1016/j.celrep.2022.110619 PMID: 35385740

68. Grams J, Morris JC, Drew ME, Wang Z, Englund PT, Hajduk SL, et al. A trypanosome mitochondrial RNA polymerase is required for transcription and replication. J Biol Chem. 2002; 277:16952–16959. https://doi.org/10.1074/jbc.M200662200 PMID: 11859084

69. Hammarton TC, Clark J, Douglas F, Boshart M, Mottram JC. Stage-specific differences in cell cycle control in Trypanosoma brucei revealed by RNA interference of a mitotic cyclin. J Biol Chem. 2003; 278:22877–22886. https://doi.org/10.1074/jbc.M300813200 PMID: 12682070

70. Mokranjac D, Bourenkov G, Hell K, Neupert W, Groll M. Structure and function of Tim14 and Tim16, the J and J-like components of the mitochondrial protein import motor. EMBO J. 2006; 25:4675–4685. https://doi.org/10.1038/sj.emboj.7601334 PMID: 16977310

71. Rocco L, Englund PT. Kinetoplast maxicircle DNA replication in Crithidia fasciculata and Trypanosoma brucei. Mol Cell Biol. 1995; 15:6794–6803. https://doi.org/10.1128/MCB.15.12.6794 PMID: 8524245

72. Hoffmann A, Käser S, Jakob M, Amodeo S, Peitsch C, Týč J, et al. Molecular model of the mitochondrial genome segregation machinery in Trypanosoma brucei. Proc Natl Acad Sci U S A. 2018; 115: E1809–E1818. https://doi.org/10.1073/pnas.1716582115 PMID: 29434039

73. Schimanski B, Aeschlimann S, Stettler P, Käser S, Gomez-Fabra GM, Bender J, et al. p166 links membrane and intramitochondrial modules of the trypanosomal tripartite attachment complex. PLoS Pathog. 2022; 18:e1010207. https://doi.org/10.1371/journal.ppat.1010207 PMID: 35709300

74. Aeschlimann S, Stettler P, Schneider A. DNA segregation in mitochondria and beyond: insights from the trypanosomal tripartite attachment complex. Trends Biochem Sci. 2023. https://doi.org/10.1016/J.TIBS.2023.08.012

75. Craig EA, Marszalek J. How do J-proteins get Hsp70 to do so many different things? Trends Biochem Sci. 2017; 42:355–368. https://doi.org/10.1016/j.tibs.2017.02.007 PMID: 28314505

76. Craig EA, Huang P, Aron R, Andrew A. The diverse roles of J-proteins, the obligate Hsp70 co-chaperone. Rev Physiol Biochem Pharmacol. 2006; 156:1–21. https://doi.org/10.1007/s10254-005-0001-0 PMID: 16634144

77. Bentley SJ, Jamabo M, Boshoff A. The Hsp70/J-protein machinery of the African trypanosome, Trypanosoma brucei. Cell Stress Chaperones. 2018; 24:125–148. https://doi.org/10.1007/s12192-018-0950-x PMID: 30506377

78. Panigrahi AK, Ogata Y, Zíková A, Anupama A, Dalley RA, Acestor N, et al. A comprehensive analysis of Trypanosoma brucei mitochondrial proteome. Proteomics. 2009; 9:434–450. https://doi.org/10.1002/pmic.200800477 PMID: 19105172

79. Acestor N, Zíková A, Dalley RA, Anupama A, Panigrahi AK, Stuart KD. Trypanosoma brucei mitochondrial respiratome: Composition and organization in procyclic form. Mol Cell Proteomics. 2011;10.

80. Acestor N, Panigrahi AK, Ogata Y, Anupama A, Stuart KD. Protein composition of Trypanosoma brucei mitochondrial membranes. Proteomics. 2009; 9:5497–5508. https://doi.org/10.1002/pmic.200900354 PMID: 19834910

81. Niemann M, Wiese S, Mani J, Chanfon A, Jackson C, Meisinger C, et al. Mitochondrial outer membrane proteome of Trypanosoma brucei reveals novel factors required to maintain mitochondrial morphology. Mol Cell Proteomics. 2013; 12:515–528. https://doi.org/10.1074/mcp.M112.023093 PMID: 23221899

82. Kityk R, Kopp J, Mayer MP. Molecular mechanism of J-domain-triggered ATP hydrolysis by Hsp70 chaperones. Mol Cell. 2018; 69:227–237.e4. https://doi.org/10.1016/j.molcel.2017.12.003 PMID: 29290615

83. Pulido P, Leister D. Novel DNAJ-related proteins in Arabidopsis thaliana. New Phytol. 2018; 217:480–490. https://doi.org/10.1111/nph.14827 PMID: 29271039

84. Tamadaddi C, Verma AK, Zambare V, Vairagkar A, Diwan D, Sahi C. J-like protein family of Arabidopsis thaliana: the enigmatic cousins of J-domain proteins. Plant Cell Rep. 2022; 1:1–13. https://doi.org/10.1007/s00299-022-02857-y PMID: 35290497

85. Woodward R, Gull K. Timing of nuclear and kinetoplast DNA replication and early morphological events in the cell cycle of Trypanosoma brucei. J Cell Sci. 1990; 95(Pt 1):49–57.

86. Moloney NM, Barylyuk K, Tromer E, Crook OM, Breckels LM, Lilley KS, et al. Mapping diversity in African trypanosomes using high resolution spatial proteomics. Nat Commun. 2023;14.

87. Schönenberger M, Brun R. Cultivation and in vitro cloning of procyclic culture forms of 'Trypanosoma brucei' in a semi-defined medium: short communication. ActaTropica. 1979; 36:289–292.

88. Hirumi H, Hirumi K. Continuous cultivation of Trypanosoma brucei blood stream forms in a medium containing a low concentration of serum protein without feeder cell layers. J Parasitol. 1989; 75:985–989. PMID: 2614608

89. Bochud-Allemann N, Schneider A. Mitochondrial Substrate Level Phosphorylation Is Essential for Growth of Procyclic Trypanosoma brucei. J Biol Chem. 2002; 277:32849–32854.

90. Oberholzer M, Morand S, Kunz S, Seebeck T. A vector series for rapid PCR-mediated C-terminal in situ tagging of Trypanosoma brucei genes. Mol Biochem Parasitol. 2006; 145:117–120. https://doi.org/10.1016/j.molbiopara.2005.09.002 PMID: 16269191

91. Mani J, Desy S, Niemann M, Chanfon A, Oeljeklaus S, Pusnik M, et al. Mitochondrial protein import receptors in Kinetoplastids reveal convergent evolution over large phylogenetic distances. Nat Commun. 2015; 6:1–12. https://doi.org/10.1038/ncomms7646 PMID: 25808593

92. Abràmoff MD, Magalhaes PJ, Ram SJ. Image Processing with ImageJ. Biophotonics Int. 2004; 11:36–42.

93. Chomczynski P, Sacchi N. Single-step method of RNA isolation by acid guanidinium thiocyanate-phenol-chloroform extraction. Anal Biochem. 1987; 162:156–159. https://doi.org/10.1006/abio.1987.9999 PMID: 2440339

94. Trikin R, Doiron N, Hoffmann A, Haenni B, Jakob M, Schnaufer A, et al. TAC102 Is a Novel Component of the Mitochondrial Genome Segregation Machinery in Trypanosomes. PLoS Pathog. 2016; 12: e1005586.

95. Liu B, Molina H, Kalume D, Pandey A, Griffith JD, Englund PT. Role of p38 in replication of Trypanosoma brucei kinetoplast DNA. Mol Cell Biol. 2006; 26:5382–5393. https://doi.org/10.1128/MCB.00369-06 PMID: 16809774

96. Lamour N, Rivière L, Coustou V, Coombs GH, Barrett MP, Bringaud F. Proline metabolism in procyclic Trypanosoma brucei is down-regulated in the presence of glucose. J Biol Chem. 2005; 280:11902–11910. https://doi.org/10.1074/jbc.M414274200 PMID: 15665328

97. Eichenberger C, Oeljeklaus S, Bruggisser J, Mani J, Haenni B, Kaurov I, et al. The highly diverged trypanosomal MICOS complex is organized in a nonessential integral membrane and an essential peripheral module. Mol Microbiol. 2019; 112:1731–1743. https://doi.org/10.1111/mmi.14389 PMID: 31541487

98. Wenger C, Harsman A, Niemann M, Oeljeklaus S, von Känel C, Calderaro S, et al. The Mba1 homologue of Trypanosoma brucei is involved in the biogenesis of oxidative phosphorylation complexes. Mol Microbiol. 2023; 119:537–550. https://doi.org/10.1111/mmi.15048 PMID: 36829306

99. Cox J, Mann M. MaxQuant enables high peptide identification rates, individualized p.p.b.-range mass accuracies and proteome-wide protein quantification. Nat Biotechnol. 2008; 26:1367–1372. https://doi.org/10.1038/nbt.1511 PMID: 19029910

100. Cox J, Neuhauser N, Michalski A, Scheltema RA, Olsen JV, Mann M. Andromeda: A peptide search engine integrated into the MaxQuant environment. J Proteome Res. 2011; 10:1794–1805. https://doi.org/10.1021/pr101065j PMID: 21254760

101. Cleveland WS, Devlin SJ. Locally Weighted Regression: An Approach to Regression Analysis by Local Fitting. J Am Stat Assoc. 1988; 83:596–610.

102. Gautier L, Cope L, Bolstad BM, Irizarry RA. Affy—Analysis of Affymetrix GeneChip data at the probe level. Bioinformatics. 2004; 20:307–315. https://doi.org/10.1093/bioinformatics/btg405 PMID: 14960456

103. Egert J, Brombacher E, Warscheid B, Kreutz C. DIMA: Data-Driven Selection of an Imputation Algorithm. J Proteome Res. 2021; 20:3489–3496.

104. Schwämmle V, León IR, Jensen ON. Assessment and improvement of statistical tools for comparative proteomics analysis of sparse data sets with few experimental replicates. J Proteome Res. 2013; 12:3874–3883. https://doi.org/10.1021/pr400045u PMID: 23875961

105. Smyth GK. Linear models and empirical bayes methods for assessing differential expression in microarray experiments. Stat Appl Genet Mol Biol. 2004;3.

106. Benjamini Y, Hochberg Y. Controlling the False Discovery Rate: A Practical and Powerful Approach to Multiple Testing. J R Stat Soc B Methodol. 1995; 57:289–300.

107. Breitling R, Herzyk P. Rank-based methods as a non-parametric alternative of the T-statistic for the analysis of biological microarray data. J Bioinform Comput Biol. 2005; 3:1171–1189. https://doi.org/10.1142/s0219720005001442 PMID: 16278953

108. Dewar CE, Oeljeklaus S, Mani J, Mühlhäuser WWD, von Känel C, Zimmermann J, et al. Mistargeting of aggregation prone mitochondrial proteins activates a nucleus-mediated posttranscriptional quality control pathway in trypanosomes. Nat Commun. 2022;13.

109. Del Carratore F, Jankevics A, Eisinga R, Heskes T, Hong F, Breitling R. RankProd 2.0: a refactored bioconductor package for detecting differentially expressed features in molecular profiling datasets. Bioinformatics. 2017; 33:2774.

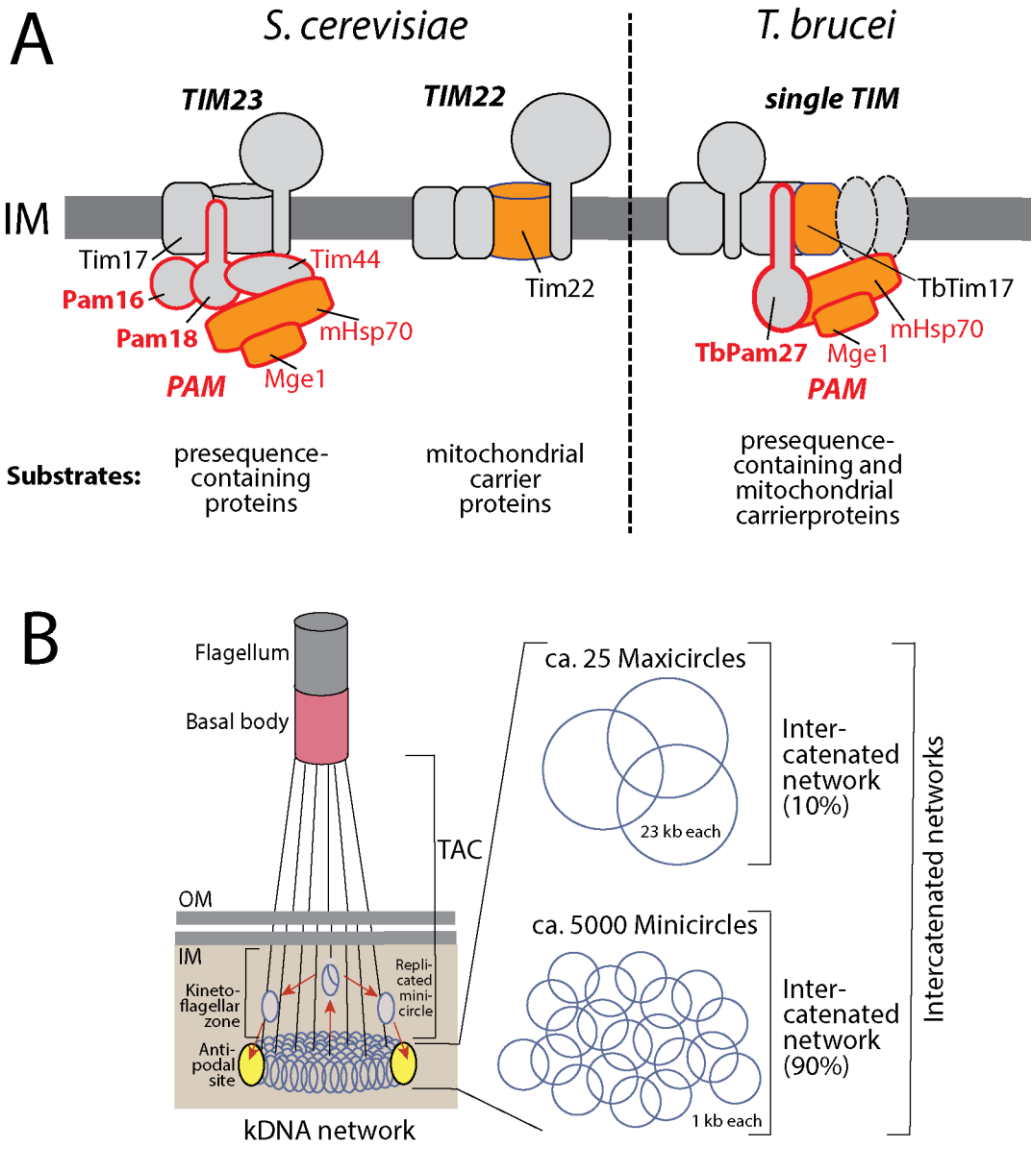

S1 Fig. Schematic depiction of mitochondrial inner membrane protein translocases and organization of the mitochondrial genome, termed kinetoplast DNA (kDNA) in T. brucei.

(A) Schematic depiction of the yeast TIM23 and TIM22 complexes (left) and the single trypanosomal TIM complex (right). In the trypanosomal TIM complex, the subunits specifically associated with presequence pathway are indicated in broken lines. Subunits of the presequence-associated import motor (PAM) are indicated in bold red lines. Unique and homologous subunits between the 2 species are indicated in gray and orange, respectively. The non-homologous J domain proteins Pam18/16 and TbPam27 are indicated in bold. (B) Organization of the single unit kDNA of *T. brucei*. The kDNA is a disk consisting of an intercalated network of maxi- and minicircles, which is physically connected, across the outer and the inner membrane, with the basal body of the flagellum via the tripartite attachment complex (TAC). Minicircles are replicated via theta structures after they have been released from the center of the network into the kinetoflagellar zone. After replication, they are reattached to the kDNA disk at the antipodal sites. Maxicircles in contrast are replicated while remaining attached to the kDNA disk.

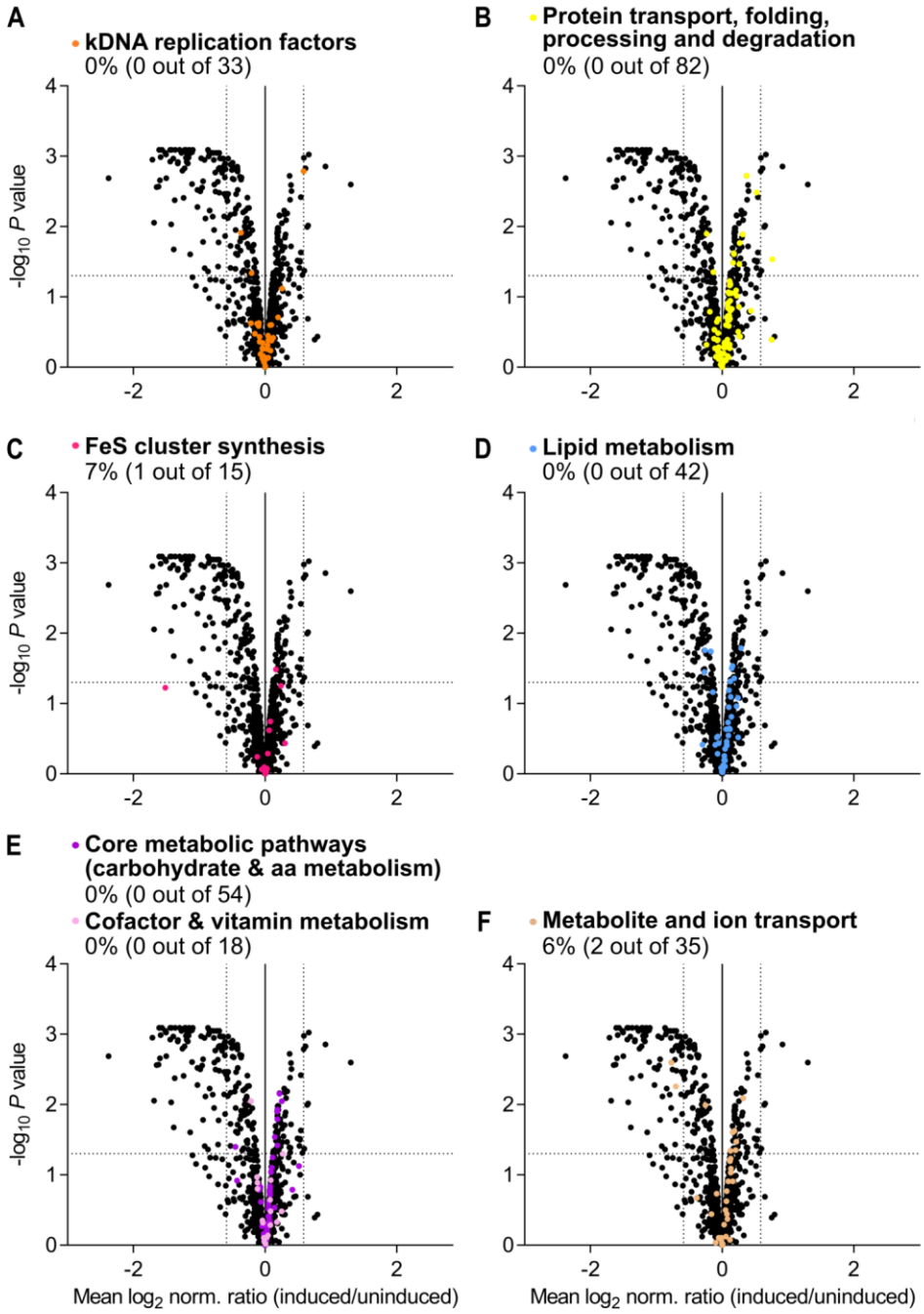

S2 Fig. TbPam18 RNAi does not affect protein subgroups exclusively consisting of nucleus-encoded proteins.

Mitochondria-enriched fractions of uninduced and 4 days induced TbPam18 RNAi cells were analyzed by SILAC-based quantitative mass spectrometry (same data set as in Fig 1B). **(A–F)** The indicated subgroups of mitochondrial proteins are highlighted in the indicated colors. The number of all more than 1.5-fold depleted proteins and the total number of all detected proteins for each subgroup are indicated in parentheses at the top of each panel. Numerical data for panel (A) to (F) are available in S1 Table.

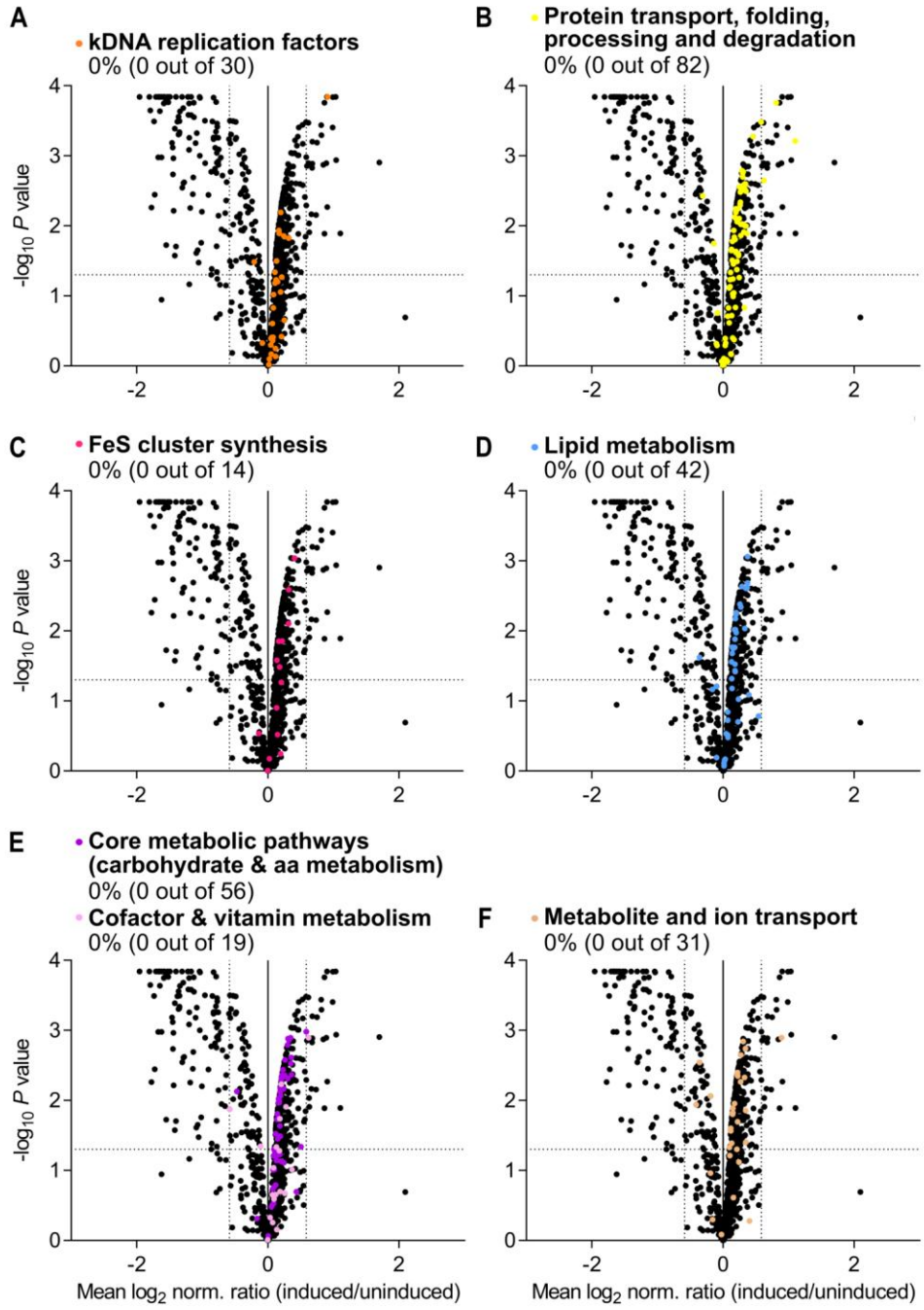

S3 Fig. TbPam16 RNAi does not affect protein subgroups exclusively consisting of nucleus-encoded proteins.

Mitochondria-enriched fractions of uninduced and 4 days induced TbPam16 RNAi cells were analyzed by SILAC-based quantitative mass spectrometry (same data set as in Fig 1B). **(A–F)** The indicated subgroups of mitochondrial proteins are highlighted in the indicated colors. The number of all more than 1.5-fold depleted proteins and the total number of all detected proteins for each subgroup are indicated in parentheses at the top of each panel. Numerical data for panel (A) and (F) are available in S1 Data.

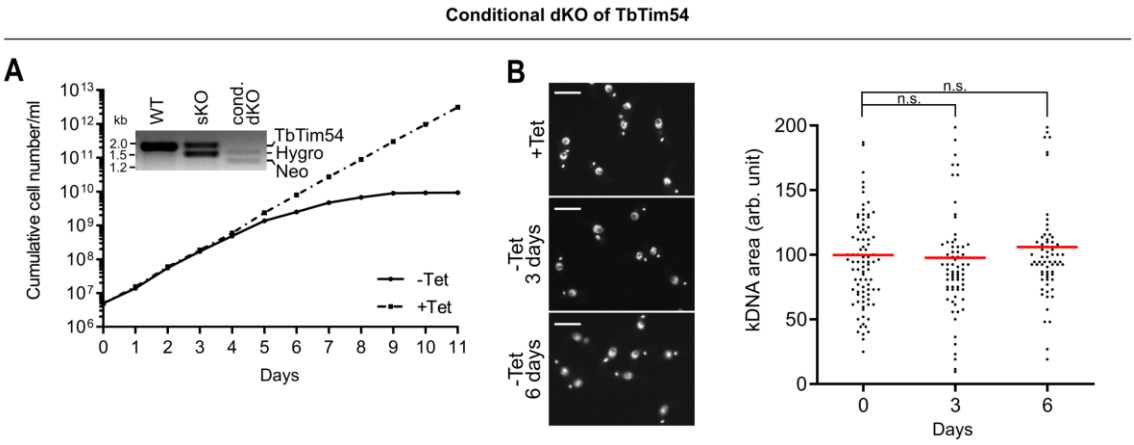

S4 Fig. TbTim54 is not required to maintain kDNA integrity.

(A) Growth curve of a TbTim54 conditional double knockout (cond. dKO) cell line. While both TbTim54 alleles are knocked out in uninduced (-Tet) as well as induced (+Tet) cells, TbTim54-HA is only ectopically expressed when tetracycline is present. Inset: Verification of single knockout (sKO) and dKO by PCR using a primer pair to amplify the TbTim54 ORF (approximately 2.0 kilobases (kb)), the hygromycin (hygro, approximately 1.5 kb), or the neomycin (neo, approximately 1.3 kb) resistance cassettes at the same time. Hygro was used to replace the first and neo was used to replace the second allele. **(B)** Left: DAPI-stained TbTim54 cond. dKO cell line grown in the presence of tetracycline (+Tet) and 3 or 6 days after the removal of tetracycline from the medium (-Tet). Right: Quantification of kDNA areas in 69 to 90 DAPI-stained cells. The red line indicates the mean of the kDNA areas for each time point. The mean of the control cells (+Tet) was set to 100%. n.s.: not significant (*P* value >0.05) as calculated by an unpaired two-tailed *t* test. Numerical data for panel (A) and (B) are available in S1 Data.

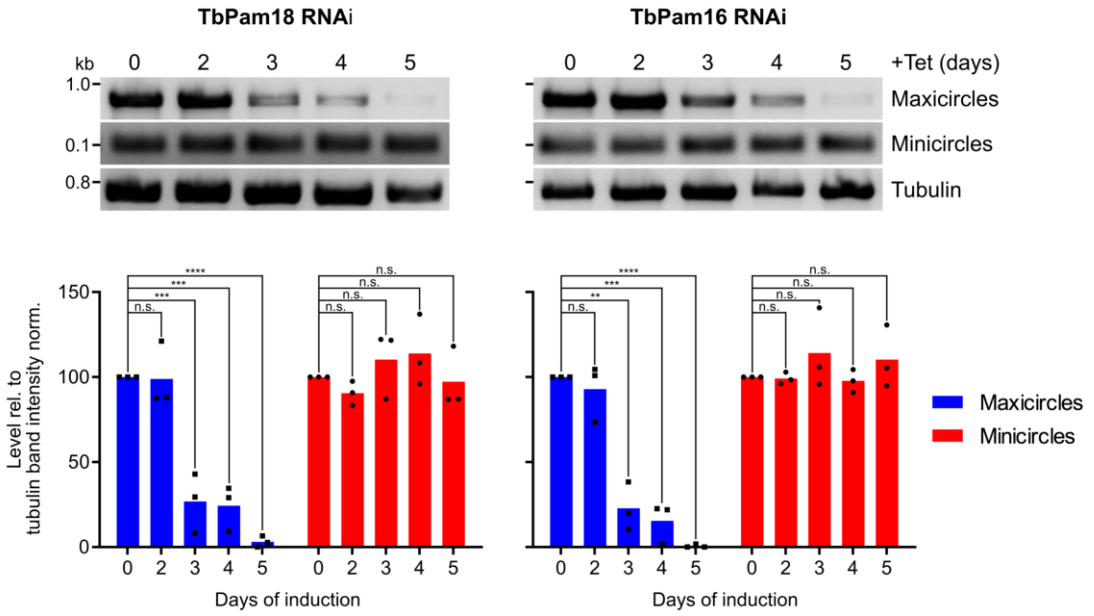

S5 Fig. Changes in mini- and maxicircle levels can be detected by quantitative PCR.

Upper panels: A quantitative PCR-based (qPCR) method was used to detect changes in steady-state levels of total mini- and maxicircles. Total DNA was extracted from uninduced and 2 to 5 days induced TbPam18 and TbPam16 RNAi cell lines. This DNA was used as the template in PCRs amplifying specific mini- and maxicircle regions or the intergenic region of tubulin. PCR products were analyzed on agarose gels. Lower panels: Densitometric quantification of mini- and maxicircle abundance as detected by qPCR. The ratio of the mini- or maxicircle band intensity and the respective control (tubulin band intensity) was normalized (norm.) to the ratios of uninduced cells. Blue (maxicircles) and red (minicircles) bars represent the mean of 3 independent biological replicates. n.s.: not significant, **: *P* value <0.05, ***: *P* value <0.005, ****: *P* value <0.0001, as calculated by an unpaired two-tailed *t* test. Numerical data are available in S1 Data.

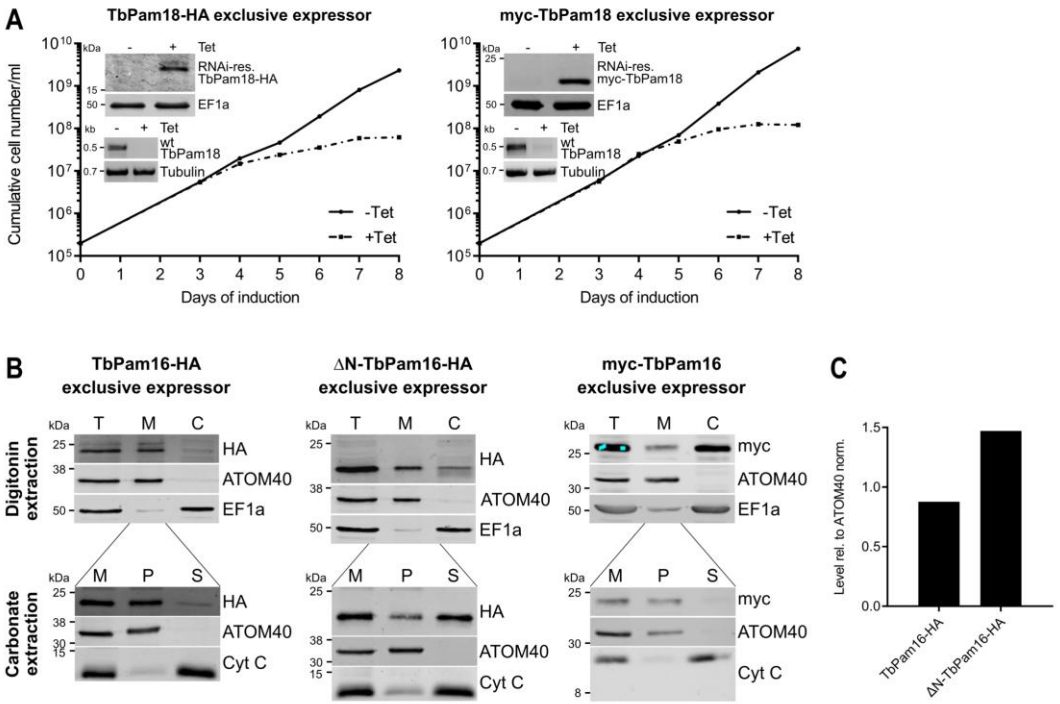

S6 Fig. Functional analysis of tagged TbPam18 and subcellular localization of TbPam16 variants.

(A) Growth curve of uninduced (-Tet) and induced (+Tet) cells expressing RNAi-resistant (RNAi-res.) TbPam18-HA (left) or myc-TbPam18 (right) in the background of RNAi against the wild type (wt) TbPam18 (TbPam18-HA and myc-TbPam18 exclusive expressors). Insets, top: Immunoblot analysis of whole cell extracts of uninduced (-) and 2 days induced (+) cells, probed for RNAi-res. TbPam18-HA or myc-TbPam18 and EF1a as loading control. Insets, bottom: RT-PCR products of the wt TbPam18 mRNA in uninduced (-) or 2 days induced (+) cells. Tubulin mRNA serves as loading control. **(B)** Upper panels: Immunoblot analysis of total cells (T), digitonin-extracted, mitochondria-enriched (M), and soluble cytosolic (C) fractions of TbPam16-HA, ΔN-TbPam16-HA, and myc-TbPam16 exclusive expressor cell lines. Blots were probed with anti-HA antibodies and antisera against ATOM40 and EF1a, which serve as mitochondrial and cytosolic markers, respectively. Lower panels: digitonin-extracted, crude mitochondrial fractions (M) were subjected to an alkaline carbonate extraction resulting in a pellet enriched in integral membrane proteins (P) and a soluble supernatant fraction (S). Immunoblots were probed with anti-HA and antisera against ATOM40 and cytochrome C (Cyt C), which serve as marker for integral membrane and soluble proteins, respectively. All immunoblots derive from the same gel. **(C)** Quantification of the expression levels in total cells, lanes T in (B), of TbPam16-HA and ΔN-TbPam16-HA normalized to ATOM40. Numerical data for panel (A) and (C) are available in S1 Data.

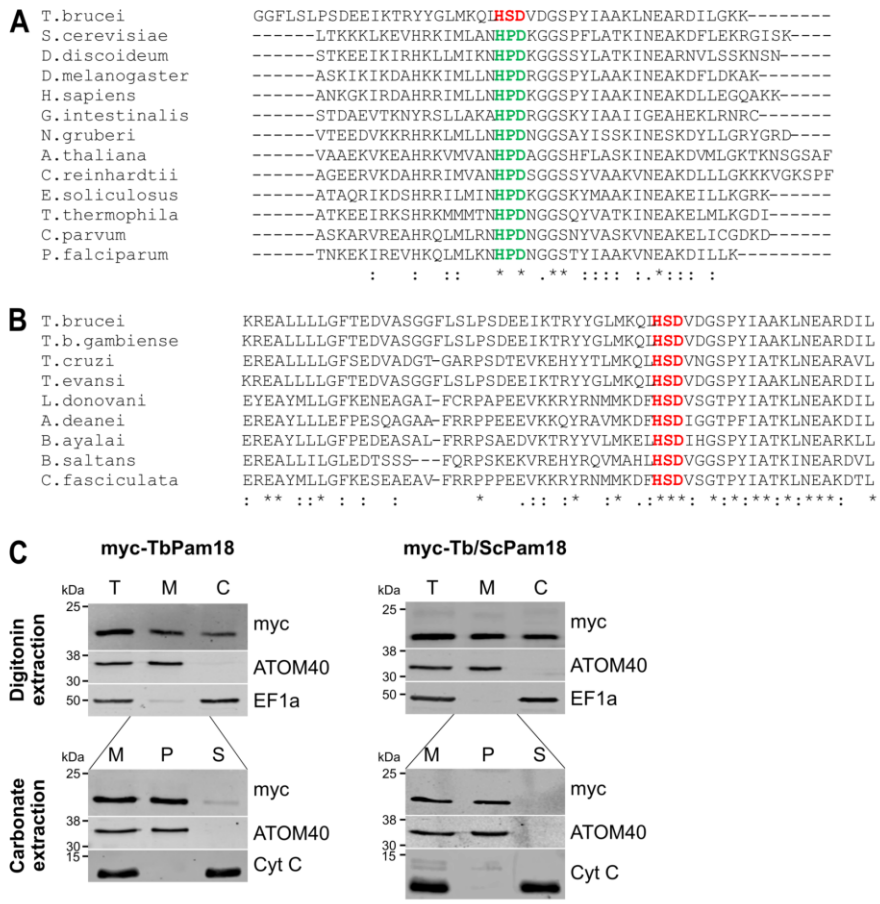

S7 Fig. Multiple sequence alignments of Pam18 homologues and subcellular localization of TbPam18 variants.

(A) Sequence alignment of N-terminal regions of Pam18 homologues of 13 representative eukaryotes. **(B)** Sequence alignment of N-terminal regions of Pam18 homologues of 9 representative trypanosomatids. In (A) and (B) Histidine-Proline-Aspartate (HPD) motifs are highlighted in red and Histidine-Serine-Aspartate (HSD) motifs in green. **(C)** Upper panels: Immunoblot analysis of total cells (T), digitonin-extracted mitochondria-enriched (M), and soluble cytosolic (C) fractions of cell lines expressing N-terminally myc-tagged TbPam18 or Tb/ScTbPam18. Blots were probed with anti-myc antibodies and antisera against ATOM40 and EF1a, which serve as mitochondrial and cytosolic markers, respectively. Lower panels: digitonin-extracted crude mitochondrial fractions (M) were subjected to an alkaline carbonate extraction resulting in a pellet enriched in integral membrane proteins (P) and a soluble supernatant fraction (S). Immunoblots were probed with anti-myc and antisera against ATOM40 and Cyt C, which serve as makers for integral membrane and soluble proteins, respectively.

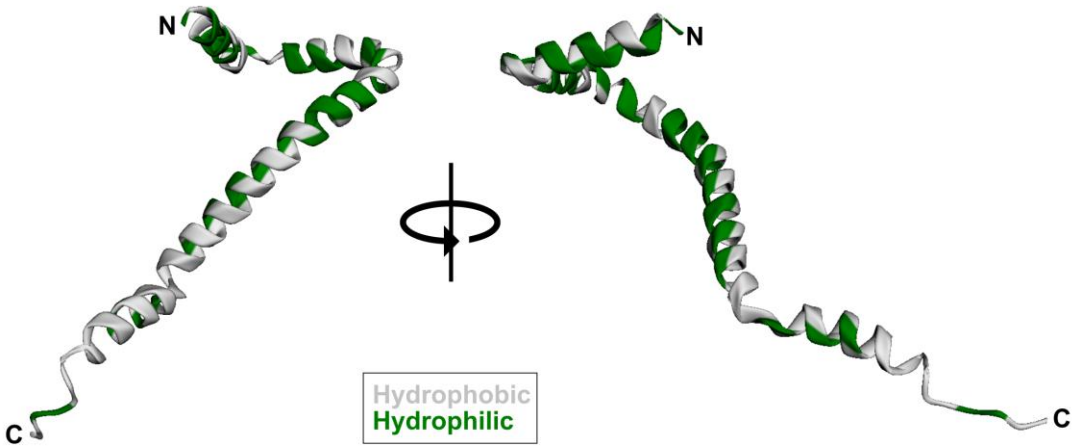

S8 Fig. AlphaFold prediction of MaRF11/Tb927.11.435.

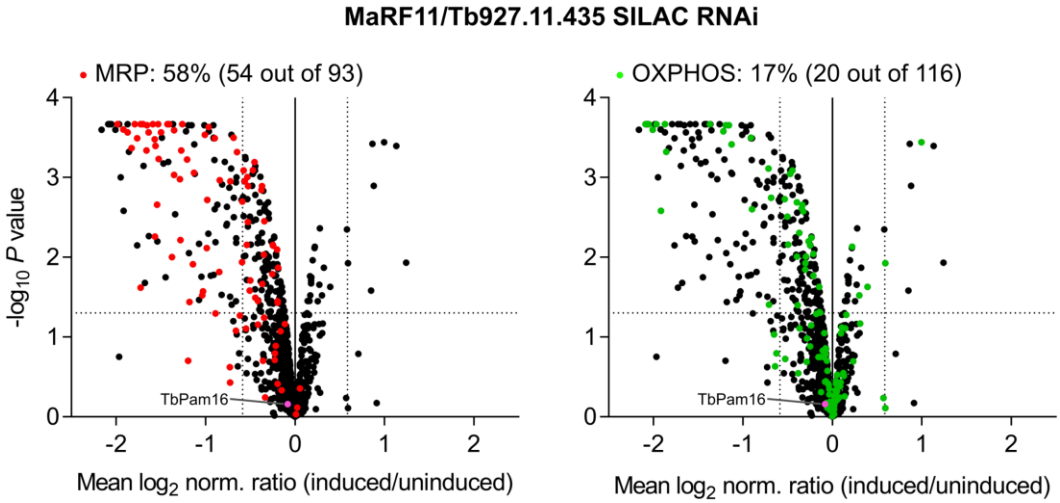

S9 Fig. Effect of MaRF11/Tb927.11.435 RNAi on the mitochondrial proteome.

Mitochondria-enriched fractions of uninduced and 4 days induced MaRF11 RNAi cells were analyzed by SILAC-based quantitative mass spectrometry. The data set was filtered for mitochondrial proteins and the mean $\log_2$ of normalized ratios (induced/uninduced) was plotted against the corresponding negative $\log_{10}$ of adjusted *P* value (limma test). Highlighted are mitochondrial ribosomal proteins (MRPs, red) and components of the oxidative phosphorylation pathway (OXPHOS, green) as well as TbPam16 (pink). The horizontal dotted line in each volcano plot marks an adjusted *P* value of 0.05. The vertical dotted lines indicate a fold-change in protein abundance of ±1.5. The percentages of all detected MRPs or OXPHOS proteins that are depleted more than 1.5-fold is indicated at the top of each panel. The number of all more than 1.5-fold depleted MRPs or OXPHOS proteins and the total number of all detected MRPs or OXPHOS proteins is shown in parentheses. MaRF11/Tb927.11.435 was not detected. Numerical data are available in S3 Table.

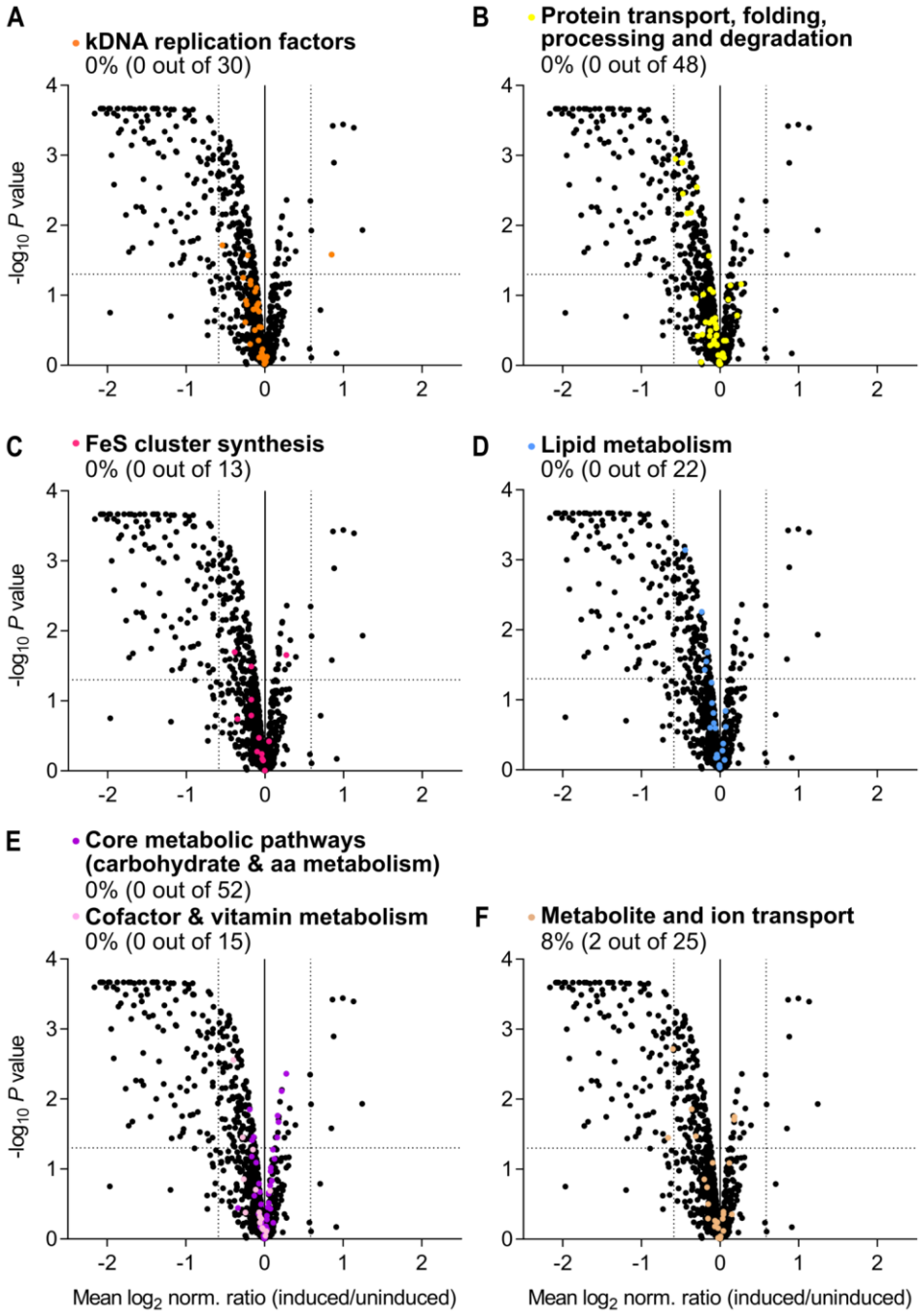

S10 Fig. MaRF11/Tb927.11.435 RNAi does not affect protein subgroups exclusively consisting of nucleus-encoded proteins.

Mitochondria-enriched fractions of uninduced and 4 days induced MaRF11 RNAi cells were analyzed by SILAC-based quantitative mass spectrometry (same data set as in S9 Fig). **(A–F)** The indicated subgroups of mitochondrial proteins are highlighted in the indicated colors. The number of all more than 1.5-fold depleted proteins and the total number of all detected proteins for each subgroup are indicated in parentheses at the top of each panel. Numerical data for panel are available in S3 Table.

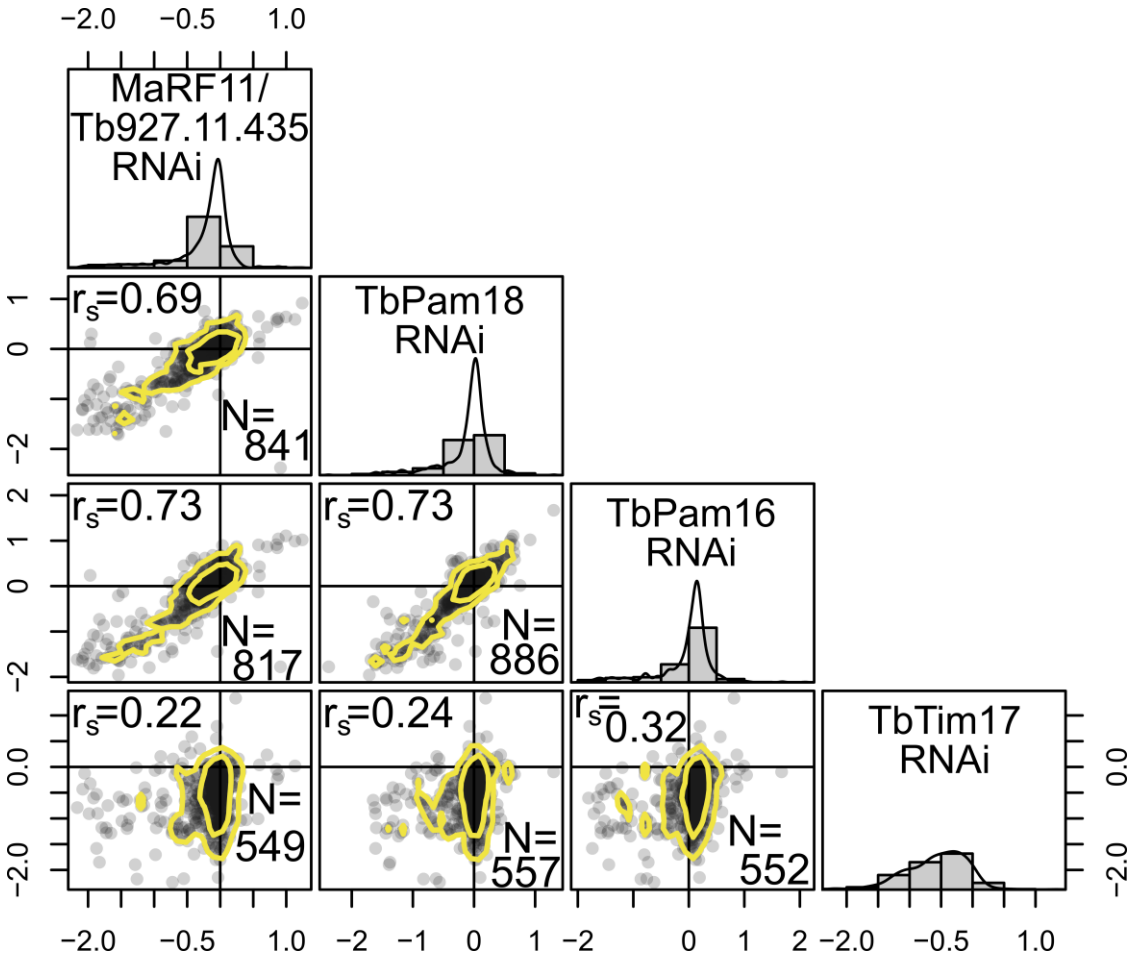

S11 Fig. Correlation analysis of TbPam18, TbPam16, MaRF11/Tb927.11.435, and TbTim17 SILAC RNAi data sets.

The mitochondrial proteins detected in the data sets of the indicated SILAC RNAi analyses were quantitatively compared in a pairs diagram created with R (version 4.2.1). The log_2-normalized foldchanges of all detected mitochondrial proteins of 1 SILAC experiment were compared to each of the other experiments in individual scatter graphs. Yellow clouds indicate the range in which 50% (inner cloud) and 90% (outer cloud) of the data points are located. The correlation between the data sets was calculated using the Spearman's rank correlation algorithm and is indicated as r_s. *N* indicates the total number of proteins that could be compared between 2 data sets. The 4 panels along the diagonal axis contain histograms combined with density graphs displaying the overall data point distribution in each experiment. As all 4 data sets have a left-skewed distribution, the Spearman's rank correlation was used as the statistical measure. Numerical data are available in S1 and S3 Tables.

RNAi-res. TbPam18

ATG GCA GCT CCG CTT GCG GCA TTG GTG CTG CTT GGA GGA GCA TAT TAT ATT TTC AGG TTG GCA CCA CGT ATT ACA CAA CGC GTG TCT ATG
GCT CAG GGT CTT ACA TGT GCT GCT AAT CGT CAA CTT CGT CCA TAC CGT CGT TAC GAA GGT GGA TTT GAA AAG TCA ATG ACA AAG CGA GAA
GCT CTT CTT CTT CTG GGT TTT ACA GAG GAC GTG GCA TCA GGA GGT TTT CTG TCA CTG CCG TCT GAC GAA GAG ATA AAG ACG CGT TAT TAC
GGA TTG ATG AAA CAG CTT CAC TCA GAC GTT GAT GGT AGC CCA TAC ATT GCT GCA AAG TTG AAC GAG GCT CGT GAC ATA CTT GGT AAA AAA
TAA

RNAi-res. ΔN-TbPam18

ATG TTC CGC TGT GTC GTC CGT TTT GGT GCC AAA GAC ATC CGT TTT GTG TCT ATG GCT CAG GGT CTT ACA TGT GCT GCT AAT CGT CAA CTT
CGT CCA TAC CGT CGT TAC GAA GGT GGA TTT GAA AAG TCA ATG ACA AAG CGA GAA GCT CTT CTT CTT CTG GGT TTT ACA GAG GAC GTG GCA
TCA GGA GGT TTT CTG TCA CTG CCG TCT GAC GAA GAG ATA AAG ACG CGT TAT TAC GGA TTG ATG AAA CAG CTT CAC TCA GAC GTT GAT GGT
AGC CCA TAC ATT GCT GCA AAG TTG AAC GAG GCT CGT GAC ATA CTT GGT AAA AAA TAA

RNAi-res. Tb/ScPam18

ATG GCA GCT CCG CTT GCG GCA TTG GTG CTG CTT GGA GGA GCA TAT TAT ATT TTC AGG TTG GCA CCA CGT ATT ACA CAA CGC GTG TCT ATG
GCT CAG GGT CTT ACA TGT GCT GCT AAT CGT CAA CTT CGT CCA TAC CGT TTC TTG AAA GGC GGA TTT GAC CCG AAA ATG AAT TCT AAA GAG
GCT CTA CAG ATT TTG AAT TTG ACA GAA AAT ACA TTG ACT AAA AAA AAG TTG AAA GAG GTT CAT AGG AAA ATT ATG TTA GCT AAT CAT CCT
GAC AAA GGT GGT TCT CCA TTT TTG GCC ACT AAG ATA AAC GAA GCT AAG GAC TTT TTG GAA AAA AGG GGT ATT AGC AAA TAA

RNAi-res. TbPam18-S98P

ATG GCA GCT CCG CTT GCG GCA TTG GTG CTG CTT GGA GGA GCA TAT TAT ATT TTC AGG TTG GCA CCA CGT ATT ACA CAA CGC GTG TCT ATG
GCT CAG GGT CTT ACA TGT GCT GCT AAT CGT CAA CTT CGT CCA TAC CGT CGT TAC GAA GGT GGA TTT GAA AAG TCA ATG ACA AAG CGA GAA
GCT CTT CTT CTT CTG GGT TTT ACA GAG GAC GTG GCA TCA GGA GGT TTT CTG TCA CTG CCG TCT GAC GAA GAG ATA AAG ACG CGT TAT TAC
GGA TTG ATG AAA CAG CTT TAC TCA GAC GTT GAT GGT AGC CCA TAC ATT GCT GCA AAG TTG AAC GAG GCT CGT GAC ATA CTT GGT AAA AAA
TAA

RNAi-res. TbPam16

ATG CGT CGT ATT ATG TCA CCA CGC GTT ATG TGC GAG GTA AAA TTT GGT AGC CGT CCA GCT CCA CTG GCC TGC AGC CGT ATG TTC TTT ATT
CCA CCA CAG CTG GCG AAA TTG ATT GTG ACA TCT GGA TTA CTG ATA GTG AAA GCA TTC CTG GTG GCT CAC CAA CAG GAA GCT AAA AGA TTG
CGT GAA GAA GAA GAA AAA GAA GGT CAC TCT GCT ACA AAC GCA CAG GTT GGT ACG GGA AGC GCA GCT CTG ATG ACG TCA TCA GAG GCT
TTG CAA ATT CTG GGT CTG CAG CCA AAC ATG TCA GTG CCG TTG ACG GCT GAA TCA GAC CGG CAA CTG GCT GCA GTT CGA TTT GAA CAC TTG
TTT GCC ATC GCG ACG CGA TGT AAG AAC GTG TTC CTG CAA GGG AAG TTG AGT GGT GCA TAC CGT GTT TGC GTG GAT CCA GAA TGG GAC TTG
AAA GAC GAG GTT AAG GAT AGT CAC GGA AAC TCA AGG GGT AAC GAT GCA ATG TGG TAA

RNAi-res. ΔN-TbPam16

ATG TTC CGC TGT GTC GTC CGT TTT GGT GCC AAA GAC ATC CGT TTT CAC CAA CAG GAA GCT AAA AGA TTG CGT GAA GAA GAA GAA AAA
GAA GGT CAC TCT GCT ACA AAC GCA CAG GTT GGT ACG GGA AGC GCA GCT CTG ATG ACG TCA TCA GAG GCT TTG CAA ATT CTG GGT CTG CAG
CCA AAC ATG TCA GTG CCG TTG ACG GCT GAA TCA GAC CGG CAA CTG GCT GCA GTT CGA TTT GAA CAC TTG TTT GCC ATC GCG ACG CGA TGT
AAG AAC GTG TTC CTG CAA GGG AAG TTG AGT GGT GCA TAC CGT GTT TGC GTG GAT CCA GAA TGG GAC TTG AAA GAC GAG GTT AAG GAT
AGT CAC GGA AAC TCA AGG GGT AAC GAT GCA ATG TGG TAA

S12 Fig. Synthetic TbPam18 and TbPam16 genes.

RNAi-resistant (RNAi-res.) TbPam18 and TbPam16 DNA sequences in black with changed nucleotides highlighted in red. In the ΔN-TbPam18 and ΔN-TbPam16 constructs, the first 81 and 156 nucleotides, respectively, were replaced by the first 45 nucleotides of TbmHsp60, which encode the mitochondrial targeting sequence of the protein (green). To generate the Tb/ScPam18 fusion protein, the first 295 nucleotides of RNAi-res. TbPam18 were fused to the last 213 nucleotides of yeast (Sc) Pam18 (blue). To generate RNAi-res. TbPam18-S98P, the cytosine at position 292 of the nucleotide sequence was exchanged against a thymine (highlighted in yellow).

4. Discussion

Eukaryotes arose from an ancient Asgard Archaeon which acquired an alphaproteobacterial endosymbiont, giving rise to the mitochondrion, the first endosymbiosis-derived organelle. Following the emergence of eukaryotes, several endosymbiotic events occurred, during which some eukaryotic lineages acquired additional organelles that enabled phototrophic (plastids) and, more recently, diazotrophic (nitroplast and diazoplast) metabolism. A defining feature of nearly all endosymbiosis-derived organelles is that they contain a genome. These genomes are highly reduced due to the loss of redundant genes, but also due to gene transfers from the organellar genome to the nucleus. Insights from the relatively young chromatophore, nitroplast, and diazoplast confirm that the targeting of “host” cell proteins to the organelle enables large parts of the organellar genome to be lost in a short period of time [120, 129, 133]. However, organellar genome reduction stagnates in most cases resulting in the retention of small sets of genes encoded in organellar genomes. A key factor in the retention of protein-coding genes in the organellar genome is the hydrophobicity of the gene product. Highly hydrophobic membrane proteins, in particular, are among the most often retained genes in organellar genomes and even in the gene-rich genomes of the nitroplast and diazoplast, the organellar genome-encoded proteome exhibits an increased hydrophobicity [162]. Organellar DNA is typically compacted into nucleoids by DNA-binding proteins. These nucleoids are loosely defined DNA-protein particles which exhibit significant variability, even within individual organelles [171]. This Thesis focused on mitochondrial nucleoids and their inheritance which have mainly been studied in species of the Opisthokonta that are classified in the eukaryotic supergroup Amorphea [144]. These organisms typically have many mitochondria per cell which undergo frequent fission and fusion events. Each mitochondrion contains one or a few nucleoids which are associated with the IM. Recent research has demonstrated that these nucleoids are actively transported by physical connections to actin filaments and microtubules [167, 186]. In addition to Amorphea, mitochondrial biogenesis has also been investigated in a few land plant species which belong to the Archaeplastida supergroup. In land plants, mitochondria are trafficked along actin filaments, and nucleoids may also be associated with the IM [166, 206]. However, the frequent observation of mitochondria without detectable DNA, as well as extensive mitochondrial fusion events during land plant germination, suggest significant differences in nucleoid inheritance between the Archaeplastida and the Amorphea [201, 203]. A third eukaryotic supergroup in which mitochondrial genome inheritance has been studied in detail are the Discoba [144]. In particular, the mitochondrial genome inheritance systems of the Trypanosomatidae are well understood. The Trypanosomatidae, including *T.*

brucei studied here, are single-celled obligate parasites that contain a single mitochondrion. Their mitochondrial genome organization is highly complex consisting of two classes of circular DNA molecules that are concatenated into a single network containing thousands of DNA molecules. The replication and segregation of this network, known as the kinetoplast, is coupled to the cell cycle [178]. As is assumed for nucleoids in Amorphea and Archaeplastida, the kinetoplast is physically linked to the IM and its segregation is controlled by extramitochondrial structures. Specifically, the kinetoplast is connected to the basal and probasal body of the flagellum via a protein structure known as the TAC [384]. The TAC consists of nine core subunits and possibly some TAC-associated factors [369, 370, 391]. However, none of these subunits are orthologs of proteins involved in nucleoid segregation or trafficking in Amorphea or Archaeplastida, which suggests that analogous nucleoid segregation systems have evolved independently multiple times during eukaryotic radiation.

The evolutionary origin of the TAC is unknown. The β-barrel structure of the OM subunits TAC40 and TAC42 suggest that at least these two proteins are of bacterial origin. However, the current lack of annotated genomes or sequencing data for kinetoplastids outside the Trypanosomatidae lineage does not allow the reconstruction of the evolutionary history of any TAC subunit. The only reasonably annotated genome of a Kinetoplastida species with a kinetoplast type other than the eukinetoplast is *Bodo saltans* [421]. *B. saltans* has a prokinetoplast that localizes close to the basal body, but it is not known whether the two structures are physically connected (see chapter 1.5.2.2). The draft genome of *B. saltans* contains high-confidence orthologs of TAC40, TAC60 and TAC65, but not of any other core TAC subunit. However, it cannot be excluded that this is due to poor sequencing quality. Interestingly, the TAC60 ortholog has only a single α-helical transmembrane domain that is predicted with low confidence, but it does contain the conserved p166-interaction domain, suggesting that an ortholog of p166 should exist. Having more annotated genomes of Kinetoplastida species with pro-, pan-, mega-, or polykinetoplasts would greatly help to study how the kDNA is segregated in other lineages and would allow to trace back the evolutionary origins of TAC subunits. Notably, in species with polykinetoplasts, a connection to the basal body would not be expected but rather multiple links to other cytoskeletal structures, as observed in several species of the Opisthokonta, might be possible. Nevertheless, TAC proteins are well conserved within the Trypanosomatidae, with orthologs of core TAC subunits found in most species. This suggests that the classical TAC, as seen in *T. brucei*, originates from the common ancestor of the Trypanosomatidae or an earlier organism.

The TAC of *T. brucei* has been extensively studied over the past two decades and it is believed that all of its core subunits have been identified [391]. The direct interaction partners of most TAC subunits are known and, with some exceptions in the OM TAC module, the continuous connection of the basal body to the kinetochore-like structure at the kDNA can be precisely mapped (Figure 18). In this Thesis, we identified the molecular details of the TAC60-p166 interaction which links the OM and IM within the TAC (chapter 3.1) and we investigated the assembly pathway of the OM TAC module (chapter 3.2).

The TAC is a permanent and highly stable protein complex that is insoluble by non-ionic detergents such as digitonin and Triton X-100. However, the molecular interactions responsible for this stability remained unknown. Surprisingly, despite the fact that the interaction domains of TAC60 and p166 contain conserved residues with side chains carrying opposite charges, we found that the TAC60-p166 interaction has a hydrophobic interface. —Hydrophobic interactions between molecules in aqueous solvent form readily because of a phenomenon known as the hydrophobic effect [422]. When hydrophobic molecules are exposed to aqueous solvents, they cause a significant solvent entropy loss due to the ordering of water molecules at the interface. Consequently, interphases between hydrophobic molecules in aqueous environments result in a significant solvent entropy gain making such interactions highly stable. Apart from this, hydrophobic molecule interphases may have a higher degree of freedom than interphases formed by stable molecular orbital contacts, which may allow more flexible molecule interphases. Hence, the presence of a hydrophobic interface at the core of the TAC60-p166 interaction, though unexpected, sheds light on how TAC stability and flexibility can be achieved. In our study, we also identified that within the expected p166-TAC102 interaction domain (p166 residues 71–210 [403]), the only conserved residues also have mostly hydrophobic side chains. Although highly speculative, this suggests a similar mode of interaction between p166 and TAC102. Indeed, hydrophobic interfaces are also expected between all OM TAC module subunits, and AlphaFold-generated structure models suggest that TAC65 may be partially OM-embedded through hydrophobic interactions with pATOM36. Therefore, it is tempting to speculate that the TAC may achieve the stability required to withstand the pulling forces at play during basal body movement and kinetoplast segregation through such hydrophobic protein interphases.

The TAC is probably cylindrical or cone-shaped [391]. Assembly occurs *de novo* and starts with p197 at the probasal body [388]. However, the OM TAC module has shown inconsistencies with a strict step-by-step assembly model. As presented in Chapter 3.2, our results demonstrated that the OM TAC module assembles from two classes of assembly intermediates. One of these

classes contains three assembly intermediates: one TAC40 oligomer and two assembly intermediates containing TAC40, TAC42, and TAC60. The second class contains an assembly intermediate comprising pATOM36 and TAC65. Notably, we demonstrated that the previously recognised essential N-terminal domain of TAC60 is required for assembly of the OM TAC module from the two classes of assembly intermediates. Our results are important as they address a knowledge gap observed in a previous study of the TAC assembly pattern of TAC65, which found that despite the direct interaction between p197 and TAC65, the latter depends on OM TAC module subunits for assembly [388]. Recognizing TAC65 as part of an assembly intermediate with pATOM36 alongside the TAC40/TAC42/TAC60 intermediates confirms these findings and provides an explanation for this assembly pattern of TAC65. To date, neither the molecular structures of the entire TAC nor of any of the subunits have been solved. Consequently, we can only speculate about the number of individual subunits and their relative stoichiometry. However, we have predicted the molecular structures of the characterized subcomplexes using AlphaFold. Strikingly, these predictions suggested that the VDAC-like TAC40 assembles into hexa- to octameric subcomplexes. This prediction was confirmed by *in vivo* experiments showing that TAC40 molecules interact with each other in a discrete high molecular weight complex. These findings are additionally in line with studies which showed that the structurally related human VDAC can also form oligomers [423, 424]. The protein complex structure predictions of the TAC40/TAC42/TAC60 and pATOM36/TAC65 subcomplexes produced plausible models. The predictions imply a higher copy number of TAC40 than of TAC42, which is consistent with previous findings [425]. However, besides this, there is little experimental data that could be used to evaluate these predictions. Nevertheless, the identification of the assembly intermediates, and especially the high confidence prediction of hexa-to octameric TAC40 complexes, provide a starting point for further experimental analysis.

The replication of the mitochondrial genome in *T. brucei*, beyond TAC-mediated segregation, has been intensively studied [178]. Nevertheless, many questions remain unanswered. Important aspects are the mechanisms that regulate kDNA replication and coordinate it with the cell cycle. In Chapter 3.3 we presented data on three newly characterized proteins involved in maxicircle level regulation. Interestingly, two of these factors, TbPam16 and TbPam18, are orthologs of PAM subunits that are required for mitochondrial protein import in other eukaryotic lineages (see chapter 1.5.1.1). However, our results show that in *T. brucei* these two proteins are not involved in mitochondrial protein import. Instead, they are required, together with the newly identified MaRF11, for maxicircle replication in procyclic *T. brucei*. TbPam16 and TbPam18 are IM proteins and this localization is essential for their function, hence, they could potentially

transmit a postulated but as yet unknown extramitochondrial signal that regulates the maxicircle replication. Furthermore, the observation that none of the three proteins regulate maxicircle replication in the bloodstream form parasites remains unexplained.

Altogether, this Thesis explored endosymbiosis-derived organelles of eukaryotes, emphasizing the maintenance and inheritance of organellar genomes. Particular focus was given to the mitochondrial membrane-spanning TAC, which passively segregates the mitochondrial genome in trypanosomatids. Our results revealed that the OM-IM connection within the TAC is formed by hydrophobic protein interfaces. Additionally, we have characterized two classes of subcomplexes forming the OM TAC module, providing insights into its assembly pathways. At a time of rapid progress in cryo-electron microscopy, it will be interesting to see what further insights the TAC has yet to reveal. Finally, the identification of a putatively IM-bound system required for maxicircle replication in procyclic *T. brucei* provided insights into how the mitochondrial genome replication of this organism may be regulated.

Bibliography

1. Brush, S.G., *The Age of the Earth in the Twentieth Century.* Earth Sciences History, 1989. **8**(2): p. 170-182.
2. Harrison, T.M., E.A. Bell, and P. Boehnke, *Hadean Zircon Petrochronology.* Reviews in Mineralogy and Geochemistry, 2017. **83**(1): p. 329-363.
3. Theobald, D.L., *A formal test of the theory of universal common ancestry.* Nature, 2010. **465**(7295): p. 219-22.
4. Moody, E.R.R., et al., *The nature of the last universal common ancestor and its impact on the early Earth system.* Nat Ecol Evol, 2024. **8**(9): p. 1654-1666.
5. Javaux, E.J., *Challenges in evidencing the earliest traces of life.* Nature, 2019. **572**(7770): p. 451-460.
6. Eme, L., et al., *Archaea and the origin of eukaryotes.* Nat Rev Microbiol, 2018. **16**(2): p. 120.
7. Craig, J.M., S. Kumar, and S.B. Hedges, *The origin of eukaryotes and rise in complexity were synchronous with the rise in oxygen.* Front Bioinform, 2023. **3**: p. 1233281.
8. Woese, C.R., O. Kandler, and M.L. Wheelis, *Towards a natural system of organisms: proposal for the domains Archaea, Bacteria, and Eucarya.* Proc Natl Acad Sci U S A, 1990. **87**(12): p. 4576-9.
9. Woese, C.R. and G.E. Fox, *Phylogenetic structure of the prokaryotic domain: the primary kingdoms.* Proc Natl Acad Sci U S A, 1977. **74**(11): p. 5088-90.
10. Bell, P.J.L., *Eukaryogenesis: The Rise of an Emergent Superorganism.* Front Microbiol, 2022. **13**: p. 858064.
11. Krupovic, M., V.V. Dolja, and E.V. Koonin, *The virome of the last eukaryotic common ancestor and eukaryogenesis.* Nat Microbiol, 2023. **8**(6): p. 1008-1017.
12. Bell, P.J.L., *Evidence supporting a viral origin of the eukaryotic nucleus.* Virus Res, 2020. **289**: p. 198168.
13. Archibald, J.M., *Endosymbiosis and Eukaryotic Cell Evolution.* Curr Biol, 2015. **25**(19): p. R911-21.
14. Sagan, L., *On the origin of mitosing cells.* J Theor Biol, 1967. **14**(3): p. 255-74.
15. Karnkowska, A., et al., *A Eukaryote without a Mitochondrial Organelle.* Curr Biol, 2016. **26**(10): p. 1274-84.
16. Williams, S.K., et al., *Extreme mitochondrial reduction in a novel group of free-living metamonads.* Nat Commun, 2024. **15**(1): p. 6805.
17. Zaremba-Niedzwiedzka, K., et al., *Asgard archaea illuminate the origin of eukaryotic cellular complexity.* Nature, 2017. **541**(7637): p. 353-358.
18. Spang, A., et al., *Complex archaea that bridge the gap between prokaryotes and eukaryotes.* Nature, 2015. **521**(7551): p. 173-179.
19. Munoz-Gomez, S.A., et al., *Site-and-branch-heterogeneous analyses of an expanded dataset favour mitochondria as sister to known Alphaproteobacteria.* Nat Ecol Evol, 2022. **6**(3): p. 253-262.
20. Liu, Y., et al., *Expanded diversity of Asgard archaea and their relationships with eukaryotes.* Nature, 2021. **593**(7860): p. 553-557.
21. Martijn, J., et al., *Deep mitochondrial origin outside the sampled alphaproteobacteria.* Nature, 2018. **557**(7703): p. 101-105.
22. Fan, L., et al., *Phylogenetic analyses with systematic taxon sampling show that mitochondria branch within Alphaproteobacteria.* Nat Ecol Evol, 2020. **4**(9): p. 1213-1219.

23. Martin, W.F., S. Garg, and V. Zimorski, *Endosymbiotic theories for eukaryote origin*. Philos Trans R Soc Lond B Biol Sci, 2015. **370**(1678): p. 20140330.
24. Lane, N. and W. Martin, *The energetics of genome complexity.* Nature, 2010. **467**(7318): p. 929-34.
25. Martin, W. and M. Muller, *The hydrogen hypothesis for the first eukaryote.* Nature, 1998. **392**(6671): p. 37-41.
26. Mills, D.B., et al., *Eukaryogenesis and oxygen in Earth history.* Nat Ecol Evol, 2022. **6**(5): p. 520-532.
27. Taylor, F.J.R., *II. IMPLICATIONS AND EXTENSIONS OF THE SERIAL ENDOSYMBIOSIS THEORY OF THE ORIGIN OF EUKARYOTES*. TAXON, 1974. **23**(2-3): p. 229-258.
28. Gololobova, M.A. and G.A. Belyakova, *Position of Algae on the Tree of Life.* Dokl Biol Sci, 2022. **507**(1): p. 312-326.
29. Medini, H., T. Cohen, and D. Mishmar, *Mitochondria Are Fundamental for the Emergence of Metazoans: On Metabolism, Genomic Regulation, and the Birth of Complex Organisms*. Annu Rev Genet, 2020. **54**: p. 151-166.
30. Shiflett, A.M. and P.J. Johnson, *Mitochondrion-related organelles in eukaryotic protists*. Annu Rev Microbiol, 2010. **64**: p. 409-29.
31. Chaldakov, G., *Human Body as a Multicrine System, with Special Reference to Cell Protein Secretion: From Vascular Smooth Muscles to Adipose Tissue.* 2017, 2017. **27**.
32. Tachezy, J. and O. Šmíd, *Mitosomes in Parasitic Protists*, in *Hydrogenosomes and Mitosomes: Mitochondria of Anaerobic Eukaryotes*, J. Tachezy, Editor. 2019, Springer International Publishing: Cham. p. 205-242.
33. Timmis, J.N., et al., *Endosymbiotic gene transfer: organelle genomes forge eukaryotic chromosomes.* Nat Rev Genet, 2004. **5**(2): p. 123-35.
34. Gray, M.W., *The endosymbiont hypothesis revisited.* Int Rev Cytol, 1992. **141**: p. 233-357.
35. Kleine, T., U.G. Maier, and D. Leister, *DNA transfer from organelles to the nucleus: the idiosyncratic genetics of endosymbiosis.* Annu Rev Plant Biol, 2009. **60**: p. 115-38.
36. Busch, J.D., et al., *Mitochondrial protein transport: Versatility of translocases and mechanisms.* Mol Cell, 2023. **83**(6): p. 890-910.
37. Dolezal, P., et al., *Giardia mitosomes and trichomonad hydrogenosomes share a common mode of protein targeting.* Proc Natl Acad Sci U S A, 2005. **102**(31): p. 10924-9.
38. Lopez, J.V., et al., *Numt, a recent transfer and tandem amplification of mitochondrial DNA to the nuclear genome of the domestic cat.* J Mol Evol, 1994. **39**(2): p. 174-90.
39. Lindmark, D.G. and M. Muller, *Hydrogenosome, a cytoplasmic organelle of the anaerobic flagellate Tritrichomonas foetus, and its role in pyruvate metabolism.* J Biol Chem, 1973. **248**(22): p. 7724-8.
40. Zhang, X., et al., *Mitochondria: one of the vital hubs for molecular hydrogen's biological functions.* Front Cell Dev Biol, 2023. **11**: p. 1283820.
41. Lill, R. and G. Kispal, *Maturation of cellular Fe-S proteins: an essential function of mitochondria*. Trends Biochem Sci, 2000. **25**(8): p. 352-6.
42. Schneider, R.E., et al., *The Trichomonas vaginalis hydrogenosome proteome is highly reduced relative to mitochondria, yet complex compared with mitosomes.* Int J Parasitol, 2011. **41**(13-14): p. 1421-34.
43. Jedelsky, P.L., et al., *The minimal proteome in the reduced mitochondrion of the parasitic protist Giardia intestinalis.* PLoS One, 2011. **6**(2): p. e17285.
44. Hacker, C., et al., *Biogenesis, inheritance, and 3D ultrastructure of the microsporidian mitosome.* Life Sci Alliance, 2024. **7**(1).
45. Gawryluk, R.M.R., et al., *The Earliest Stages of Mitochondrial Adaptation to Low Oxygen Revealed in a Novel Rhizarian.* Curr Biol, 2016. **26**(20): p. 2729-2738.
46. Wexler-Cohen, Y., et al., *A dynamin-related protein contributes to Trichomonas vaginalis hydrogenosomal fission*. FASEB J, 2014. **28**(3): p. 1113-21.

47. Voleman, L. and P. Dolezal, *Mitochondrial dynamics in parasitic protists.* PLoS Pathog, 2019. **15**(11): p. e1008008.
48. van der Bliek, A.M., M.M. Sedensky, and P.G. Morgan, *Cell Biology of the Mitochondrion.* Genetics, 2017. **207**(3): p. 843-871.
49. Verner, Z., et al., *Malleable mitochondrion of Trypanosoma brucei.* Int Rev Cell Mol Biol, 2015. **315**: p. 73-151.
50. Zorov, D.B., et al., *Mitocentricity.* Biochemistry (Mosc), 2024. **89**(2): p. 223-240.
51. Yang, Z., et al., *Mitochondrial Membrane Remodeling.* Front Bioeng Biotechnol, 2021. **9**: p. 786806.
52. Zorova, L.D., et al., *Mitochondrial membrane potential.* Anal Biochem, 2018. **552**: p. 50-59.
53. Lamb, I.M., et al., *Unique Properties of Apicomplexan Mitochondria.* Annu Rev Microbiol, 2023. **77**: p. 541-560.
54. Preminger, N. and M. Schuldiner, *Beyond fission and fusion-Diving into the mysteries of mitochondrial shape.* PLoS Biol, 2024. **22**(7): p. e3002671.
55. Thakur, V., et al., *A dynamin-like protein in Plasmodium falciparum plays an essential role in parasite growth, mitochondrial development and homeostasis during asexual blood stages.* Biochim Biophys Acta Mol Cell Res, 2025. **1872**(5): p. 119940.
56. Friedman, J.R. and J. Nunnari, *Mitochondrial form and function.* Nature, 2014. **505**(7483): p. 335-43.
57. Sibbald, S.J. and J.M. Archibald, *Genomic Insights into Plastid Evolution.* Genome Biol Evol, 2020. **12**(7): p. 978-990.
58. Shih, P.M. and N.J. Matzke, *Primary endosymbiosis events date to the later Proterozoic with cross-calibrated phylogenetic dating of duplicated ATPase proteins.* Proc Natl Acad Sci U S A, 2013. **110**(30): p. 12355-60.
59. Ponce-Toledo, R.I., et al., *An Early-Branching Freshwater Cyanobacterium at the Origin of Plastids.* Curr Biol, 2017. **27**(3): p. 386-391.
60. Sanchez-Baracaldo, P., et al., *Early photosynthetic eukaryotes inhabited low-salinity habitats.* Proc Natl Acad Sci U S A, 2017. **114**(37): p. E7737-E7745.
61. Strassert, J.F.H., et al., *A molecular timescale for eukaryote evolution with implications for the origin of red algal-derived plastids.* Nat Commun, 2021. **12**(1): p. 1879.
62. Bengtson, S., et al., *Three-dimensional preservation of cellular and subcellular structures suggests 1.6 billion-year-old crown-group red algae.* PLoS Biol, 2017. **15**(3): p. e2000735.
63. Parfrey, L.W., et al., *Estimating the timing of early eukaryotic diversification with multigene molecular clocks.* Proc Natl Acad Sci U S A, 2011. **108**(33): p. 13624-9.
64. Garcia, P.S., F. Barras, and S. Gribaldo, *Components of iron-Sulfur cluster assembly machineries are robust phylogenetic markers to trace the origin of mitochondria and plastids.* PLoS Biol, 2023. **21**(11): p. e3002374.
65. Moore, K.R., et al., *An Expanded Ribosomal Phylogeny of Cyanobacteria Supports a Deep Placement of Plastids.* Front Microbiol, 2019. **10**: p. 1612.
66. Sato, N., et al., *Chloroplasts with clefts and holes: a reassessment of the chloroplast shape using 3D FE-SEM cellular reconstruction of two species of Chlamydomonas.* Protoplasma, 2025. **262**(1): p. 207-218.
67. Sato, N., *Complex origins of chloroplast membranes with photosynthetic machineries: multiple transfers of genes from divergent organisms at different times or a single endosymbiotic event?* J Plant Res, 2020. **133**(1): p. 15-33.
68. Pribil, M., M. Labs, and D. Leister, *Structure and dynamics of thylakoids in land plants.* J Exp Bot, 2014. **65**(8): p. 1955-72.
69. Stirbet, A., et al., *Photosynthesis: basics, history and modelling.* Ann Bot, 2020. **126**(4): p. 511-537.

70. Choi, H., T. Yi, and S.H. Ha, *Diversity of Plastid Types and Their Interconversions.* Front Plant Sci, 2021. **12**: p. 692024.
71. Shutova, T., *Photosynthetic water oxidation: The function of two extrinsic proteins.* 2007.
72. Liang, K., et al., *Structural insights into the chloroplast protein import in land plants.* Cell, 2024. **187**(20): p. 5651-5664 e18.
73. Smith, D.R. and R.W. Lee, *A plastid without a genome: evidence from the nonphotosynthetic green algal genus Polytomella.* Plant Physiol, 2014. **164**(4): p. 1812-9.
74. Molina, J., et al., *Possible loss of the chloroplast genome in the parasitic flowering plant Rafflesia lagascae (Rafflesiaceae).* Mol Biol Evol, 2014. **31**(4): p. 793-803.
75. Krupinska, K., J. Melonek, and K. Krause, *New insights into plastid nucleoid structure and functionality.* Planta, 2013. **237**(3): p. 653-64.
76. Palomar, V.M., et al., *Membrane association of active genes organizes the chloroplast nucleoid structure.* Proc Natl Acad Sci U S A, 2024. **121**(28): p. e2309244121.
77. Nishimura, Y., *Plastid Nucleoids: Insights into Their Shape and Dynamics.* Plant Cell Physiol, 2024. **65**(4): p. 551-559.
78. Melonek, J., et al., *The core of chloroplast nucleoids contains architectural SWIB domain proteins.* Plant Cell, 2012. **24**(7): p. 3060-73.
79. Majeran, W., et al., *Nucleoid-enriched proteomes in developing plastids and chloroplasts from maize leaves: a new conceptual framework for nucleoid functions.* Plant Physiol, 2012. **158**(1): p. 156-89.
80. Rose, R.J., *Sustaining Life: Maintaining Chloroplasts and Mitochondria and their Genomes in Plants.* Yale J Biol Med, 2019. **92**(3): p. 499-510.
81. Odahara, M., et al., *Dynamic Interplay between Nucleoid Segregation and Genome Integrity in Chlamydomonas Chloroplasts.* Plant Physiol, 2016. **172**(4): p. 2337-2346.
82. Cho, H.S., et al., *DNA gyrase is involved in chloroplast nucleoid partitioning.* Plant Cell, 2004. **16**(10): p. 2665-82.
83. Kobayashi, Y., et al., *Holliday junction resolvases mediate chloroplast nucleoid segregation.* Science, 2017. **356**(6338): p. 631-634.
84. Boffey, S.A. and D. Lloyd, *Division and segregation of organelles*. Vol. 35. 1988: Cambridge University Press.
85. Kamimura, Y., et al., *Chloroplast nucleoids as a transformable network revealed by live imaging with a microfluidic device.* Commun Biol, 2018. **1**: p. 47.
86. Terasawa, K. and N. Sato, *Visualization of plastid nucleoids in situ using the PEND-GFP fusion protein.* Plant Cell Physiol, 2005. **46**(4): p. 649-60.
87. Misumi, O., et al., *Isolation and phenotypic characterization ofChlamydomonas reinhardtii mutants defective in chloroplast DNA segregation.* Protoplasma, 1999. **209**(3): p. 273-282.
88. Guiry, M.D., *How many species of algae are there? A reprise. Four kingdoms, 14 phyla, 63 classes and still growing.* J Phycol, 2024. **60**(2): p. 214-228.
89. Guiry, M.D., *How Many Species of Algae Are There?* J Phycol, 2012. **48**(5): p. 1057-63.
90. Archibald, J.M. and P.J. Keeling, *Recycled plastids: a 'green movement' in eukaryotic evolution.* Trends Genet, 2002. **18**(11): p. 577-84.
91. McFadden, G.I., *The cryptomonad nucleomorph.* Protoplasma, 2017. **254**(5): p. 1903-1907.
92. Zauner, S., et al., *The Known, the New, and a Possible Surprise: A Re-Evaluation of the Nucleomorph-Encoded Proteome of Cryptophytes.* Genome Biol Evol, 2019. **11**(6): p. 1618-1629.
93. Marinov, G.K., et al., *The chromatin organization of a chlorarachniophyte nucleomorph genome.* Genome Biol, 2022. **23**(1): p. 65.

94. Kim, J.I., et al., *Gene loss, pseudogenization, and independent genome reduction in non-photosynthetic species of Cryptomonas (Cryptophyceae) revealed by comparative nucleomorph genomics.* BMC Biol, 2022. **20**(1): p. 227.
95. Douglas, S., et al., *The highly reduced genome of an enslaved algal nucleus.* Nature, 2001. **410**(6832): p. 1091-6.
96. Deane, J.A., et al., *Evidence for nucleomorph to host nucleus gene transfer: light-harvesting complex proteins from cryptomonads and chlorarachniophytes.* Protist, 2000. **151**(3): p. 239-52.
97. McKerracher, L. and S.P. Gibbs, *Cell and nucleomorph division in the alga Cryptomonas.* Canadian Journal of Botany, 1982. **60**(11): p. 2440-2452.
98. Morrall, S. and A. Greenwood, *Ultrastructure of nucleomorph division in species of Cryptophyceae and its evolutionary implications.* Journal of Cell Science, 1982. **54**(1): p. 311-328.
99. Gillott, M.A. and S.P. Gibbs, *THE CRYPTOMONAD NUCLEOMORPH: ITS ULTRASTRUCTURE AND EVOLUTIONARY SIGNIFICANCE 1*. Journal of Phycology, 1980. **16**(4): p. 558-568.
100. Onuma, R., N. Mishra, and S.Y. Miyagishima, *Regulation of chloroplast and nucleomorph replication by the cell cycle in the cryptophyte Guillardia theta.* Sci Rep, 2017. **7**(1): p. 2345.
101. Hopkins, J.F., et al., *Proteomics reveals plastid- and periplastid-targeted proteins in the chlorarachniophyte alga Bigelowiella natans.* Genome Biol Evol, 2012. **4**(12): p. 1391-406.
102. Mathur, V., et al., *Multiple Independent Origins of Apicomplexan-Like Parasites.* Curr Biol, 2019. **29**(17): p. 2936-2941 e5.
103. Janouskovec, J., et al., *Apicomplexan-like parasites are polyphyletic and widely but selectively dependent on cryptic plastid organelles.* Elife, 2019. **8**.
104. Chen, X., et al., *The apicoplast biogenesis and metabolism: current progress and questions.* Trends Parasitol, 2024. **40**(12): p. 1144-1158.
105. Janouskovec, J., et al., *Factors mediating plastid dependency and the origins of parasitism in apicomplexans and their close relatives.* Proc Natl Acad Sci U S A, 2015. **112**(33): p. 10200-7.
106. Elaagip, A., S. Absalon, and A. Florentin, *Apicoplast Dynamics During Plasmodium Cell Cycle.* Front Cell Infect Microbiol, 2022. **12**: p. 864819.
107. Verhoef, J.M.J., et al., *Detailing organelle division and segregation in Plasmodium falciparum*. J Cell Biol, 2024. **223**(12).
108. Wilson, R.J., et al., *Complete gene map of the plastid-like DNA of the malaria parasite Plasmodium falciparum.* J Mol Biol, 1996. **261**(2): p. 155-72.
109. Fichera, M.E. and D.S. Roos, *A plastid organelle as a drug target in apicomplexan parasites.* Nature, 1997. **390**(6658): p. 407-9.
110. Matsuzaki, M., et al., *Large amounts of apicoplast nucleoid DNA and its segregation in Toxoplasma gondii.* Protoplasma, 2001. **218**(3-4): p. 180-91.
111. Martins-Duarte, E.S., et al., *Replication and partitioning of the apicoplast genome of Toxoplasma gondii is linked to the cell cycle and requires DNA polymerase and gyrase.* Int J Parasitol, 2021. **51**(6): p. 493-504.
112. Marin, B., E.C. Nowack, and M. Melkonian, *A plastid in the making: evidence for a second primary endosymbiosis.* Protist, 2005. **156**(4): p. 425-32.
113. Yoon, H.S., et al., *A single origin of the photosynthetic organelle in different Paulinella lineages.* BMC Evol Biol, 2009. **9**: p. 98.
114. Delaye, L., C. Valadez-Cano, and B. Perez-Zamorano, *How Really Ancient Is Paulinella Chromatophora?* PLoS Curr, 2016. **8**.

115. Gabr, A., A.R. Grossman, and D. Bhattacharya, *Paulinella, a model for understanding plastid primary endosymbiosis.* J Phycol, 2020. **56**(4): p. 837-843.
116. Kies, L., *[Electron microscopical investigations on Paulinella chromatophora Lauterborn, a thecamoeba containing blue-green endosymbionts (Cyanelles) (author's transl)].* Protoplasma, 1974. **80**(1): p. 69-89.
117. Macorano, L., et al., *DNA-binding and protein structure of nuclear factors likely acting in genetic information processing in the Paulinella chromatophore.* Proc Natl Acad Sci U S A, 2023. **120**(27): p. e2221595120.
118. Nowack, E., *Paulinella chromatophora - Rethinking the transition from endosymbiont to organelle.* Acta Societatis Botanicorum Poloniae, 2014. **83**: p. 387-397.
119. Nowack, E.C., M. Melkonian, and G. Glockner, *Chromatophore genome sequence of Paulinella sheds light on acquisition of photosynthesis by eukaryotes.* Curr Biol, 2008. **18**(6): p. 410-8.
120. Lhee, D., et al., *Evolutionary dynamics of the chromatophore genome in three photosynthetic Paulinella species.* Sci Rep, 2019. **9**(1): p. 2560.
121. Gabr, A., T.G. Stephens, and D. Bhattacharya, *Loss of key endosymbiont genes may facilitate early host control of the chromatophore in Paulinella.* iScience, 2022. **25**(9): p. 104974.
122. Singer, A., et al., *Massive Protein Import into the Early-Evolutionary-Stage Photosynthetic Organelle of the Amoeba Paulinella chromatophora.* Curr Biol, 2017. **27**(18): p. 2763-2773 e5.
123. Nowack, E.C., et al., *Gene transfers from diverse bacteria compensate for reductive genome evolution in the chromatophore of Paulinella chromatophora.* Proc Natl Acad Sci U S A, 2016. **113**(43): p. 12214-12219.
124. Garcia, A.K., et al., *Nitrogenase resurrection and the evolution of a singular enzymatic mechanism.* Elife, 2023. **12**.
125. Kneip, C., et al., *Nitrogen fixation in eukaryotes--new models for symbiosis.* BMC Evol Biol, 2007. **7**: p. 55.
126. Tschitschko, B., et al., *Rhizobia-diatom symbiosis fixes missing nitrogen in the ocean.* Nature, 2024. **630**(8018): p. 899-904.
127. Frail, S., et al., *Genomes of nitrogen-fixing eukaryotes reveal a non-canonical model of organellogenesis.* bioRxiv, 2025.
128. Coale, T.H., et al., *Nitrogen-fixing organelle in a marine alga.* Science, 2024. **384**(6692): p. 217-222.
129. Moulin, S.L.Y., et al., *The endosymbiont of Epithemia clementina is specialized for nitrogen fixation within a photosynthetic eukaryote.* ISME Commun, 2024. **4**(1): p. ycae055.
130. Thompson, A.W., et al., *Unicellular cyanobacterium symbiotic with a single-celled eukaryotic alga.* Science, 2012. **337**(6101): p. 1546-50.
131. Turk-Kubo, K.A., et al., *Distinct ecological niches of marine symbiotic N(2) -fixing cyanobacterium Candidatus Atelocyanobacterium thalassa sublineages.* J Phycol, 2017. **53**(2): p. 451-461.
132. Harding, K., et al., *Symbiotic unicellular cyanobacteria fix nitrogen in the Arctic Ocean.* Proc Natl Acad Sci U S A, 2018. **115**(52): p. 13371-13375.
133. Cornejo-Castillo, F.M., et al., *Cyanobacterial symbionts diverged in the late Cretaceous towards lineage-specific nitrogen fixation factories in single-celled phytoplankton.* Nat Commun, 2016. **7**: p. 11071.
134. Suzuki, S., et al., *Unstable Relationship Between Braarudosphaera bigelowii (= Chrysochromulina parkeae) and Its Nitrogen-Fixing Endosymbiont.* Front Plant Sci, 2021. **12**: p. 749895.

135. Tripp, H.J., et al., *Metabolic streamlining in an open-ocean nitrogen-fixing cyanobacterium.* Nature, 2010. **464**(7285): p. 90-4.
136. Zehr, J.P., et al., *Globally distributed uncultivated oceanic N2-fixing cyanobacteria lack oxygenic photosystem II.* Science, 2008. **322**(5904): p. 1110-2.
137. Cornejo-Castillo, F.M., et al., *Metabolic trade-offs constrain the cell size ratio in a nitrogen-fixing symbiosis.* Cell, 2024. **187**(7): p. 1762-1768 e9.
138. Skibbe, O., et al., *Exploring diatom diversity through cultures - a case study from the Bow River, Canada.* Journal of Limnology, 2022. **81**.
139. Schvarcz, C.R., et al., *Overlooked and widespread pennate diatom-diazotroph symbioses in the sea.* Nat Commun, 2022. **13**(1): p. 799.
140. Nakayama, T., et al., *Spheroid bodies in rhopalodiacean diatoms were derived from a single endosymbiotic cyanobacterium.* J Plant Res, 2011. **124**(1): p. 93-7.
141. Prechtl, J., et al., *Intracellular spheroid bodies of Rhopalodia gibba have nitrogen-fixing apparatus of cyanobacterial origin.* Mol Biol Evol, 2004. **21**(8): p. 1477-81.
142. Mora, C., et al., *How many species are there on Earth and in the ocean?* PLoS Biol, 2011. **9**(8): p. e1001127.
143. Blaxter, M., et al., *Why sequence all eukaryotes?* Proc Natl Acad Sci U S A, 2022. **119**(4).
144. Burki, F., et al., *The New Tree of Eukaryotes.* Trends in Ecology & Evolution, 2020/01/01. **35**(1).
145. Tikhonenkov, D.V., et al., *Microbial predators form a new supergroup of eukaryotes.* Nature, 2022. **612**(7941): p. 714-719.
146. Zardoya, R., *Recent advances in understanding mitochondrial genome diversity.* F1000Res, 2020. **9**.
147. Hutchison, C.A., 3rd, et al., *Design and synthesis of a minimal bacterial genome.* Science, 2016. **351**(6280): p. aad6253.
148. Obornik, M. and J. Lukes, *The Organellar Genomes of Chromera and Vitrella, the Phototrophic Relatives of Apicomplexan Parasites.* Annu Rev Microbiol, 2015. **69**: p. 129-44.
149. Burger, G., et al., *Strikingly bacteria-like and gene-rich mitochondrial genomes throughout jakobid protists.* Genome Biol Evol, 2013. **5**(2): p. 418-38.
150. Wideman, J.G., et al., *Unexpected mitochondrial genome diversity revealed by targeted single-cell genomics of heterotrophic flagellated protists.* Nat Microbiol, 2020. **5**(1): p. 154-165.
151. Roger, A.J., S.A. Munoz-Gomez, and R. Kamikawa, *The Origin and Diversification of Mitochondria.* Curr Biol, 2017. **27**(21): p. R1177-R1192.
152. Harada, R., et al., *Complete mitochondrial genomes of ancyromonads provide clues for the gene content and genome structures of ancestral mitochondria.* bioRxiv, 2025: p. 2025.03.26.645259.
153. Kannan, S., I.B. Rogozin, and E.V. Koonin, *MitoCOGs: clusters of orthologous genes from mitochondria and implications for the evolution of eukaryotes.* BMC Evol Biol, 2014. **14**: p. 237.
154. Veeraragavan, S., M. Johansen, and I.G. Johnston, *Evolution and maintenance of mtDNA gene content across eukaryotes.* Biochem J, 2024. **481**(15): p. 1015-1042.
155. Shutt, T.E. and M.W. Gray, *Bacteriophage origins of mitochondrial replication and transcription proteins.* Trends Genet, 2006. **22**(2): p. 90-5.
156. Lang, B.F., et al., *An ancestral mitochondrial DNA resembling a eubacterial genome in miniature.* Nature, 1997. **387**(6632): p. 493-7.
157. Kelly, S., *The economics of organellar gene loss and endosymbiotic gene transfer.* Genome Biol, 2021. **22**(1): p. 345.
158. Butenko, A., et al., *Mitochondrial genomes revisited: why do different lineages retain different genes?* BMC Biol, 2024. **22**(1): p. 15.

159. Allen, J.F., *Why chloroplasts and mitochondria retain their own genomes and genetic systems: Colocation for redox regulation of gene expression.* Proc Natl Acad Sci U S A, 2015. **112**(33): p. 10231-8.
160. Bjorkholm, P., et al., *Mitochondrial genomes are retained by selective constraints on protein targeting.* Proc Natl Acad Sci U S A, 2015. **112**(33): p. 10154-61.
161. Bjorkholm, P., et al., *Why mitochondria need a genome revisited.* FEBS Lett, 2017. **591**(1): p. 65-75.
162. Johnston, I.G., *The Nitroplast and Its Relatives Support a Universal Model of Features Predicting Gene Retention in Endosymbiont and Organelle Genomes.* Genome Biol Evol, 2024. **16**(7).
163. Smith, D.R. and P.J. Keeling, *Mitochondrial and plastid genome architecture: Reoccurring themes, but significant differences at the extremes.* Proc Natl Acad Sci U S A, 2015. **112**(33): p. 10177-84.
164. Sloan, D.B., et al., *Rapid evolution of enormous, multichromosomal genomes in flowering plant mitochondria with exceptionally high mutation rates.* PLoS Biol, 2012. **10**(1): p. e1001241.
165. Kleckner, N., et al., *The bacterial nucleoid: nature, dynamics and sister segregation.* Curr Opin Microbiol, 2014. **22**: p. 127-37.
166. Dai, H., et al., *Structural and functional characterizations of mung bean mitochondrial nucleoids.* Nucleic Acids Res, 2005. **33**(15): p. 4725-39.
167. Miyakawa, I., *Organization and dynamics of yeast mitochondrial nucleoids.* Proc Jpn Acad Ser B Phys Biol Sci, 2017. **93**(5): p. 339-359.
168. Bonekamp, N.A. and N.G. Larsson, *SnapShot: Mitochondrial Nucleoid.* Cell, 2018. **172**(1-2): p. 388-388 e1.
169. Farge, G. and M. Falkenberg, *Organization of DNA in Mammalian Mitochondria.* Int J Mol Sci, 2019. **20**(11).
170. Lee, S.R. and J. Han, *Mitochondrial Nucleoid: Shield and Switch of the Mitochondrial Genome.* Oxid Med Cell Longev, 2017. **2017**: p. 8060949.
171. Isaac, R.S., et al., *Single-nucleoid architecture reveals heterogeneous packaging of mitochondrial DNA.* Nat Struct Mol Biol, 2024. **31**(3): p. 568-577.
172. Kukat, C., et al., *Super-resolution microscopy reveals that mammalian mitochondrial nucleoids have a uniform size and frequently contain a single copy of mtDNA.* Proc Natl Acad Sci U S A, 2011. **108**(33): p. 13534-9.
173. Vozarikova, V., et al., *Mitochondrial HMG-Box Containing Proteins: From Biochemical Properties to the Roles in Human Diseases.* Biomolecules, 2020. **10**(8).
174. Kukat, C., et al., *Cross-strand binding of TFAM to a single mtDNA molecule forms the mitochondrial nucleoid.* Proc Natl Acad Sci U S A, 2015. **112**(36): p. 11288-93.
175. Ciesielski, G.L., M.T. Oliveira, and L.S. Kaguni, *Animal Mitochondrial DNA Replication.* Enzymes, 2016. **39**: p. 255-92.
176. Chen, X.J. and G.D. Clark-Walker, *Unveiling the mystery of mitochondrial DNA replication in yeasts.* Mitochondrion, 2018. **38**: p. 17-22.
177. Morley, S.A. and B.L. Nielsen, *Plant mitochondrial DNA.* FBL, 2017. **22**(6): p. 1023-1032.
178. Amodeo, S., I. Bregy, and T. Ochsenreiter, *Mitochondrial genome maintenance-the kinetoplast story.* FEMS Microbiol Rev, 2023. **47**(6).
179. Krasich, R. and W.C. Copeland, *DNA polymerases in the mitochondria: A critical review of the evidence.* Front Biosci (Landmark Ed), 2017. **22**(4): p. 692-709.
180. Wang, H., A.I. Bowman, and G.R. Bowman, *Chromosome Segregation in Alphaproteobacteria*, in *Cell Cycle Regulation and Development in Alphaproteobacteria*, E. Biondi, Editor. 2022, Springer International Publishing: Cham. p. 143-162.
181. Satoh, M. and T. Kuroiwa, *Organization of multiple nucleoids and DNA molecules in mitochondria of a human cell.* Exp Cell Res, 1991. **196**(1): p. 137-40.

182. Gustafsson, C.M., M. Falkenberg, and N.G. Larsson, *Maintenance and Expression of Mammalian Mitochondrial DNA*. Annu Rev Biochem, 2016. **85**: p. 133-60.
183. Alam, T.I., et al., *Human mitochondrial DNA is packaged with TFAM*. Nucleic Acids Res, 2003. **31**(6): p. 1640-5.
184. Wang, C., et al., *Dynamic tubulation of mitochondria drives mitochondrial network formation*. Cell Res, 2015. **25**(10): p. 1108-20.
185. Macuada, J., I. Molina-Riquelme, and V. Eisner, *How are mitochondrial nucleoids trafficked?* Trends Cell Biol, 2025. **35**(3): p. 194-204.
186. Qin, J., et al., *ER-mitochondria contacts promote mtDNA nucleoids active transportation via mitochondrial dynamic tubulation*. Nat Commun, 2020. **11**(1): p. 4471.
187. Rajala, N., et al., *Replication factors transiently associate with mtDNA at the mitochondrial inner membrane to facilitate replication*. Nucleic Acids Res, 2014. **42**(2): p. 952-67.
188. Westermann, B., *Organelle dynamics: ER embraces mitochondria for fission*. Curr Biol, 2011. **21**(22): p. R922-4.
189. Miyakawa, I., et al., *DNA Content of Individual Mitochondrial Nucleoids Varies Depending on the Culture Conditions of the Yeast Saccharomyces cerevisiae*. CYTOLOGIA, 2004. **69**(1): p. 101-107.
190. Diffley, J.F. and B. Stillman, *A close relative of the nuclear, chromosomal high-mobility group protein HMG1 in yeast mitochondria*. Proc Natl Acad Sci U S A, 1991. **88**(17): p. 7864-8.
191. Lidman, J., et al., *Structure and dynamics of the mitochondrial DNA-compaction factor Abf2 from S. cerevisiae*. J Struct Biol, 2023. **215**(3): p. 108008.
192. Miyakawa, I., et al., *Characterization of DNA-binding proteins involved in the assembly of mitochondrial nucleoids in the yeast Saccharomyces cerevisiae*. Plant Cell Physiol, 1995. **36**(7): p. 1179-88.
193. Yaffe, M.P., et al., *Microtubules mediate mitochondrial distribution in fission yeast*. Proc Natl Acad Sci U S A, 1996. **93**(21): p. 11664-8.
194. Simon, V.R., T.C. Swayne, and L.A. Pon, *Actin-dependent mitochondrial motility in mitotic yeast and cell-free systems: identification of a motor activity on the mitochondrial surface*. J Cell Biol, 1995. **130**(2): p. 345-54.
195. Drubin, D.G., H.D. Jones, and K.F. Wertman, *Actin structure and function: roles in mitochondrial organization and morphogenesis in budding yeast and identification of the phalloidin-binding site*. Mol Biol Cell, 1993. **4**(12): p. 1277-94.
196. Chernyakov, I., F. Santiago-Tirado, and A. Bretscher, *Active segregation of yeast mitochondria by Myo2 is essential and mediated by Mmr1 and Ypt11*. Curr Biol, 2013. **23**(18): p. 1818-24.
197. Kornmann, B., C. Osman, and P. Walter, *The conserved GTPase Gem1 regulates endoplasmic reticulum-mitochondria connections*. Proc Natl Acad Sci U S A, 2011. **108**(34): p. 14151-6.
198. Murley, A., et al., *ER-associated mitochondrial division links the distribution of mitochondria and mitochondrial DNA in yeast*. Elife, 2013. **2**: p. e00422.
199. Møller, I.M., A.G. Rasmusson, and O. Van Aken, *Plant mitochondria - past, present and future*. Plant J, 2021. **108**(4): p. 912-959.
200. Sakai, A., H. Takano, and T. Kuroiwa, *Organelle nuclei in higher plants: structure, composition, function, and evolution*. Int Rev Cytol, 2004. **238**: p. 59-118.
201. Arimura, S., et al., *Frequent fusion and fission of plant mitochondria with unequal nucleoid distribution*. Proc Natl Acad Sci U S A, 2004. **101**(20): p. 7805-8.

202. Broz, A.K., D.B. Sloan, and I.G. Johnston, *Stochastic organelle genome segregation through Arabidopsis development and reproduction.* New Phytol, 2024. **241**(2): p. 896-910.
203. Rose, R.J. and D.W. McCurdy, *New Beginnings: Mitochondrial Renewal by Massive Mitochondrial Fusion.* Trends Plant Sci, 2017. **22**(8): p. 641-643.
204. Sheahan, M.B., R.J. Rose, and D.W. McCurdy, *Organelle inheritance in plant cell division: the actin cytoskeleton is required for unbiased inheritance of chloroplasts, mitochondria and endoplasmic reticulum in dividing protoplasts.* Plant J, 2004. **37**(3): p. 379-90.
205. Krupinska, K., et al., *WHIRLIES Are Multifunctional DNA-Binding Proteins With Impact on Plant Development and Stress Resistance.* Front Plant Sci, 2022. **13**: p. 880423.
206. Kim, M., et al., *mTERF18 and ATAD3 are required for mitochondrial nucleoid structure and their disruption confers heat tolerance in Arabidopsis thaliana.* New Phytol, 2021. **232**(5): p. 2026-2042.
207. Lukes, J., et al., *African trypanosome strategies for conquering new hosts and territories: the end of monophyly?* Trends Parasitol, 2022. **38**(9): p. 724-736.
208. Steverding, D., *The history of African trypanosomiasis.* Parasit Vectors, 2008. **1**(1): p. 3.
209. Hollingshead, C.M. and R. Bermudez, *Human African Trypanosomiasis (Sleeping Sickness)*, in *StatPearls*. 2025: Treasure Island (FL).
210. Franco, J.R., et al., *The elimination of human African trypanosomiasis: Monitoring progress towards the 2021-2030 WHO road map targets.* PLoS Negl Trop Dis, 2024. **18**(4): p. e0012111.
211. Barrett, M.P., et al., *Elimination of human African trypanosomiasis: The long last mile.* PLoS Negl Trop Dis, 2024. **18**(5): p. e0012091.
212. Cayla, M., et al., *African trypanosomes.* Parasit Vectors, 2019. **12**(1): p. 190.
213. Perez-Molina, J.A. and I. Molina, *Chagas disease.* Lancet, 2018. **391**(10115): p. 82-94.
214. Pace, D., *Leishmaniasis.* J Infect, 2014. **69 Suppl 1**: p. S10-8.
215. Jaskowska, E., et al., *Phytomonas: trypanosomatids adapted to plant environments.* PLoS Pathog, 2015. **11**(1): p. e1004484.
216. Kostygov, A.Y., et al., *Euglenozoa: taxonomy, diversity and ecology, symbioses and viruses.* Open Biol, 2021. **11**(3): p. 200407.
217. Poinar, G., Jr. and R. Poinar, *Paleoleishmania proterus n. gen., n. sp., (Trypanosomatidae: Kinetoplastida) from Cretaceous Burmese amber.* Protist, 2004. **155**(3): p. 305-10.
218. Lukes, J., et al., *Evolution of parasitism in kinetoplastid flagellates.* Mol Biochem Parasitol, 2014. **195**(2): p. 115-22.
219. Capewell, P., et al., *A co-evolutionary arms race: trypanosomes shaping the human genome, humans shaping the trypanosome genome.* Parasitology, 2015. **142 Suppl 1**(Suppl 1): p. S108-19.
220. Reichard, R.E., *Area-wide biological control of disease vectors and agents affecting wildlife.* Rev Sci Tech, 2002. **21**(1): p. 179-85.
221. Kamidi, C.M., et al., *Multiple evolutionary origins of Trypanosoma evansi in Kenya.* PLoS Negl Trop Dis, 2017. **11**(9): p. e0005895.
222. Kay, C., T.A. Williams, and W. Gibson, *Mitochondrial DNAs provide insight into trypanosome phylogeny and molecular evolution.* BMC Evol Biol, 2020. **20**(1): p. 161.
223. Cuypers, B., et al., *Genome-Wide SNP Analysis Reveals Distinct Origins of Trypanosoma evansi and Trypanosoma equiperdum.* Genome Biol Evol, 2017. **9**(8): p. 1990-1997.
224. Stevens, J., H. Noyes, and W. Gibson, *The evolution of trypanosomes infecting humans and primates.* Mem Inst Oswaldo Cruz, 1998. **93**(5): p. 669-76.
225. Balmer, O., et al., *Phylogeography and taxonomy of Trypanosoma brucei.* PLoS Negl Trop Dis, 2011. **5**(2): p. e961.
226. Weir, W., et al., *Population genomics reveals the origin and asexual evolution of human infective trypanosomes.* Elife, 2016. **5**: p. e11473.

227. MacLeod, A., A. Tait, and C.M. Turner, *The population genetics of Trypanosoma brucei and the origin of human infectivity.* Philos Trans R Soc Lond B Biol Sci, 2001. **356**(1411): p. 1035-44.
228. Vanhamme, L., et al., *Apolipoprotein L-I is the trypanosome lytic factor of human serum.* Nature, 2003. **422**(6927): p. 83-7.
229. Pereira, S.H., F.P. Alves, and S.M.R. Teixeira, *Animal Trypanosomiasis: Challenges and Prospects for New Vaccination Strategies.* Microorganisms, 2024. **12**(12).
230. Solano, P., et al., *[Towards elimination of human African trypanosomiasis].* Med Trop Sante Int, 2023. **3**(1).
231. Pays, E., M. Radwanska, and S. Magez, *The Pathogenesis of African Trypanosomiasis.* Annu Rev Pathol, 2023. **18**: p. 19-45.
232. Lai, D.H., et al., *Adaptations of Trypanosoma brucei to gradual loss of kinetoplast DNA: Trypanosoma equiperdum and Trypanosoma evansi are petite mutants of T. brucei.* Proc Natl Acad Sci U S A, 2008. **105**(6): p. 1999-2004.
233. Dean, S., et al., *Single point mutations in ATP synthase compensate for mitochondrial genome loss in trypanosomes.* Proc Natl Acad Sci U S A, 2013. **110**(36): p. 14741-6.
234. Desquesnes, M., et al., *Trypanosoma evansi and surra: a review and perspectives on transmission, epidemiology and control, impact, and zoonotic aspects.* Biomed Res Int, 2013. **2013**: p. 321237.
235. Sazmand, A., M. Desquesnes, and D. Otranto, *Trypanosoma evansi.* Trends Parasitol, 2022. **38**(6): p. 489-490.
236. Gizaw, Y., M. Megersa, and T. Fayera, *Dourine: a neglected disease of equids.* Trop Anim Health Prod, 2017. **49**(5): p. 887-897.
237. Van Vinh Chau, N., et al., *A Clinical and Epidemiological Investigation of the First Reported Human Infection With the Zoonotic Parasite Trypanosoma evansi in Southeast Asia.* Clin Infect Dis, 2016. **62**(8): p. 1002-1008.
238. Siegel, T.N., et al., *Gene expression in Trypanosoma brucei: lessons from high-throughput RNA sequencing.* Trends Parasitol, 2011. **27**(10): p. 434-41.
239. Urbaniak, M.D., M.L. Guther, and M.A. Ferguson, *Comparative SILAC proteomic analysis of Trypanosoma brucei bloodstream and procyclic lifecycle stages.* PLoS One, 2012. **7**(5): p. e36619.
240. Gunasekera, K., et al., *Proteome remodelling during development from blood to insect-form Trypanosoma brucei quantified by SILAC and mass spectrometry.* BMC Genomics, 2012. **13**: p. 556.
241. Wheeler, R.J., K. Gull, and J.D. Sunter, *Coordination of the Cell Cycle in Trypanosomes.* Annu Rev Microbiol, 2019. **73**: p. 133-154.
242. Vickerman, K., *Developmental cycles and biology of pathogenic trypanosomes.* Br Med Bull, 1985. **41**(2): p. 105-14.
243. Vickerman, K., *Antigenic variation in trypanosomes.* Nature, 1978. **273**(5664): p. 613-7.
244. Kennedy, P.G.E. and J. Rodgers, *Clinical and Neuropathogenetic Aspects of Human African Trypanosomiasis.* Front Immunol, 2019. **10**: p. 39.
245. Horn, D., *The molecular control of antigenic variation in Trypanosoma brucei.* Curr Mol Med, 2004. **4**(6): p. 563-76.
246. Cross, G.A., H.S. Kim, and B. Wickstead, *Capturing the variant surface glycoprotein repertoire (the VSGnome) of Trypanosoma brucei Lister 427.* Mol Biochem Parasitol, 2014. **195**(1): p. 59-73.
247. Aresta-Branco, F., et al., *Mechanistic Similarities between Antigenic Variation and Antibody Diversification during Trypanosoma brucei Infection.* Trends Parasitol, 2019. **35**(4): p. 302-315.

248. Vassella, E., et al., *Differentiation of African trypanosomes is controlled by a density sensing mechanism which signals cell cycle arrest via the cAMP pathway.* J Cell Sci, 1997. **110 (Pt 21)**: p. 2661-71.
249. Rojas, F., et al., *Oligopeptide Signaling through TbGPR89 Drives Trypanosome Quorum Sensing.* Cell, 2019. **176**(1-2): p. 306-317 e16.
250. Silvester, E., K.R. McWilliam, and K.R. Matthews, *The Cytological Events and Molecular Control of Life Cycle Development of Trypanosoma brucei in the Mammalian Bloodstream.* Pathogens, 2017. **6**(3).
251. MacGregor, P., et al., *Transmission stages dominate trypanosome within-host dynamics during chronic infections.* Cell Host Microbe, 2011. **9**(4): p. 310-8.
252. Dyer, N.A., et al., *Flying tryps: survival and maturation of trypanosomes in tsetse flies.* Trends Parasitol, 2013. **29**(4): p. 188-96.
253. Roditi, I. and M. Liniger, *Dressed for success: the surface coats of insect-borne protozoan parasites.* Trends Microbiol, 2002. **10**(3): p. 128-34.
254. Vassella, E., et al., *Multiple procyclin isoforms are expressed differentially during the development of insect forms of Trypanosoma brucei.* J Mol Biol, 2001. **312**(4): p. 597-607.
255. Urwyler, S., et al., *A family of stage-specific alanine-rich proteins on the surface of epimastigote forms of Trypanosoma brucei.* Mol Microbiol, 2007. **63**(1): p. 218-28.
256. Rotureau, B. and J. Van Den Abbeele, *Through the dark continent: African trypanosome development in the tsetse fly.* Front Cell Infect Microbiol, 2013. **3**: p. 53.
257. Rotureau, B., et al., *A new asymmetric division contributes to the continuous production of infective trypanosomes in the tsetse fly.* Development, 2012. **139**(10): p. 1842-50.
258. Tielens, A.G. and J.J. van Hellemond, *Surprising variety in energy metabolism within Trypanosomatidae.* Trends Parasitol, 2009. **25**(10): p. 482-90.
259. Ford, W.C. and I.B. Bowman, *Metabolism of proline by the culture midgut form of Trypanosoma rhodesiense.* Trans R Soc Trop Med Hyg, 1973. **67**(2): p. 257.
260. Evans, D.A. and R.C. Brown, *The utilization of glucose and proline by culture forms of Trypanosoma brucei.* J Protozool, 1972. **19**(4): p. 686-90.
261. Lamour, N., et al., *Proline metabolism in procyclic Trypanosoma brucei is down-regulated in the presence of glucose.* J Biol Chem, 2005. **280**(12): p. 11902-10.
262. Bochud-Allemann, N. and A. Schneider, *Mitochondrial substrate level phosphorylation is essential for growth of procyclic Trypanosoma brucei.* J Biol Chem, 2002. **277**(36): p. 32849-54.
263. Zikova, A., et al., *A paradigm shift: The mitoproteomes of procyclic and bloodstream Trypanosoma brucei are comparably complex.* PLoS Pathog, 2017. **13**(12): p. e1006679.
264. Jakob, M., et al., *Mitochondrial growth during the cell cycle of Trypanosoma brucei bloodstream forms.* Sci Rep, 2016. **6**: p. 36565.
265. Maguire, F. and T.A. Richards, *Organelle evolution: a mosaic of 'mitochondrial' functions.* Curr Biol, 2014. **24**(11): p. R518-20.
266. Lill, R., et al., *Is there an answer? Why are mitochondria essential for life?* IUBMB Life, 2005. **57**(10): p. 701-3.
267. Bily, T., et al., *Ultrastructural Changes of the Mitochondrion During the Life Cycle of Trypanosoma brucei.* J Eukaryot Microbiol, 2021. **68**(3): p. e12846.
268. Rugen, N., M. Senkler, and H.P. Braun, *Deep proteomics reveals incorporation of unedited proteins into mitochondrial protein complexes in Arabidopsis.* Plant Physiol, 2024. **195**(2): p. 1180-1199.
269. Morgenstern, M., et al., *Quantitative high-confidence human mitochondrial proteome and its dynamics in cellular context.* Cell Metab, 2021. **33**(12): p. 2464-2483 e18.

270. Di Bartolomeo, F., et al., *Absolute yeast mitochondrial proteome quantification reveals trade-off between biosynthesis and energy generation during diauxic shift.* Proc Natl Acad Sci U S A, 2020. **117**(13): p. 7524-7535.
271. Peikert, C.D., et al., *Charting organellar importomes by quantitative mass spectrometry.* Nat Commun, 2017. **8**: p. 15272.
272. Wang, Z. and M. Wu, *An integrated phylogenomic approach toward pinpointing the origin of mitochondria.* Sci Rep, 2015. **5**: p. 7949.
273. Lang, B.F., et al., *A comparative genomics approach to the evolution of eukaryotes and their mitochondria.* J Eukaryot Microbiol, 1999. **46**(4): p. 320-6.
274. Schneider, A., *Evolution of mitochondrial protein import - lessons from trypanosomes.* Biol Chem, 2020. **401**(6-7): p. 663-676.
275. Schneider, A., *Evolution and diversification of mitochondrial protein import systems.* Curr Opin Cell Biol, 2022. **75**: p. 102077.
276. Mani, J., C. Meisinger, and A. Schneider, *Peeping at TOMs-Diverse Entry Gates to Mitochondria Provide Insights into the Evolution of Eukaryotes.* Mol Biol Evol, 2016. **33**(2): p. 337-51.
277. Doan, K.N., et al., *The Mitochondrial Import Complex MIM Functions as Main Translocase for alpha-Helical Outer Membrane Proteins.* Cell Rep, 2020. **31**(4): p. 107567.
278. Guna, A., et al., *MTCH2 is a mitochondrial outer membrane protein insertase.* Science, 2022. **378**(6617): p. 317-322.
279. Kaser, S., et al., *Outer membrane protein functions as integrator of protein import and DNA inheritance in mitochondria.* Proc Natl Acad Sci U S A, 2016. **113**(31): p. E4467-75.
280. Vitali, D.G., et al., *Independent evolution of functionally exchangeable mitochondrial outer membrane import complexes.* Elife, 2018. **7**.
281. Straub, S.P., et al., *Dynamic organization of the mitochondrial protein import machinery.* Biol Chem, 2016. **397**(11): p. 1097-1114.
282. Harsman, A. and A. Schneider, *Mitochondrial protein import in trypanosomes: Expect the unexpected.* Traffic, 2017. **18**(2): p. 96-109.
283. Mani, J., et al., *Mitochondrial protein import receptors in Kinetoplastids reveal convergent evolution over large phylogenetic distances.* Nat Commun, 2015. **6**: p. 6646.
284. Desy, S., et al., *TbLOK1/ATOM19 is a novel subunit of the noncanonical mitochondrial outer membrane protein translocase of Trypanosoma brucei.* Mol Microbiol, 2016. **102**(3): p. 520-529.
285. Wang, W., et al., *Atomic structure of human TOM core complex.* Cell Discov, 2020. **6**: p. 67.
286. Tucker, K. and E. Park, *Cryo-EM structure of the mitochondrial protein-import channel TOM complex at near-atomic resolution.* Nat Struct Mol Biol, 2019. **26**(12): p. 1158-1166.
287. Araiso, Y., et al., *Structure of the mitochondrial import gate reveals distinct preprotein paths.* Nature, 2019. **575**(7782): p. 395-401.
288. Roumia, A.F., et al., *Landscape of Eukaryotic Transmembrane Beta Barrel Proteins.* J Proteome Res, 2020. **19**(3): p. 1209-1221.
289. Quinones, L.S., et al., *Unique Interactions of the Small Translocases of the Mitochondrial Inner Membrane (Tims) in Trypanosoma brucei.* Int J Mol Sci, 2024. **25**(3).
290. Wenger, C., et al., *A trypanosomal orthologue of an intermembrane space chaperone has a non-canonical function in biogenesis of the single mitochondrial inner membrane protein translocase.* PLoS Pathog, 2017. **13**(8): p. e1006550.
291. Takeda, H., et al., *A multipoint guidance mechanism for beta-barrel folding on the SAM complex.* Nat Struct Mol Biol, 2023. **30**(2): p. 176-187.
292. Sharma, S., U.K. Singha, and M. Chaudhuri, *Role of Tob55 on mitochondrial protein biogenesis in Trypanosoma brucei.* Mol Biochem Parasitol, 2010. **174**(2): p. 89-100.

293. Herrmann, J.M. and J. Riemer, *The intermembrane space of mitochondria.* Antioxid Redox Signal, 2010. **13**(9): p. 1341-58.
294. Haindrich, A.C., et al., *The intermembrane space protein Erv1 of Trypanosoma brucei is essential for mitochondrial Fe-S cluster assembly and operates alone.* Mol Biochem Parasitol, 2017. **214**: p. 47-51.
295. Harsman, A., et al., *The non-canonical mitochondrial inner membrane presequence translocase of trypanosomatids contains two essential rhomboid-like proteins.* Nat Commun, 2016. **7**: p. 13707.
296. Doyle, S.R., et al., *Evidence of evolutionary constraints that influences the sequence composition and diversity of mitochondrial matrix targeting signals.* PLoS One, 2013. **8**(6): p. e67938.
297. Rout, S., et al., *Determinism and contingencies shaped the evolution of mitochondrial protein import.* Proc Natl Acad Sci U S A, 2021. **118**(6).
298. Singha, U.K., et al., *Characterization of the mitochondrial inner membrane protein translocator Tim17 from Trypanosoma brucei.* Mol Biochem Parasitol, 2008. **159**(1): p. 30-43.
299. Zhang, Y., et al., *Structure of the mitochondrial TIM22 complex from yeast.* Cell Res, 2021. **31**(3): p. 366-368.
300. von Kanel, C., et al., *Intermembrane space-localized TbTim15 is an essential subunit of the single mitochondrial inner membrane protein translocase of trypanosomes.* Mol Microbiol, 2024. **121**(6): p. 1112-1126.
301. Desy, S., A. Schneider, and J. Mani, *Trypanosoma brucei has a canonical mitochondrial processing peptidase.* Mol Biochem Parasitol, 2012. **185**(2): p. 161-4.
302. von Kanel, C., et al., *Homologue replacement in the import motor of the mitochondrial inner membrane of trypanosomes.* Elife, 2020. **9**.
303. Hancock, K. and S.L. Hajduk, *The mitochondrial tRNAs of Trypanosoma brucei are nuclear encoded.* J Biol Chem, 1990. **265**(31): p. 19208-15.
304. Schneider, A., J. Martin, and N. Agabian, *A nuclear encoded tRNA of Trypanosoma brucei is imported into mitochondria.* Mol Cell Biol, 1994. **14**(4): p. 2317-22.
305. Hauser, R. and A. Schneider, *tRNAs are imported into mitochondria of Trypanosoma brucei independently of their genomic context and genetic origin.* EMBO J, 1995. **14**(17): p. 4212-20.
306. Mottram, J.C., et al., *tRNAs of Trypanosoma brucei. Unusual gene organization and mitochondrial importation.* J Biol Chem, 1991. **266**(27): p. 18313-7.
307. Suzuki, T., A. Nagao, and T. Suzuki, *Human mitochondrial tRNAs: biogenesis, function, structural aspects, and diseases.* Annu Rev Genet, 2011. **45**: p. 299-329.
308. Schneider, A., *Mitochondrial tRNA import and its consequences for mitochondrial translation.* Annu Rev Biochem, 2011. **80**: p. 1033-53.
309. Kapushoc, S.T., et al., *End processing precedes mitochondrial importation and editing of tRNAs in Leishmania tarentolae.* J Biol Chem, 2000. **275**(48): p. 37907-14.
310. Huot, J.L., S. Shikha, and A. Schneider, *Inducible orthogonal aminoacylation demonstrates that charging is required for mitochondrial tRNA import in Trypanosoma brucei.* Sci Rep, 2019. **9**(1): p. 10836.
311. Bouzaidi-Tiali, N., et al., *Elongation factor 1a mediates the specificity of mitochondrial tRNA import in T. brucei.* EMBO J, 2007. **26**(20): p. 4302-12.
312. Shikha, S., et al., *tRNA Biology in Trypanosomes.* Chimia (Aarau), 2019. **73**(5): p. 395-405.
313. Niemann, M., et al., *tRNAs and proteins use the same import channel for translocation across the mitochondrial outer membrane of trypanosomes.* Proc Natl Acad Sci U S A, 2017. **114**(37): p. E7679-E7687.

314. Shikha, S., et al., *tRNA import across the mitochondrial inner membrane in T. brucei requires TIM subunits but is independent of protein import.* Nucleic Acids Res, 2020. **48**(21): p. 12269-12281.
315. Parrot, C., et al., *Peculiarities of aminoacyl-tRNA synthetases from trypanosomatids.* J Biol Chem, 2021. **297**(2): p. 100913.
316. Rettig, J., et al., *Dual targeting of isoleucyl-tRNA synthetase in Trypanosoma brucei is mediated through alternative trans-splicing.* Nucleic Acids Res, 2012. **40**(3): p. 1299-306.
317. Espanol, Y., et al., *A mechanism for functional segregation of mitochondrial and cytosolic genetic codes.* Proc Natl Acad Sci U S A, 2009. **106**(46): p. 19420-5.
318. Charriere, F., et al., *Dual targeting of a tRNAAsp requires two different aspartyl-tRNA synthetases in Trypanosoma brucei.* J Biol Chem, 2009. **284**(24): p. 16210-16217.
319. Charriere, F., et al., *Dual targeting of a single tRNA(Trp) requires two different tryptophanyl-tRNA synthetases in Trypanosoma brucei.* Proc Natl Acad Sci U S A, 2006. **103**(18): p. 6847-52.
320. Knight, R.D., S.J. Freeland, and L.F. Landweber, *Rewiring the keyboard: evolvability of the genetic code.* Nat Rev Genet, 2001. **2**(1): p. 49-58.
321. RajBhandary, U.L., *Initiator transfer RNAs.* J Bacteriol, 1994. **176**(3): p. 547-52.
322. Tan, T.H., et al., *Eukaryotic-type elongator tRNAMet of Trypanosoma brucei becomes formylated after import into mitochondria.* Proc Natl Acad Sci U S A, 2002. **99**(3): p. 1152-7.
323. Bouzaidi-Tiali, N., et al., *Type 3 peptide deformylases are required for oxidative phosphorylation in Trypanosoma brucei.* Mol Microbiol, 2007. **65**(5): p. 1218-28.
324. Charriere, F., T.H. Tan, and A. Schneider, *Mitochondrial initiation factor 2 of Trypanosoma brucei binds imported formylated elongator-type tRNA(Met).* J Biol Chem, 2005. **280**(16): p. 15659-65.
325. Schneider, A., *A short history of guide RNAs: The intricate path that led to the discovery of a basic biological concept.* EMBO Rep, 2020. **21**(12): p. e51918.
326. Aphasizheva, I., et al., *Lexis and Grammar of Mitochondrial RNA Processing in Trypanosomes.* Trends Parasitol, 2020. **36**(4): p. 337-355.
327. Ramrath, D.J.F., et al., *Evolutionary shift toward protein-based architecture in trypanosomal mitochondrial ribosomes.* Science, 2018. **362**(6413).
328. Jensen, R.E. and P.T. Englund, *Network news: the replication of kinetoplast DNA.* Annu Rev Microbiol, 2012. **66**: p. 473-91.
329. Hajduk, S. and T. Ochsenreiter, *RNA editing in kinetoplastids.* RNA Biol, 2010. **7**(2): p. 229-36.
330. McDermott, S.M., et al., *The Architecture of Trypanosoma brucei editosomes.* Proc Natl Acad Sci U S A, 2016. **113**(42): p. E6476-E6485.
331. Koslowsky, D., et al., *The insect-phase gRNA transcriptome in Trypanosoma brucei.* Nucleic Acids Res, 2014. **42**(3): p. 1873-86.
332. Kirby, L.E., et al., *Analysis of the Trypanosoma brucei EATRO 164 Bloodstream Guide RNA Transcriptome.* PLoS Negl Trop Dis, 2016. **10**(7): p. e0004793.
333. Blum, B., N. Bakalara, and L. Simpson, *A model for RNA editing in kinetoplastid mitochondria: "guide" RNA molecules transcribed from maxicircle DNA provide the edited information.* Cell, 1990. **60**(2): p. 189-98.
334. Cooper, S., et al., *Assembly and annotation of the mitochondrial minicircle genome of a differentiation-competent strain of Trypanosoma brucei.* Nucleic Acids Res, 2019. **47**(21): p. 11304-11325.
335. Maslov, D.A. and L. Simpson, *The polarity of editing within a multiple gRNA-mediated domain is due to formation of anchors for upstream gRNAs by downstream editing.* Cell, 1992. **70**(3): p. 459-67.

336. Liu, S., et al., *Structural basis of gRNA stabilization and mRNA recognition in trypanosomal RNA editing.* Science, 2023. **381**(6653): p. eadg4725.
337. Ochsenreiter, T., M. Cipriano, and S.L. Hajduk, *Alternative mRNA editing in trypanosomes is extensive and may contribute to mitochondrial protein diversity.* PLoS One, 2008. **3**(2): p. e1566.
338. Kirby, L.E. and D. Koslowsky, *Mitochondrial dual-coding genes in Trypanosoma brucei.* PLoS Negl Trop Dis, 2017. **11**(10): p. e0005989.
339. Ochsenreiter, T., et al., *Alternative RNA editing produces a novel protein involved in mitochondrial DNA maintenance in trypanosomes.* Mol Cell Biol, 2008. **28**(18): p. 5595-604.
340. Liu, K., et al., *Accurate de novo peptide sequencing using fully convolutional neural networks.* Nat Commun, 2023. **14**(1): p. 7974.
341. Eloff, K., et al., *InstaNovo enables diffusion-powered de novo peptide sequencing in large-scale proteomics experiments.* Nature Machine Intelligence 2025, 2025.
342. Greber, B.J. and N. Ban, *Structure and Function of the Mitochondrial Ribosome.* Annu Rev Biochem, 2016. **85**: p. 103-32.
343. Rodriguez-Almonacid, C.C., et al., *Ribosome Specialization in Protozoa Parasites.* Int J Mol Sci, 2023. **24**(8).
344. Dass, S., M.W. Mather, and H. Ke, *Divergent Mitochondrial Ribosomes in Unicellular Parasitic Protozoans.* Trends Parasitol, 2020. **36**(4): p. 318-321.
345. Wang, C., et al., *Apicomplexan mitoribosome from highly fragmented rRNAs to a functional machine.* Nat Commun, 2024. **15**(1): p. 10689.
346. Shikha, S., et al., *Numerous rRNA molecules form the apicomplexan mitoribosome via repurposed protein and RNA elements.* Nat Commun, 2025. **16**(1): p. 817.
347. Watson, Z.L., et al., *Structure of the bacterial ribosome at 2 A resolution.* Elife, 2020. **9**.
348. Bieri, P., B.J. Greber, and N. Ban, *High-resolution structures of mitochondrial ribosomes and their functional implications.* Curr Opin Struct Biol, 2018. **49**: p. 44-53.
349. Saurer, M., et al., *Mitoribosomal small subunit biogenesis in trypanosomes involves an extensive assembly machinery.* Science, 2019. **365**(6458): p. 1144-1149.
350. Lukes, J., et al., *Kinetoplast DNA network: evolution of an improbable structure.* Eukaryot Cell, 2002. **1**(4): p. 495-502.
351. Thiemann, O.H., D.A. Maslov, and L. Simpson, *Disruption of RNA editing in Leishmania tarentolae by the loss of minicircle-encoded guide RNA genes.* EMBO J, 1994. **13**(23): p. 5689-700.
352. Geerts, M., et al., *Deep kinetoplast genome analyses result in a novel molecular assay for detecting Trypanosoma brucei gambiense-specific minicircles.* NAR Genom Bioinform, 2022. **4**(4): p. lqac081.
353. Herreros-Cabello, A., et al., *Mitochondrial DNA Structure in Trypanosoma cruzi.* Pathogens, 2025. **14**(1).
354. Shapiro, T.A. and P.T. Englund, *The structure and replication of kinetoplast DNA.* Annu Rev Microbiol, 1995. **49**: p. 117-43.
355. Schneider, A., *Unique aspects of mitochondrial biogenesis in trypanosomatids.* Int J Parasitol, 2001. **31**(13): p. 1403-15.
356. Xu, C.W., et al., *Nucleus-encoded histone H1-like proteins are associated with kinetoplast DNA in the trypanosomatid Crithidia fasciculata.* Mol Cell Biol, 1996. **16**(2): p. 564-76.
357. Milman, N., et al., *Mitochondrial origin-binding protein UMSBP mediates DNA replication and segregation in trypanosomes.* Proc Natl Acad Sci U S A, 2007. **104**(49): p. 19250-5.
358. Savill, N.J. and P.G. Higgs, *A theoretical study of random segregation of minicircles in trypanosomatids.* Proc Biol Sci, 1999. **266**(1419): p. 611-20.

359. Carpenter, L.R. and P.T. Englund, *Kinetoplast maxicircle DNA replication in Crithidia fasciculata and Trypanosoma brucei.* Mol Cell Biol, 1995. **15**(12): p. 6794-803.
360. Packer, J.A., et al., *Characterization of Allobodo yubaba sp. nov. and Novijibodo darinka gen. et sp. nov., cultivable free-living species of the phylogenetically enigmatic kinetoplastid taxon Allobodonidae.* J Eukaryot Microbiol, 2025. **72**(1): p. e13072.
361. Blom, D., et al., *Mitochondrial minicircles in the free-living bodonid Bodo saltans contain two gRNA gene cassettes and are not found in large networks.* RNA, 2000. **6**(1): p. 121-35.
362. Blom, D., et al., *RNA editing in the free-living bodonid Bodo saltans.* Nucleic Acids Res, 1998. **26**(5): p. 1205-13.
363. Lukes, J., et al., *Massive mitochondrial DNA content in diplonemid and kinetoplastid protists.* IUBMB Life, 2018. **70**(12): p. 1267-1274.
364. Lukescaron, J., et al., *Pankinetoplast DNA structure in a primitive bodonid flagellate, Cryptobia helicis.* EMBO J, 1998. **17**(3): p. 838-46.
365. Gerasimov, E.S., et al., *Mitochondrial RNA editing in Trypanoplasma borreli: New tools, new revelations.* Comput Struct Biotechnol J, 2022. **20**: p. 6388-6402.
366. Stolba, P., M. Jirku, and J. Lukes, *Polykinetoplast DNA structure in Dimastigella trypaniformis and Dimastigella mimosa (Kinetoplastida).* Mol Biochem Parasitol, 2001. **113**(2): p. 323-6.
367. Zikova, A., et al., *Cruzella marina (Bodonina, Kinetoplastida): non-catenated structure of poly-kinetoplast DNA.* Exp Parasitol, 2003. **104**(3-4): p. 159-61.
368. Tikhonenkov, D.V., et al., *First finding of free-living representatives of Prokinetoplastina and their nuclear and mitochondrial genomes.* Sci Rep, 2021. **11**(1): p. 2946.
369. Aeschlimann, S., P. Stettler, and A. Schneider, *DNA segregation in mitochondria and beyond: insights from the trypanosomal tripartite attachment complex.* Trends Biochem Sci, 2023. **48**(12): p. 1058-1070.
370. Schneider, A. and T. Ochsenreiter, *Failure is not an option - mitochondrial genome segregation in trypanosomes.* J Cell Sci, 2018. **131**(18).
371. Gluenz, E., et al., *The kinetoplast duplication cycle in Trypanosoma brucei is orchestrated by cytoskeleton-mediated cell morphogenesis.* Mol Cell Biol, 2011. **31**(5): p. 1012-21.
372. Robertson, M., *Notes on the life-history of Trypanosoma gambiense, with a brief reference to the cycles of Trypanosoma nanum and Trypanosoma pecorum in Glossina palpalis.* Philosophical Transactions of the Royal Society of London. Series B, Containing Papers of a Biological Character, 1913. **203**(294-302).
373. Cadena, L.R., et al., *A novel nabelschnur protein regulates segregation of the kinetoplast DNA in Trypanosoma brucei.* Curr Biol, 2024. **34**(20): p. 4803-4812 e3.
374. Pena-Diaz, P., et al., *A leucine aminopeptidase is involved in kinetoplast DNA segregation in Trypanosoma brucei.* PLoS Pathog, 2017. **13**(4): p. e1006310.
375. Povelones, M.L. and M.L. Ginger, *Bric-a-brac, an 'umbilical cord' and trypanosome kinetoplast segregation.* Trends Parasitol, 2024. **40**(12): p. 1072-1074.
376. Wheeler, R.J., et al., *Cytokinesis in Trypanosoma brucei differs between bloodstream and tsetse trypomastigote forms: implications for microtubule-based morphogenesis and mutant analysis.* Mol Microbiol, 2013. **90**(6): p. 1339-55.
377. Zhou, Q., et al., *A coiled-coil- and C2-domain-containing protein is required for FAZ assembly and cell morphology in Trypanosoma brucei.* J Cell Sci, 2011. **124**(Pt 22): p. 3848-58.
378. Kohl, L., D. Robinson, and P. Bastin, *Novel roles for the flagellum in cell morphogenesis and cytokinesis of trypanosomes.* EMBO J, 2003. **22**(20): p. 5336-46.

379. Souza Onofre, T., et al., *The microtubule quartet protein SNAP1 in Trypanosoma brucei facilitates flagellum and cell division plane positioning by promoting basal body segregation.* J Biol Chem, 2023. **299**(11): p. 105340.
380. Pham, K.T.M., et al., *A Spef1-interacting microtubule quartet protein in Trypanosoma brucei promotes flagellar inheritance by regulating basal body segregation.* J Biol Chem, 2022. **298**(7): p. 102125.
381. Gheiratmand, L., et al., *Biochemical characterization of the bi-lobe reveals a continuous structural network linking the bi-lobe to other single-copied organelles in Trypanosoma brucei.* J Biol Chem, 2013. **288**(5): p. 3489-99.
382. Dong, X., et al., *Basal Body Protein TbSAF1 Is Required for Microtubule Quartet Anchorage to the Basal Bodies in Trypanosoma brucei.* mBio, 2020. **11**(3).
383. Robinson, D.R. and K. Gull, *Basal body movements as a mechanism for mitochondrial genome segregation in the trypanosome cell cycle.* Nature, 1991. **352**(6337): p. 731-3.
384. Ogbadoyi, E.O., D.R. Robinson, and K. Gull, *A high-order trans-membrane structural linkage is responsible for mitochondrial genome positioning and segregation by flagellar basal bodies in trypanosomes.* Mol Biol Cell, 2003. **14**(5): p. 1769-79.
385. Povelones, M.L., *Beyond replication: division and segregation of mitochondrial DNA in kinetoplastids.* Mol Biochem Parasitol, 2014. **196**(1): p. 53-60.
386. Zhao, Z., et al., *p166, a link between the trypanosome mitochondrial DNA and flagellum, mediates genome segregation.* EMBO J, 2008. **27**(1): p. 143-54.
387. Schnarwiler, F., et al., *Trypanosomal TAC40 constitutes a novel subclass of mitochondrial beta-barrel proteins specialized in mitochondrial genome inheritance.* Proc Natl Acad Sci U S A, 2014. **111**(21): p. 7624-9.
388. Hoffmann, A., et al., *Molecular model of the mitochondrial genome segregation machinery in Trypanosoma brucei.* Proc Natl Acad Sci U S A, 2018. **115**(8): p. E1809-E1818.
389. Amodeo, S., M. Jakob, and T. Ochsenreiter, *Characterization of the novel mitochondrial genome replication factor MiRF172 in Trypanosoma brucei.* J Cell Sci, 2018. **131**(8).
390. Amodeo, S., et al., *Characterization of two novel proteins involved in mitochondrial DNA anchoring in Trypanosoma brucei.* PLoS Pathog, 2023. **19**(7): p. e1011486.
391. Jetishi, C., et al., *Beyond a Linear Structure: The Tubular Organization of the Tripartite Attachment Complex and the Functional Role of TAC53.* bioRxiv, 2025: p. 2025.05.14.653994.
392. Aeschlimann, S., et al., *Single p197 molecules of the mitochondrial genome segregation system of Trypanosoma brucei determine the distance between basal body and outer membrane.* Proc Natl Acad Sci U S A, 2022. **119**(40): p. e2204294119.
393. Berriman, M., et al., *The genome of the African trypanosome Trypanosoma brucei.* Science, 2005. **309**(5733): p. 416-22.
394. Naguleswaran, A., et al., *Developmental changes and metabolic reprogramming during establishment of infection and progression of Trypanosoma brucei brucei through its insect host.* PLoS Negl Trop Dis, 2021. **15**(9): p. e0009504.
395. Rabuffo, C., et al., *Inter-chromosomal transcription hubs shape the 3D genome architecture of African trypanosomes.* Nat Commun, 2024. **15**(1): p. 10716.
396. Bregy, I., et al., *Cryo-electron tomography sheds light on the elastic nature of the Trypanosoma brucei tripartite attachment complex.* bioRxiv, 2023-03-07.
397. Stebeck, C.E., et al., *Kinetoplastid membrane protein-11 (KMP-11) is differentially expressed during the life cycle of African trypanosomes and is found in a wide variety of kinetoplastid parasites.* Mol Biochem Parasitol, 1995. **71**(1): p. 1-13.
398. Li, Z. and C.C. Wang, *KMP-11, a basal body and flagellar protein, is required for cell division in Trypanosoma brucei.* Eukaryot Cell, 2008. **7**(11): p. 1941-50.

399. Aeschlimann, S.J., *From the basal body to the mitochondrial genome: linking up the tripartite attachment complex subunits in Trypanosoma brucei*, in *Departement for Chemistry, Biochemistry, and Pharmaceutical Sciences*. 2022, University of Bern.
400. Pusnik, M., et al., *An essential novel component of the noncanonical mitochondrial outer membrane protein import system of trypanosomatids.* Mol Biol Cell, 2012. **23**(17): p. 3420-8.
401. Kaser, S., et al., *Biogenesis of the mitochondrial DNA inheritance machinery in the mitochondrial outer membrane of Trypanosoma brucei.* PLoS Pathog, 2017. **13**(12): p. e1006808.
402. Schimanski, B., et al., *p166 links membrane and intramitochondrial modules of the trypanosomal tripartite attachment complex.* PLoS Pathog, 2022. **18**(6): p. e1010207.
403. Baudouin, H.C.M., L. Pfeiffer, and T. Ochsenreiter, *A comparison of three approaches for the discovery of novel tripartite attachment complex proteins in Trypanosoma brucei.* PLoS Negl Trop Dis, 2020. **14**(9): p. e0008568.
404. Trikin, R., et al., *TAC102 Is a Novel Component of the Mitochondrial Genome Segregation Machinery in Trypanosomes.* PLoS Pathog, 2016. **12**(5): p. e1005586.
405. Beck, K., et al., *Trypanosoma brucei Tb927.2.6100 is an essential protein associated with kinetoplast DNA.* Eukaryot Cell, 2013. **12**(7): p. 970-8.
406. Amodeo, S., et al., *Characterization of the novel mitochondrial genome segregation factor TAP110 in Trypanosoma brucei.* J Cell Sci, 2021. **134**(5).
407. Andre, J., et al., *The tubulin cofactor C family member TBCCD1 orchestrates cytoskeletal filament formation.* J Cell Sci, 2013. **126**(Pt 23): p. 5350-6.
408. Ochsenreiter, T. and S.L. Hajduk, *Alternative editing of cytochrome c oxidase III mRNA in trypanosome mitochondria generates protein diversity.* EMBO Rep, 2006. **7**(11): p. 1128-33.
409. Schnaufer, A., *Evolution of dyskinetoplastic trypanosomes: how, and how often?* Trends Parasitol, 2010. **26**(12): p. 557-8.
410. Schnaufer, A., G.J. Domingo, and K. Stuart, *Natural and induced dyskinetoplastic trypanosomatids: how to live without mitochondrial DNA.* Int J Parasitol, 2002. **32**(9): p. 1071-84.
411. Sykes, S.E. and S.L. Hajduk, *Dual Functions of α-Ketoglutarate Dehydrogenase E2 in the Krebs Cycle and Mitochondrial DNA Inheritance in.* Eukaryotic Cell, 2013. **12**(1): p. 78-90.
412. Clayton, A.M., et al., *Depletion of mitochondrial acyl carrier protein in bloodstream-form Trypanosoma brucei causes a kinetoplast segregation defect.* Eukaryot Cell, 2011. **10**(3): p. 286-92.
413. Speck, S., *The impact of ACP RNAi on the tripartite attachment complex (TAC) in Trypanosoma brucei*, in *Departement for Chemistry, Biochemistry, and Pharmaceutical Sciences*. 2023, University of Bern.
414. Billington, K., et al., *Genome-wide subcellular protein map for the flagellate parasite Trypanosoma brucei.* Nat Microbiol, 2023. **8**(3): p. 533-547.
415. Sunter, J.D., S. Dean, and R.J. Wheeler, *TrypTag.org: from images to discoveries using genome-wide protein localisation in Trypanosoma brucei.* Trends Parasitol, 2023. **39**(5): p. 328-331.
416. Yague-Capilla, M., et al., *A Mitochondrial Orthologue of the dNTP Triphosphohydrolase SAMHD1 Is Essential and Controls Pyrimidine Homeostasis in Trypanosoma brucei.* ACS Infect Dis, 2021. **7**(2): p. 318-332.
417. Pyrih, J., et al., *Comprehensive sub-mitochondrial protein map of the parasitic protist Trypanosoma brucei defines critical features of organellar biology.* Cell Rep, 2023. **42**(9): p. 113083.

418. Cadena, L.R., et al., *Characterization of novel and essential kinetoplast-associated proteins in Trypanosoma brucei.* bioRxiv, 2024-04-23.
419. Kalichava, A. and T. Ochsenreiter, *Ultrastructure expansion microscopy in Trypanosoma brucei.* Open Biol, 2021. **11**(10): p. 210132.
420. Chen, F., P.W. Tillberg, and E.S. Boyden, *Optical imaging. Expansion microscopy.* Science, 2015. **347**(6221): p. 543-8.
421. Jackson, A.P., M.A. Quail, and M. Berriman, *Insights into the genome sequence of a free-living Kinetoplastid: Bodo saltans (Kinetoplastida: Euglenozoa).* BMC Genomics, 2008. **9**: p. 594.
422. Sun, Q., *The Hydrophobic Effects: Our Current Understanding.* Molecules, 2022. **27**(20).
423. Kim, J., et al., *VDAC oligomers form mitochondrial pores to release mtDNA fragments and promote lupus-like disease.* Science, 2019. **366**(6472): p. 1531-1536.
424. Keinan, N., D. Tyomkin, and V. Shoshan-Barmatz, *Oligomerization of the mitochondrial protein voltage-dependent anion channel is coupled to the induction of apoptosis.* Mol Cell Biol, 2010. **30**(24): p. 5698-709.
425. Stettler, P., *Quantification of TAC40 and TAC42 Reveals Insights into the Molecular Composition and Structure of the Tripartite Attachment Complex*, in *Departement for Chemistry, Biochemistry, and Pharmaceutical Sciences*. 2019, University of Bern.

Acknowledgements

This thesis could not have been realized without the professional and personal support of many people. I am thankful to everyone who guided and supported me in the past years.

I am grateful to my supervisor, André Schneider. Under your supervision, I had the opportunity to grow as a scientist and continuously improve my skill set. You gave me the freedom to drive projects and develop new approaches and ideas, while supporting my work and guiding me with your critical thinking. I thank you for the trust in me and my work.

I thank my thesis co-advisor Torsten Ochsenreiter. As a TAC researcher, you have been the perfect person for this position. I am grateful for the numerous discussions we had about my projects and all the input I could take from them. I also thank my thesis mentor, Tosso Leeb, for assessing my annual GCB reports and for being the GCB representative of my thesis committee. Furthermore, I thank Megan Povelones for assessing this thesis as an external co-referee. I am honoured that you, as one of the researchers involved in the discovery of the first TAC subunit, have been involved in my work.

Special thanks go to all members of the final season of the Schneider group. Research is not the effort of a single person, but a collective of inputs, suggestions, criticism, contaminations, and collaborations. However, research is also not everything, and working not with colleagues but with friends is a gift I am grateful for.

I thank you, Bernd Schimanski, for all personal and scientific support. I initially joined the Schneider group because the Bachelor's thesis project about the TAC sounded interesting, but I stayed in this lab because you taught me to acknowledge the beauty of a simple SDS-PAGE and because you exemplified to me that what we do is not called "re"search for no reason. It is thanks to your genius SDS-PAGE-blotting-sandwich-assembly technique that I have not torn a single gel.

Thank you Salome Aeschlimann, for all your support and advice. To add a citation to this paragraph: I may not always be right, but plasmid dephosphorylation is always wrong. Anyways, no one is perfect, but a dephosphorylated plasmid is clearly not. Alright, I digress, it has been a pleasure working with you on this beautiful protein complex, team TAC forever! Many thanks, Simona Amodeo, for all your help and advice you had to give me as my office and bench neighbour. I hereby apologize for hiding Günter and his friends in your drawer, over and over again. Corinne von Känel, I thank you for MaRF11. Jokes aside, many thanks for all your help and the plentiful donkey walks and plant shoppings! Advaitha Iyer, I thank you for all the horrible

jokes and for an amazing time on the Hudson river, sorry that I made you wet. I thank you, Markus Gerber, for all your generous financial support, and the fun times in the lab or as roommates on meetings. I know a Metal-Star! Stephan Berger, the last Schneidi standing, I thank you for all your support, the great time in Barcelona, and for providing a negative control of sunscreen use. I thank Siri Speck and Carmela Esposito as well as all past group members not mentioned by their names for being a part of my PhD journey.

Outside the workplace, I am grateful to have a second workplace, the Papiliorama. Even though the people there have not been involved in my scientific work, I am grateful for all friends and colleagues I have there. There is no other place that frees my mind more.

I am grateful for all the support I have from my family and friends. This thesis is thanks to all of you. I especially thank my mother and father, who continuously support me and never have a doubt about me or my plan(t)s. I thank my two sisters, which may not always make my life more enjoyable but certainly more interesting <3. Our family dog will never be forgotten. Last but certainly not least, I thank my grandfather, who sparked my fascination for nature.

Declaration of originality

Last name, first name: Stettler, Philip

Matriculation number: 16-108-037

I hereby declare that this thesis represents my original work and that I have used no other sources except as noted by citations.

All data, tables, figures and text citations which have been reproduced from any other source, including the internet, have been explicitly acknowledged as such.

During the preparation of this work, I have used 'ChatGPT-4.0'-based large language models to improve the readability of self-written text. I reviewed and edited the generated text as needed and take full responsibility for the content. I am aware that in case of dis-compliance, the generated text is considered as plagiarism with its legal consequences.

I am aware that in case of non-compliance, the Senate is entitled to withdraw the doctorate degree awarded to me on the basis of the present thesis, in accordance with the "Statut der Universität Bern (Universitätsstatut; UniSt)", Art. 69, of 7 June 2011.

Place, date: Bern, 12.06.2025

Signature